Winter 2014

Development of hybrid composite co-pultruded structural members

Hart Noah Honickman
University of Windsor

Recommended Citation

Honickman, Hart Noah, "Development of hybrid composite co-pultruded structural members" (2014). *Electronic Theses and Dissertations*. Paper 5018.

DEVELOPMENT OF HYBRID COMPOSITE CO-PULTRUDED STRUCTURAL MEMBERS

by
Hart Noah Honickman

A Dissertation
Submitted to the Faculty of Graduate Studies
through Mechanical, Automotive, & Materials Engineering
in Partial Fulfillment of the Requirements for
the Degree of Doctor of Philosophy at the
University of Windsor

Windsor, Ontario, Canada

DEVELOPMENT OF HYBRID COMPOSITE CO-PULTRUDED STRUCTURAL MEMBERS

by

Hart Noah Honickman

APPROVED BY:

Dr. J. Wood, External Examiner
The University of Western Ontario

Dr. S. Cheng
Department of Civil & Environmental Engineering

Dr. W. Altenhof
Department of Mechanical, Automotive, & Materials Engineering

---

Dr. N. Zamani
Department of Mechanical, Automotive, & Materials Engineering

---

Dr. J. Johrendt, Advisor
Department of Mechanical, Automotive, & Materials Engineering

---

Dr. P. Frise, Co-Advisor
Department of Mechanical, Automotive, & Materials Engineering

December 5, 2013

Declaration of Co-Authorship and Previous Publication

Co-Authorship Declaration

I hereby declare that this thesis incorporates material that is result of joint research, as follows:

- This dissertation incorporates parts of a state-of-the-art review of literature that was included in a manuscript that was produced in collaboration with Dr. Derek Northwood. Some content from this review of literature is included in Sections 1.2.3, 1.2.4, 1.2.5, & 1.2.9 of this dissertation. In all cases, the key ideas and primary contributions were provided by the author, and the contribution of the co-authors was primarily of a supervisory nature.

I am aware of the University of Windsor Senate Policy on Authorship and I certify that I have properly acknowledged the contribution of other researchers to my thesis, and have obtained written permission from each of the co-author(s) to include the above material(s) in my thesis.

I certify that, with the above qualification, this thesis, and the research to which it refers, is the product of my own work.

Declaration of Previous Publication

This thesis includes content from two original manuscripts that have been previously published in peer reviewed journals and/or conference proceedings, as follows:

Dissertation Section	**Publication title / full citation**	**Publication status**
Sections 1.2.3, 1.2.4, 1.2.5, & 1.2.9	H. Honickman, J. Johrendt, D. Northwood, and P. Frise. Design of a pultruded steel-GFRP hybrid structural member. In *proceedings of the ASME 2010 International Mechanical Engineering Congress and Exposition*, number IMECE2010-37378, Vancouver, British Columbia, Canada, November 12–18, 2010. American Society of Mechanical Engineers (ASME).	Published
Section 3.11	H. Honickman, J. Johrendt, and P. Frise. On the torsional stiffness of thick laminated plates. *Journal of Composite Materials*, pages 1–17. published online before print September 11, 2013, DOI 10.1177/0021998313501919.	Published online before print

I certify that I have obtained a written permission from the copyright owner(s) to include the above published material(s) in my thesis. I certify that the above material describes work completed during my registration as graduate student at the University of Windsor.

I declare that, to the best of my knowledge, my thesis does not infringe upon anyone's copyright nor violate any proprietary rights and that any ideas, techniques, quotations, or any other material from the work of other people included in my thesis, published or otherwise, are fully acknowledged in accordance with the standard referencing practices. Furthermore, to the extent that I have included copyrighted material that surpasses the bounds of fair dealing within the meaning of the Canada Copyright Act, I certify that I have obtained a written permission from the copyright owner(s) to include such material(s) in my thesis.

I declare that this is a true copy of my thesis, including any final revisions, as approved by my thesis committee and the Graduate Studies office, and that this thesis has not been submitted for a higher degree to any other University or Institution.

Abstract

Fibre reinforced polymer (FRP) materials offer many advantages over conventional metallic structural materials due to their high specific strength and stiffness, long fatigue life, and resistance to environmental corrosion. However, these materials present some unique engineering challenges due to their anisotropy and heterogeneity. The connection of these composite parts to adjacent components often results in complex and counter-intuitive states of stress that can be quite difficult to model. Furthermore, since these materials are, in a sense, synthesized during the fabrication of the final part, the mechanical properties that can be expected from FRP structures are largely dependent upon highly skilled workmanship.

Pultrusion is a manufacturing technique that is intended for the mass-production of long FRP parts having continuous cross-sectional geometry. Although it has not yet been optimized for the aerospace industry, with some qualification research, pultrusion may prove to offer many benefits over conventional methods of manufacturing composite aircraft parts. The present dissertation investigates the possibility of co-pultruding FRP parts with embedded non-FRP materials (such as metallic materials), which could serve as integral hard points to facilitate serviceable mechanical connections to adjacent parts. It is shown that these hybrid co-pultruded members offer substantial light-weighting benefits over conventional metallic components, while retaining the ability to employ serviceable mechanical fasteners.

Simple unidimensional beam models are of great value when validating the results of complex finite element analyses of aircraft wing-stringers, or other similar structural members. It is demonstrated in the present dissertation that classical unidimensional beam-type analytical models often yield unconservative predictions (over-predictions) of stiffness and elastic stability when used for the analyses of FRP beams and columns. In fact, specific examples are included in which classical methods are shown to over-predict torsional stiffness by 111.3%, over-predict warping stiffness by 40.3%, and over-predict critical column buckling loads by 103.63%. As such, this dissertation presents additional analytical procedures that enhance the fidelity of these classical analytical methods such that they can be utilized to accurately assess the stiffness and elastic stability of FRP beams and columns, including the hybrid composite co-pultruded members that are proposed in this dissertation.

I lovingly dedicate this dissertation
to my wife, Sophia,
&
to my parents, Gloria & Howard.

Acknowledgements

I would like to begin by thanking my supervisors, Dr. Jennifer Johrendt and Dr. Peter Frise, for the mentoring, inspiration, guidance, and expertise that they have provided throughout my doctoral studies. Specifically, I would like to thank Dr. Johrendt for always making herself available for my many impromptu meetings, and for allowing me just enough liberty in my research that I could freely follow my interests while simultaneously ensuring that I never strayed too far off task. I would also like to thank Dr. Frise for sharing his profound wisdom of practical engineering considerations, and for providing a wealth of networking opportunities, including one that facilitated an indispensable internship with Bombardier Inc.

In addition, I would like to thank my doctoral committee members, Dr. William Altenhof, Dr. Nader Zamani, Dr. Shaohong Cheng, and Dr. Jeff Wood, for providing their feedback on this dissertation.

This research would not have been possible without the financial contributions of the Natural Sciences and Engineering Research Council of Canada, the AUTO21 Network Centres of Excellence, the Ontario Centres of Excellence, Bombardier Inc., and the University of Windsor.

I would like to extend special thanks to Leo Kok, Moshe Domb, Graham Elliott, and Jonathan Hack of Bombardier Aerospace (Bombardier Inc.). Their willingness to share their wealth of engineering knowledge afforded me an intensity of learning that I have never before experienced.

I would like to extend my gratitude to my office mates, Rob Rieveley, Mike Johnston, Kevin Martin, Sean Maloney, André Levesque, and Mike Doody, for countless stimulating theoretical discussions, both relevant and irrelevant to this dissertation; these are the types of discussions that put the passion into engineering and science, and keep me coming back to it every day. Special thanks goes to Rob Rieveley for providing valuable mentorship and encouragement during the early phases of my studies, and to Mike Doody for sharing the burden of being amongst the very few FRP composites researchers at the University of Windsor. I also owe profound gratitude to Dr. Bruce Minaker for sharing countless informal technical discussions, and a for voluntarily providing me with a great deal of technical feedback throughout my doctoral research.

I also owe thanks for the technical and administrative assistance of Andrew Jenner, Patrick Seguin, Bruce Durfy, Matthew St. Louis, Jeannette Stewart, and Rosemarie Gignac.

I would like to extend special thanks to Dr. Amir Fam for inspiring and encouraging me to pursue graduate studies in engineering. It was under his tutelage, as both an undergraduate research assistant and as a Master's student, that I first became enamoured of academic research and structural engineering science.

I am eternally grateful to my parents, Gloria and Howard, who raised me to value education, and to passionately pursue my interests. I am also grateful to my sister, Julia, who has always lovingly encouraged and supported me throughout my studies.

Finally, I would like to thank my wonderful wife, Sophia, for all of her help with illustrations, and more importantly, for her ever enduring patience, support, and encouragement. For all intents and purposes, Sophia took it upon herself to essentially do everything necessary to keep me alive so that I could remain focused on my studies. I cannot imagine how I could possibly have completed this dissertation without her.

Hart Noah Honickman

Contents

List of Tables

List of Figures

List of Units and Abbreviations

Units

π	Ratio between circumference and diameter of a circle (approximately 3.141593)
%	Percent
C	Celsius
°	Degree (temperature or angle)
mm	Millimetre
cm	Centimetre
m	Metre
km	Kilometre
g	Gram
kg	Kilogram
N	Newton
kN	Kilonewton
Pa	Pascal
kPa	Kilopascal
MPa	Megapascal
GPa	Gigapascal
b	Bit
B	Byte (eight bits)
MB	Megabyte
GB	Gigabyte
Hz	Hertz
MHz	Megahertz
GHz	Gigahertz

Abbreviations and Acronyms

AC	Alternating Current
AFRP	Aramid Fibre Reinforced Polymer
ASTM	American Society for Testing and Materials
CAE	Computer Aided Engineering
CFM	Continuous Filament Mat (of randomly oriented fibres)
CFRP	Carbon Fibre Reinforced Polymer
CLPT	Classical Laminated Plate Theory
CNC	Computer Numeric Control
CTE	Coefficient of Thermal Expansion
DC	Direct Current
FE	Finite Element
FEA	Finite Element Analysis
FRP	Fibre Reinforced Polymer
GFRP	Glass Fibre Reinforced Polymer
ICAN	Integrated Composites Analyzer
MLB	Mechanics of Laminated Beams
PRSEUS	Pultruded Rod Stitched Efficient Unitized Structure
RAM	Random-Access Memory
VABS	Variational Asymptotic Beam Section
VAM	Variational Asymptotic Method
VOC	Volatile Organic Compound

Notation

General Notation

ε_{11} & σ_{11}	Normal strain and stress in the 1 direction, respectively
ε_{22} & σ_{22}	Normal strain and stress in the 2 direction, respectively
ε_{33} & σ_{33}	Normal strain and stress in the 3 direction, respectively
γ_{23} & τ_{23}	Engineering shear strain and shear stress in the 2-3 direction, respectively
γ_{13} & τ_{13}	Engineering shear strain and shear stress in the 1-3 direction, respectively
γ_{12} & τ_{12}	Engineering shear strain and shear stress in the 1-2 direction, respectively
E_{11}, E_{22}, & E_{33}	Normal elastic moduli in the 1, 2, and 3 directions, respectively
G_{23}, G_{13}, & G_{12}	Shear moduli in the 2-3, 1-3, and 1-2 directions, respectively
ν_{23}, ν_{13}, & ν_{12}	Poisson's ratios in the 2-3, 1-3, and 1-2 directions, respectively
u, v, & w	Displacements in the x, y, and z directions, respectively
ε_{xx} & σ_{xx}	Normal strain and stress in the x direction, respectively
ε_{yy} & σ_{yy}	Normal strain and stress in the y direction, respectively
ε_{zz} & σ_{zz}	Normal strain and stress in the z direction, respectively
γ_{yz} & τ_{yz}	Engineering shear strain and shear stress in the y-z direction, respectively
γ_{xz} & τ_{xz}	Engineering shear strain and shear stress in the x-z direction, respectively
γ_{xy} & τ_{xy}	Engineering shear strain and shear stress in the x-y direction, respectively
E_{xx}, E_{yy}, & E_{zz}	Normal elastic moduli in the x, y, and z directions, respectively
G_{yz}, G_{xz}, & G_{xy}	Shear moduli in the y-z, x-z, and x-y directions, respectively
ν_{yz}, ν_{xz}, & ν_{xy}	Poisson's ratios in the y-z, x-z, and x-y directions, respectively
ε_{XX} & σ_{XX}	Normal strain and stress in the X direction, respectively
ε_{YY} & σ_{YY}	Normal strain and stress in the Y direction, respectively
ε_{ZZ} & σ_{ZZ}	Normal strain and stress in the Z direction, respectively
γ_{YZ} & τ_{YZ}	Engineering shear strain and shear stress in the Y-Z direction, respectively
γ_{XZ} & τ_{XZ}	Engineering shear strain and shear stress in the X-Z direction, respectively
γ_{XY} & τ_{XY}	Engineering shear strain and shear stress in the X-Y direction, respectively

E_{XX}, E_{YY}, & E_{ZZ}	Normal elastic moduli in the X, Y, and Z directions, respectively
G_{YZ}, G_{XZ}, & G_{XY}	Shear moduli in the Y-Z, X-Z, and X-Y directions, respectively
ν_{YZ}, ν_{XZ}, & ν_{XY}	Poisson's ratios in the Y-Z, X-Z, and X-Y directions, respectively
$E_{X'X'}$, $E_{Y'Y'}$, & $E_{Z'Z'}$	Normal elastic moduli in the X', Y', and Z' directions, respectively
$G_{Y'Z'}$, $G_{X'Z'}$, & $G_{X'Y'}$	Shear moduli in the Y'-Z', X'-Z', and X'-Y' directions, respectively
$G_{XY'}$ & $G_{XZ'}$	Shear moduli in the X-Y' and X-Z' directions, respectively

Notation Used for Composite Laminate Analyses

E_f	Elastic modulus of fibres
E_m	Elastic modulus of polymeric resin matrix
ν_f	Poisson's ratio of fibres
ν_m	Poisson's ratio of polymeric resin matrix
V_f	Fibre volume fraction of FRP composite material
n	Total number of laminae (plies) within the laminate
h	Total thickness of the laminate, measured parallel to z axis
$\mathbf{S_{3D}}$	Three dimensional orthotropic compliance matrix
$\mathbf{Q}$	Lamina (ply) stiffness matrix within 1-2-3 local coordinate system
Q_{mn}	mn term of the $\mathbf{Q}$ matrix
$\bar{\mathbf{Q}}$	Lamina (ply) stiffness matrix within x-y-z laminate coordinate system
$\bar{Q}_{mn}$	mn term of the $\bar{\mathbf{Q}}$ matrix
$\bar{\mathbf{Q}}_\mathbf{k}$	Lamina (ply) stiffness matrix for k^{th} lamina, within x-y-z laminate coordinate system
$\bar{Q}_{mnk}$	mn term of the $\bar{\mathbf{Q}}_\mathbf{k}$ matrix for the k^{th} lamina
θ	Angle of fibres within lamina of interest relative to x axis of laminate coordinate system
$\mathbf{A}$	Extensional stiffness matrix for the laminate
$\mathbf{B}$	Coupling stiffness matrix for the laminate
$\mathbf{D}$	Bending stiffness matrix for the laminate
A_{mn}	mn term of the $\mathbf{A}$ matrix for the laminate
B_{mn}	mn term of the $\mathbf{B}$ matrix for the laminate
D_{mn}	mn term of the $\mathbf{D}$ matrix for the laminate
$\mathbf{C}$	Laminate stiffness matrix, comprising the $\mathbf{A}$, $\mathbf{B}$, and $\mathbf{D}$ matrices ($[\mathbf{C}] = [\mathbf{S}]^{-1}$)
$\mathbf{a}$	Extensional compliance matrix for the laminate
$\mathbf{b}$	Coupling compliance matrix for the laminate
$\mathbf{d}$	Bending compliance matrix for the laminate

a_{mn}	mn term of the **a** matrix for the laminate
b_{mn}	mn term of the **b** matrix for the laminate
d_{mn}	mn term of the **d** matrix for the laminate
S	Laminate compliance matrix, comprising the **a**, **b**, and **d** matrices ($[\mathbf{S}] = [\mathbf{C}]^{-1}$)
$z_{T\,k}$	Distance from the mid-plane of the laminate to the top surface of the k^{th} lamina
$z_{B\,k}$	Distance from the mid-plane of the laminate to the bottom surface of the k^{th} lamina
z_k	Elevation of the mid-plane of lamina k above the mid-plane of the laminate
$\sigma_{xx\,k}$	Normal stress in the x direction within lamina k
$\sigma_{yy\,k}$	Normal stress in the y direction within lamina k
$\tau_{xy\,k}$	In-plane x-y shear stress within lamina k
$\varepsilon_{xx\,k}$	Normal strain in the x direction within lamina k
$\varepsilon_{yy\,k}$	Normal strain in the y direction within lamina k
$\gamma_{xy\,k}$	In-plane x-y shear strain (engineering strain) within lamina k
N_{xx}	Normal force in the x direction, per unit width of laminate
N_{yy}	Normal force in the y direction, per unit width of laminate
N_{xy}	In-plane x-y shear force, per unit width of laminate
M_{xx}	Bending moment in the x-z plane, per unit width of laminate
M_{yy}	Bending moment in the y-z plane, per unit width of laminate
M_{xy}	Twisting moment, per unit width of laminate
ε_{xx}^{0}	Mid-plane normal strain in the x direction of the laminate
ε_{yy}^{0}	Mid-plane normal strain in the y direction of the laminate
γ_{xy}^{0}	Mid-plane in-plane x-y shear strain (engineering strain) in the laminate
k_{xx}	Bending curvature of the laminate in the x-z plane
k_{yy}	Bending curvature of the laminate in the y-z plane
k_{xy}	Twisting curvature of the laminate
e_{NAyy}	Vertical elevation of flexural neutral axis above laminate mid-plane
e_{npPT}	Vertical elevation of twisting neutral plane above laminate mid-plane, for pure torsion
e_{npFT}	Vertical elevation of twisting neutral plane above laminate mid-plane, for free torsion
$\frac{dEI_{yy}}{dy}$	Out-of-plane bending stiffness per unit width of laminate about its y axis

Notation Used for General Beam Analyses

A_E	Cross-sectional area of beam, normalized with respect to longitudinal elastic modulus
A_G	Cross-sectional area of beam, normalized with respect to shear modulus

A_i	Cross-sectional area of the i^{th} nodal region of the section
A_j	Cross-sectional area of the j^{th} leg of the section
b_j	Effective width of leg j for bending applications
$e_{Y'}$	Y' component of distance from the centroid to the shear-centre of a section
$e_{Z'}$	Z' component of distance from the centroid to the shear-centre of a section
$E_{xx\,i}$	Value of E_{xx} within the i^{th} nodal region of the section
$E_{xx\,j}$	Value of E_{xx} within the j^{th} leg of the section
$E_{xx\,s}$	Value of E_{xx} at position s
$E_{xx\,S}$	Value of E_{xx} at position S
$G_{xy\,i}$	Value of G_{xy} within the i^{th} nodal region of the section
$G_{xy\,j}$	Value of G_{xy} within the j^{th} leg of the section
$G_{xy\,s}$	Value of G_{xy} at position s
$G_{xy\,S}$	Value of G_{xy} at position S
$EI_{YY\,par\,j}$	Y-Y bending stiffness of a leg (leg j) that is oriented parallel to the Y axis
$EI_{YY\,perp\,j}$	Y-Y bending stiffness of a leg (leg j) that is oriented perpendicular to the Y axis
$EI_{YY\,node\,i}$	Y-Y bending stiffness of node i
$EI_{YY\,total}$	Total Y-Y bending stiffness of built-up beam section
$EI_{ZZ\,par\,j}$	Z-Z bending stiffness of a leg (leg j) that is oriented parallel to the Z axis
$EI_{ZZ\,perp\,j}$	Z-Z bending stiffness of a leg (leg j) that is oriented perpendicular to the Z axis
$EI_{ZZ\,node\,i}$	Z-Z bending stiffness of node i
$EI_{ZZ\,total}$	Total Z-Z bending stiffness of built-up beam section
$EI_{YZ\,total}$	Total Y-Z product of inertia stiffness of built-up beam section
$EQ_{Y'Y'\,S}$	Integral of first moment of normal longitudinal stiffnesses about Y'-Y' axis, for all material on one side of coordinate S
$EQ_{Z'Z'\,S}$	Integral of first moment of normal longitudinal stiffnesses about Z'-Z' axis, for all material on one side of coordinate S
h_s	Total thickness of the laminate at position s
h_S	Total thickness of the laminate at position S
h_{LY1} & h_{LY2}	Thicknesses of two intersecting legs oriented parallel to the Y axis
h_{LZ1} & h_{LZ2}	Thicknesses of two intersecting legs oriented parallel to the Z axis
I_C	Area polar moment of inertia of section about its centroid
I_O	Area polar moment of inertia of section about its shear-centre
I_{YY}	Second area moment of inertia about Y-Y axis
I_{ZZ}	Second area moment of inertia about Z-Z axis
I_{YZ}	Y-Z product of inertia
$\phi_{principal}$	Counter-clockwise angle from Y and Z axes to Y' and Z' axes, respectively

$I_{Y'Y'}$	Second area moment of inertia about Y'-Y' axis
$I_{Z'Z'}$	Second area moment of inertia about Z'-Z' axis
$I_{Y'Z'}$	Y'-Z' product of inertia
L	Total length of beam or column
M_{YY}	Bending moment about Y-Y axis
M_{ZZ}	Bending moment about Z-Z axis
$M_{Y'Y'}$	Bending moment about Y'-Y' axis
$M_{Z'Z'}$	Bending moment about Z'-Z' axis
N_L	Total number of legs within the section
N_N	Total number of nodal regions within the section
P_{node}	Bulk modulus value of nodal region
P_{LY1} & P_{LY2}	Bulk modulus values of two intersecting legs oriented parallel to the Y axis
P_{LZ1} & P_{LZ2}	Bulk modulus values of two intersecting legs oriented parallel to the Z axis
q_s	Shear flow at coordinate s
q_S	Shear flow at coordinate S
$r_{perp\,Os}$	Moment arm of s coordinate about shear-centre of the section, measured perpendicular to the surface of the laminate at coordinate s
$r_{par\,Os}$	Moment arm of s coordinate about shear-centre of the section, measured parallel to the surface of the laminate at coordinate s
s	Coordinate along a curvilinear path defined by mid-plane of system of thin-shells that make up cross-section of beam
S	Coordinate along a curvilinear path defined by mid-plane of system of thin-shells that make up cross-section of beam
m	Entire length over which the coordinates s and S are defined
V_Y	Transverse shear force applied parallel to Y axis
V_Z	Transverse shear force applied parallel to Z axis
$V_{Y'}$	Transverse shear force applied parallel to Y' axis
$V_{Z'}$	Transverse shear force applied parallel to Z' axis
$Y_{NA\,ZZ}$	Elevation of Z-Z flexural neutral axis, measured parallel to the Y axis
$\bar{Y}'_s$	Distance from Z'-Z' neutral axis to coordinate s, measured parallel to the Y' axis
$Z_{NA\,YY}$	Elevation of Y-Y flexural neutral axis, measured parallel to the Z axis
$\bar{Z}'_s$	Distance from Y'-Y' neutral axis to coordinate s, measured parallel to the Z' axis
β_{YY}	Timoshenko shear correction factor for shear loads applied in the Z direction
β_{ZZ}	Timoshenko shear correction factor for shear loads applied in the Y direction
$\beta_{Y'Y'}$	Timoshenko shear correction factor for shear loads applied in the Z' direction
$\beta_{Z'Z'}$	Timoshenko shear correction factor for shear loads applied in the Y' direction

Φ_{YY}	Angle of rotation of cross-sectional plane about Y-Y axis due to bending
Φ_{ZZ}	Angle of rotation of cross-sectional plane about Z-Z axis due to bending
$\Phi_{Y'Y'}$	Angle of rotation of cross-sectional plane about Y'-Y' axis due to bending
$\Phi_{Z'Z'}$	Angle of rotation of cross-sectional plane about Z'-Z' axis due to bending

Notation Used for Torsion and Warping Analyses

T	Applied torsion moment about longitudinal x or X axis (general case)
T_{SV}	Saint-Venant torsion moment (excluding warping) about longitudinal X axis
$T_{\omega 1}$	Primary warping moment about longitudinal X axis
$T_{\omega 2}$	Secondary warping moment about longitudinal X axis
T_{ω}	Total warping moment (excluding Saint-Venant torsion) about longitudinal X axis
T_{XX}	Total torsion and warping moment about longitudinal X axis
G	Isotropic shear modulus
b	Width of laminated plate, measured parallel to y axis
C	Saint-Venant's torsional stiffness
C_{FE}	Value of Saint-Venant's torsional stiffness found using FE method
C_{1B1}	Vlasov primary warping stiffness
C_{1B2}	Secondary (out-of-plane) warping stiffness
C_{1B}	Total warping stiffness
C_{1S}	Warping-shear coefficient
C_{TS}	Warping-shear stiffness
C_{lamPT}	Pure torsional stiffness of thin laminated plate
C_{lamFT}	Free torsional stiffness of thin laminated plate
$C_{lamThickPT}$	Pure torsional stiffness of thick laminated plate
$C_{lamThickFT}$	Free torsional stiffness of thick laminated plate
h	Total thickness of laminated plate, measured parallel to z axis
J	Geometric torsion constant (excluding shear modulus)
J_{Thick}	High fidelity value of J for thick plates, accounting for through-thickness shear effects
J_{Thin}	Approximate value of J for thin plates, neglecting through-thickness shear effects
L_g	Length of torsional gauge region
θ_k	Angle of fibres within k^{th} lamina relative to x axis of laminate coordinate system
η_{geom}	True geometric width-to-thickness aspect ratio of plate
η_{effPT}	Effective aspect ratio of a laminated plate for calculation of its pure torsional stiffness

η_{effFT}	Effective aspect ratio of a laminated plate for calculation of its free torsional stiffness
κ	Relevant modifier of effective width-to-thickness aspect ratio
κ_{PT}	Modifier of effective width-to-thickness aspect ratio for pure torsion
κ_{FT}	Modifier of effective width-to-thickness aspect ratio for free torsion
G_{effT}	Effective smeared shear modulus for relevant torsion calculations
G_{effPT}	Effective smeared shear modulus for pure torsion calculations
G_{effFT}	Effective smeared shear modulus for free torsion calculations
$G_{xyPT\,k}$	In-plane x-y shear modulus of lamina k for cases of pure torsion
$G_{xyFT\,k}$	In-plane x-y shear modulus of lamina k for cases of free torsion
$G_{xz\,k}$	Through-thickness x-z shear modulus of lamina k
$t_{ply\,i}$	Thickness of lamina i
$t_{ply\,k}$	Thickness of lamina k
$t_{ply\,k-1}$	Thickness of lamina $k-1$
$z_{mid\,k}$	Vertical elevation of mid-plane of lamina k relative to laminate mid-plane
$z_{ply\,k}$	Vertical elevation above bottom surface of lamina k ($z_{ply\,k} \leq t_{ply\,k}$)
$z_{botNP\,i}$	Vertical elevation of bottom surface of lamina i relative to twisting neutral plane
$z_{botNP\,k}$	Vertical elevation of bottom surface of lamina k relative to twisting neutral plane
ψ	Through-thickness linear gradient of in-plane x-y shear strains
ψ_{Lam}	Through-thickness gradient of x-y shear strains in laminated plate
ψ_{Hom}	Through-thickness gradient of x-y shear strains in homogeneous isotropic plate
$Q_{yT\,k}$	First moment of x-y shear moduli about twisting neutral plane, for material below k
$\aleph_{geom}$	Torsional stiffness correction factor, based upon true geometric aspect ratio, η_{geom}
$\aleph_{effPT}$	Pure torsional stiffness correction factor, based upon effective aspect ratio, η_{effPT}
$\aleph_{effFT}$	Free torsional stiffness correction factor, based upon effective aspect ratio, η_{effFT}
ω	Warping function
ω_s	Sectorial area swept by a radial line between section the shear-centre of the section and mid-plane of the section walls, from one free edge to coordinate s
$\bar{\omega}_s$	Average value of ω_s over entire cross-sectional area
ϕ	Angle of twist about longitudinal x or X axis
ϕ_g	Angle of twist measured over the length of the torsional gauge region
ϕ_1	Angle of twist about longitudinal X axis due to classical Vlasov effects
ϕ_2	Additional angle of twist about longitudinal X axis due to warping-shear effects

Notation Used for Buckling Analyses

P	Compression force applied to both ends of column
i_s	Number of half-sin waves over length of column, for the $i_s{}^{\text{th}}$ entry of a Fourier series
n	Number of half-sin waves over length of column, defining its deformed shape
A	Amplitude of sinusoidal shape of initially curved undeformed column
A_{i_s}	Amplitude of $i_s{}^{\text{th}}$ sin wave of Fourier series describing initially curved shape of column
w	Lateral perturbation of column at position of interest
$w\,(X)$	Lateral perturbation of column at position X
$w\left(\frac{L}{2}\right)$	Lateral perturbation of column at its mid-span
w_o	Lateral eccentricity of undeformed initially curved column at position of interest
$w_o\,(X)$	Lateral eccentricity of undeformed initially curved column at position X
$w_o\left(\frac{L}{2}\right)$	Lateral eccentricity of undeformed initially curved column at its mid-span
$P_{cr\,Eu\,Y'Y'}$	Euler critical flexural buckling load about Y'-Y' axis
$P_{cr\,Eu\,Z'Z'}$	Euler critical flexural buckling load about Z'-Z' axis
$P_{cr\,En\,Y'Y'}$	Engesser critical flexural-shear buckling load about Y'-Y' axis
$P_{cr\,En\,Z'Z'}$	Engesser critical flexural-shear buckling load about Z'-Z' axis
$P_{cr\,V\,\phi}$	Critical torsional buckling load
$P_{cr\,S\,\phi}$	Critical torsional-shear buckling load
$P_{cr\,FT}$	Critical flexural-torsional buckling load
$P_{cr\,FTS}$	Critical flexural-torsional-shear buckling load

Chapter 1

Introduction

1.1 Background

Fibre reinforced polymer (FRP) materials offer many advantages over conventional metallic structural materials due to their high specific strength and stiffness, long fatigue life, and resistance to environmental corrosion. As such, these materials have already enjoyed broad acceptance and use in the aerospace industry, and are increasingly being adopted by the automotive, athletic equipment, prosthetics, and civil engineering industries. However, these materials present some unique engineering challenges due to their anisotropy and heterogeneity. The connection of these composite parts to adjacent components often results in complex and counter-intuitive states of stress that can be quite difficult to model. Furthermore, since these materials are, in a sense, synthesized during the fabrication of the final part, the mechanical properties that can be expected from FRP structures are largely dependent upon highly skilled workmanship. Consequently, a general lack of confidence in FRP materials for primary structural applications tends to necessitate extremely cautious use of these high performance materials, thus yielding excessively conservative designs.

In addition, the present state-of-the-art in analytical modelling of FRP structural members leaves much to be desired. While finite element (FE) modelling techniques have become accepted as the structural analysis method of choice for most engineers in the automotive and aerospace industries, there remains a need for simplified analytical methods as well. The results of a finite element analysis (FEA) can communicate a great deal of information pertaining to the strength and stiffness of a structure, but a FE analysis will not always clearly indicate which specific structural phenomena are at fault for the observed shortcomings of a design. As such, industry engineers often bolster FE analyses with simplified analytical calculations that are based upon classical theorems, which helps to validate their understanding of the mechanisms that are responsible for the performance of their designs. Ultimately, despite the vast capabilities of modern FEA computer software, engineers continue to be hesitant to employ structural FRP composite materials in a manner that cannot also be understood (at least partially) using simple analytical methodologies that are based upon classical theorems. Unfortunately, the anisotropy and heterogeneity of FRP materials severely complicates their analysis. In fact, many of the classical analytical calculations that would be familiar to most structural engineers are dependent upon simplifying assumptions that are not appropriate for the analysis of structures that comprise FRP composite materials.

The aerospace industry demands some of the highest performance structural engineering solutions currently available, and was among the first industries to adopt FRP technology for the design of primary structures. Aircraft designs typically comprise a complex amalgamation of relatively simplistic structural members that can be thought of as simple beams, columns, skins, and bars. Fuselage and wing structures are typically designed using semi-monocoque architectures, whereby the wing and fuselage skins are structurally loaded members, but they are reinforced by stringers that are fastened to the internal surfaces of these skins. These wing and fuselage stringers are responsible for resisting local longitudinal tensile and compression forces that occur as a result of global bending moments imposed upon the fuselage and wing structural systems. Lower wing stringers are typically exposed to dominantly tensile forces, whereas upper wing stringers are typically exposed to dominantly compressive forces. The compressive loading imposed upon the upper wing skin-stringer assembly essentially renders this structural system as a classical column of short to moderate effective buckling length. Column buckling is a particularly interesting problem in the field of elastic stability because it can potentially depend upon the response of the column to a plethora of structural phenomena, such as: compression, bending, shear, torsion, and warping.

Section 1.2 of this chapter provides a general overview of the pertinent engineering theory relevant to the design and analysis of structures composed of laminated FRP composites. Section 1.3 provides a review of recent literature relevant to the hybrid co-pultruded composite technology that is presented in Chapter 2 of this dissertation. Section 1.4 provides a review of recent literature relevant to the analytical model that is presented in Chapter 3 of this dissertation. Section 1.5 provides a summary of the broader research objectives, and the general layout of all subsequent chapters.

1.2 Theory

1.2.1 General

A fibre reinforced polymer (FRP) is a composite material composed of high tensile strength fibres that are bound by a polymeric resin matrix that fills the voids between these fibres. Fibres commonly used in FRP composites are ceramic based (carbon, glass, or basalt), metal based (steel, boron, or titanium), or polymeric (aramid). These fibres are very fine, typically measuring 5-15μm in diameter, depending upon the type of fibre being used. Ceramic fibres offer excellent tensile strength due to the relatively low incidence of imperfections on their surfaces; the resin matrix impregnating these fibres enables the use of these high strength fibres for macroscopic structural applications. In general, continuous-fibre reinforced composites exhibit very high specific strength (strength divided by density). The specific stiffness (elastic modulus divided by density) of fibre reinforced polymers is highly dependent upon the fibres used, the orientation of the fibres, and the ratio between the volume of fibres and the total combined volume of resin and fibrous constituents present within the FRP composite (fibre volume fraction). Most fibre reinforced polymers enjoy excellent corrosion resistance (provided that metallic fibres are not employed). In general, FRP laminates exhibit behaviour that is approximately linear elastic and brittle (unless metallic fibres are employed).

The following section will provide a general overview of the structural engineering science relevant to the design of laminated FRP composite materials. Topics to be covered in this section include: a selection of commonly used manufacturing processes, detailed information pertaining to the selection of constituents to be used in laminated FRP composites, a brief introduction to the analytical methods that are most commonly used to predict the elastic behaviour of laminated FRP composites, and some practical considerations that can sometimes govern the design of FRP laminates.

1.2.2 Manufacturing Processes for Continuous-Fibre Reinforced Polymers

General

The following are descriptions of a selection of six manufacturing techniques that are commonly used for the fabrication of laminated FRP components. By no means is this an exhaustive list of all FRP manufacturing techniques in existence; however, it does serve as a general overview of the types of manufacturing processes that are commonly used in the FRP industry, and helps to illustrate the circumstances under which each of these techniques might be considered applicable.

Wet layup

The wet layup manufacturing process is perhaps the simplest method of producing laminated composite structures. In the wet layup technique, fibres, fibrous mats, or woven cloths of fibre are soaked in resin and pressed into a mould in the designed laminate stacking sequence. In some cases, it is desirable to employ a vacuum bagging operation, whereby a thin plastic film is placed over the uncured resin-impregnated laminate, and a partial vacuum is introduced to evacuate any unwanted air voids or excess resin from the laminate. Autoclaving is sometime employed to improve curing of resin and maximize resin strength. The wet layup technique is good for low volume production due to minimal set-up and tooling costs. It is commonly used to create irregular shapes having double curvatures and intricate details, such as boat hulls and automobile body shells. Unfortunately, the wet layup technique can be quite labour intensive, and it is difficult to ensure quality control.

Fibre volume fractions (volume of fibrous constituents divided by total combined volume of resin and fibrous constituents) can vary dramatically, and ultimately, the mechanical properties of the finished product are highly dependent upon the quality of workmanship.

Autoclave Cured Pre-preg

In some cases, fibres, fibrous mats, or woven cloths are available from the factory pre-impregnated with a resin that is designed to cure when heated. These pre-impregnated (or “pre-preg”) materials can be pressed into a mould by hand in the designed laminate stacking sequence. Autoclaving is then used to cure the resin once the hand layup process is complete. The pressure differential within the autoclave helps to minimize voids within the laminate. Pre-preg materials facilitate the achievement of relatively high and repeatable fibre volume fractions, and are ideal for the creation of irregular shapes where very high fibre volume fraction and good quality control is needed. This autoclave cured pre-preg process offers superior quality control in comparison with the wet layup process; however, mechanical properties still remain highly dependent upon quality of craftsmanship. Unfortunately, autoclave cured pre-preg manufacturing techniques are extremely labour intensive and time consuming. Care must be taken to ensure that un-cured pre-preg cloths are stored at low temperature and are used prior to the manufacturer’s stipulated expiration date; this can lead to expensive wasted material if resources and time are not managed carefully.

Filament winding

Filament winding is a manufacturing process whereby fibres are pulled through a resin bath such that they become saturated with resin, and are individually wound around a collapsible rotating mandrel. This deposition of fibres onto the mandrel is typically governed by computer numeric control (CNC) systems in order to ensure that the designed laminate stacking sequence is precisely achieved. This technique is excellent for optimizing fibre orientations in specific regions of the structure, and facilitates the creation of continuous one-piece structures that contain no free-edges or discontinuities between the two ends of the mandrel. In addition, filament winding offers precise and repeatable control of fibre volume fraction, thus yielding structures of admirable mechanical properties. Unfortunately, a time-consuming set-up process is necessary prior to the creation of each individual part, and filament winding is ultimately a relatively slow process. In addition, this technique is limited to the creation of convex shapes; concave shapes cannot be fabricated using the filament winding process. Finally, while fibre orientation can be carefully controlled by the filament winding process, it can be quite difficult to deposit fibres that are parallel to the axis of the filament winding mandrel. Ultimately, filament winding is ideal for convex shaped high performance structures having variable cross-sectional geometries, such as aircraft fuselages and sail-boat masts.

Resin-transfer moulding

Resin-transfer moulding is a manufacturing process whereby a fibrous mat or stitched complex is laid into a closed mould (usually a two-sided mould), which is subsequently impregnated with a polymeric resin using a combination of a vacuum system and a positive displacement pump. The mould is then heated to rapidly cure the part, and the part is then ejected from the mould. This manufacturing process lends itself to mass production of moderately complex parts featuring discrete complex geometries. The implementation of the vacuum system helps to minimize the development of voids within the cured composite part, resulting in relatively good repeatability of mechanical properties. In addition, the envelopment of un-cured resin within the sealed mould prevents the release of volatile organic compounds (VOCs), which helps to alleviate worker health concerns and environmental concerns. Unfortunately, resin-transfer moulding necessitates expensive tooling and capital investment that can be prohibitive for low production volumes. In addition, it can be difficult to achieve proper fibre wet-out (impregnation with resin) when high fibre volume fractions are employed.

Resin-infusion moulding

Resin-infusion moulding is a manufacturing process that is quite similar to resin-transfer moulding, but is tailored for the use of one-sided moulds. As such, in resin-infusion moulding, a fibrous mat or stitched complex is laid into a one-sided mould, and a film membrane (rigid or flexible) is placed over the part and sealed around the periphery of the mould. A vacuum system is then attached to the sealed mould to evacuate air and shrink the voids between the fibres. Utilizing this already existing partial vacuum, a polymeric resin is then drawn into the mould until the fibrous material is completely saturated with resin. The resin inlet is closed and vacuum pressure is maintained until the resin has cured. As with resin-transfer moulding, the implementation of the vacuum system helps to minimize the development of voids within the cured composite part, resulting in relatively good repeatability of mechanical properties. In resin-infusion moulding, this benefit is somewhat amplified due to the intermediate step of evacuating air from the fibrous material prior to enabling the flow of resin into the voids. In fact, resin-infusion moulding is capable of producing high quality parts having mechanical properties often comparable to those produced using autoclave cured pre-preg systems. In addition, the envelopment of un-cured resin within the sealed mould / film system prevents the release of volatile organic compounds (VOCs), which helps to alleviate worker health concerns and environmental concerns. In comparison with resin-transfer moulding, resin-infusion moulding necessitates a relatively low initial capital investment, and is relatively cost-effective for large one-piece parts. In fact, resin-infusion moulding requires only a slightly more expensive initial capital investment on equipment than wet layup open moulding techniques. Unfortunately, resin-infusion moulding is a relatively slow manufacturing process. In some cases, considerable waste materials can be produced from each moulding, which ultimately increases the cost of production, and tarnishes the environmental cleanliness of the manufacturing process.

Pultrusion

Pultrusion is a continuous manufacturing process intended for the mass-production of FRP structural members of constant cross-sectional geometry. The pultrusion process commences by fibrous material (individual fibres, fibre rovings, fibrous mats, or woven cloths) being pulled from creels and through a resin bath (or resin injection box) where it is saturated (impregnated) with resin. The fibrous material is then pulled through a heated die where it is formed into the desired cross-sectional geometry, and the resin is cured. The finished product is continuously pulled by a pulling machine, which perpetuates all of the aforementioned processes. Pultrusion is ideal for long structural members of constant cross sectional dimensions and properties. This manufacturing technique offers good control over fibre volume fraction, and facilitates the creation of parts having relatively high fibre volume fractions. Figure 1.1 is a simplified schematic diagram that illustrates the various steps of the pultrusion process.

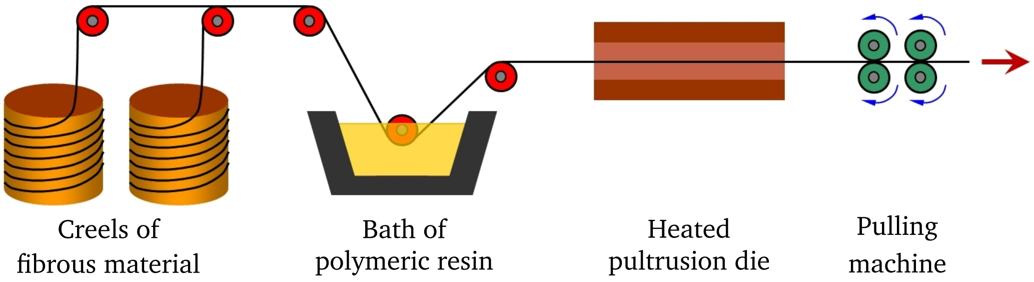

Figure 1.1: Simplified schematic diagram illustrating the various steps of the pultrusion process. Note that this drawing shows the pultrusion process propagating from the creels depicted on the left side of the figure toward the finished part depicted on the right side of the figure.

Because pultrusion is a continuous manufacturing process, mechanical properties are highly repeatable over the length of a single pultrusion run. Although the initial set-up of a pultrusion run can be costly and time consuming, once the putrusion process has commenced and is stabilized, a single pultrusion run can yield many miles of continuous composite parts with minimal human intervention. As such, this manufacturing process is very efficient for mass production of long parts of constant cross-sectional geometry, and offers excellent economies of scale. Unfortunately, high set-up and tooling costs and long set-up times virtually prohibit prototyping or low volume production of any sort using this process. Pultrusion is commonly used for ladder steps and rails, sail spars for sail-boats and wind surfers, sheet piles for civil engineering retaining wall applications, and beams and columns for light weight civil engineering structures requiring enhanced corrosion resistance.

Co-pultrusion is a manufacturing process whereby a predominantly FRP structural member is pultruded, and one or more additional longitudinally oriented structural or non-structural elements are passed through the pultrusion die along with the FRP constituents such that they become embedded within the final cured structural member. Such embedded elements could exist in the form of extruded metallic or plastic elements, metallic wires or strands, foam core materials, smaller previously pultruded FRP members, or any other material that could be continuously passed through a pultrusion die without succumbing to the heat and pressure present within the die. As such, co-pultrusion is an excellent means for creating long hybrid composite members of constant cross-sectional geometry.

All subsequent discussion in this dissertation will focus primarily on the development and analysis of hybrid composite structures that were fabricated using pultrusion and/or co-pultrusion technologies.

1.2.3 Reinforcing Fibres

> This section includes work that was reproduced and adapted from [35]. It incorporates parts of a state-of-the-art review of literature that was produced in collaboration with Dr. Derek Northwood. In all cases, the key ideas and primary contributions were provided by the author, and the contribution of the co-authors was primarily of a supervisory nature. Permission to reproduce this content has been granted by the co-authors (see Appendix E) and the copyright owner (see Appendix F).

General

There are many types of reinforcing fibres that can be used in FRP composite materials. The most common types of fibres are carbon, glass, and aramid. These fibres may be selected for their mechanical properties, physical properties, cost, and availability. As one might expect, the general trend in common fibres for polymer matrix composites dictates that structural performance (strength and stiffness) is proportional to cost, and inversely proportional to availability. In this section, the physical and mechanical properties of various common types of reinforcing fibres will be discussed. It should be noted, however, that the stated strengths and stiffnesses in this section are for the fibres themselves; the mechanical properties of the resulting polymer matrix fibre composite will be considerably lower than these values, and will depend upon the fibre volume fraction, the fibre orientations, and the mechanical properties of the polymeric resin matrix that is used. While most pultrusion has historically employed glass fibres, this is merely due to the specific industry sectors that have adopted pultrusion technology so far; there is no tangible reason that any other type of ceramic, metallic, or polymeric fibre could not be just as easily employed within a pultruded part.

Carbon

Carbon fibres offer extremely high strength and stiffness at a remarkably low weight. In fact, carbon fibres generally exhibit tensile strengths in the order of 3 GPa, but sometimes as high as 5 GPa; the elastic modulus of carbon fibres is generally between 200 and 400 GPa, but in some cases can even exceed 700 GPa [71]. These numbers clearly illustrate that, when carbon fibres are used, it is possible to produce a FRP composite with elastic modulus and ultimate tensile strength values exceeding those of typical structural steel. Unfortunately, carbon fibres tend to be extremely expensive to produce, and their availability can be quite limited. Furthermore, carbon is a conductor of electricity, which raises concerns regarding galvanic corrosion if metal elements are to be embedded within a hybrid composite member, or even if metallic fasteners are to be in direct contact with with a carbon FRP structural member.

Glass

Glass fibres are, by far, the most commonly used type of reinforcing fibre for polymer matrix fibre composites. They have very high strength, are relatively economical, and are readily available in a wide variety of pre-prepared fibre assemblies such as unidirectional fibre rovings, woven rovings (fabrics), mats, surfacing veils, and stitched complexes. Typical glass reinforcing fibres exhibit tensile strengths in the order of 3.5 GPa, which is not vastly inferior to the tensile strength of most carbon fibres; however, the elastic modulus of glass fibres tends to range between 70 GPa and 90 GPa, which is considerably lower than the elastic modulus of typical carbon fibres [71]. Glass fibres are available in a range of chemical compositions which are designated as A, C, D, E, ECR, R, and S. The highest performance glass fibres are S-glass fibres, which have an elastic modulus of 88 GPa and an ultimate tensile strength of approximately 4.6 GPa [71]. However, the most commonly used and most readily available type of glass fibres are E-glass fibres, which generally have an elastic modulus of 72.5 GPa and an ultimate tensile strength of approximately 3.4 GPa [71].

Aramid

Another high performance fibre that is sometimes used in polymer matrix fibre composites is aramid. Aramid fibres, developed by DuPont™ under the Kevlar® trade name, are polymer fibres of very high tensile strength, generally equalling or exceeding that of most carbon fibres; however, the compressive strength of aramid is considerably lower than its tensile strength [71]. The elastic modulus of aramid fibres can vary considerably; Kevlar 29® has a stiffness only slightly greater than that of E-glass fibres, whereas Kevlar 49® has a stiffness rivalling some carbon fibres [71]. Aramid fibres are also of lower density than both glass and carbon fibres. Unfortunately, aramid fibres are very expensive to produce, and are difficult to work with. Furthermore, if not sufficiently protected, aramid fibres can be susceptible to water absorption, which can cause the fibres to swell and weaken.

While aramid fibres have become somewhat unpopular for applications in the primary structures of aircraft and land vehicles, it is sometimes beneficial to utilize the excellent puncture resistance of woven aramid fabrics (often used in bullet-resistant vests). For example, the safety of a laminated composite automotive vehicle structure could be improved by employing a layer of woven aramid fabric over the inner surface of this laminated shell structure. In the event of a crash, this aramid reinforced lamina could help to protect the occupants of the vehicle from intrusion of foreign objects, as well as prevent jagged shards or splinters of the primary reinforcing fibres (glass and/or carbon) of the laminate from protruding into the vehicle.

As mentioned earlier, Kevlar 29® exhibits an elastic modulus that is similar to that of E-glass fibres; therefore, Kevlar 29® could potentially be used to strengthen a laminate composed primarily of E-glass reinforcing fibres without attracting load and generating stress concentrations or excessive interlaminar stresses between adjacent laminae of these dissimilar types of fibres. Conversely, if a laminate were to include carbon fibre reinforced laminae adjacent to E-glass fibre reinforced laminae, the substantially higher elastic modulus of the carbon would cause the carbon fibre reinforced laminae to attract load (stress) while the E-glass fibre reinforced laminae would tend to shed load (stress), which could lead to stress concentrations and premature failure of the laminate.

Hybrid Rovings

Another interesting product that could be useful in the design of aircraft or land vehicle structures is hybrid rovings that comprise more than one type of fibre. These hybrid rovings may serve to provide a blended behaviour of the various types of fibres, with a reduced risk of stress concentrations or elevated interlaminar stresses when compared with hybrid structures that employ separate laminae of different types of reinforcing fibres. For example, rovings that combine glass and carbon fibres or glass and aramid fibres would offer higher strength and stiffness than purely glass fibre rovings, but at a lower cost than purely carbon or aramid rovings. Such hybrid rovings are often found in high-performance sporting goods such as skis, hockey sticks, canoes, and kayaks.

1.2.4 Resin Matrix

> This section includes work that was reproduced and adapted from [35]. It incorporates parts of a state-of-the-art review of literature that was produced in collaboration with Dr. Derek Northwood. In all cases, the key ideas and primary contributions were provided by the author, and the contribution of the co-authors was primarily of a supervisory nature. Permission to reproduce this content has been granted by the co-authors (see Appendix

E) and the copyright owner (see Appendix F).

General

Another critical aspect of the design of FRP composite structural members is the type of polymeric resin matrix that is used. There are countless resin systems on the market; however, only a few of these systems are commonly used in pultrusion. While some pultrusions do employ thermoplastics, most pultrusion is done using thermoset polymer resins. This is largely due to the fact that the curing process for thermoset resins is well suited to the manner in which pultrusion lines were originally developed. The most commonly used families of thermoset resins for pultrusion are thermoset unsaturated polyester resins and thermoset vinyl ester resins. In addition to these very popular resin systems, some of the other families of thermoset resin systems that are less commonly used for pultrusion include: thermoset polyurethane resins, epoxy resins, phenolic resins, and acrylic thermoset liquid resins. While the selection of a resin system may be based upon many possible mechanical and physical characteristics, nine specific parameters were selected as most important for the purposes of evaluating the suitability of each resin family for pultruded parts intended for aerospace and/or automotive applications; these parameters include: pultrusion processing speed and temperature, mechanical performance (strength and stiffness), fibre-resin bond quality, durability, toughness, resistance to moisture absorption, heat resistance, and fire safety.

Pultrusion Processing Speed and Temperature

Pultrusion processing speed may be defined as the linear speed at which it is possible to draw material through the pultrusion die, and hence, the rate at which pultruded material is produced. One of the primary parameters that can affect processing speed is resin viscosity; resins with relatively high viscosity require a higher pulling force and more time to establish proper fibre wet-out, and hence, a slower processing speed is necessary. Another resin characteristic that can affect processing speed is the reactivity of the resin; a highly reactive resin will cure more quickly, thus allowing a faster pultrusion speed. If processing speed is limited by resin reactivity, then this speed can often be increased by increasing die temperature, thus increasing the rate at which the resin is cured. For this reason, processing speed and temperature are quite interrelated. Unfortunately, this increased temperature may be undesirable for the purposes of hybrid co-pultruded members due to the potential development of thermal stresses. It should be noted that processing speed and temperature can also be affected by certain aspects of a pultrusion design that are unrelated to the resin selection, such as die geometry and cross-sectional area. As such, it is difficult to compare different pieces of literature to gain an objective assessment of the relative performances of the various families of thermoset resins for pultrusion.

Overall, thermoset unsaturated polyester resins and thermoset vinyl ester resins generally have good processing speeds of 0.6 to 1.5 m/minute [71], which is partially why they are so widely used. Similar processing speeds can be achieved using thermoset polyurethane resins; but this is generally only possible at elevated die temperatures of 200° C to 250° C [80]. However, it should be noted that some newer thermoset polyurethane resin systems, such as Huntsman International's RIMLINE® system, have enabled processing speeds of up to 2.5 m/minute, while limiting die temperatures to under 205° C. Phenolic resins can be pultruded at processing speeds of up to 1.3 m/minute; however, this is only possible at highly elevated temperatures approaching 250° C [81]. At more typical die temperatures, phenolic resins tend to be limited to much lower processing speeds of around 0.7 m/minute [81]. Extremely high processing speeds approaching 6 m/minute have been demonstrated with acrylic thermoset liquid resins, perhaps owing to the low viscosity and high reactivity of such resins [71]. Conversely, epoxy resins tend to have relatively high viscosity, leading to poor fibre wet-out, and consequently limiting possible processing speeds to 10 cm/minute or less; this renders epoxy resins quite impractical for mass production purposes [71].

Mechanical Properties

Where high fibre volume fractions are employed, the strength and stiffness of FRP composites tend to be largely dependent upon the mechanical properties of the fibres alone, and much less dependent upon the mechanical properties of the resin matrix. In simple laminates, this relationship can be described by the rule of mixtures (see Section 1.2.6). However, this relationship only holds true if the fibres and the resin matrix are perfectly bonded and in a state of iso-strain. If this fibre-matrix bond fails prematurely, then the fibres will not be able to achieve their failure strain prior to slipping relative to the resin matrix, and the strength of the composite will be diminished substantially. As such, the adhesion strength of the resin is perhaps of greater importance than the mechanical strength of the hardened resin material itself. It should be noted, however, that not all types of fibres are manufactured with the same type of sizing agents (chemical coatings or surface treatments); consequently, some resins may exhibit good adhesion to one type of fibre and poor adhesion to another type of fibre. Epoxy resins tend to be very well suited for bonding to carbon fibres, but this advantage is perhaps less pronounced when bonding to glass fibres. With the inclusion of embedded co-pultruded elements within a pultruded FRP member, the importance of bond quality becomes increasingly critical.

Thermoset unsaturated polyester resins and vinyl ester resins are the most commonly used resins for applications involving glass FRP (GFRP) composites; however, it has been shown that thermoset polyurethane resins offer far superior bond performance with glass fibres, which also leads to relatively high interlaminar bond strength [74]. An experimental program was carried out in which GFRP pultrusions of longitudinal unidirectional glass fibre rovings with thermoset polyurethane resins were compared with similar pultrusions that employed thermoset unsaturated polyester resins; the longitudinal bending strength and transverse bending strength were found to be 88% and 120% higher, respectively, for the pultrusions that employed the thermoset polyurethane resin [19]. The high bond strength and low elastic modulus of thermoset polyurethane resins tend to result in relatively high toughness and durability in GFRP composites employing this type of resin system [74]. In fact, Creative Pultrusions™, Inc. has reported that their Series 4000 GFRP pultrusions employing a thermoset polyurethane resin matrix exhibit a Notched Izod Impact toughness that is nearly four times greater than a comparable pultrusion employing a thermoset unsaturated polyester resin matrix, in accordance with ASTM D256. While phenolic resin systems do not share the excellent toughness and bond properties of thermoset polyurethane resins, it has been shown that these two resin systems can be blended as a co-polymer such that the good toughness and bond properties of thermoset polyurethane resins can be combined with some of the admirable properties of phenolic resins [94].

Resistance to Water Absorption

Since most aircraft and land vehicles spend the majority of their life cycles outside, it is important that they are designed to be well protected from environmental effects. Most FRP materials are generally quite resistant to corrosion and other forms of deterioration; however, over extended periods of time, some polymer resin systems tend to absorb small quantities of water. This water absorption often leads to blistering of the laminate, which can adversely affect the overall strength of the composite. In some cases, water absorption can also lead to hydrolysis, causing further deterioration of the composite. Water absorption levels as high as 4% by mass have been reported for thermoset polyurethane resins; however, Creative Pultrusions™, Inc. claims that their Series 4000 GFRP pultrusions employing a thermoset polyurethane resin matrix exhibit water absorption of only 0.3% by mass, in accordance with ASTM D570. This level of water absorption is approximately half of what can be expected of a pultrusion employing a thermoset unsaturated polyester resin; however, vinyl ester resins have been shown to offer even lower levels of water absorption than thermoset polyurethane resins [37]. Conversely, Huntsman Polyurethanes has demonstrated that the water absorption resistance of their thermoset polyurethane resins is 42% better than what can be expected of typical vinyl ester resin systems [20]. Regardless of which resin matrix is employed, the water resistance of any FRP can be vastly enhanced simply by incorporating a protective waterproof surface coating or barrier, such as a gelcoat. Such coatings also protect the constituents of the underlying FRP composite from deterioration due to ultraviolet radiation.

Heat Resistance and Fire Safety

It is important that aircraft and land vehicle structures are capable of maintaining sufficient strength and stiffness in high temperature environments. The ability of an FRP to maintain its strength and stiffness at high temperatures is largely dependent upon the glass transition temperature of its polymeric resin matrix. Above its glass transition temperature, the matrix will soften and begin to exhibit ductility, thus drastically reducing the strength and stiffness of the composite structure. Phenolic resins exhibit consistently high glass transition temperatures generally ranging from 220° C to 250° C [37]. Some epoxy resins also exhibit very high glass transfer temperatures, sometimes approaching 260° C [37]; however, glass transition temperatures vary substantially within the epoxy family of resins. The other resin systems discussed in this dissertation tend to exhibit substantially lower glass transition temperatures, generally ranging between 100° C and 150° C [37].

It is not entirely uncommon for aircraft or land vehicles to catch fire. Fires could be caused by an electrical short circuit, a fuel or oil leak, an engine backfire, and many other causes [1]. The primary danger of a vehicle fire is generally the heat that is given off, the risk of igniting fumes from the fuel tank, and the potential for structural failure; however, some materials emit poisonous gasses when they are subjected to heat and flames, which can substantially increase the danger of a fire. Unfortunately, some of the polymer resins that are used for the matrix of FRP composite materials exhibit this dangerous characteristic. In particular, thermoset unsaturated polyester resins and vinyl ester resins can be quite toxic when exposed to fire. These resin systems are also quite environmentally hazardous during processing due to the presence of styrene in their formulation as a thinning agent. Conversely, phenolic resins and acrylic thermoset liquid resins share excellent resistance to combustion, and both resins exhibit low smoke, flame, and toxicity products when they are exposed to flames; this admirable fire safety can be further enhanced with the addition of specially formulated filler agents in the resin [71]. Thermoset polyurethane resins are also capable of good fire safety with the addition of filler agents, and are completely free of styrene in their composition [37] [41] [40].

1.2.5 Laminate Stacking Sequence

> This section includes work that was reproduced and adapted from [35]. It incorporates parts of a state-of-the-art review of literature that was produced in collaboration with Dr. Derek Northwood. In all cases, the key ideas and primary contributions were provided by the author, and the contribution of the co-authors was primarily of a supervisory nature. Permission to reproduce this content has been granted by the co-authors (see Appendix E) and the copyright owner (see Appendix F).

General

In order to concisely describe the fibre orientations and stacking sequences of the laminates discussed in this dissertation, the standard lamination code [54] will sometimes be employed. It should be noted that any time a fibre angle or lamina angle is mentioned, the angle is to be measured relative to the longitudinal x axis of the laminate. A lamina angle refers to the angle of the fibres within that lamina. All laminae in this discussion shall be assumed to comprise unidirectional continuous-fibre rovings.

Laminate Architectures

While any laminate stacking sequence can be precisely described using the standard lamination code, it is also possible to infer some of the expected behaviours of a complex laminate simply by establishing some general characteristics of the laminate architecture used. The general type of laminate used is often defined using common descriptor terms such as: balanced, unbalanced, symmetric, anti-symmetric, and unsymmetric. Table 1.1 defines each of these laminate architecture descriptor terms.

Table 1.1: Common laminate architecture descriptor terms – Reproduced and adapted from [35].

Laminate Descriptor	**Explanation**
Balanced	Any lamina composed of fibres at some angle $+\theta^\circ$ that is not 0° or 90° must be accompanied somewhere else in the laminate by another lamina of equal thickness composed of fibres at an angle of $-\theta^\circ$
Unbalanced	A lamina composed of fibres at some angle $+\theta^\circ$ that is not 0° or 90° is not always accompanied somewhere else in the laminate by another lamina composed of fibres at an angle of $-\theta^\circ$
Symmetric	Any lamina at some distance above the midplane of the laminate is always matched with an identical lamina at the same distance below the midplane of the laminate
Anti-symmetric	Any lamina located some distance above the midplane of the laminate and having fibres oriented at $+\theta^\circ$ is balanced with a similar lamina at the same distance below the midplane of the laminate and having fibres oriented at $-\theta^\circ$
Unsymmetric	A lamina at some distance above the midplane of the laminate is not always matched with an identical lamina at the same distance below the midplane of the laminate

It should be noted that any symmetric or anti-symmetric laminate must also be a balanced laminate. Conversely, an unsymmetric laminate may be either balanced or unbalanced.

Free-Edge Effects

Lagunegrand et al [46] discussed the importance of the laminate stacking sequence in preventing excessive interlaminar stresses near the edges of a laminate incorporating multiple unidirectional laminae with varied orientations. This problem, known as free-edge effects, dictates that each lamina of unidirectional fibres depends upon interlaminar stresses in order to equilibrate in-plane forces with adjacent laminae of differently oriented unidirectional fibres, thus generating localized regions of elevated interlaminar stresses near the edges of the laminate. Consequently, delamination may be initiated along the free edges of a laminate, resulting in premature failure of the structure prior to realizing the full potential of the reinforcing fibres. This problem is most severe where two adjacent laminae are composed of unidirectional continuous fibres oriented at very different angles relative to each other, such that they exhibit very different Poisson's Ratios when observed within a common coordinate system. The problem is further exacerbated if each of these laminae are very thick, or if a pair laminae with the same fibre orientation is adjacent to another pair of laminae with a very different fibre orientation. The analysis of laminates subjected to free-edge effects has been studied extensively since the late 1960's [61][64][55].

In the context of pultruded structural members, one potential remedy for free-edge effects might be to stitch all of the laminae together with glass or carbon fibres prior to pulling the resultant stitched fabric through the pultrusion die; this through-thickness stitching would provide a mechanical connection between the laminae which may help to retard the propagation of delamination by reducing the tendency for the laminae to separate from one another. Unfortunately, such through-thickness stitching may not be conducive for implementation during pultrusion as it would be difficult to ensure sufficient fibre wet-out. In the absence of highly complex solutions such as through-thickness stitching, free-edge effects can be minimized simply by designing a laminate such that it has a smooth through-thickness transition between vastly differing fibre orientations, and so that there are no regions within the thickness of the laminate that exhibit excessive concentrations of any one fibre orientation [54]. Therefore, a laminate composed of 0°, +45° , and −45° laminae should have a stacking sequence such that each +45° lamina and −45° lamina are separated by a 0° or 90° lamina, and under no circumstances should two laminae with the same fibre orientation be adjacent to one another.

1.2.6 Local Material Properties

All subsequent discussion in this section will be tailored for applications pertaining to laminated composites comprising laminae of unidirectional continuous-fibre reinforced polymers. The first step in the establishment of local lamina (ply) properties is to define a 1-2-3 lamina coordinate system at the mid-thickness of each lamina (ply), whereby the 1 axis is parallel to the fibre orientation, the 2 axis is in the plane of each lamina and oriented perpendicular to the fibres, and the 3 axis is oriented normal to the plane of the lamina. This 1-2-3 lamina coordinate system is illustrated in Figure 1.2.

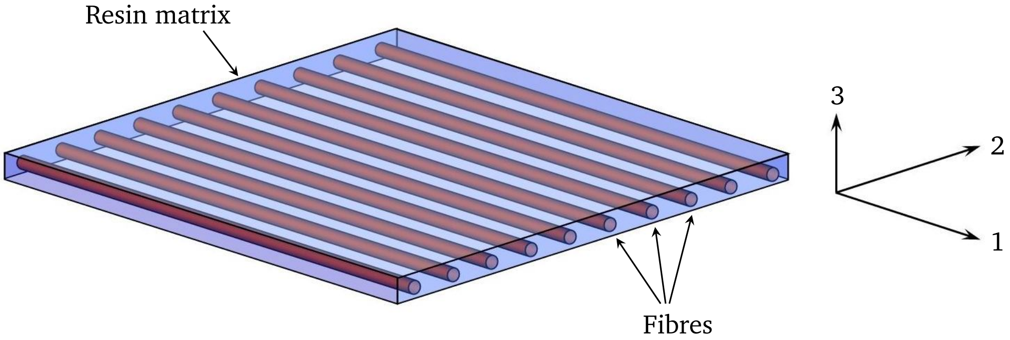

Figure 1.2: 1-2-3 lamina coordinate system, shown for a single lamina (ply) of unidirectional FRP material.

While FRP composites are frequently described as anisotropic materials, unidirectional continuous-fibre composites can generally be described as transversely isotropic materials, whereby there exists a single plane within which these materials exhibit isotropic mechanical behaviours. In the case of unidirectional continuous-fibre composites, the axis of the fibres (1 direction) is normal to this plane of isotropic behaviour; hence, the mechanical behaviour of the material is the same along the 2 and 3 directions of the lamina coordinate system (perpendicular to the axis of the fibres), whereas unique mechanical properties are exhibited along the 1 direction of the lamina coordinate system (parallel to the axis of the fibres). As such, these transversely isotropic materials can be modelled as orthotropic materials having equal constitutive relationships along the 2 and 3 axes of their local material coordinate systems. The stress versus strain relationship of a general orthotropic material can be defined in accordance with its material compliance matrix $\mathbf{S_{3D}}$ as follows:

$$\begin{Bmatrix} \varepsilon_{11} \\ \varepsilon_{22} \\ \varepsilon_{33} \\ \gamma_{23} \\ \gamma_{13} \\ \gamma_{12} \end{Bmatrix} = \begin{bmatrix} \frac{1}{E_{11}} & \frac{\nu_{21}}{E_{22}} & \frac{\nu_{31}}{E_{33}} & 0 & 0 & 0 \\ \frac{\nu_{12}}{E_{11}} & \frac{1}{E_{22}} & \frac{\nu_{32}}{E_{33}} & 0 & 0 & 0 \\ \frac{\nu_{13}}{E_{11}} & \frac{\nu_{23}}{E_{22}} & \frac{1}{E_{33}} & 0 & 0 & 0 \\ 0 & 0 & 0 & \frac{1}{G_{23}} & 0 & 0 \\ 0 & 0 & 0 & 0 & \frac{1}{G_{13}} & 0 \\ 0 & 0 & 0 & 0 & 0 & \frac{1}{G_{12}} \end{bmatrix} \begin{Bmatrix} \sigma_{11} \\ \sigma_{22} \\ \sigma_{33} \\ \tau_{23} \\ \tau_{13} \\ \tau_{12} \end{Bmatrix} = \left[\mathbf{S_{3D}}\right] \begin{Bmatrix} \sigma_{11} \\ \sigma_{22} \\ \sigma_{33} \\ \tau_{23} \\ \tau_{13} \\ \tau_{12} \end{Bmatrix} \tag{1.1}$$

where:

ε_{11} and σ_{11} are the normal strain and stress in the 1 direction, respectively

ε_{22} and σ_{22} are the normal strain and stress in the 2 direction, respectively

ε_{33} and σ_{33} are the normal strain and stress in the 3 direction, respectively

γ_{23} and τ_{23} are the engineering shear strain and shear stress in the 2-3 direction, respectively
γ_{13} and τ_{13} are the engineering shear strain and shear stress in the 1-3 direction, respectively
γ_{12} and τ_{12} are the engineering shear strain and shear stress in the 1-2 direction, respectively
E_{11}, E_{22}, and E_{33} are the normal elastic moduli in the 1, 2, and 3 directions, respectively
G_{23}, G_{13}, and G_{12} are the shear moduli in the 2-3, 1-3, and 1-2 directions, respectively
ν_{23}, ν_{13}, and ν_{12} are the Poisson's ratios in the 2-3, 1-3, and 1-2 directions, respectively

In order to populate the terms of the orthotropic compliance matrix $\mathbf{S_{3D}}$ present in equation (1.1), it is necessary to employ numerous micro-mechanics modelling techniques. The ratio between the volume of fibres and the total combined volume of resin and fibrous constituents present in a given FRP is commonly referred to as the fibre volume fraction V_f, and is an important characteristic in determining the mechanical properties of FRP composites. For a lamina composed of unidirectional continuous fibres, the composite elastic modulus in the direction parallel to the fibre orientation (1 direction) can be calculated in accordance with the rule of mixtures using the following equation [54]:

$$E_{11} = E_f\left(V_f\right) + E_m\left(1 - V_f\right) \tag{1.2}$$

where E_{11} is the composite elastic modulus in the longitudinal 1 direction (parallel to the axis of the fibres), E_f is the elastic modulus of the fibres, E_m is the elastic modulus of the polymeric resin matrix, and V_f is the fibre volume fraction. It is apparent from this equation that the resin matrix and the fibres are working in parallel to resist deformation in the longitudinal direction. Conversely, the composite elastic modulus of the lamina in the direction perpendicular to the fibre orientation (2 and/or 3 directions) can be calculated from the rule of mixtures using the following equation [54]:

$$E_{22} = E_{33} = \frac{E_f E_m}{E_f - V_f\left(E_f - E_m\right)} \tag{1.3}$$

where E_{22} is the composite elastic modulus in the transverse 2 direction (perpendicular to the axis of the fibres), and E_{33} is the composite elastic modulus in the through-thickness 3 direction (perpendicular to the axis of the fibres). It is apparent from this equation that the resin matrix and the fibres are working in series to resist deformation in the transverse direction. Similarly, the in-plane and through-thickness composite shear moduli can be calculated from the rule of mixtures for materials in series, as follows [54]:

$$G_{12} = G_{21} = G_{13} = G_{31} = \frac{G_f G_m}{G_f - V_f\left(G_f - G_m\right)} \tag{1.4}$$

where G_{12} is the composite shear modulus in the plane of the lamina, G_{13} is the composite shear modulus through the thickness of the lamina, G_f is the shear modulus of the fibres, and G_m is the shear modulus of the polymeric resin matrix. The in-plane composite Poisson's ratios can be calculated from the rule of mixtures for materials in parallel, as follows [54]:

$$\nu_{12} = \nu_f\left(V_f\right) + \nu_m\left(1 - V_f\right) \qquad \& \qquad \nu_{21} = \frac{E_{22}}{E_{11}}\nu_{12} \tag{1.5}$$

where ν_{12} is the composite Poisson's ratio from the longitudinal 1 direction to the transverse 2 direction, ν_{21} is the composite Poisson's ratio from the transverse 2 direction to the longitudinal 1 direction, ν_f is the Poisson's ratio of the fibres, and ν_m is the Poisson's ratio of the polymeric resin matrix. Similarly, the through-thickness composite Poisson's ratios can be calculated from the rule of mixtures for materials in parallel, as follows [54]:

$$\nu_{13} = \nu_f\left(V_f\right) + \nu_m\left(1 - V_f\right) \qquad \& \qquad \nu_{31} = \frac{E_{33}}{E_{11}}\nu_{13} \tag{1.6}$$

where ν_{13} is the composite Poisson's ratio from the longitudinal 1 direction to the through-thickness 3 direction, and ν_{31} is the composite Poisson's ratio from the through-thickness 3 direction to the longitudinal 1 direction.

It has been shown [18] that the transverse out-of-plane Poisson's Ratios of unidirectional continuous-fibre composite materials can be calculated as a function of the known in-plane Poisson's Ratios using the following relationship:

$$\nu_{23} = \nu_{32} = \nu_{12}\frac{1 - \nu_{21}}{1 - \nu_{12}} \tag{1.7}$$

Finally, the remaining transverse out-of-plane shear modulus can be calculated as follows:

$$G_{23} = G_{32} = \frac{E_{22}}{2\left(1 + \nu_{23}\right)} \tag{1.8}$$

The aforementioned rule of mixtures equations for materials in series have been shown to under-predict experimentally determined values of transverse bulk stiffness properties E_{22}, E_{33}, G_{12}, G_{21}, G_{13}, and G_{31} [17]. This is likely due to volumetric packing (interlocking) of the fibres, which causes these continuous-fibre reinforced composite materials to behave much like particulate reinforced composite materials in directions perpendicular to the axis of the fibres. The Halpin-Tsai equations were developed as a simplified amalgamation of existing complex micro-mechanics models, and have been experimentally shown to more accurately predict the aforementioned transverse bulk stiffness values [29]. Many variants of the Halpin-Tsai equations have been developed, but perhaps the most robust form of these equations for applications in calculating the transverse bulk properties of unidirectional continuous-fibre reinforced composite materials are those adapted by Hewitt and de Malherbe [33] as follows:

$$E_{22} = E_{33} = E_m\frac{1 - \xi_{E22}\,\eta_{E22}\,V_f}{1 - \eta_{E22}\,V_f} \tag{1.9}$$

where:

$$\xi_{E22} = 2 + 40\ V_f^{10} \qquad \& \qquad \eta_{E22} = \frac{\left(E_f/E_m\right) - 1}{\left(E_f/E_m\right) + \xi_{E22}} \tag{1.10}$$

And similarly:

$$G_{12} = G_{21} = G_{13} = G_{31} = G_{23} = G_{32} = G_m \frac{1 - \xi_{G12}\, \eta_{G12}\, V_f}{1 - \eta_{G12}\, V_f} \tag{1.11}$$

where:

$$\xi_{G12} = 1 + 40\ V_f^{10} \qquad \& \qquad \eta_{G12} = \frac{\left(G_f/G_m\right) - 1}{\left(G_f/G_m\right) + \xi_{G12}} \tag{1.12}$$

While there have been some examples in the literature where it was shown that a simple rule of mixtures formulation yielded reasonably accurate estimates of transverse bulk modulus values E_{22}, E_{33}, G_{12}, G_{21}, G_{13}, and G_{31}, it is generally accepted that the Halpin-Tsai equations more consistently yield accurate predictions of these values [4]. The analytical / semi-imperical derivation of the Halpin-Tsai equations is based upon a higher fidelity representation of the cross-sectional geometric distribution of materials in unidirectional continuous-fibre reinforced composite materials; as such, it is not surprising that this formulation yields superior correlation with experimental results when compared with the rule of mixtures for materials in series.

1.2.7 Local Ply Constitutive Relationships

In the following section, the mechanical behaviour of a single lamina (ply) of unidirectional continuous FRP composite will be assessed within the plane of this individual lamina. It will be assumed here that only in-plane loads are imposed upon the lamina, and through thickness (out-of-plane) normal strains are unrestrained; hence, the lamina is in a state of plane stress within the plane of its 1 and 2 material axes. As such, by removing all terms of the orthotropic compliance matrix $\mathbf{S_{3D}}$ that are relevant to through thickness (3 direction) behaviours (see equation (1.1)), and subsequently inverting the resultant 3 by 3 matrix, a local ply stiffness matrix $\mathbf{Q}$ can be formulated to account for all in-plane structural phenomena that result from in-plane strain events acting parallel and/or perpendicular to the axis of the fibres, as follows [54]:

$$\begin{Bmatrix} \sigma_{11} \\ \sigma_{22} \\ \tau_{12} \end{Bmatrix} = \begin{bmatrix} Q_{11} & Q_{12} & 0 \\ Q_{21} & Q_{22} & 0 \\ 0 & 0 & Q_{66} \end{bmatrix} \begin{Bmatrix} \varepsilon_{11} \\ \varepsilon_{22} \\ \gamma_{12} \end{Bmatrix} = [\mathbf{Q}] \begin{Bmatrix} \varepsilon_{11} \\ \varepsilon_{22} \\ \gamma_{12} \end{Bmatrix} \tag{1.13}$$

where σ_{11}, σ_{22}, and τ_{12} are longitudinal, transverse, and shear stresses, respectively; ε_{11}, ε_{22}, and γ_{12} are longitudinal, transverse, and shear strains in the local coordinate system of the lamina, respectively. Based upon the assumption of plane stress conditions, the elements of the **Q** matrix can be calculated using the following formulae [54]:

$$Q_{11} = \frac{E_{11}}{1 - \nu_{12}\nu_{21}} \tag{1.14}$$

$$Q_{22} = \frac{E_{22}}{1 - \nu_{12}\nu_{21}} \tag{1.15}$$

$$Q_{12} = Q_{21} = \frac{\nu_{12}E_{22}}{1 - \nu_{12}\nu_{21}} = \frac{\nu_{21}E_{11}}{1 - \nu_{12}\nu_{21}} \tag{1.16}$$

$$Q_{66} = G_{12} \tag{1.17}$$

This stiffness matrix applies only when loadings occur parallel and/or perpendicular to the axis of the fibres; however, it is often also necessary to calculate the stress versus strain relationship in directions at some angle to the axis of the fibres. This is of particular importance when analyzing a composite laminate having different fibre orientations in each ply. As such, an x-y-z laminate coordinate system shall be defined at the mid-thickness of the complete laminate whereby the x axis is parallel to the longitudinal axis of the structural member, the y axis is in the plane of the laminate and oriented perpendicular to the longitudinal axis of the member, and the z axis is oriented normal to the plane of the laminate. The angles of the fibres within each ply are measured with respect to the x axis of the laminate coordinate system. It is now possible to formulate a general orthotropic stiffness matrix $\bar{\mathbf{Q}}$ for the ply (lamina) of interest in the laminate x-y-z coordinate system, which may be used as follows [54]:

$$\begin{Bmatrix} \sigma_{xx} \\ \sigma_{yy} \\ \tau_{xy} \end{Bmatrix} = \begin{bmatrix} \bar{Q}_{11} & \bar{Q}_{12} & \bar{Q}_{16} \\ \bar{Q}_{21} & \bar{Q}_{22} & \bar{Q}_{26} \\ \bar{Q}_{61} & \bar{Q}_{62} & \bar{Q}_{66} \end{bmatrix} \begin{Bmatrix} \varepsilon_{xx} \\ \varepsilon_{yy} \\ \gamma_{xy} \end{Bmatrix} = \left[\bar{\mathbf{Q}}\right] \begin{Bmatrix} \varepsilon_{xx} \\ \varepsilon_{yy} \\ \gamma_{xy} \end{Bmatrix} \tag{1.18}$$

where:

σ_{xx} = normal stress in the x direction
σ_{yy} = normal stress in the y direction
τ_{xy} = in-plane x-y shear stress
ε_{xx} = normal strain in the x direction
ε_{yy} = normal strain in the y direction
γ_{xy} = in-plane x-y shear strain (engineering strain)

The elements in the $\bar{\mathbf{Q}}$ matrix can be calculated using the following formulae [54]:

$$\begin{aligned}
\bar{Q}_{11} &= Q_{11}\cos^4\theta + 2\left(Q_{12}+2Q_{66}\right)\sin^2\theta\cos^2\theta + Q_{22}\sin^4\theta \\
\bar{Q}_{12} = \bar{Q}_{21} &= Q_{12}\left(\sin^4\theta+\cos^4\theta\right) + \left(Q_{11}+Q_{22}-4Q_{66}\right)\sin^2\theta\cos^2\theta \\
\bar{Q}_{22} &= Q_{11}\sin^4\theta + 2\left(Q_{12}+2Q_{66}\right)\sin^2\theta\cos^2\theta + Q_{22}\cos^4\theta \\
\bar{Q}_{16} = \bar{Q}_{61} &= \left(Q_{11}-Q_{12}-2Q_{66}\right)\sin\theta\cos^3\theta + \left(Q_{12}-Q_{22}+2Q_{66}\right)\sin^3\theta\cos\theta \\
\bar{Q}_{26} = \bar{Q}_{62} &= \left(Q_{11}-Q_{12}-2Q_{66}\right)\sin^3\theta\cos\theta + \left(Q_{12}-Q_{22}+2Q_{66}\right)\sin\theta\cos^3\theta \\
\bar{Q}_{66} &= \left(Q_{11}+Q_{22}-2Q_{12}-2Q_{66}\right)\sin^2\theta\cos^2\theta + Q_{66}\left(\sin^4\theta+\cos^4\theta\right)
\end{aligned} \tag{1.19}$$

where θ is the angle of the fibres within the lamina (ply) of interest relative to the x axis of the laminate x-y-z coordinate system. Since each lamina (ply) may have a unique stiffness matrix and orientation, it is convenient to denote the $\bar{\mathbf{Q}}$ matrix within lamina k as $\bar{\mathbf{Q}}_{\mathbf{k}}$ and re-write equation (1.18) in a manner that is specific to lamina k, as follows:

$$\left\{\begin{matrix}\sigma_{xx\,k}\\ \sigma_{yy\,k}\\ \tau_{xy\,k}\end{matrix}\right\} = \begin{bmatrix}\bar{Q}_{11\,k} & \bar{Q}_{12\,k} & \bar{Q}_{16\,k}\\ \bar{Q}_{21\,k} & \bar{Q}_{22\,k} & \bar{Q}_{26\,k}\\ \bar{Q}_{61\,k} & \bar{Q}_{62\,k} & \bar{Q}_{66\,k}\end{bmatrix} \left\{\begin{matrix}\varepsilon_{xx\,k}\\ \varepsilon_{yy\,k}\\ \gamma_{xy\,k}\end{matrix}\right\} = \left[\bar{\mathbf{Q}}_{\mathbf{k}}\right] \left\{\begin{matrix}\varepsilon_{xx\,k}\\ \varepsilon_{yy\,k}\\ \gamma_{xy\,k}\end{matrix}\right\} \tag{1.20}$$

where:

$\sigma_{xx\,k}$ = normal stress in the x direction within lamina k
$\sigma_{yy\,k}$ = normal stress in the y direction within lamina k
$\tau_{xy\,k}$ = in-plane x-y shear stress within lamina k
$\varepsilon_{xx\,k}$ = normal strain in the x direction within lamina k
$\varepsilon_{yy\,k}$ = normal strain in the y direction within lamina k
$\gamma_{xy\,k}$ = in-plane x-y shear strain (engineering strain) within lamina k

1.2.8 Classical Laminated Plate Theory

Basic Assumptions Implicit in Classical Laminated Plate Theory:

Classical Laminated Plate Theory (CLPT) is based upon a series of assumptions that are similar to those which govern Euler-Bernoulli beam theory and plate theory. As such, CLPT is only valid for thin laminates where the in-plane dimensions of the laminate are much greater (typically ten times or more) than the thickness of the laminate, and is only applicable when displacements are relatively small in the transverse direction. In essence, it is governed by Kirchoff-Love thin plate assumptions [43][53], as follows:

1. Surface normals remain straight.

2. Surface normals remain perpendicular to the mid-plane of the laminate.

3. The thickness of the laminate does not change during deformation.

It is important to note that, although it was assumed that the thickness of the laminate does not change during deformation, CLPT is based upon the assumption that a state of plane stress exists within each lamina (ply) of the laminate. Strictly speaking, this condition of plane stress implies that through-thickness (out-of-plane) strains are non-zero; however, within the context of CLPT analyses, it is reasonable to assume that these through-thickness deformations are negligible; hence, the thickness of the laminate does not change appreciably during deformation.

Furthermore, perfect interlaminar bonding is assumed. As such, the following assumptions regarding interlaminar bonds are made:

1. All interlaminar bonds are infinitesimally small, and there are no flaws or gaps between the laminae.
2. Interlaminar bonds exhibit no shear deformation, and laminae do not slip relative to each other.
3. Interlaminar bonds exhibit infinite strength.

In addition to the aforementioned assumptions, CLPT requires that each lamina (ply) comprises a uniform material composition and orientation. As such, the aforementioned lamina stiffness matrix $\mathbf{\bar{Q}_k}$ shall be considered constant over the thickness of each lamina (ply).

General Use

A laminate can comprise many laminae (plies), each with different thicknesses, compositions, and fibre orientations, in order to achieve desired mechanical properties for the laminate. For a given laminate x-y-z coordinate system, it is possible to develop stiffness matrices (extensional, coupling, and bending stiffness matrices) that can be used to describe the axial, shear, twisting, and flexural behaviour of such laminates within that coordinate system. The mathematical principals used to formulate these matrices are often referred to as Classical Laminated Plate Theory (CLPT). The origins of CLPT can be traced to work that was carried out by Reissner, Stavsky, Dong, Matthiesen, Pister, and Taylor in the early 1960's [67][23][24]; however, highly detailed and refined descriptions of CLPT are presented in most modern texts on the mechanics of composite materials [54][39]. The extensional **A**, coupling **B**, and bending **D** stiffness matrices are each 3x3 matrices comprising elements that can be calculated using the following formulae:

$$\begin{aligned}
[\mathbf{A}] &= \begin{bmatrix} A_{11} & A_{12} & A_{16} \\ A_{21} & A_{22} & A_{26} \\ A_{61} & A_{62} & A_{66} \end{bmatrix} & A_{mn} &= \sum_{k=1}^{n}\left(\bar{Q}_{mn\,k}\left(z_{T\,k}-z_{B\,k}\right)\right) \\
[\mathbf{B}] &= \begin{bmatrix} B_{11} & B_{12} & B_{16} \\ B_{21} & B_{22} & B_{26} \\ B_{61} & B_{62} & B_{66} \end{bmatrix} & B_{mn} &= \frac{1}{2}\sum_{k=1}^{n}\left(\bar{Q}_{mn\,k}\left(z_{T\,k}^{2}-z_{B\,k}^{2}\right)\right) \\
[\mathbf{D}] &= \begin{bmatrix} D_{11} & D_{12} & D_{16} \\ D_{21} & D_{22} & D_{26} \\ D_{61} & D_{62} & D_{66} \end{bmatrix} & D_{mn} &= \frac{1}{3}\sum_{k=1}^{n}\left(\bar{Q}_{mn\,k}\left(z_{T\,k}^{3}-z_{B\,k}^{3}\right)\right)
\end{aligned} \tag{1.21}$$

where:

n = total number of laminae (plies) in the laminate

$\bar{Q}_{mn\,k}$ = mn term of the $\bar{\mathbf{Q}}_{\mathbf{k}}$ matrix for the k^{th} lamina (see equation (1.20))

A_{mn} = mn term of the **A** matrix for the laminate

B_{mn} = mn term of the **B** matrix for the laminate

D_{mn} = mn term of the **D** matrix for the laminate

$z_{T\,k}$ = distance from the mid-plane of the laminate to the top surface of the k^{th} lamina

$z_{B\,k}$ = distance from the mid-plane of the laminate to the bottom surface of the k^{th} lamina

These extensional **A**, coupling **B**, and bending **D** stiffness matrices can be assembled into one large laminate stiffness matrix **C**, which can then be used to relate forces and moments to mid-plane strains and curvatures as follows [54] [39]:

$$\text{Laminate stiffness matrix} = [\mathbf{C}] = \begin{bmatrix} [\mathbf{A}] & [\mathbf{B}] \\ [\mathbf{B}] & [\mathbf{D}] \end{bmatrix} \tag{1.22}$$

$$\begin{Bmatrix} N_{xx} \\ N_{yy} \\ N_{xy} \\ M_{xx} \\ M_{yy} \\ M_{xy} \end{Bmatrix} = \begin{bmatrix} A_{11} & A_{12} & A_{16} & B_{11} & B_{12} & B_{16} \\ A_{21} & A_{22} & A_{26} & B_{21} & B_{22} & B_{26} \\ A_{61} & A_{62} & A_{66} & B_{61} & B_{62} & B_{66} \\ B_{11} & B_{12} & B_{16} & D_{11} & D_{12} & D_{16} \\ B_{21} & B_{22} & B_{26} & D_{21} & D_{22} & D_{26} \\ B_{61} & B_{62} & B_{66} & D_{61} & D_{62} & D_{66} \end{bmatrix} \begin{Bmatrix} \varepsilon_{xx}^{0} \\ \varepsilon_{yy}^{0} \\ \gamma_{xy}^{0} \\ k_{xx} \\ k_{yy} \\ k_{xy} \end{Bmatrix} = [\mathbf{C}] \begin{Bmatrix} \varepsilon_{xx}^{0} \\ \varepsilon_{yy}^{0} \\ \gamma_{xy}^{0} \\ k_{xx} \\ k_{yy} \\ k_{xy} \end{Bmatrix} \tag{1.23}$$

where:

N_{xx} = normal force in the x direction, per unit width of laminate

N_{yy} = normal force in the y direction, per unit width of laminate

N_{xy} = in-plane x-y shear force, per unit width of laminate

M_{xx} = bending moment in the x-z plane, per unit width of laminate
M_{yy} = bending moment in the y-z plane, per unit width of laminate
M_{xy} = twisting moment, per unit width of laminate
ε^0_{xx} = mid-plane normal strain in the x direction of the laminate
ε^0_{yy} = mid-plane normal strain in the y direction of the laminate
γ^0_{xy} = mid-plane in-plane x-y shear strain (engineering strain) in the laminate
k_{xx} = bending curvature of the laminate in the x-z plane
k_{yy} = bending curvature of the laminate in the y-z plane
k_{xy} = twisting curvature of the laminate

The laminate compliance matrix **S** can be obtained by taking the inverse of the laminate stiffness matrix, resulting in the following relationship:

$$\text{Laminate compliance matrix} = [\mathbf{S}] = [\mathbf{C}]^{-1} = \begin{bmatrix} [\mathbf{a}] & [\mathbf{b}] \\ [\mathbf{b}]^{\mathrm{T}} & [\mathbf{d}] \end{bmatrix} \tag{1.24}$$

$$\begin{Bmatrix} \varepsilon^0_{xx} \\ \varepsilon^0_{yy} \\ \gamma^0_{xy} \\ k_{xx} \\ k_{yy} \\ k_{xy} \end{Bmatrix} = \begin{bmatrix} a_{11} & a_{12} & a_{16} & b_{11} & b_{12} & b_{16} \\ a_{21} & a_{22} & a_{26} & b_{21} & b_{22} & b_{26} \\ a_{61} & a_{62} & a_{66} & b_{61} & b_{62} & b_{66} \\ b_{11} & b_{21} & b_{61} & d_{11} & d_{12} & d_{16} \\ b_{12} & b_{22} & b_{62} & d_{21} & d_{22} & d_{26} \\ b_{16} & b_{26} & b_{66} & d_{61} & d_{62} & d_{66} \end{bmatrix} \begin{Bmatrix} N_{xx} \\ N_{yy} \\ N_{xy} \\ M_{xx} \\ M_{yy} \\ M_{xy} \end{Bmatrix} = [\mathbf{S}] \begin{Bmatrix} N_{xx} \\ N_{yy} \\ N_{xy} \\ M_{xx} \\ M_{yy} \\ M_{xy} \end{Bmatrix} \tag{1.25}$$

Basis of Derivation and Implications

In order to properly understand the aforementioned constitutive relationships for laminated plates, it is valuable to examine the strain-displacement relationships upon which CLPT is based. The following equations describe the in-plane strains within each lamina (ply) of a laminate, as a function of laminate displacement derivatives and the elevation of the relevant ply within the laminate:

$$\begin{aligned} \varepsilon_{xx\,k} &= \frac{\partial u}{\partial x} - z_k \frac{\partial^2 w}{\partial x^2} \\ \varepsilon_{yy\,k} &= \frac{\partial v}{\partial y} - z_k \frac{\partial^2 w}{\partial y^2} \\ \gamma_{xy\,k} &= \frac{\partial u}{\partial y} + \frac{\partial v}{\partial x} - 2z_k \frac{\partial^2 w}{\partial x \partial y} \end{aligned} \tag{1.26}$$

where:

u, v, and w represent mid-plane displacements in the x, y, and z directions, respectively

$\varepsilon_{xx\,k}$ = normal strain in the x direction within lamina k
$\varepsilon_{yy\,k}$ = normal strain in the y direction within lamina k
$\gamma_{xy\,k}$ = in-plane x-y shear strain (engineering strain) within lamina k
z_k = elevation of lamina k above the mid-plane of the laminate

In deriving CLPT, the following definitions are stipulated in order to simplify the assembly of the laminate stiffness matrix:

$$\begin{aligned} \varepsilon_{xx}^0 &= \frac{\partial u}{\partial x} & \varepsilon_{yy}^0 &= \frac{\partial v}{\partial y} & \gamma_{xy}^0 &= \frac{\partial u}{\partial y} + \frac{\partial v}{\partial x} \\ k_{xx} &= -\frac{\partial^2 w}{\partial x^2} & k_{yy} &= -\frac{\partial^2 w}{\partial y^2} & k_{xy} &= -2\frac{\partial^2 w}{\partial x \partial y} \end{aligned} \tag{1.27}$$

where:

u, v, and w represent mid-plane displacements in the x, y, and z directions, respectively
ε_{xx}^0 = mid-plane normal strain in the x direction of the laminate
ε_{yy}^0 = mid-plane normal strain in the y direction of the laminate
γ_{xy}^0 = mid-plane in-plane x-y shear strain (engineering strain) in the laminate
k_{xx} = bending curvature of the laminate in the x-z plane
k_{yy} = bending curvature of the laminate in the y-z plane
k_{xy} = twisting curvature of the laminate

It is evident from the aforementioned relationships that ε_{xx}^0, ε_{yy}^0, γ_{xy}^0, k_{xx}, and k_{yy} are defined in a manner that is consistent with common stress analysis conventions. Conversely, the definition for k_{xy} results in a twisting curvature that is double of what is typically utilized in other realms of stress analysis. Compounding this peculiarity is the fact that, in CLPT, twisting moments are assumed to have been applied to all four edges of a square stress element; hence, the value of M_{xy} is, in fact, half of the total torque imposed upon the laminate. This discrepancy is discussed in more detail in Section 3.11.3.

Based upon the elements of the laminate compliance matrix **S** in conjunction with an understanding of the aforementioned definitions used in the derivation of CLPT, it is possible to determine objective values of some of the bulk composite mechanical properties of a laminate within its laminate x-y-z coordinate system, as follows:

$$\begin{aligned}
\text{Elastic modulus along the } x \text{ axis} = \quad & E_{xx} = \frac{1}{h * S_{11}} \\
\text{Elastic modulus along the } y \text{ axis} = \quad & E_{yy} = \frac{1}{h * S_{22}} \\
\text{Shear modulus in the } x\text{-}y \text{ plane} = \quad & G_{xy} = \frac{1}{h * S_{33}} \\
\text{Poisson's ratio in the } x\text{-}y \text{ direction} = \quad & \nu_{xy} = -\frac{S_{21}}{S_{11}} = -\frac{S_{12}}{S_{11}} \\
\text{Poisson's ratio in the } y\text{-}x \text{ direction} = \quad & \nu_{yx} = -\frac{S_{21}}{S_{22}} = -\frac{S_{12}}{S_{22}}
\end{aligned} \tag{1.28}$$

where h is the total thickness of the laminate, and S_{mn} is the mn term of the laminate compliance matrix **S** (see equations (1.24) and (1.25)).

1.2.9 Coupling Effects

> This section includes work that was reproduced and adapted from [35]. It incorporates parts of a state-of-the-art review of literature that was produced in collaboration with Dr. Derek Northwood. In all cases, the key ideas and primary contributions were provided by the author, and the contribution of the co-authors was primarily of a supervisory nature. Permission to reproduce this content has been granted by the co-authors (see Appendix E) and the copyright owner (see Appendix F).

It is evident from inspection of the stiffness and compliance matrices from CLPT that it is possible for coupling to exist between the various possible loadings and displacements in a fibre-composite laminate. For example, if bending-twisting coupling exists, then a laminate that is experiencing a simple out-of-plane uniaxial bending moment about its transverse axis would respond by exhibiting both flexural deformation and torsional deformation. The types of coupling that may exist in a laminate include: extensional-shear, extensional bending, bending-twisting, bending-shear, twisting-shear, and extensional-twisting. The cause of some of these coupling behaviours may seem logical simply by examining the stacking sequence of a laminate. However, it is also possible to predict when each type of coupling will occur by examining the terms in the extensional **A**, coupling **B**, and bending **D** stiffness matrices [54]; if certain terms of these matrices have a value of zero, then the associated coupling phenomenon is eliminated. Table 1.2 shows which stiffness matrix terms control each of the aforementioned coupling phenomena, and which common types of laminate architectures are resistant to each type of coupling. It can be inferred from Table 1.2 that it is impossible to simultaneously eliminate all forms of coupling in a single laminate. Therefore, when designing a laminate, one must decide which types of coupling would pose the greatest detriment to the performance of the structure, or conversely, which types of coupling could be most beneficial.

Table 1.2: Coupling phenomena in various common types of laminate architectures – Reproduced and adapted from [35].

Coupling Type	**Relevant Stiffness Matrix Terms**	**Type of Laminate Architecture**			
		Unbalanced	**Balanced Unsymmetric**	**Balanced Symmetric**	**Balanced Anti-symmetric**
Extensional-Shear	A_{16} / A_{26}	May be non-zero	0	0	0
Extensional-Bending	B_{11} / B_{12} / B_{22}	May be non-zero	May be non-zero	0	0
Bending-Twisting	D_{16} / D_{26}	May be non-zero	May be non-zero	May be non-zero	0
Bending-Shear	B_{16} / B_{26}	May be non-zero	May be non-zero	0	May be non-zero
Twisting-Shear	B_{66}	May be non-zero	May be non-zero	0	0
Extensional-Twisting	B_{16} / B_{26}	May be non-zero	May be non-zero	0	May be non-zero

1.3 Review of Recent Literature Relevant to the Proposed Structural System

1.3.1 General

Fibre reinforced polymer (FRP) composite laminates are becoming increasingly prevalent in the design of automotive and aerospace structures. Among the most commonly cited benefits of these materials is the ability to create complex and unusual shapes as large, single-component structures; this serves to enhance aerodynamic and aesthetic cleanliness, reduces weight (the mass of metallic mechanical fasteners can add up to a significant percentage of a total aircraft's mass), and dramatically reduces time spent installing mechanical fasteners during fabrication. However, mechanical fasteners do remain a necessary and important part of most laminated composite aerospace and automotive structures; they facilitate serviceability by enabling temporary deconstruction and access to internal components, and they substantially ease replacement of parts that have been damaged beyond reasonable repair. Unfortunately, the current state-of-the-art in mechanical fasteners for laminated composites leaves much to be desired. The present author is of the opinion that hybrid composite technology could help to facilitate improved mechanical joints in laminated composite structures, and that one method of fabricating these hybrid structural members might be to utilize co-pultrusion technology. The following sections include a brief review of literature pertaining to mechanical fasteners for FRP composite laminates, as well as some existing examples of hybrid co-pultrusion technology being utilized in industry.

1.3.2 Mechanical Fastening of Fibre Reinforced Polymer Composites

In 1989, Vinson produced a comprehensive review of literature pertaining to the design and analysis of mechanical fastening techniques for fibre reinforced polymer composites [84]. It was made clear from this work that the behaviour of mechanically fastened FRP laminates is dependent upon a plethora of complex mechanical principals that require considerably more rigorous engineering analysis techniques than similarly joined metallic structurally members. Ultimately, it was concluded that the only safe approach to designing mechanical connections for FRP laminates is through empirical techniques. In addition, it was stated that the strength and reliability of a mechanical joint are considerably enhanced when the joint is supplemented with adhesive bonding; however, such an adhesive bond would negate the serviceability of the mechanical connection, thus defeating one of the primary benefits of employing mechanical fasteners.

The Hi-Shear Corporation (now a division of Lisi Aerospace) developed a series of threaded mechanical fasteners called HI-LITE™ and HI-LOK™. Both HI-LITE™ and HI-LOK™ systems comprise a threaded metallic pin and a self-locking threaded collar with a hexed portion that can be tightened using a pneumatically driven socket wrench. The hexed portion of the collar is designed to shear (break) off of the collar at a pre-determined torque value, thus ensuring that the fastener is tightened to the correct specification without the aid of a torque monitoring device. In addition, these fasteners are designed to enable one-sided installation, thus dramatically reducing time and logistical concerns during fabrication of large structural systems such as aircraft fuselages. HI-LITE™ and HI-LOK™ fasteners have seen broad acceptance and implementation by the aerospace industry to serve as mechanical fasteners for both metallic and composite structures. These fasteners are available in a multitude of high performance metals; when carbon FRP laminates are to be mechanical fastened, it is often necessary to employ titanium HI-LITE™ fasteners in order to prevent galvanic corrosion. Lisi Aerospace subsequently improved upon the aforementioned fasteners when they developed the PULL-IN™ and PULL-STEM™ fastening systems. A plethora of similar fasteners have been developed for various specialized applications (ultra-light weight, corrosion resistance, improved sealing properties, gentler installation for composites, etc.), but most are comparable to the fundamental design principal of the HI-LITE™ and HI-LOK™ fastener systems. Figures 1.3 and 1.4 are photographs of titanium HI-LITE™ fasteners used in a hybrid CFRP and aluminium aircraft fuselage structure. Figure 1.3 is an exterior view that shows the flush head of this type of fastener, and Figure 1.4 is an interior view that shows the collar and threaded pin of this type of faster.

Figure 1.3: Exterior view of a titanium HI-LITE™ fastener used to mechanically fasten a CFRP laminate to an aluminium part. Note that the flush head of the fastener is visible in this photograph.

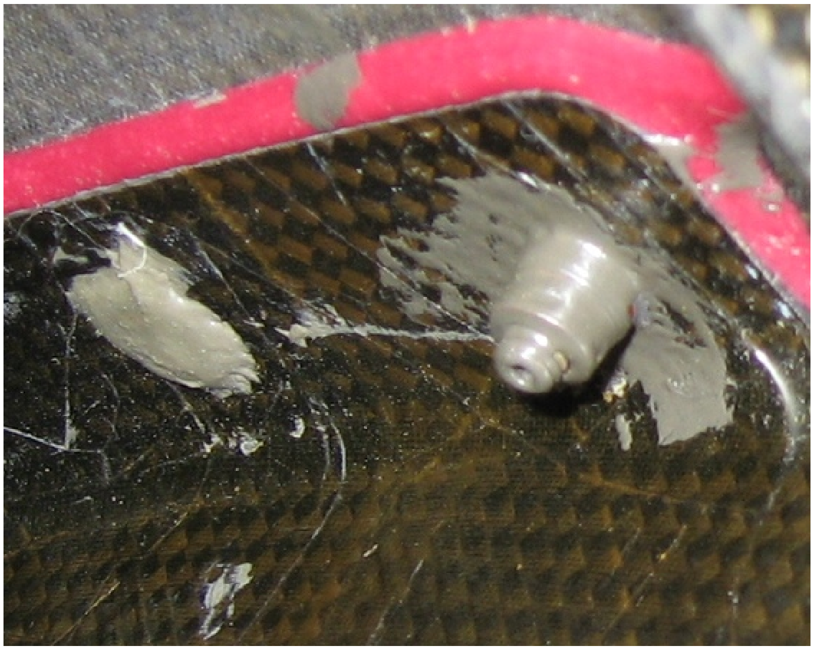

Figure 1.4: Interior view of a titanium HI-LITE™ fastener used to mechanically fasten two CFRP laminates together. Note that the collar and threaded pin of the fastener are visible in this photograph, but are somewhat obscured by a polymeric sealant.

While conventional bucked solid AN (Air Force / Navy specifications) rivets are commonplace in metallic aircraft structures, damage caused by the bucking process can present difficulties when employing these fasteners for laminated composite aircraft structures. Nevertheless, Cherry Aerospace® has developed the Cherry Hollow End E-Z Buck® rivet, which is a hollow ended solid AN style rivet composed of a Titanium-Columbium alloy. The corrosion resistant properties and hollow ended design of the Cherry Hollow End E-Z Buck® rivet make it ideal for the creation of double-flush (flush on both exposed surfaces) mechanical connections in metallic and/or laminated composite structures. Cherry Aerospace® also developed the Cherry 1900 rivet, which is a pull type blind rivet that has been specifically engineered to facilitate structural riveting of laminated composite materials. In essence, the Cherry 1900 rivet was designed as an improvement upon the NSA1900, NAS1919, and NAS1921 rivet specifications, which have become commonplace in aerospace laminated composite structures. Numerous competing manufacturers have released products that are similar to the Cherry 1900 rivet.

1.3.3 Hybrid Composite Technology

Van Dijk Pultrusion Products (DPP) of the Netherlands advertises its capability of producing co-pultruded products with embedded optical cables, copper wires, and polyether ether ketone (PEEK) tubes. While DPP is not specific in advertising the intended purpose of including these co-pultruded materials, it seems that their primary purpose would be for the transmission of fluids (PEEK tubing), electricity (copper wires), or optical signals (optical cables) through a pultruded part. In addition, DPP advertises their ability to pultrude members that incorporate both glass fibres and carbon fibres. Conversely, DPP makes no explicit mention of the inclusion of co-pultruded metallic elements that would be used for structural purposes, or that could serve as hard-points to accept serviceable mechanical fasteners.

International patent WO 2001/024993 A1 [8] details a hybrid thermoplastic pultrusion / co-extrusion window frame system called “FibrePlas™”. In essence, FibrePlas™ is an extruded thermoplastic window frame system that incorporates embedded co-extruded glass FRP (GFRP) pultruded elements that serve to stiffen the extrusion without the aid of metallic components. Prior to the advent of FibrePlas™, extruded thermoplastic window frames often necessitated internal metallic stiffening elements; the relatively high thermal conductivity of these metallic stiffening elements detracted from the overall thermal insulation afforded by the glazing system. While the technology is most commonly referred to as FibrePlas™, the original collaborative development and funding of the technology appears to have been managed by Pera Technology under the project name “Stiffex”. The details of this collaborative development are unclear to the present author.

International patent WO 2004/101909 A1 [15] proposed a pultruded glass FRP (GFRP) profile reinforced by embedded co-pultruded metal cords. The purpose of the embedded metal cords is to increase the strength and stiffness of the pultrusion without the aid of more costly reinforcing fibres such as carbon fibres. The physical form of metal cords (a twisted bundle of smaller metal filaments) offers greater surface area than solid metals wires of comparable cross-sectional area; as such the inventors suggest that metal cords can potentially facilitate a superior adhesive bond to the surrounding polymer resin. The inventors also claim that metal cords offer superior fatigue resistance in comparison with similarly sized solid metal wires. Finally, the inventors claim that the superior flexibility of metal cords would offer easier handling during the pultrusion process, in comparison with the use of solid metal wires. Unfortunately, the physical form of metal cords renders them non-conducive for use as integral hard-points to accept mechanical fasteners.

NASA and Boeing conducted a large body of work on a novel structural system called "Pultruded Rod Stitched Efficient Unitized Structure (PRSEUS)" [83][52][82][47], which capitalizes on pultruded carbon FRP (CFRP) rod technology for use as the cords at the bulbous tips of T-stringers. PRSEUS is intended to be used as the primary structural system for blended wing aircraft, which present a plethora of particularly daunting structural problems for aerospace engineers. PRSEUS utilizes a laminated CFRP skin with an overlaid grid of intersecting CFRP T-frames and T-stringers. Pre-pultruded CFRP rods are enveloped within the bulbous tip of each T-frame and T-stringer. The flanges of these T-stringers are fastened to the composite skin of the aircraft using a complex blend of overlapped laminae (frame cap stacks and stringer tear straps) and through-thickness stitching. This entire system of stitched carbon fabrics and pre-pultruded CFRP rods is assembled dry, and is subsequently impregnated with resin using the resin infusion process. Although the unitized nature of this structural system may be advantageous from the standpoint of durability (superior crack-arresting capability) and structural efficiency (light weight due to minimal mechanical fasteners), the non-serviceable permanent connections between the stringers and the skins will likely complicate repairs considerably.

1.4 Review of Recent Literature Relevant to the Present Analytical Method

1.4.1 General

Over the past half-century, a wealth of engineering methodologies has been developed for the analysis of fibre reinforce polymer composite laminates. However, it is the opinion of the present author that the complexity of most of these analytical methodologies are well beyond the scope of what can reasonably be expected for regular use by an industry engineer. The following sections detail the current state-of-the-art in analytical methodologies that are relevant to the present structural problem of a hybrid co-pultruded composite aircraft stringer.

1.4.2 Composite Thin-Walled Open Sections

In 1993, Barbero, Lopez-Anido, and Davalos produced a manuscript on the mechanics of thin-walled laminated composite beams [5]. This highly influential piece of work detailed one of the first formal approaches developed to model the elastic mechanics of built-up laminated composite beams having arbitrary cross-sectional geometries, and it included the first published instance of the term "Mechanics of Laminated Beams (MLB)". In essence, the goal of MLB is to arrive upon a unidimensional beam model that is analogous to the analytical models that are typically used for the structural analysis of beams composed of conventional homogeneous and isotropic engineering materials. MLB employs Classical Laminated Plate Theory (CLPT) to ascertain the relevant elastic constants of each individual laminated leg of the section, and then integrates these elastic constants over the cross-sectional area in order to arrive upon the global elastic properties of the entire built-up thin-walled beam. A Timoshenko transverse shear correction factor is employed in MLB, which is formulated based upon shear energy equivalence (arguably the most broadly accepted method found in the literature). This 1993 work of Barbero et al also provided a comprehensive review of relevant literature (prior to 1993) pertaining to the analysis of built-up thin-walled laminated beams. In particular, this literature review discussed the origins of laminated beam theories (which were very much in their infancy at the time), and went on to cite a plethora of references concerned with the calculation of a Timoshenko transverse shear correction factor. While this 1993 work on MLB served as an excellent starting point for future work, it failed to provide the full suite of beam constants necessary to perform a full flexural-torsional buckling analysis. In particular, torsional stiffness and warping stiffness were not addressed at all in this 1993 publication. Having said that, although its formulation does lack fidelity and versatility, MLB remains today as one of the most pragmatic and robust methods of determining the general elastic response of built-up thin-walled laminated beams, and was used extensively as a baseline for the formulation of the author's present analytical method.

In 2000, Ascione, Feo, and Mancusi formulated a unidimensional beam model to predict the mechanical behaviour of built-up thin-walled laminated beams, while accounting for the effects of in-plane shear compliance [3]. In 2010, Feo and Mancusi refined the aforementioned analytical method by formulating a general approach to model the effects of in-plane shear compliance in thin-walled laminated composite beams [28]. The derivation of this model employed a variational formulation to solve for a series of unknown kinematic functions. The authors approximated the mid-plane in-plane shear stress field using assumed polynomial shape functions that were defined such that equilibrium requirements were satisfied. Strictly speaking, this is a relatively accurate method of analysis since compatibility issues often emerge in conventional techniques that recover the normal stress fields and shear stress fields sequentially. Unfortunately, this methodology appears to complicate matters to the extent that the underlying mechanical principals are all but lost. The implementation of an assumed mid-plane in-plane shear stress field seems needlessly complex given that a fairly accurate (for practical purposes) stress field can be ascertained by assuming a linear normal stress field and subsequently calculating the resulting mid-plane in-plane shear stress field in accordance with equilibrium requirements [25][89]. In both of the aforementioned manuscripts [3][28], the model was validated using the finite element method, and the results were compared with conventional Vlasov warping analyses (ignoring the effects of in-plane shear compliance). The validation cases that were modelled included concentric 4-point bending and eccentric 4-point bending. Unfortunately, while the authors suggest that a logical application of their analytical method is in the case of laminated composite beams, the aforementioned manuscripts [3][28] make no effort to employ coupled anisotropic elastic constants, and instead employ simple homogeneous and orthotropic material models. As such, any use of this method for the analysis of beams comprising laminated composites would necessitate further development and adaptation of the presented analytical method to account for the peculiarities of laminated composites. Ultimately, while the aforementioned analytical models may be conducive for implementation in commercial finite element analysis (FEA) software, it is the opinion of the present author that these works are dependent upon a level of mathematical rigour that is far beyond the practical limitations for common use by engineers in an industry setting.

A plethora of manuscripts have been produced since 1997 with regards to a new software tool entitled “Variational Asymptotic Beam Section (VABS)” [16][87][97][96][42]. As its name suggests, VABS is a software tool that can be used to determine a suite of section constants to be used in 1-dimensional analyses of beams having complex cross-sectional geometries and material compositions. It does so using the “Variational Asymptotic Method (VAM)”, whereby variational energy methods are employed to dimensionally collapse the behaviour of a complex 3-dimensional beam (such as a built-up laminated composite beam) into a unidimensional beam model. While the present author does not doubt the obvious benefits of VABS for the purpose of dramatically reducing computing time in comparison with conventional finite element analysis techniques, the philosophical concept of VABS does not appear to be compatible with the goals of the present author’s work. Ultimately, VABS can be viewed as a computational means of determining constants that can subsequently be used in simplified analytical hand calculations. However, VABS fails to maintain the involvement of the engineer in the formulation of these section constants; and while accurate, it provides limited information pertaining to the cause of any shortcomings in one or more of these section constants. As such, the present author has given very limited attention to this particular analytical technique. In 2001, Volovoi, Hodges, Cesnik, and Popescu summarized some of the existing state-of-the-art composite beam theories, and provided an assessment of these theories within the context of helicopter rotor blade analyses [88]; among the theories assessed in this work was the aforementioned VABS software tool, which was shown to perform admirably in comparison with some of its contemporary analytical theorems. Unfortunately, the conclusions presented in this work appear to have been drawn with a distinct bias toward the VABS software, which was developed by some of the same authors.

In 2001, Kollár created a comprehensive piece of work [44] that detailed an analytical procedure for calculating the flexural-torsional buckling response of thin-walled open sections having laminated composite walls. Kollár's work accounted for the effects of in-plane shear compliance, and was formulated in a manner that was intended to be more simplistic than previously developed works such that it could be realistically employed in industry engineering applications. Nevertheless, Kollár's work seems to focus a great deal on new and unique concerns that would be foreign to most industry engineers who are more familiar with classical structural analysis techniques. For example, Kollár discusses the issue that the position of the shear-centre of a thin-walled open section can vary depending upon whether it is being used for the analysis of bending deformations or for shear deformations. In addition, Kollár explains that a thin-walled open section has a set of flexural principal axes that are not necessarily the same as the principal axes that would be relevant during the application of transverse shear loads. While these concerns may be valid in some extreme cases, the present author questions whether their significance is as great as some more basic concerns such as overlapped cross-sectional areas at the intersection of two or more section walls (see Section 3.6), or insufficient fidelity in the calculation of the torsional stiffness of the walls (legs) of the section (see Section 3.11). In addition, Kollár's work is limited to the analysis of members that comprise laminates that are free from axial-shear coupling; to the present author, this limitation seems to be of comparable or greater significance than the aforementioned rigour with which shear-centre and principal axes are treated. Having said that, Kollár's work was highly influential in the development of subsequent analytical models, and was certainly used as a guide in the development in the present author's analytical model.

In 2002, Kollár and Pluzsik developed an analytical model to predict the behaviour of general built-up thin-walled open sections having walls of arbitrary laminate stacking sequences [45]. In this work, the effects of in-plane shear compliance were neglected; instead, focus was placed upon careful treatment of the anisotropy of the laminated section walls, and the various coupling phenomena that result. The authors made direct recommendations as to when each form of coupling may be neglected, and hence, under what circumstances it would be reasonable to employ simplified analysis techniques whereby various terms of the laminate stiffness matrix can be ignored. In 2002, Pluzsik and Kollár carried out a comparative study between the aforementioned analytical model and the results of a plethora of finite element analyses [62]. The authors discussed the implications of neglecting the effects of shear deformations under various circumstances, and made some practical engineering suggestions as to when it would likely be reasonable to neglect these effects. The present author believes that these two clearly written manuscripts [45][62] have provided a substantial contribution to the general body of composites engineering science. The methodologies and recommendations discussed in these manuscripts can serve as a basis for future composite beam analytical methods; although future developments should likely incorporate provisions for the effects of in-plane shear compliance.

In 2003, De Lorenzis and La Tegola produced an analytical model to predict the behaviour of pultruded composite beams that are composed of transversely isotropic materials having material coordinate systems aligned with the longitudinal axis of the member [22]. In this work, the authors utilized an existing theory developed by Capurso in 1964 [11][12][13][14] for members composed of isotropic materials, and adopted this theory for applications involving transversely isotropic materials. The aforementioned model improves upon Vlasov thin-walled beam theory [85] by accurately modelling the interaction between in-plane shear stresses and longitudinal normal stresses at the mid-plane of the walls of the beam. Throughout the manuscript, the authors repeatedly referred to their model as an “exact theory”, despite its dependence upon a plethora of engineering assumptions. In particular, the work of De Lorenzis and La Tegola ignores all out-of-plane compliance, and is therefore limited to the analysis of members comprising shells that can be modelled in accordance with thin-plate assumptions, whereby out-of-plane effects are negligible. While this may not be problematic within the context of the intended purpose of the model, the present author takes exception to the use of the term “exact theory” in this context, given that the degree of accuracy afforded by this model is dependent upon the thickness of the walls of the member that is to be modelled.

In 2004, Lee and Lee produced an analytical model to predict the flexural-torsional behaviour of thin-walled laminated composite beams having I-shaped cross-sections subjected to transverse and/or torsional loadings [49]. This model was based upon Classical Laminated Plate Theory (CLPT), and was formulated to account for bending-twisting coupling in beams comprising arbitrary laminate stacking sequences. In essence, the authors drew upon Vlasov’s kinematic assumptions for thin-walled beams, and applied CLPT to the resulting model. A variational formulation based upon internal strain energy and external work was used to derive the fully coupled stiffness matrix of the beam. Ultimately, the model was validated against numerical data from finite element analyses. While accurate within the context of the presented validation cases, the presented analytical model failed to account for the effects of in-plane shear compliance, which could lead to dangerous overpredictions of transverse stiffness and/or elastic buckling loads in some cases. Ultimately, this 2004 work of Lee and Lee was a valuable contribution to the literature because it demonstrated a means to account for the effects of bending-twisting coupling in thin-walled laminated beams; however, because of its failure to incorporate the effects of in-plane shear compliance, the model may be unfit for the analysis of some laminated composite beams having low in-plane shear moduli.

In 2005, Lee developed an analytical model to predict the flexural behaviour of thin-walled composite beams whilst accounting for shear effects [48]. In 2009, Vo and Lee built upon this aforementioned piece of work by developing an analytical model to predict the buckling load of thin-walled composite beams whilst accounting for sixfold coupled effects [86]. Both of these works appear to have been influenced by the aforementioned 2001 work of Kollár [44], but were formulated in a manner that facilitates the inclusion of fully anisotropic laminates. However, while the work of Vo and Lee does account for in-plane shear compliance, it is assumed that shear strains are uniformly distributed over the entire cross-section; hence, mid-plane in-plane shear stresses do not vanish at the free edges. This differs from the 2001 work of Kollár [44], which more accurately accounted for the the distribution of in-plane shear stresses by employing proper equilibrium and compatibility relationships. It is also worth mentioning that the aforementioned works of Vo and Lee incorporated rigorous analytical provisions intended to account for the contribution of out-of-plane shear strains through the thickness of each individual leg of a thin-walled open section; however, it is possible that the increased fidelity gained by the inclusion of this behaviour is outweighed by the failure to account for vanishing of mid-plane in-plane shear stresses at the free edges of the section.

In 2006, Erkmen and Mohareb developed an analytical model to predict the warping behaviour of open thin-walled beams, while accounting for additional warping compliance due to the effects of mid-plane in-plane shear strains [25]. A new coefficient was introduced to account for additional warping compliance due to mid-plane in-plane shear effects, which was calculated as a function of the distribution of in-plane shear strains at the mid-planes of the laminates. This new term was then substituted into the total complimentary energy equation, the variation of this equation was taken, and upon some manipulation, the differential field equation describing the warping behaviour of the beam was recovered. The authors used examples to demonstrate the increased warping compliance predicted by their model in comparison with conventional Vlasov warping analysis techniques that ignore in-plane shear compliance. Unfortunately, the examples selected by the authors only exhibited a 2% discrepancy between these two techniques, which understates the importance of their proposed analytical methodology. The authors then went a step further by developing two bespoke beam elements that could facilitate implementation of their warping model into commercial finite element analysis software.

In 2011, Ascione, Giordano, and Spadea produced an analytical model for the lateral buckling of pultruded fibre reinforced polymer (FRP) beams that accounts for additional warping compliance caused by mid-plane in-plane shear strains [2]. This work discretized warping rotations into two components: those caused by conventional Vlasov warping effects, and those caused by in-plane shear compliance. In this way, this manuscript is somewhat reminiscent of the aforementioned 2006 work of Erkmen and Mohareb [25], but employs a variational formulation that is severely mathematically intensive. In fact, it is the opinion of the present author that the level of mathematical rigour employed in this work is far beyond the practical limitations for common use by engineers in an industry setting. In addition, the 2011 work of Ascione et al made no effort to demonstrate how one would employ their analytical method for the analysis of thin-walled open sections comprising laminated composites. Conversely, the examples discussed in this manuscript simply employed homogeneous and orthotropic material models.

In 2012, Wang, Zhao, Zhang, and Gong [89] produced a clear and explanatory piece of work detailing an analytical model for the restrained warping of thin-walled open beams having non-trivial in-plane shear compliance. This work was reminiscent of the 2006 work of Erkmen and Mohareb [25] and the 2001 work of Kollár [44], but featured a more detailed and clearly described derivation that was purely analytical in nature and based upon logical mechanical principals. The distribution and magnitude of mid-plane in-plane shear stresses were calculated in accordance with equilibrium and compatibility requirements. A new coefficient was introduced to account for additional warping compliance due to warping-shear effects, which was calculated as a function of integrated in-plane shear strain energy at the mid-plane of each laminate. The total warping deformation due to conventional Vlasov assumptions (neglecting in-plane shear compliance) was calculated, and the additional warping compliance due to mid-plane in-plane shear strains was then added by super-position. The authors then validated their model using the finite element method, and compared the results with those yielded by other existing warping models found in the literature.

It is interesting to note that the 2012 work of Wang, Zhao, Zhang, and Gong [89] yielded a slightly different warping relationship than the model presented by Erkmen and Mohareb in 2006 [25]. Wang et al utilized a strictly analytical approach whereby the additional warping compliance due to shear effects were completely de-coupled from the deformations yielded by the conventional Vlasov warping model (neglecting in-plane shear compliance), and these two sources of twisting compliance were then added by super-position. Conversely, Erkmen and Mohareb utilized a fully coupled complimentary energy equation accounting for all sources of strain energy, thus yielding a single differential equation that accounts for all sources of twisting deformation (Vlasov warping and additional compliance due to mid-plane in-plane shear effects). As a consequence, the derivation presented by Erkmen and Mohareb is considerably more complex than that presented by Wang et al. While it could be argued that the work of Erkmen and Mohareb employed a more rigorous attention to energy balance and must therefore be more correct, the present author is not convinced that this increased rigour and complexity is justified. Furthermore, the present author is not convinced of the validity of the compatibility condition that was ultimately postulated by Erkmen and Mohareb. In both models, the calculation of longitudinal normal strains due to warping deformation is first carried out in the absence of any mid-plane in-plane shear strains; hence, for this calculation, it is assumed that the sectoral normal strain gradient (rate of change of longitudinal normal strains along the mid-plane of the thin-walls of the cross-section) is linear. Subsequent calculations of shear strains and shear stresses is carried out as a function of this previously assumed normal strain distribution. Strictly speaking, this sequential stress calculation technique will always lead to an incorrect stress field that fails to meet all compatibility requirements; however, it is based upon reasonable engineering assumptions and would generally yield reasonably accurate stress field predictions in the context of most common beam geometries. Due to the de-coupled manner in which shear stresses and normal stresses were derived, it seems reasonable to de-couple the strain energies that result from these sources as well, which is precisely the approach that was taken by Wang et al. Ultimately, these two analytical models [25][89] yield similar results; however, the simplicity of the model presented by Wang et al might render it more practical and appealing for industry engineering applications.

1.4.3 Torsional Stiffness of Composite Laminates

In 1998, Jian and Sijian investigated a means of reducing the computational time and effort necessary when employing 3-dimensional finite element analysis (FEA) techniques to model the torsional behaviour of thick laminated plates [38]. In this work, Jian and Sijian focused on the investigation of laminated plates having a large number of layers comprising smaller repeating stacking sequences, often referred to as "sublaminates". The majority of the laminate was modelled using a relatively coarse mesh of 3-dimensional isoparametric elements having smeared composite effective elastic constants. In regions where high stress concentrations and/or steep stress gradients were expected to occur (at the free-edges of the laminate, near the mid-plane of the laminate, and near the surfaces of the laminate), a more refined mesh was employed whereby each lamina (ply) was modelled with a single layer of solid elements having the relevant local lamina (ply) constitutive properties and coordinate system. This type of analysis is quite valuable for the assessment of detailed stress distributions in complex structures comprising thick laminates. In fact, many of the existing commercial FEA software packages (such as MARC® of the MSC™ Software Corporation) now include specialized sublaminate elements that have been formulated specifically for this type of analysis. However, even with the implementation of sublaminate analysis techniques employing smeared composite effective elastic constants, this type of analysis necessitates diligent attention to convergence and careful mesh refinement. In cases where an engineer is more interested in global stiffness or elastic stability (as opposed to detailed stress contour plots), the aforementioned 3-dimensional FEA based technique would likely be needlessly time consuming. Although the necessary computational time and effort for 3-dimensional FEA is gradually being alleviated by ever-increasing computing power, it can be argued that the creation and refinement of a 3-dimensional mesh of a thick laminated plate remains prohibitively time consuming for many applications. As such, it is the opinion of the present author that there exists a strong need for an accurate analytical means of ascertaining the torsional stiffness of thick laminated plates, without depending upon 3-dimensional FEA.

In 1972, Whitney developed a detailed energy-based derivation for a shear correction factor intended to account for through-thickness shear deformations in laminated plates subjected to transverse loadings [90]. In the early 1990's, Whitney subsequently studied through-thickness shear effects in laminated plates subjected to torsional loadings using an analytical technique that was based upon Classical Laminated Plate Theory (CLPT) [91][92][93]; however, in these works, he chose to utilize an approximate general purpose shear correction factor based upon Reissner assumptions [65][66] in lieu of higher fidelity calculations. Unfortunately, this general purpose shear correction factor was formulated in a manner that utilizes a polynomial-based weighting function that ultimately fails to account for the relationship between through-thickness and in-plane shear moduli within the laminate. As such, the accuracy of Whitney's formulation is likely limited to cases in which it can be assumed that the in-plane shear modulus of the laminate is approximately uniform through its thickness.

In 1993, Savoia and Tullini proposed a method of accurately calculating the torsional stiffness of thick laminated plates comprising orthotropic plies [69], which was based upon the treatment of each ply using a method presented by Lekhnitskii for the analysis of single-layer orthotropic plates [50]. Although highly accurate and versatile, the method presented by Savoia and Tullini [69] employs an infinite series; as such, it necessitates careful attention to convergence requirements, and might be considered too cumbersome for some practical engineering applications.

In 1998, Swanson developed a simplified version of the aforementioned analytical method presented by Savoia and Tullini for applications in the analysis of laminated plates having moderate width-to-thickness aspect ratios [75]. Unfortunately, Swanson's formulation [75] does not appear to fully account for the through-thickness distribution of through-thickness shear moduli. As such, the accuracy of Swanson's formulation is likely limited to cases in which it can be assumed that the through-thickness shear modulus of the laminate is approximately uniform through its thickness. This may be a fairly reasonable assumption in the context of laminates having a stacking sequence whereby each lamina (ply) has the same composition (fibres, resin, and fibre volume fraction); however, if one or more laminae (plies) within the laminate have different compositions than the others, then the aforementioned formulation developed by Swanson would likely diverge from the correct solution considerably.

1.4.4 Other Noteworthy Works

Throughout the 1980's and early 1990's, NASA researchers developed a laminated composite analysis software tool called "Integrated Composites Analyzer (ICAN)" [59][60]. In essence, ICAN carried out calculations comprising an amalgamation of many of the state-of-the-art analytical and empirical models available at the time to provide a suite of meaningful data pertaining to the expected behaviour of a given fibre composite laminate. While ICAN placed particular importance on the analysis of hygrothermal effects, a wealth of engineering data was afforded by this software. In particular, ICAN provided outputs that included: ply stress-strain influence coefficients, coefficients for micro-mechanics modelling, stress-concentration factors for select scenarios, predictions of probable delamination locations for select scenarios, stresses due to free-edge effects, failure analysis, and transverse (out-of-plane) stresses. In addition, ICAN was capable of generating material input cards to be used with NASTRAN® and/or MARC® finite element analysis solvers. ICAN also included a database of commonly used material constituents (fibres and resin matrices) and fabrication techniques; users could select materials and fabrication techniques from this database and allow ICAN to automatically calculate the resulting composite material properties.

In 2012, Li and Batra derived a method of calculating the critical buckling load of a Timishenko beam composed of functionally graded materials (FGM), restrained using clamped-simply supported (fixed-pinned) boundary conditions [51]. This was accomplished by first finding the buckling loads in accordance with conventional Euler-Bernoulli beam theory, and then offsetting the result with the aid of two new constants that are were determined as a function of the through-thickness distribution of elastic moduli in the functionally graded material. Although closed form solutions exist for the direct calculation of the critical buckling load of Timishenko beams (accounting for transverse shear compliance) under most of the possible boundary conditions [30][31][26][27], it was suggested in this manuscript that the case of clamped-simply supported (fixed-pinned) conditions cannot be modelled using these existing methods. As such, while Li and Batra did not provide a direct closed form solution to this problem, they did provide a closed form relationship between the Euler-Bernoulli solution (neglecting the effects of transverse shear compliance) and the Timishenko solution (accounting for the effects of transverse shear compliance) under the relevant clamped-simply supported (fixed-pinned) boundary conditions.

1.5 Research Objectives

The goal of this dissertation is to address some of the shortcomings in the current state-of-the-art of composite structures. The author has contributed to two main aspects of composite structural engineering: manufacturing and analytical modelling.

The connection of composite structural members to adjacent components often results in complex and counter-intuitive states of stress that can be difficult to model, and generally constitutes a weak point in the overall structural system. The common remedy for this shortcoming in the aerospace industry is simply to over-design structural components in the vicinity of these mechanical connections, which often results in excessively conservative structures. Furthermore, since FRP materials are, in a sense, synthesized during the fabrication of the final part, the mechanical properties that can be expected from FRP structures are largely dependent upon highly skilled workmanship, and can be inconsistent during a production run. This variability of mechanical properties necessitates further conservatism in structural designs. Pultrusion is a production technique that is intended for mass-production of long FRP parts having continuous cross-sectional geometry. Although it has not yet been optimized for the aerospace industry, with some qualification research, pultrusion may prove to offer many benefits over conventional methods of manufacturing composite aircraft parts. In addition, it is possible to co-pultrude FRP parts with embedded non-FRP materials (such as metallic materials), which could serve as integral hard points to facilitate serviceable mechanical connections to adjacent parts. Chapter 2 introduces a novel hybrid co-pultrusion manufacturing process that might enable the implementation of serviceable mechanical fasteners in composite structural members, while simultaneously facilitating economical mass-production, and improved repeatability of mechanical properties. Aircraft wing stringers are proposed as one potential application of this technology. Some novel automotive and rail-road applications are contemplated as well. A prototype hybrid co-pultrusion manufacturing run was carried out, and the feasibility of the proposed manufacturing process was assessed (see Section 2.5). While the proposed hybrid co-pultrusion technology could potentially benefit many applications involving long slender structural members of constant cross-sectional geometry, much of this dissertation focuses on the context of aircraft wing stringers.

The author has identified some shortcomings in the current state-of-the-art of analytical models intended to predict the mechanical response of FRP structures, and has developed new analytical methods to address these shortcomings. In particular, analytical methods have been developed to predict: the bending stiffness of built-up open sections having laminated walls of moderate thickness, the unrestrained torsional stiffness of thick FRP laminates, the restrained torsional response (torsion and warping) of thin-walled open sections having non-trivial in-plane shear compliance, and the buckling response of initially curved beams having non-trivial transverse shear compliance. The aforementioned analytical models have been combined with a wealth of existing analytical methods found in the literature, and amalgamated into a comprehensive computer program (written in MathWorks® MATLAB®) intended for the structural analysis of beams having open sections comprising laminated FRP composite walls. The initial purpose of this computer program was, in fact, to predict the elastic buckling behaviour of hybrid composite co-pultruded aircraft wing stringers; however, the analysis of this problem is dependent upon a plethora of simpler discrete structural phenomena, which may each be treated individually, or in conjunction with any of the other discussed phenomena. As such, by building a computer program intended for the structural analysis of beams subjected to elastic column buckling, the author has ultimately arrived upon a comprehensive analysis tool that is capable of providing a full suite of section properties that can be used to assess the performance of a beam under a large variety of structural loadings. The engineering science upon which this analysis computer program was based is derived and explained in Chapter 3. This computer program was computationally validated for coupled flexural-torsional-shear buckling analyses using the finite element method (see Section 3.18). In addition, an experimental program was carried out in order to validate the aforementioned analytical model intended to predict the restrained torsional response (torsion and warping) of thin-walled open sections having non-trivial in-plane shear compliance (see Chapter 4).

Chapter 2

Proposed Hybrid Composite Co-Pultrusion Technology

2.1 General

Pultrusion is a manufacturing technique that enables the mass production of long polymer-matrix fibre-composite structural elements having constant cross-sectional geometry. It is possible, however, to produce co-pultrusions containing longitudinally oriented embedded elements composed of materials that are dissimilar to the bulk composite constituents of the pultrusion. These embedded elements would pass through the pultrusion die along with the fibre reinforced polymer (FRP) constituents during the pultrusion run. The embedded elements would be oriented parallel to the longitudinal axes, and would therefore resist longitudinal and flexural stresses. Conversely, the FRP webs between these longitudinally oriented embedded elements would serve to resist in-plane shear stresses; hence, it would likely be desirable to design the FRP laminate such that it is composed primarily of angle-ply laminae, such as those having ±45° fibre orientations. The inclusion of embedded elements composed of metallic materials might be beneficial for the following reasons:

1. The composite modulus of elasticity (both specific and absolute) would be increased along the axis of the metal elements (assuming that a metal of higher elastic modulus than the surrounding FRP is selected for these elements), which would help to address the issue of the relatively low elastic modulus that is typically exhibited by some FRP laminates such as glass FRP (GFRP) or aramid FRP (AFRP).
2. The embedded metal elements would serve as hard points that are integral to the structure; these hard points may be used to accept mechanical fasteners to facilitate serviceable connections to other parts of the structure.

3. The energy management characteristics (crashworthiness) of this hybrid system would likely be improved due to the inherent ductility of most metals. FRP composite materials tend to exhibit brittle mechanical properties; however, the inclusion of embedded ductile metallic materials could help to absorb energy (in the form of plastic strain energy) during impact and crash events.

It is useful to illustrate these benefits with the aid of an example. One such example of the aforementioned structural concept could be a glass FRP (GFRP) pultruded box-section member having steel rods (round bars) co-pultruded at the corners of the member. The inclusion of the embedded steel rods would provide numerous advantages over conventional GFRP pultrusions:

1. The steel rods would improve the bulk mechanical properties of the member, while minimizing the incremental increase in bulk density due to the relatively small cross-sectional area of the included steel rods.
2. The exposed ends of the steel rods could be drilled and tapped in order to accept mechanical fasteners for connection to other components of the structure. Hence, the embedded steel elements would effectively be serving as hard points that are integral to the structure, and offer a direct load path through the hybrid structural member.
3. The member could be cross-drilled at intermediate locations along its length where the embedded steel elements are intersected, thus facilitating mechanical fasteners at locations that are distant from the ends of the member. Hence, the embedded steel elements would effectively be serving as hard points that are integral to the structure.
4. The inherent ductility of the embedded steel elements would help to improve the energy management characteristics of the member (such as in the context of automotive crash-worthiness).

Co-pultrusion does not have to be limited to GFRP and steel constituents. In fact, the aforementioned steel rods could be replaced with pre-fabricated mass-produced unidirectional carbon FRP (CFRP) pultruded rods that are passed through the pultrusion machine in the same way that steel rods could be. The inclusion of embedded CFRP rods in a predominantly GFRP pultrusion would help to improve the bulk mechanical properties of the member, while simultaneously reducing its bulk density (CFRP generally has a lower density than GFRP). Unfortunately, embedded CFRP rods would not provide the added benefit of serving as hard points for mechanical connections to other structural elements. Alternatively, the bulk pultruded FRP material could comprise carbon FRP or aramid FRP, rather than the aforementioned glass FRP material.

2.2 Hybrid Composite Co-Pultruded Aircraft Stringers

Hybrid co-pultrusion technology could potentially be beneficial in numerous parts of an aircraft airframe. One such application could be the replacement of the extruded aluminium stringers that are conventionally used to reinforce wing-skins. These aluminium stringers could conceivable be replaced by GFRP or CFRP T-section (blade section) pultrusions with two embedded co-pultruded elements: a previously pultruded CFRP rod could serve as a cord at the tip of the web (similar to that used in PRSEUS), and a thin aluminium strip could be embedded within the flange. The CFRP rod would serve to increase axial and bending stiffness. The aluminium strip would also increase axial and bending stiffness while simultaneously serving as a hard point to accept mechanical fasteners such as rivets, thus facilitating a serviceable mechanical connection to the wing skin. Since the flexural stresses would be resisted primarily by the CFRP rod, the aluminium strip, and the wing skin itself, the GFRP or CFRP web of the T-section would be primarily responsible for resisting shear flow between the flange and the CFRP cord. As such, it would be logical to employ a GFRP or CFRP laminate composed primarily of ±45° fibres. Figure 2.1 is a cross-sectional rendering of the proposed T-section hybrid composite co-pultruded aircraft wing-stringer.

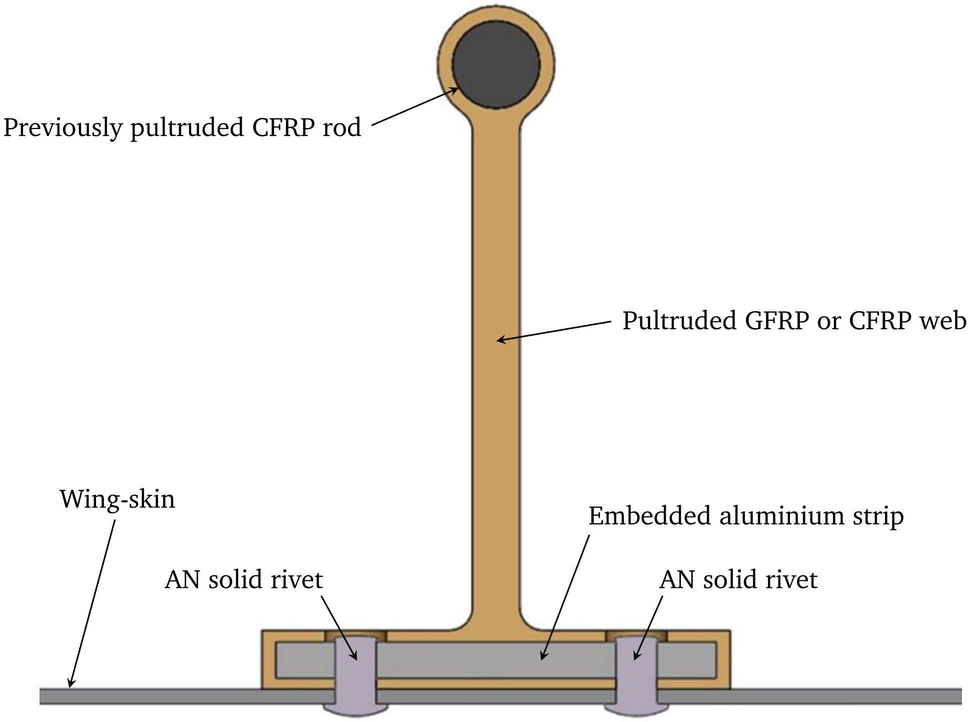

Figure 2.1: Cross-sectional rendering of T-section hybrid composite co-pultruded aircraft wing-stringer. Note that this figure shows the proposed wing-stringer riveted to a wing-skin, utilizing the embedded aluminium strip as an integral hard-point to accept the AN solid rivets.

The aforementioned T-stringer would likely be an improvement over conventional extruded aluminium stringers for the following reasons:

1. Both specific strength and specific stiffness would likely be increased.
2. In the event that a GFRP laminate is employed, corrosion resistance would be substantially improved since the aluminium strip would be fully enveloped within GFRP. In the event that a CFRP laminate is employed, it might be necessary to envelop the aluminium within a thin veil of GFRP or polymeric fibres in order to electrically insulate the aluminium from the conductive carbon fibres present within the CFRP laminate (which might otherwise cause galvanic corrosion).
3. The embedded metal elements may also facilitate electrical bonding of the airframe while simultaneously contributing to structural performance. This may help to eliminate the need for heavy non-structural electrical bonding elements that are often necessary in composite airframes.
4. The embedded metal elements would serve as hard points that are integral to the structure; these hard points may be used to accept mechanical fasteners to facilitate serviceable connections to other parts of the aircraft, such as wing-skins.
5. These hybrid composite co-pultruded stringers would be fully compatible with conventional aluminium-skinned airframes due to their ability to accept conventional mechanical fasteners such as rivets and/or HI-LITE™ fasteners.
6. Although unit cost would likely increase due to manufacturing complexity and the inclusion of CFRP, manufacturability and quality control would likely remain relatively unchanged.
7. Most of the light-weighting benefits afforded by the current state-of-the-art CFRP aircraft structural systems would be retained, while simultaneously offering the manufacturability and serviceability that previously could only be afforded by conventional metallic (aluminium) aircraft structural systems constructed using mechanical fasteners. In fact, Section 3.18.5 uses an example to demonstrate that a hypothetical CFRP-aluminium hybrid co-pultruded stringer could potentially achieve a column buckling strength per unit weight that is approximately 80% greater than that attainable by a conventional aluminium stringer having identical exterior geometric dimensions.

Pultruded CFRP rods are already commercially mass produced with close tolerances and careful quality control; as such, the suggested use of embedded previously pultruded CFRP rod elements might help to improve upon the repeatability of the mechanical properties of longitudinally oriented CFRP material, where such material is necessary in the cross-section. Strictly speaking, the use of a previously pultruded CFRP rod is not absolutely necessary; longitudinally oriented carbon fibres can be pultruded along with the other FRP constituents during the co-pultrusion run. This would allow for the longitudinally oriented carbon fibres to adopt any cross-sectional geometry, rather than being restricted to the cross-sectional geometry of a previously pultruded CFRP rod.

The aforementioned hybrid composite co-pultruded aircraft wing-stringer does not necessarily have to adopt the T-section geometry that was illustrated in Figure 2.1. In fact, it is possible to produce hybrid composite co-pultruded stringers having any of the cross-sectional geometries that are commonly used in aircraft wing-stringer applications, such as: Z-sections, I-sections, J-sections, and C-channels.

2.3 Other Potential Applications of Hybrid Composite Co-Pultrusion Technology

2.3.1 General

While the primary focus of this dissertation is on aerospace structural applications, the aforementioned hybrid composite co-pultrusion technology may also prove to be beneficial to a broad range of structural applications outside of the aerospace industry. Ultimately, any structural system that comprises members of constant cross-sectional geometry is a potential candidate for the use of the proposed technology. The following sections propose two additional potential applications of the presently discussed hybrid co-pultrusion technology: automotive chassis structures, and railway car structures.

2.3.2 Hybrid Composite Co-Pultruded Automotive Chassis Structure

A monocoque automobile chassis structure can be created using the aforementioned hybrid co-pultrusion technology [35][36]. The primary structure of the entire vehicle can be built up using members cut from three unique pultrusions.

A large pultrusion representing the entire main central cabin section (tub) of the vehicle can be created using a glass fibre reinforced polymer (GFRP) laminate, with co-pultruded steel or stainless steel rods embedded longitudinally at key locations along the edges of the member. The ends of these steel rods would be drilled and tapped in order to accept mechanical fasteners, which would be used to connect bulkheads to either end of this central tub. This central tub would likely have a modified “W” shaped cross section, as shown in Figure 2.2. Since the embedded steel or stainless steel rods would be responsible for resisting most of the bending moments and axial loads imposed upon this central tub structure, the GFRP laminates in this central tub pultrusion would likely be optimized for in-plane shear strength and stiffness. As such, these laminates would likely be composed primarily of laminae incorporating continuous fibres oriented at +45° and −45° relative to the longitudinal axis of the pultrusion. However, it may be necessary to also include some longitudinally oriented continuous fibres in order to increase the bending stiffness of the central tub structure. Although the primary laminate would likely be reinforced by glass fibres, it might be beneficial to include a lamina of bi-directional woven aramid fabric over the interior surface of the central tub laminate; in the event of a collision, this aramid reinforced lamina could help to protect the occupants of the vehicle from intrusion of foreign objects, as well as prevent jagged shards or splinters of the primary reinforcing fibres (E-glass) of the laminate from protruding into the vehicle. The ends of this central tub must be cut in a “keyed” fashion in order to allow for mechanical interlock with the corrugated shape of the bulkheads that will be mounted to each end of the central tub.

Figure 2.2: Cross-sectional rendering of a steel-GFRP hybrid pultruded section to serve as the central tub section of the vehicle. Note the small embedded steel round bars at various key locations in the cross-sectional geometry.

A corrugated pultrusion representing the bulkheads at each end of the central tub can be created using a glass fibre reinforced polymer (GFRP) laminate, with co-pultruded steel or stainless steel flat bars embedded along the upper and lower flanges (peaks and valleys) of each corrugation, as shown in Figure 2.3. These steel flat bars would be cross-drilled such that the corrugated bulkheads can be fastened to the drilled and tapped exposed ends of the embedded steel rods in the central tub of the vehicle. These steel or stainless steel flat bars would be responsible for resisting most of the bending moments imposed upon these bulkhead structures. Conversely, the GFRP laminates in the bulkhead pultrusions would likely be optimized for in-plane shear strength and stiffness. As such, these laminates would likely be composed primarily of laminae incorporating continuous fibres oriented at +45° and −45° relative to the longitudinal axis of the pultrusion. As with the aforementioned central tub section, it might be beneficial to include a lamina of bi-directional woven aramid fabric over the surface each bulkhead that will face the interior of the vehicle; in the event of a collision, this aramid reinforced lamina could help to protect the occupants of the vehicle from intrusion of foreign objects, as well as prevent jagged shards or splinters of the primary reinforcing fibres (E-glass) of the laminate from protruding into the vehicle. It may also be beneficial to include fire-retardant filling agents in the thermoset polyurethane resin matrix of these bulkhead pultrusions.

Figure 2.3: Cross-sectional rendering of a steel-GFRP hybrid pultruded section to serve as the front and read bulkheads of the vehicle. Note the embedded steel flat bars located at each of the peaks and valleys of the corrugated cross-sectional geometry.

A trapezoidal pultrusion representing the fore and aft frame rails can be created using a glass fibre reinforced polymer (GFRP) laminate, with co-pultruded steel rods embedded longitudinally along the four edges of the member, as shown in Figure 2.4. The ends of these steel rods would be drilled and tapped in order to accept mechanical fasteners, which would be used to connect these frame rails to the bulkheads that are connected to either end of the central tub. Once again, since the embedded steel or stainless steel rods would be responsible for resisting most of the bending moments and axial loads imposed upon these frame rail structures, the GFRP laminates in these frame rail pultrusions would likely be optimized for in-plane shear strength and stiffness. As such, these laminates would likely be composed primarily of laminae incorporating continuous fibres oriented at $+45°$ and $-45°$ relative to the longitudinal axis of the pultrusion. It may be beneficial to include fire-retardant filling agents in the thermoset polyurethane resin matrix of these frame rail pultrusions. These members should be designed such that the inherent ductility of the embedded steel rods can be utilized for energy dissipation in the event of a crash. The ends of these frame rail members must be cut in a “keyed” fashion in order to allow for mechanical interlock with the corrugated shape of the bulkheads to which these frame rails will be fastened.

Figure 2.4: Cross-sectional rendering of a steel-GFRP hybrid pultruded section to serve as the front and read frame rails of the vehicle. Note the small embedded steel round bars located at each of the four corners of the cross-sectional geometry.

The assembled vehicle structure, composed of the central tub, bulkheads, and frame rails, is shown in Figure 2.5.

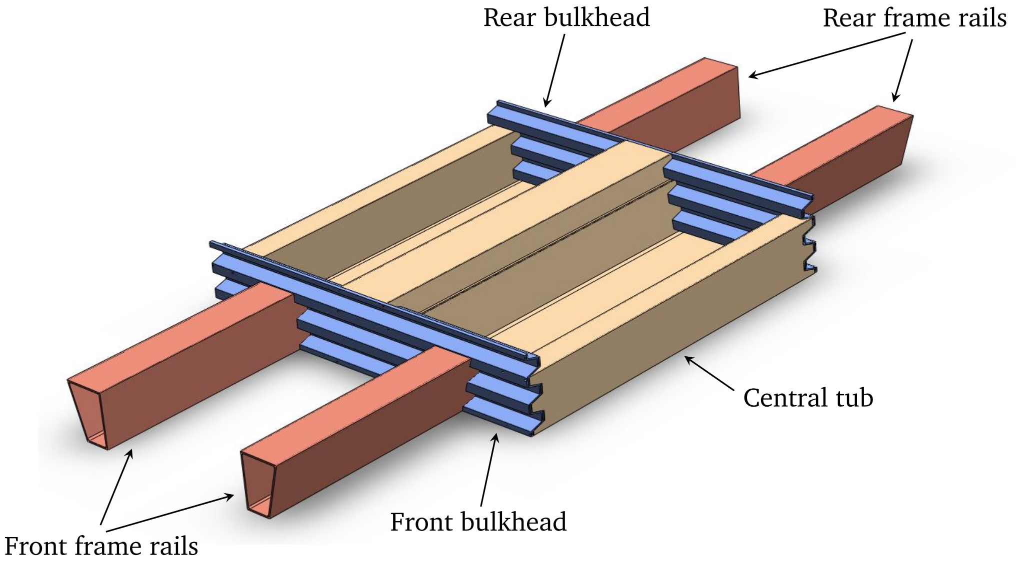

Figure 2.5: Automobile structural system composed of steel-GFRP hybrid pultruded members. This structural system comprises the aforementioned central tub (see Figure 2.2), bulkhead (see Figure 2.3), and frame rail (see Figure 2.4) pultrusions.

The aforementioned vehicle structure could offer many of the benefits of a typical composite monocoque automobile structure; however, it would likely be faster, easier, and less costly to produce due to its utilization of pultrusion technology. Some of the expected advantages of utilizing this type of a structural system for an automotive chassis include:

1. Reduced total weight of the structural system would lead to improved fuel economy, particularly in an urban driving environment.

2. Improved fatigue resistance in comparison with aluminium space-frame type automotive structures.
3. Improved corrosion resistance in comparison with conventional automobiles that employ predominantly steel and/or aluminium structures.
4. Magnetic transparency of glass FRP laminates would simplify inspections that might be necessary at border crossings, or demanded by law-enforcement officers.
5. The implementation of mechanical fasteners would dramatically improve upon the serviceability of the automobile structure. This contrasts conventional welded or spot-welded automotive body structures, which are often built as single-piece structures (unibodies) that sometimes have regions of poor accessibility. Furthermore, the use of serviceable mechanical connections means that individual damaged components can be replaced with ease.

2.3.3 Hybrid Composite Co-Pultruded Railway Car Structure

Railway cars are often represented by long rectangular prismatic shapes that exhibit constant cross-sectional geometries along their lengths. As such, while it would likely be difficult and impractical to create a single pultrusion die large enough to produce a one-piece pultruded railway car, it might be feasible that such a railway car could be fabricated from a series of mechanically fastened hybrid composite co-pultruded parts. The exact architecture employed by this assembly would be dependent upon the maximum permissible size of each individual co-pultruded part; however, the overall design philosophy would ultimately be quite similar to that which was adopted in the aforementioned automotive chassis structural system that was discussed in Section 2.3.2. In essence, a series of bespoke hybrid composite co-pultruded structural members (stringers, panels, frames, and other components) could be fabricated and connected to each other using mechanical fasteners, and utilizing the embedded co-pultruded metallic elements as hard points to accept these mechanical fasteners.

Some of the expected advantages of utilizing this type of a structural system for railway cars include:

1. Reduced total weight of the structural system means that more of the maximum allowable gross weight of the railway car can be utilized for payload.
2. Improved corrosion resistance in comparison with conventional metallic railway cars.
3. Magnetic transparency of glass FRP laminates would simplify inspections of railway cars, which might be necessary at border crossings.

4. The implementation of mechanical fasteners would dramatically improve upon the serviceability of the railway car structure. In addition, the use of serviceable mechanical connections means that individual damaged components can be replaced with ease.

2.4 Potential Limitations of the Proposed Hybrid Composite Co-Pultrusion Technology

While the proposed hybrid composite co-pultrusion technology would likely offer a plethora of promising attributes, it is not without shortcomings. The following is a list of limitations that could attenuate the range of applications that could potentially be realized by the present technology:

1. Pultrusion and/or co-pultrusion are only applicable to structural members having a constant cross-sectional geometry over their length. This limitation stems from the nature of a pultrusion die as a rigid and unmoving entity. While some researchers have proposed and experimented with post-pultrusion forming techniques that allow for the creation of members having variable cross-sectional geometries [72][73], these techniques have not yet achieved broad industry acceptance, and are unlikely to be applicable to the presently discussed hybrid co-pultrusion technology.

2. The embedded co-pultruded metallic elements must be continuous, and must be oriented parallel to the longitudinal axis of the member, which is parallel to the axis along which the pultrusion run propagates.

3. The proposed technology is limited to the use of polymeric resin systems that have been specifically engineered for pultrusion applications. In general, pultrusion requires the use of resin systems that exhibit a specific set of characteristics (see Section 1.2.4), such as: good mould releasing properties, fast cure rate, low cure temperature, and moderate cure shrinkage. While many pultrusion resin systems have been developed over the past half century, there remain a relatively limited number of high-performance pultrusion resin systems that exhibit physical and mechanical properties that would be appropriate for aerospace applications. Ultimately, even the highest performance pultrusion resin systems (such as some thermoset polyurethane resin systems) would have to undergo expensive and time-consuming aerospace certification processes before they could legally be used in the airframes of certified aircraft. Unfortunately, this certification process could deter aircraft manufacturers from adopting pultrusion technology.

4. The inclusion of a numerous materials having dissimilar coefficients of thermal expansion (CTE) could lead to the development of thermal stresses and strains due to the thermal loads

imposed upon these materials within the pultrusion die during manufacturing. In fact, depending upon the severity of the mismatch of the various CTE values of the constituents present within the co-pultrusion, it is possible that in-service thermal loadings could also be of sufficient magnitude to induce non-trivial thermal stresses and strains within the hybrid member. As such, it is important that the constituents of the hybrid member are carefully selected to have CTE values that are sufficiently similar such that the in-service thermal loadings that are expected for the completed hybrid member will not result in excessively dissimilar magnitudes of thermal strain for the various constituents of the hybrid member.

5. The complete envelopment of the embedded co-pultruded metallic elements could create difficulties if ever there were a need to inspect these embedded metallic elements for unknown and/or dormant failures. However, the likelihood and consequences of such unknown and/or dormant failures existing within the embedded metallic elements are no more severe than unknown and/or dormant failures that might exist within more conventional laminated FRP components. Much the same way that laminated carbon FRP components must be periodically ultrasonically scanned for interlaminar disbonding, the proposed hybrid composite co-pultruded members would necessitate similar proactive inspections. However, since the intent of the proposed technology is to employ mechanical fasteners, it is possible that these fasteners might help to prevent the propagation of interlaminar disbonding. Unfortunately, it is also possible that other forms of unknown and/or dormant failures (such as fatigue crack growth near mechanical fasteners) could develop within the embedded metallic parts, which would constitute new and unfamiliar types of failures.

2.5 Prototype Hybrid Co-Pultruded Stringers

2.5.1 General

While the author was able to hypothesize some of the challenges that might emerge during the manufacturing of the proposed hybrid composite co-pultruded structural members, it was decided that the best approach to ascertaining which aspects of this manufacturing process would ultimately govern its development would be to carry out an actual prototype manufacturing run. As such, an experimental prototype co-pultrusion run was carried out, and the feasibility of the proposed hybrid composite co-pultrusion manufacturing process was assessed.

It should be noted the this prototype co-pultrusion run was intended to provide a qualitative assessment of the feasibility of the proposed hybrid co-pultrusion technology. As such, although some quantitative data are provided in this section, these data have little relevance to the discussions and conclusions that are subsequently drawn.

It should also be noted that, although effort was made carry out this prototype co-pultrusion in a manner that is representative of hypothetical applications in the aerospace industry, some allowances were made in order to reduce the financial cost of this investigation. In particular, glass fibres were used in place of carbon fibres despite the fact that carbon fibres are more likely to be used in actual aircraft wing-stringer applications of the proposed technology. In addition, the selected cross-sectional geometry is not one that would likely be used in the context of an aircraft wing-stringer; however, it provided sufficient information to aid in forming a qualitative assessment of the proposed technology.

2.5.2 Design of Prototype Hybrid Co-Pultruded Stringers

The first task involved in designing a pultruded or co-pultruded member is to design the external cross-sectional geometry of the member, which in turn dictates the design of the pultrusion die. Pultrusion dies typically measure approximately 1 m in length, and are otherwise dimensioned to accomodate the cross-sectional dimensions of the part that is to be pultruded. Pultrusion dies are usually precision machined from large billets of steel, and are subsequently hardened and/or hard plated. With the exception of the pultrusion machine itself, the pultrusion die typically constitutes the greatest initial financial expense governing the pultrusion of a part. As such, in the interest of limiting the financial costs of the present prototype pultrusion run, the author elected to utilize an existing pultrusion die that required only minor modifications.

C-channel ladder-frame members are among the most commonly pultruded geometries in the entire pultrusion industry; therefore, C-channel pultrusion dies are generally quite plentiful and readily available. The author located a C-channel pultrusion die owned by the Martin Pultrusion Group of Cleveland, Ohio, USA, and designed a series of slight dimensional modifications that were carried out by a local machine shop. The final designed C-channel cross-sectional geometry of the prototype hybrid co-pultruded member is illustrated in Figure 2.9. While C-channels are not the most commonly used cross-sectional geometries for aircraft wing-stringers, it was decided that such a geometry would serve to facilitate prototyping the proposed hybrid co-pultrusion technology. The singly-symmetric nature of C-channel cross-sections renders them fully susceptible to geometric deformations caused by thermal loadings. Figure 2.6 is a photograph of the C-channel pultrusion die that was used for the present prototype hybrid co-pultrusion run. It should be noted that the upper and lower halves of the pultrusion die are slightly mis-aligned in this photograph; this helps to more clearly illustrate the location of the parting line.

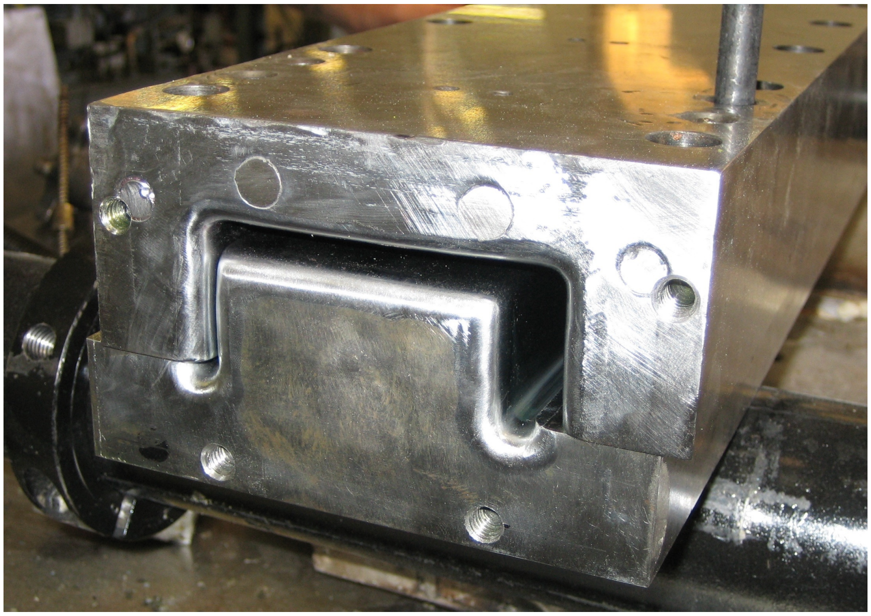

Figure 2.6: C-channel pultrusion die used for prototype hybrid co-pultrusion run. Note that the upper and lower halves of the pultrusion die are slightly mis-aligned in this photograph; this helps to more clearly illustrate the location of the parting line.

While thermoset unsaturated polyesters and thermoset vinyl esters are the resin families that are most commonly used in pultrusion processing, neither of these types of resin systems typically offer strong adhesive bonding performance. As discussed in Section 1.2.4, thermoset polyurethane pultrusion resins have been shown to offer superior bond strength and mechanical toughness when compared with the aforementioned more conventional pultrusion resin systems. Therefore, in order to maximize the potential bond strength between the resin matrix and the embedded metallic elements, the BAYDUR® PUL 2500 thermoset polyurethane pultrusion resin system, manufactured by Bayer MaterialScience LLC, was selected as the resin matrix that was employed for the present prototype co-pultrusion run. While most pultrusion resin systems utilize the conventional open-bath technique to impregnate the fibrous material with resin, thermoset polyurethane resins require a close injection box system, which is typically mounted directly to the entrance end of the pultrusion die. The use of this injection box system is necessary to accommodate the fast gel time of thermoset polyurethane resin systems. For the present prototype co-pultrusion run, the Martin Pultrusion Group, of Cleveland, Ohio, USA, was commissioned to fabricate a bespoke resin injection box in accordance with their proprietary design methodologies.

In order to investigate the effects of including embedded metallic elements within select regions of the co-pultrusion, it was decided that 6061-T6 aluminium strips would be co-pultruded within the upstanding flanges of the C-channel section, whereas the central web (between these upstanding flanges) would not include any embedded metallic elements. Furthermore, in order to test the sensitivity of the pultrusion run to the thickness of the embedded aluminium, it was decided that two different co-pultrusion runs would be carried out utilizing aluminium strips of two different nominal thicknesses. The first co-pultrusion run incorporated aluminium strips measuring 1.600 mm in nominal thickness (as-built measured thickness of 1.613 ± 0.025 mm), and the second co-pultrusion run incorporated aluminium strips measuring 2.540 mm in nominal thickness (as-built measured thickness of 2.593 ± 0.038 mm). Both types of aluminium strips were designed to have nominal widths of 25.400 mm (as-built measured width of 24.917 ± 0.274 mm). All aluminium strips were prepared and supplied by Bombardier Aerospace of Bombardier Inc., in Toronto, Ontario, Canada. Figure 2.9 is a schematic illustration showing the designed widths and positions of these embedded co-pultruded aluminium strips within the cross-sectional geometry of the co-pultruded member.

It was decided that the aluminium strips should receive some sort of a surface treatment in order to improve upon the strength of the adhesive bond that could be realized between the thermoset polyurethane resin matrix and the embedded aluminium strips. Ideally, it would have been desirable to simply employ an unsealed anodizing treatment immediately prior to carrying out the co-pultrusion run. Unsealed anodized aluminium would exhibit a highly porous surface that would likely enhance adhesive bonding due to infiltration of the thermoset polyurethane resin matrix into the pore spaces of the anodized surface. Unfortunately, this technique was not practical for the present prototype co-pultrusion run since the aluminium strips were to be prepared in Toronto, Ontario, Canada, whereas the co-pultrusion process was to be carried out in Cleveland, Ohio, USA. As such, an unsealed anodized surface might have become contaminated with oils and other foreign matter while the aluminium strips were in transit between these locations. Therefore, it was decided that an epoxy primer would be applied to the unsealed anodized surfaces in order to prevent contamination, and simultaneously provide a smooth, clean, and consistent epoxy surface to which the thermoset polyurethane pultrusion resin could bond. This surface treatment (both anodizing and epoxy priming) was carried out by Bombardier Aerospace of Bombardier Inc., in Toronto, Ontario, Canada. The anodizing and epoxy priming procedures that were used are proprietary trade secrets of Bombardier Inc.; however, the author can report that both of these processes are standard surface treatments that are commonly used to prepare structural components of aircraft airframes. It should be noted that the aforementioned as-built dimensions of the aluminium strips were measured after these surface treatments had already been applied; as such, these as-built dimensions have limited value in the context of structural performance. Figure 2.7 is a photograph of one of the aluminium strips after having been treated with the aforementioned anodizing and epoxy priming processes.

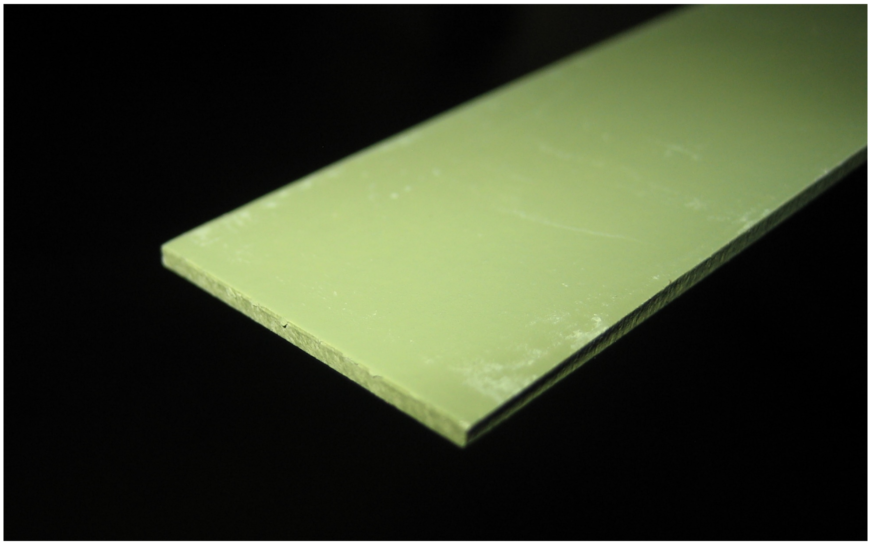

Figure 2.7: Anodized and epoxy primed aluminium strip to be embedded within upstanding flanges of co-pultruded C-channel stringer.

In conventional pultrusions, the majority of the fibrous material comprises longitudinally oriented unidirectional fibre rovings. These longitudinal rovings are necessary to resist the pulling forces imposed upon a pultruded part during processing. HYBON® 2025 13013-70182 113 yield E-glass fibre rovings, manufactured by PPG Industries Ohio, Inc., were selected to serve as the longitudinally oriented rovings within the presently discussed prototype co-pultrusion run. This type of roving has a tex of 4400 g/km. Recognizing that E-glass fibres have a density of 0.002606 g/mm^3, it can be shown that each of these 113 yield rovings has a fibre volume of 1.6884 mm^3 for every 1 mm length of the roving. It was noted that approximately 200 of these 113 yield rovings were included in each pultrusion run; however, the exact number of these rovings that were included in each pultrusion run is not known because this number was adjusted during the early phase of each pultrusion run in order to achieve acceptable pulling force values. Figure 2.9 is a schematic illustration showing the approximate designed positioning of these 113 yield rovings within the cross-sectional geometry of the co-pultruded member.

For processing purposes, some regions of the cross-section also necessitated the inclusion of bulky (blown) rovings, which are rovings that have a somewhat frayed texture; HYBON® 118 yield E-glass fibre bulky rovings, manufactured by PPG Industries Ohio, Inc., were used for this purpose. This type of roving has a tex of 4214 g/km, which is lower than that of the aforementioned 113 yield rovings; however, the 118 yield rovings are volumetrically broader (including resin) due to their bulky (blown) format. Recognizing that E-glass fibres have a density of 0.002606 g/mm^3, it can be shown that each of these 118 yield rovings has a fibre volume of 1.6170 mm^3 for every 1 mm length of the roving. A total of four 118 yield rovings were employed in the prototype pultrusion run; two of these rovings were positioned at the tip of each upstanding flange of the cross-section. Figure 2.9 is a schematic illustration showing the approximate designed positioning of these 118 yield rovings within the cross-sectional geometry of the co-pultruded member.

It is often desirable to also employ fibres that are oriented transversely, or at angles relative the the longitudinal axis of a pultrusion; this can help to increase the transverse strength and stiffness, and the shear strength and stiffness of the resulting structural member. In the pultrusion industry, this is most often achieved by including laminae of continuous filament mats (CFM) of randomly oriented fibres; however, CFM laminae are not appropriate for applications where high specific strength and stiffness are desired (such as in aerospace applications) due to poor fibre alignment and low attainable fibre volume fractions. As such, in order to simulate the intended aerospace application of the proposed technology, the author elected to envelope all of the aforementioned constituents of the pultrusion between two layers of VectorPly® E-QX-3600 quasi-isotropic E-glass fibre stitched complexes. Each of these stitched complexes has a stacking sequence of $[0/45/90/-45]$ (see explanation of standard stacking sequence notation in [54]), and each dry ply (excluding resin) has a mass of 304 g for every 1 m^2 area of the stitched complex. Recognizing that E-glass fibres have a density of 0.002606 $\mathrm{g/mm}^3$, it can be shown that each ply of the stitched complex has a fibre volume of 0.117 mm^3 for every 1 mm^2 area of the stitched complex. Figure 2.9 is a schematic illustration showing the approximate designed positioning of these stitched complexes within the cross-sectional geometry of the co-pultruded member.

Figure 2.8 is a close-up photograph showing the VectorPly® E-QX-3600 E-glass fibre stitched complex (upper left region of the photograph) and the HYBON® 113 yield E-glass fibre rovings (lower right region of the photograph).

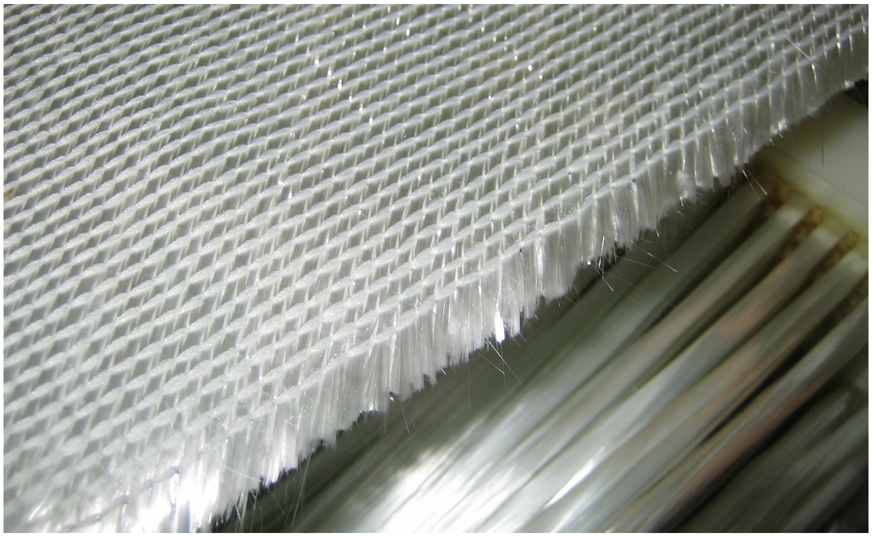

Figure 2.8: Close-up photograph showing E-glass fibre stitched complex and 113 yield E-glass fibre rovings. The VectorPly® E-QX-3600 E-glass fibre stitched complex is visible in the upper left region of this photograph. The HYBON® 113 yield E-glass fibre rovings are visible in the lower right region of this photograph.

Figure 2.9 is an illustration showing the designed cross-sectional geometry and composition of the prototype co-pultruded specimens. Although the outside geometry of the cross-section has been drawn to approximate scale, the various constituents of the co-pultrusion have only been drawn in a manner that is intended as a schematic representation of their approximate position within the cross-sectional geometry. As such, the number and size of each type of E-glass fibre roving, the exact position of each E-glass fibre roving, the thicknesses of the E-glass fibre stitched complexes, and the thickness of the aluminium strips are not accurately depicted in this illustration.

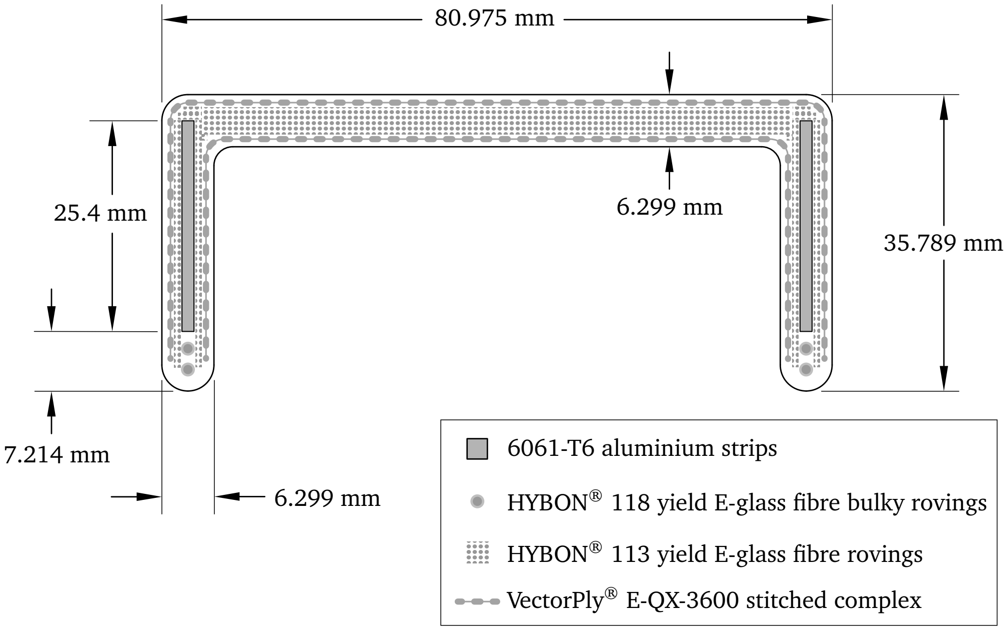

Figure 2.9: Designed cross-sectional geometry and composition of prototype hybrid co-pultrusion. Note that, while the outside geometry of the cross-section has been drawn to approximate scale, the various constituents of the co-pultrusion have only been drawn to schematically represent their approximate position within the cross-sectional geometry. As such, the number and size of each type of E-glass fibre roving is not accurately depicted in this rendering, and neither are the thicknesses of the E-glass fibre stitched complexes and aluminium strips.

2.5.3 Fabrication of Prototype Hybrid Co-Pultruded Stringers

The Martin Pultrusion Group, of Cleveland, Ohio, USA, was commissioned to perform the present prototype hybrid co-pultrusion run. Although the Martin Pultrusion Group did not have any prior experience with the type of hybrid co-pultruded members discussed in this dissertation, they do have experience working with customers on unusual prototype pultrusion operations. The author travelled to Cleveland, Ohio, USA to observe and photograph the present prototype co-pultrusion run, and to ensure that the prototype specimens were fabricated as desired.

As part of the set-up process that preceded the co-pultrusion, the Martin Pultrusion Group was also responsible for fabricating a pre-forming system. This pre-forming system comprised a series of perforated plastic panels (pre-forming gates); the fibrous material and aluminium strips passed through the holes in these pre-forming gates en-route to the injection box and pultrusion die. The purpose of this pre-forming system was to ensure that all of the constituents of the co-pultruded part arrived at the pultrusion die in the correct designed position within the cross-sectional area of the part, as well as to prevent any of the constituents from becoming tangled as they were drawn into the pultrusion die. Figure 2.10 is a photograph of this pre-forming system. In this photograph, the stitched complexes, 113 yield fibre rovings, and aluminium strips are all visible being drawn through the preforming system, into the injection box, and into pultrusion die. Note that the injection box and pultrusion die are somewhat visible near the right edge of this photograph, despite dim lighting.

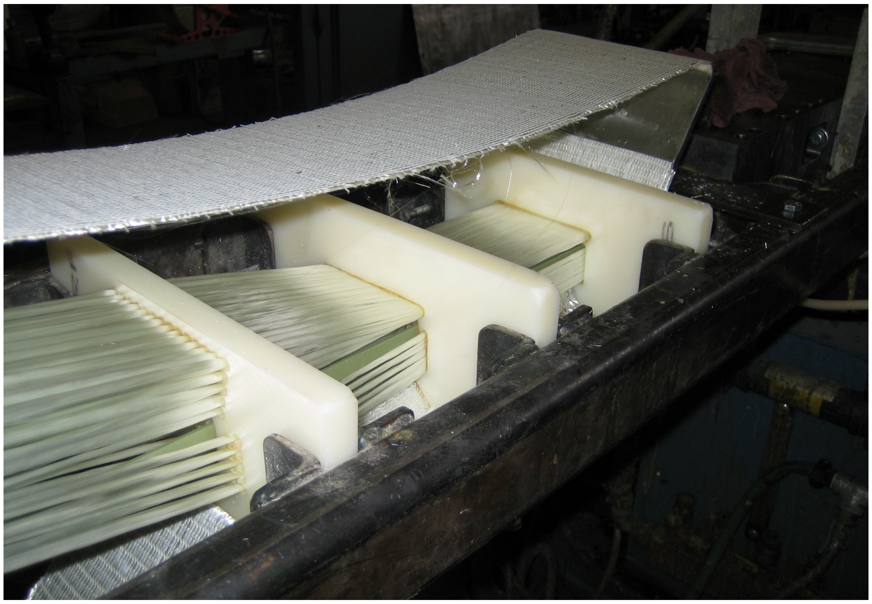

Figure 2.10: Photograph of pre-forming system used during prototype hybrid co-pultrusion run. The stitched complexes, 113 yield fibre rovings, and aluminium strips are all visible in this photograph. Note that the injection box and pultrusion die are located in the upper right region of this photograph; as such, the constituents of the co-pultrusion generally move from left to right in this photograph.

Figure 2.11 is a photograph that more broadly shows the constituents of the hybrid co-pultrusion being drawn through the pre-forming system, through the injection box, and into the pultrusion die. The 113 yield fibre rovings (central region of photograph), stitched complexes (above and below the 113 yield fibre rovings), 118 yield fibre rovings (bottom right region of the photograph), and aluminium strips (slightly below and within 113 yield fibre rovings) are all visible in this photograph. It is worth noting that the injection box and pultrusion die are visible near the right edge of this photograph; as such, the constituents of the co-pultrusion generally move from left to right in this photograph.

Figure 2.11: Photograph showing hybrid co-pultrusion constituents being drawn through the pre-forming system, through the injection box, and into the pultrusion die. The stitched complexes, 113 yield fibre rovings, 118 yield fibre rovings (bottom right region of the photograph), and aluminium strips are all visible in this photograph. Note that the injection box and pultrusion die are visible near the right edge of this photograph; as such, the constituents of the co-pultrusion generally move from left to right in this photograph.

As the constituents were drawn closer to the injection box, the pre-forming gates gradually moved them closer to the final configuration that was to be realized within the pultrusion die. Figures 2.12 and 2.13 are close-up photographs (top view and bottom view, respectively) showing the constituents of the hybrid co-pultrusion being drawn through the final stages of the pre-forming system, and subsequently into the injection box (visible near the right edge of these photographs). Also visible in these photographs is a small amount of thermoset polyurethane resin that was leaking out from the entrance of the injection box.

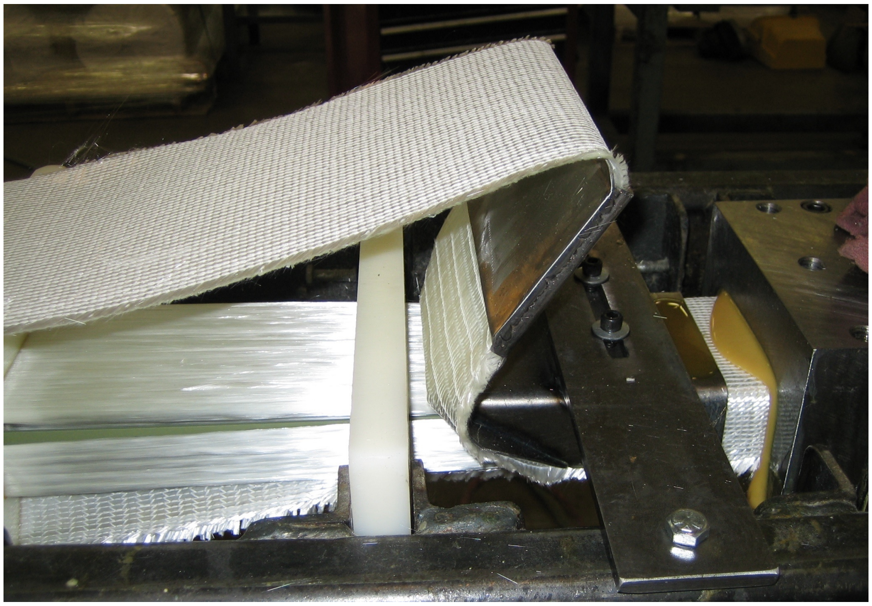

Figure 2.12: Close-up photograph showing top view of hybrid co-pultrusion constituents being drawn through the final stages of the pre-forming system, and subsequently into the injection box. Note the excess thermost polyurethane resin leaking from the injection box entrance, which is visible near the right edge of this photograph.

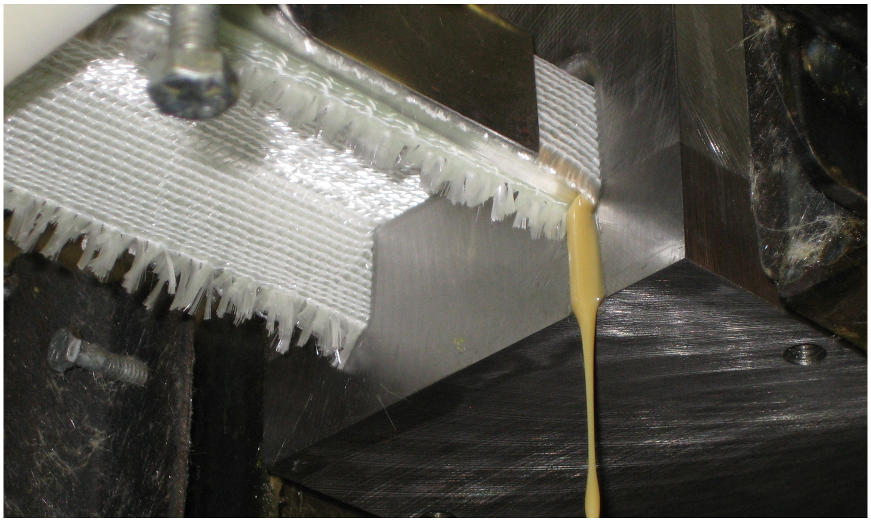

Figure 2.13: Close-up photograph showing bottom view of hybrid co-pultrusion constituents being drawn into the injection box. Note the excess thermost polyurethane resin leaking from the injection box entrance, which is visible in the lower right region of this photograph. The C-channel cross-sectional geometry is clearly evident in this photograph.

Figure 2.14 is a wide-angle photograph showing the entire hybrid co-pultrusion set-up while in progress. The creels of fibrous material are visible in the upper left region of this photograph, the pre-forming system is visible near the centre of this photograph, the injection box and pultrusion die are visible to the right of the pre-forming system, and the finished pultruded part can be seen emerging from the pultrusion die near the right edge of the photograph.

Figure 2.14: Photograph showing entire hybrid co-pultrusion set-up while in progress. Note the creels of fibrous material in the upper left region of this photograph, the pre-forming system near the centre of the photograph, the injection box and pultrusion die to the right of the pre-forming system, and the finished pultruded part emerging from the pultrusion die near the right edge of the photograph.

Finally, Figure 2.15 is a photograph showing a completed hybrid co-pultruded specimen emerging from the pultrusion die. The pultrusion die is visible on the left side of this photograph, and heater plates can be seen above and below this pultrusion die. Close inspection of Figures 2.11 and 2.14 reveals that there were three pairs of these heater plates mounted along the length of the pultrusion die, and an additional pair of smaller heater plates mounted to the injection box. This assembly of heater plates was responsible for maintaining the correct distribution of temperatures within the pultrusion die, which was necessary to ensure that the thermoset polyurethane resin was exposed to a full and proper cure schedule.

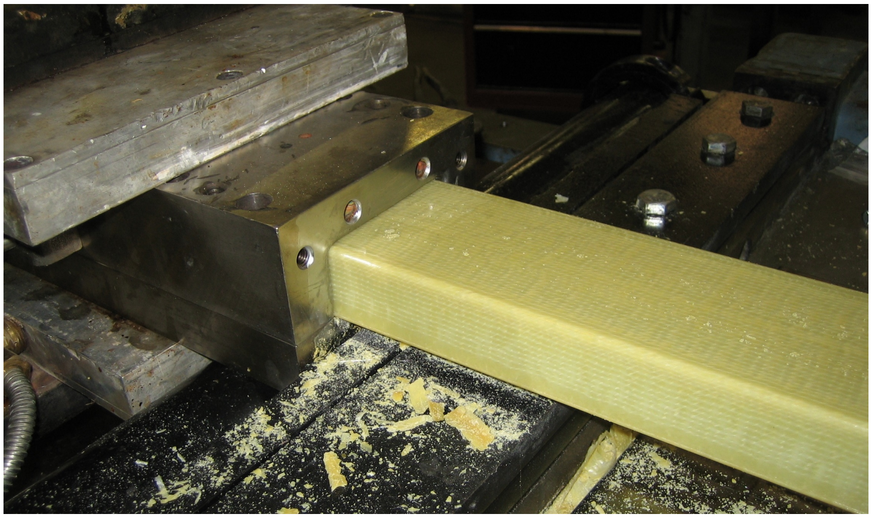

Figure 2.15: Photograph showing completed hybrid co-pultruded specimen emerging from the pultrusion die. Note the pultrusion die and heater plates visible on the left side of this photograph.

2.5.4 Observations During Fabrication and Subsequent Inspection of Prototype Hybrid Co-Pultruded Stringers

Overall, the prototype hybrid composite co-pultrusion run proceeded as expected, and the resulting specimens exhibited desirable physical and mechanical properties. Considering the experimental nature of this manufacturing run, the author is pleased with the amount of control and repeatability that was afforded by the proposed technique. It is clear that, once refined, the proposed technology could offer excellent economies of scale, which could enable the use of high performance FRP materials in a mass-production setting. Nevertheless, numerous observations were made that indicate a necessity for further refinement to the proposed technology.

Typical production pultrusion runs are carried out with precise control of processing parameters, such as: number of rovings (which ultimately dictates fibre volume fraction), die temperature, pull speed, and resin injection rate. By maintaining consistent values of each of these parameters, it is possible to ensure highly consistent mechanical properties of the material that is produced over the duration of a single pultrusion run. Unfortunately, the challenges presented by the experimental nature of the present prototype co-pultrusion run meant that it was necessary to continuously adjust many of these parameters throughout this prototype co-pultrusion run. In general, pull speeds were recorded to be approximately 40 cm per minute, and die temperatures were recorded to be approximately 210° C (lower temperatures near the exit of the die); however, these values varied throughout the prototype co-pultrusion run. Furthermore, the exact number of E-glass fibre rovings that were included in each prototype co-pultrusion is not known; as such, the exact fibre volume fraction of the

FRP constituents within each hybrid co-pultruded specimen is not known. In a production setting, the values of these parameters would be allowed to stabilize before any of the material produced was deemed usable. This is indicative of the nature of pultrusion as a mass-production manufacturing technique that is not well suited for small prototype manufacturing runs, such as the prototype hybrid co-pultrusion run discussed in this section.

Gas-filled blisters were observed to develop at the interfaces between the FRP material and the embedded aluminium strips that were co-pultruded along with the FRP material (see Figure 2.16). These blisters formed periodically along the length of the pultruded specimens. It was suggested that these blisters likely formed as a result of off-gassing of the epoxy primer coating that was applied to the aluminium strips prior to the pultrusion run. Although the manufacturer of the epoxy primer claims that it contains only a very small amount of volatile organic compounds (VOC), the author suspects that the high temperatures within the pultrusion die exacerbated the situation to the extent that even this small VOC content was enough to cause blistering of the prototype co-pultruded specimens.

As expected, the prototype hybrid co-pultruded members adopted a curved shape upon emerging from the pultrusion machine. This curvature was caused by the dissimilar coefficients of thermal expansion possessed by each of the constituents present within each of these co-pultruded specimens. Since the embedded aluminium elements had the highest coefficient of thermal expansion of all of the materials present within these specimens, the aluminium exhibited a relatively large amount of thermal expansion within the heated pultrusion die (before the polymeric resin matrix had cured); the aluminium subsequently exhibited a relatively large amount of thermal contraction after the specimen exited the pultrusion die (after the polymeric resin had cured), thus causing each co-pultruded specimen to curve toward the region of its cross-section that contained the greatest amount of aluminium. This explanation is consistent with the observed direction of curvature.

Figure 2.16 is a photograph looking along the length of one of the upstanding flanges of a hybrid co-pultruded C-channel specimen. Some of the aforementioned blister defects are clearly visible in this photograph, as is the global curvature of the member that was caused by the thermal loading that occurred within the pultrusion die.

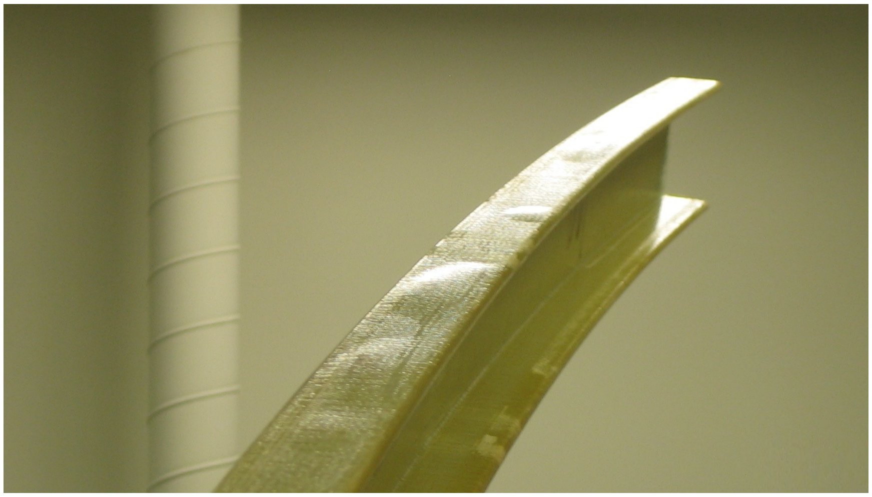

Figure 2.16: Photograph showing blister defects within upstanding flange of hybrid co-pultruded specimen, as well as a the global curvature of the specimen that was caused by the thermal loading within the pultrusion die.

The author attempted to cut the hybrid co-pultruded specimens using both a mechanical saw (band-saw) and a water-jet cutting machine. It was noted that both of these cutting operations sometimes caused disbonding of the embedded metallic elements from the surrounding FRP constituents; this disbonding can likely be attributed to the heat, vibration, water-pressure, and burring that are generated during these cutting operations. Unfortunately, this observed disbonding could cause difficulties if there is a need to employ flange growing (local increases of cross-sectional area to accommodate mechanical fasteners) or flange scalloping (regional reductions of cross-sectional area to reduce mass) operations, which are popularly used to optimize and reduce the weight of aircraft wing-stringers. It might be possible to include elongated upper flanges in Z-sections that are free from any embedded metallic elements; these upper flanges could potentially be milled shorter toward the tips of the wing, thus approximation the effect of a more global scalloping type operation. However, it might prove to be considerably more challenging to scallop material between the fasteners where the embedded metallic elements would be present.

The aluminium strips that were embedded within the aforementioned hybrid co-pultruded specimens were each only 3.05 m in length. Therefore, this experimental co-pultrusion run was not carried out as a continuous process; on the contrary, periodic human intervention was necessary to insert two 3.05 m long aluminium strips into the pultrusion die for every 3.05 m of hybrid co-pultruded material that emerged from the exit of the pultrusion die (approximately 7.6 minutes elapsed between the insertions of each pair of aluminium strips).

2.5.5 Suggested Remedial Actions & Improvements for Hybrid Co-Pultruded Stringers

In order to prevent blistering at the interface between the embedded aluminium and the FRP constituents, it is suggested that future prototype hybrid co-pultrusion runs should be carried out without the use of any polymeric primer coatings applied to the embedded metallic elements. If embedded aluminium elements are to be employed, it is suggested that these aluminium elements undergo an unsealed anodizing treatment immediately prior to the pultrusion run. The unsealed anodized aluminium would have a highly porous surface, which would likely enhance adhesive bonding due to infiltration of the polymeric resin matrix into the pore spaces of the anodized surface. In addition, the absence of a primer coating eliminates concerns regarding blistering caused by high temperature off-gassing of VOC materials present within the primer coating.

One method of preventing the development of curvatures due to thermal strains might be to utilize a curved pultrusion die. In order to achieve this, it would first be necessary to predict the curvature caused by thermal strains using either computational or analytical modelling. The pultrusion die can then be fabricated such that its cavity is curved in the opposite direction to that of the expected thermal deformation, but with the same magnitude of curvature. As such, upon exiting the pultrusion die, the pultruded specimens would initially adopt a curved shape, but would subsequently return to a nearly straight shape once the specimen has cooled to ambient temperatures. Although this technique might facilitate the creation of geometrically straight co-pultruded specimens, this technique would not alleviate the development of residual thermal stresses within the specimens. In fact, the magnitude and distribution of thermal stresses within the cross-section of a member fabricated using such a curved pultrusion die would be nearly identical to the magnitude and distribution of thermal stresses that would be present within a similar member fabricated using a conventional straight pultrusion die. As such, the part would still be susceptible to fatigue and durability concerns that can result from the presence of thermal stresses.

Another method of preventing the development of curvatures due to thermal strains might be to impose pre-stressing tensile forces upon various select constituents of the co-pultruded specimen as they are being pulled into the pultrusion die. These pre-stressing forces would be applied in the direction that is opposite to the progression of the pultrusion run, and would cause mechanical tensile strains to be generated within the loaded constituents as they enter the pultrusion die. If the coefficient of thermal expansion (CTE) of each constituent is known, then it might be possible to calibrate the magnitude of these pre-stressing tensile forces such that the sum of the mechanical and thermal strains within each constituent of the member reaches the same value as it passes through the pultrusion die. Greater pre-stressing forces would be imposed upon constituents having relatively low CTE values than those having higher CTE values. As such, once within the pultrusion die, the materials having high CTE values would exhibit greater thermal expansion, whereas the materials having low

CTE values would undergo greater mechanical strains due to the aforementioned pre-stressing forces applied to them. Using this technique, it might be possible to generate a state of iso-strain (or near iso-strain) at the position within the pultrusion die where the gel point is reached. If such a state of iso-strain could be achieved within the pultrusion die, then it is possible that the specimen would adopt a straight geometry once all mechanical and thermal loads have been removed. Unfortunately, application of the necessary pre-stressing forces might prove to be quite challenging in a practical setting. Furthermore, it can be difficult to ascertain at what location within the pultrusion die the polymeric resin matrix reaches its gel point. As such, although the temperature distribution within the pultrusion die can be measured fairly easily, it can be quite difficult to ascertain at what temperature the constituents of the pultruded specimen begin to solidify. Consequently, precise calibration of the aforementioned pre-stressing forces might prove to be quite challenging.

Another method of partially mitigating the development of curvatures due to thermal strains might be to utilize titanium rather than aluminium for the embedded co-pultruded metallic elements. Titanium has a considerably lower coefficient of thermal expansion than aluminium (less than half); as such, the use of titanium in place of aluminium would result in considerably reduced thermal effects generated within the heated pultrusion die during manufacturing, or during any in-service thermal loadings. Unfortunately, financial and availability constraints prohibited the author from experimenting with titanium during the present investigation; however, it would not be financially unreasonable for titanium to be utilized within aerospace applications of the present hybrid co-pultrusion technology.

One potential method of simulating scalloped material between the fasteners of a hybrid co-pultruded aircraft wing-stringer might be to consider only removing material from the embedded metallic strips (perhaps by creating elliptical cut-outs), and then filling the resulting voids in the metallic strips with a light-weight filler (such as a closed cell foam) prior to passing these metallic strips through the pultrusion die. As such, the net exterior cross-sectional geometry of the stringer would be constant, but the internal material composition would fluctuate along the length of the stringer such that far more embedded metal would be present in the vicinity of each mechanical fastener. Ultimately, the FRP composite material would be responsible for resisting most longitudinal loads; as such, it is logical that the FRP material should have a continuous cross-sectional geometry and composition over the length of the member. Conversely, the primary purpose of the embedded metallic strips would be to accept mechanical fasteners and gently transfer load into the surrounding FRP composite material, while minimizing stress concentrations; as such, it would be logical to reduce the cross-sectional area of these metallic strips between mechanical fasteners.

In order to ensure that hybrid co-pultrusion can be carried out as a continuous manufacturing process, it would be necessary to ensure that the embedded metallic constituents are continuously pulled into the pultrusion die without the need for human intervention. One method of achieving this might be to employ long coiled strips or wires of metallic materials to serve as embedded co-pultruded metallic elements; doing so would facilitate a continuous co-pultrusion process for the entire length of the coiled metallic material. Another method of achieving a continuous manufacturing process might be to employ an extrusion process that exists in series with a subsequent co-pultrusion process, such that extruded metallic elements could proceed directly from the an extrusion die into a pultrusion die as one continuous hybrid extrusion/co-pultrusion manufacturing process.

Chapter 3

Analytical Model

3.1 General

Many of the engineering structural analysis techniques that are currently popular in the automotive and aerospace industries are based largely upon the finite element (FE) method. While finite element analysis (FEA) is a proven methodology that is capable of providing extremely high fidelity simulations, it does so in a manner that leaves the engineer somewhat decoupled from the analytical procedure. As such, the results of a FE analysis can be likened to those of a thoroughly instrumented experimental test; a large amount of data is available from the output of a FE analysis, but ultimately these data are subject to interpretation by the engineer.

The general term “hand-calculation” will be defined here as any calculation that can reasonably be carried out by an industry engineer without the aid of any existing commercial computer software that was specifically formulated for the purpose of stress-analysis or structural-analysis. In the context of structural analyses involving conventional engineering materials, engineers are afforded a plethora of well established approximate analytical methods that can be used to validate experimental and/or FEA results using a quick “hand-calculation” type approach. Prudent engineers will recognize the dangers of depending exclusively upon commercial FEA computer software, and will validate all FEA simulations using a series of simple approximate “hand-calculation” type analyses. This is not to say that commercial FEA computer software has a tendency to generate false results; however, there are certainly dangers that arise from the extreme sensitivity of FEA to such parameters as mesh structure, material model, boundary conditions, and element formulation, each of which can present unique challenges to even the most experienced structural engineers. Unfortunately, the existing analytical methodologies for laminated composite materials are not generally conducive for use in such “hand-calculation” type analyses. The heterogeneity and anisotropy of laminated continuous-fibre reinforced polymer composites often result in extremely complex coupling phenomena which, in many cases, would render “hand-calculation” type analyses virtually impossible. As such, while much of the state-of-the-art literature in composite materials is focused on developing increasingly high fidelity analytical methods, the present author is of the belief that more efforts should be made to develop approximate analytical models that would facilitate “hand-calculation” type analyses of structures comprising laminated composite materials.

The following section describes an analytical model that is intended to predict the elastic behaviour of long and slender structural members (beams, stringers, and long columns) that have built-up open sections comprising composite laminates. The purpose of this analytical model is to facilitate approximate predictions of the structural response of the hybrid co-pultruded stringers discussed in Chapter 2. The goal is to do so in a manner that compartmentalizes the global behaviour of the stringers into discrete structural phenomena, in much the same way that conventional metallic structures are analyzed using classical techniques. This form of analysis provides important insight to the engineer, and facilitates an in-depth understanding of the cause for any short-coming of a given design. Ultimately, it will be shown that even the present analytical model is sufficiently complex to necessitate a computer program to carry out its computations with reasonable haste; as such, a computer program was written using MathWorks® MATLAB® to carry out each of the analytical procedures discussed in this chapter (see Section 3.17). However, this computer program was written in a manner that utilizes the aforementioned compartmentalized technique such that the user can retain a complete understanding of the analytical procedure, and can visualize each of the discrete mechanical phenomena involved in the analysis.

3.2 Philosophical Description of the Present Analytical Method

The present analytical model can, in many ways, be likened to the 1993 work of Barbero et al [5] on the mechanics of laminated beams (MLB), the 2009 work of Vo and Lee [86] on sixfold coupled buckling analyses of thin-walled beams, and many of the other works that were discussed in Section 1.4.2. In essence, the general approach that is adopted by the present analytical method is to quantify the local bulk stiffness properties of the laminates present at any given location within the cross-section of the member, and then integrate these stiffnesses over the entire cross-sectional area in order to arrive upon a series of global section properties that can subsequently be used for unidimensional beam analyses. What differentiates this present analytical model from those discussed in Section 1.4.2 largely stems from its philosophical goal.

Many of the works discussed in Section 1.4.2 strived to achieve fully-coupled, high fidelity, unidimensional beam models that can serve to either replace the finite element method, or function as new beam elements that can be implemented into FE solvers. Consequently, many of these analytical models employed computational procedures that would be completely unfamiliar to most structural engineers who are more accustomed the analysis of structures composed of conventional isotropic and homogeneous materials. The analytical procedures in these works are generally quite rigorous and complete; however, their derivations are often presented very concisely and directly, and in a manner that bi-passes any analogues that could potentially be drawn to classical analytical methods for conventional engineering materials. Ultimately, the rigorous pursuit of a fully coupled high fidelity model renders these analytical methods virtually unusable for the "hand-calculation" type analyses that were discussed in Section 3.1.

The purpose of the present analytical method is to serve as a means of approximating the behaviour of laminated composite members using methodologies that would be somewhat familiar to stress analysts that are well-versed in the analysis of conventional metallic structures. Since most laminated composite beams used in the aerospace and automotive industries comprise balanced symmetric and/or balanced anti-symmetric laminates, the present analytical method is formulated in manner that is only applicable to beams comprising these types of laminates. Although this limitation may detract somewhat from the versatility of the present analytical method, it eliminates the majority of the more peculiar coupling phenomena that are exhibited by laminated composites (see Section 1.2.9); this, in turn, enables the present analytical model to take a form that more closely resembles classical analytical methods for metallic structures.

Although many of the previously developed analytical models discussed in Section 1.4.2 strived to account for complex phenomena such as coupling effects and in-plane shear compliance, most of these works were formulated in a manner that is restricted to the analysis of members having thin-walled sections. In general, aircraft wing stringers are often sufficiently thick-walled that the use of the aforementioned analysis techniques discussed in Section 1.4.2 would likely lead to erroneous predictions of structural performance. In particular, the thin-wall assumptions employed by these analysis techniques would tend to result in misrepresented cross-sectional areas at the intersection of two or more legs of the cross-section, over-prediction of torsional stiffness, and under-prediction of warping stiffness. As such, the present analytical method has been formulated to incorporate some provisions to facilitate the analysis of open-sectioned members having legs of moderate thickness. While "moderate thickness" is a subjective term here, the intent of this statement is simply to indicate that some provisions have been made to account for the aforementioned concerns regarding leg thickness such that the present analytical model can be used for the analysis of aircraft wing stringers. However, the reader should note that the present analytical method remains largely based upon analytical techniques that are intended for thin-walled sections. As such, while some provisions have been made to improve upon the fidelity of analyses involving sections having walls of "moderate thickness", there are limitations to these provisions that must not be overlooked (see Section 3.19).

In the following discussions, particular attention has been given to aspects of the analytical procedure that are ill-supported in the literature. In particular, additional attention has been given to the torsional stiffness of thick laminated plates (see Section 3.11.4), the warping stiffness of thin-walled open sections having relatively low in-plane shear moduli (see Sections 3.12.3 and 3.13), and the buckling analysis of initially curved columns having relatively low in-plane shear moduli (see Section 3.14.3). In fact, the analytical procedure for torsional stiffness discussed in Section 3.11.4 is an entirely new analytical method that was developed by the present author to help address the distinct lack of support for this particular issue in the current state-of-the-art literature. As such, while the present analytical model for built-up open sections was primarily devised in a manner that was intended to be more simplistic than the works discussed in Section 1.4.2, the torsional analysis technique presented in Section 3.11.4 offers a level of analytical fidelity that is disproportionately high in comparison with most other aspects of the present analytical model. Consequently, while many aspects of the presently discussed analytical model are not conducive to the analysis of members incorporating unsymmetric laminates that are susceptible to complex coupling effects (see Sections 3.5 and 3.19), it will be shown that the torsional analysis technique presented in Section 3.11.4 is a fully coupled model that is capable of predicting the torsional stiffness of laminates having any composition and stacking sequence (including fully unbalanced and unsymmetric laminates). While this may seem inconsistent with the rest of the present analytical model, the author decided that it was necessary to contribute a fully developed high fidelity model for this particular aspect of the analysis (torsional stiffness of thick laminated plates) in order to bolster this ill-supported subject in the present state-of-the-art of engineering science. Furthermore, while it could be argued that the methodology presented in Section 3.11.4 is disproportionately complex in comparison with most other derivations discussed in the present work, it will be shown (see Section 3.11.5) that this torsion model can easily be integrated into any existing computer program or spreadsheet for Classical Laminated Plate Theory (CLPT); hence, for practical purposes, the method presented in Section 3.11.4 is ultimately no more cumbersome than any other analytical method that is dependent upon first carrying out a laminate analysis in accordance with CLPT.

3.3 Coordinate Systems

Three coordinate systems shall be defined for use in all subsequent discussions in this chapter. A 1-2-3 lamina coordinate system shall be defined at the mid-thickness of each lamina (ply) whereby the 1 axis is parallel to the fibre orientation, the 2 axis is in the plane of each lamina and oriented perpendicular to the fibres, and the 3 axis is oriented normal to the plane of the lamina. An x-y-z laminate coordinate system shall be defined at the mid-thickness of the complete laminate whereby the x axis is parallel to the longitudinal axis of the member, the y axis is in the plane of the laminate and oriented perpendicular to the longitudinal axis of the member, and the z axis is oriented normal to the plane of the laminate. The angles of the fibres within each ply are measured with respect to the x axis of the laminate coordinate system. An X-Y-Z global coordinate system shall be defined at the centroid of the cross-section of the member whereby the X axis is parallel to the longitudinal axis of the member, the Y axis is oriented vertically within the cross-sectional plane of the member and is measured positive above the centroid, and the Z axis is oriented horizontally within the cross-sectional plane of the member and is measured positive to the left of the centroid.

3.4 Assumed Geometry

For the purposes of the analytical model discussed in this dissertation, a general cross-sectional geometry was designed to enable the user to model a broad range of commonly used structural sections. This general geometry (shown in Figure 3.1) comprises 20 straight limbs (legs) that are arranged orthogonally, such that each of these legs is parallel to either the Y or Z axis of the global coordinate system. While each leg may be unique in its composition and laminate stacking sequence, it is assumed that material composition and laminate stacking sequence is constant over the length of each individual leg. The input-file for this analytical model permits the user to stipulate the length of each leg, as well as information pertaining to the material composition and laminate stacking sequence within each leg, such as: thickness of each ply, angle of the fibres within each ply θ, mechanical properties of the resin in each ply, mechanical properties of the fibres in each ply, and fibre volume fraction within each ply.

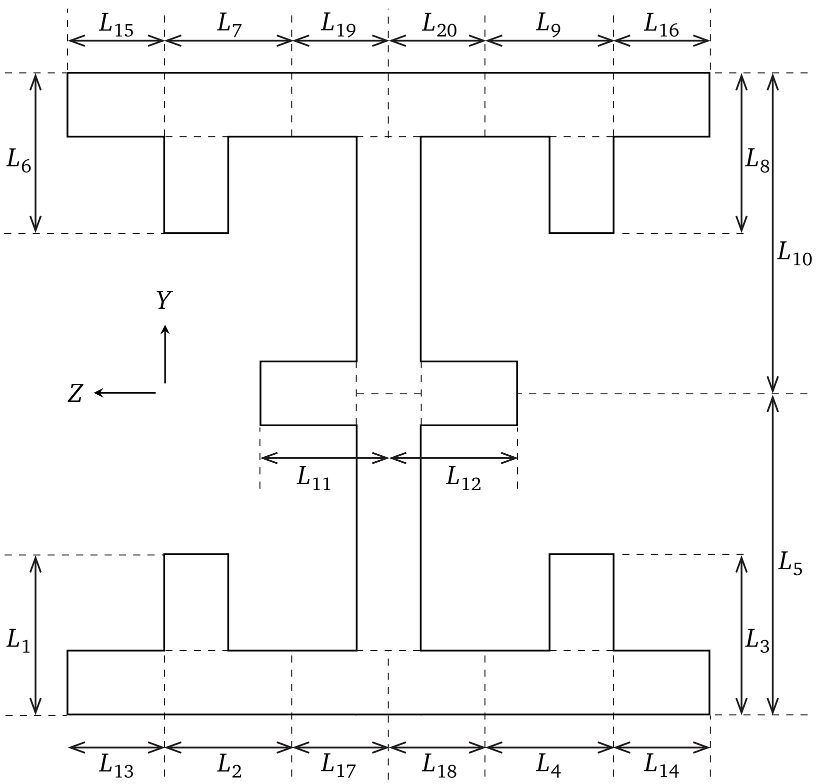

Figure 3.1: Assumed general cross-sectional geometry of stringer. The present analytical model can be used to analyze a stringer having any cross-sectional geometry that can be cut from this general cross-sectional geometry.

It is evident from Figure 3.1 that omission of one or more of the legs present in the general cross-sectional geometry (setting its length to zero) would enable the creation of many possible open sections, such as: I-sections, C-channels, Z-sections, T-sections (otherwise known as "blade" sections), L-sections (otherwise known as "angle" sections), simple flat-bar sections (or rectangular plates), and a multitude of other possible geometries. From this general cross-sectional geometry, one can create section geometries that are doubly-symmetric, singly-symmetric, or completely unsymmetric.

3.5 Mechanical Properties

As mentioned in Section 3.4, each leg of the cross-section may be given a unique set of materials and laminate data; therefore, each leg of the section can have a unique set of mechanical properties. These mechanical properties are calculated in accordance with the rule of mixtures, the Halpin-Tsai equations [29], and Classical Laminated Plate Theory (CLPT), as discussed in Sections 1.2.6, 1.2.7, and 1.2.8.

The analytical model discussed in this dissertation features an input parameter that allows the user to stipulate which constitutive formulation is used for the calculation of the each lamina's local transverse bulk modulus properties E_{22}, G_{12}, G_{23}, and G_{31}; for these transverse properties, the user may choose to use either the inverse rule of mixtures (equations (1.3), (1.4), (1.5), (1.7), and (1.8)) or the Halpin-Tsai equations (equations (1.9), (1.10), (1.11), and (1.12)).

Upon completion of the full CLPT laminate analysis, the bulk stiffness values of each leg are assigned using the terms of the laminate stiffness matrix **C** (see equation (1.23)) and the laminate compliance matrix **S** (see equation (1.25)) for the relevant leg.

The effective elastic centroid of each leg of the section is not necessarily positioned on the mid-plane of that leg. In the case of structural loadings where longitudinal normal stresses dominate the elastic response, such as axial loadings or bending moments, the through-thickness elevation of the elastic centroid of each leg should be taken as the elevation of the flexural neutral axis of that leg for bending about its local transverse y-y axis, which can be calculated as follows [62]:

$$e_{NAyy} = -\frac{b_{11}}{d_{11}} \tag{3.1}$$

where b_{11} is taken from the laminate coupling compliance matrix **b** of the relevant leg, d_{11} is taken from the laminate bending compliance matrix **d** of the relevant leg, and e_{NAyy} is the elevation of the flexural neutral axis of the leg along its local z axis, measured with respect to the mid-plane of the leg. A positive value of e_{NAyy} indicates that the neutral axis is positioned above the mid-plane of the laminate. In the case of structural loadings where in-plane shear stresses dominate the elastic response, such as in-plane shear loadings or twisting moments, the through-thickness elevation of the elastic centroid of each leg should be taken as the elevation at which twisting curvatures do not generate any in-plane x-y shear strains; this elevation will be denoted here as the "twisting neutral plane", and can be calculated for cases of free torsion as follows [62]:

$$e_{npFT} = -\frac{b_{66}}{d_{66}} \tag{3.2}$$

where b_{66} is taken from the laminate coupling compliance matrix **b** of the relevant leg, d_{66} is taken from the laminate bending compliance matrix **d** of the relevant leg, and e_{npFT} is the elevation of the free torsion twisting neutral plane of the leg along its local z axis, measured with respect to the mid-plane of the leg. A positive value of e_{npFT} indicates that the neutral axis is positioned above the mid-plane of the laminate. The definition of e_{npFT} is discussed again in more detail in Section 3.11.3. In the case of balance symmetric and/or balanced anti-symmetric laminates, the elevations of both the flexural neutral axis and the twisting neutral plane will be coincident with the mid-plane of the laminate, and the values of e_{NAyy} and e_{npFT} will be zero.

In the event that the values of e_{NAyy} and/or e_{npFT} are not equal to zero, any bulk stiffness terms that are derived from the laminate compliance matrix would require that the terms of the laminate compliance matrix are first adjusted in accordance with the parallel axis theorem for the relevant elevation. The modified terms of the laminate compliance matrix can be evaluated at the elevation of the flexural neutral axis e_{NAyy}, as follows [62]:

$$\begin{aligned} a_{ijNAyy} &= a_{ij} + 2\,e_{NAyy}\,b_{ij} + e_{NAyy}^2\,d_{ij} \\ b_{ijNAyy} &= b_{ij} + e_{NAyy}\,d_{ij} \\ d_{ijNAyy} &= d_{ij} \end{aligned} \tag{3.3}$$

where a_{ij} is the ij term of the laminate extensional compliance matrix $\mathbf{a}$, b_{ij} is the ij term of the laminate coupling compliance matrix $\mathbf{b}$, d_{ij} is the ij term of the laminate bending compliance matrix $\mathbf{d}$, and the values a_{ijNAyy}, b_{ijNAyy}, and d_{ijNAyy} are the modified values of a_{ij}, b_{ij}, and d_{ij} at the elevation of the flexural neutral axis e_{NAyy}, respectively. Similarly, the modified terms of the laminate compliance matrix can be evaluated at the elevation of the free torsion twisting neutral plane e_{npFT}, as follows [62]:

$$\begin{aligned} a_{ij\,npFT} &= a_{ij} + 2\,e_{npFT}\,b_{ij} + e_{npFT}^2\,d_{ij} \\ b_{ij\,npFT} &= b_{ij} + e_{npFT}\,d_{ij} \\ d_{ij\,npFT} &= d_{ij} \end{aligned} \tag{3.4}$$

where $a_{ij\,npFT}$, $b_{ij\,npFT}$, and $d_{ij\,npFT}$ are the modified values of a_{ij}, b_{ij}, and d_{ij} at the elevation of the free torsion twisting neutral plane e_{npFT}, respectively.

The 1993 work of Barbero, Lopez-Anido, and Davalos [5] on the mechanics of laminated beams (MLB) incorporated a semi-coupled model that accounted for extensional-flexural coupling. In this work, the normal elastic modulus along the longitudinal x axis of each leg (parallel to the X axis of the member) was calculated as a function of the modified values of the laminate compliance matrix at the elevation of the flexural neutral axis e_{NAyy} (see equation (3.3)), as follows:

$$E_{xx} = \frac{1}{h\,a_{11NAyy}} = \frac{d_{11}}{h\left(a_{11}d_{11} - b_{11}^2\right)} \tag{3.5}$$

where h is the total thickness of the laminate, a_{11} is taken from the laminate extensional compliance matrix $\mathbf{a}$ of the relevant leg, b_{11} is taken from the laminate coupling compliance matrix $\mathbf{b}$ of the relevant leg, and d_{11} is taken from the laminate bending compliance matrix $\mathbf{d}$ of the relevant leg. Provided that the structural member of interest comprises exclusively balanced symmetric and/or balanced anti-symmetric laminates, values of e_{NAyy} and b_{11} for each leg will be zero, and equation (3.5) can be simplified as follows:

$$E_{xx} = \frac{1}{h\,a_{11}} \tag{3.6}$$

Since twisting is a structural loading that is dominantly dependent upon in-plane shear strains, the x-y shear modulus within the plane of each leg can be calculated as a function of the modified values of the laminate compliance matrix at the elevation of the free torsion twisting neutral plane e_{npFT} (see equation (3.4)), as follows:

$$G_{xy} = \frac{1}{h\,a_{66\,npFT}} = \frac{d_{66}}{h\left(a_{66}d_{66} - b_{66}^2\right)} \tag{3.7}$$

where a_{66} is taken from the laminate extensional compliance matrix **a** of the relevant leg, b_{66} is taken from the laminate coupling compliance matrix **b** of the relevant leg, and d_{66} is taken from the laminate bending compliance matrix **d** of the relevant leg. Once again, in the event that the structural member of interest comprises exclusively balanced symmetric and/or balanced anti-symmetric laminates, values of e_{npFT} and b_{66} for each leg will be zero, and equation (3.7) can be simplified as follows:

$$G_{xy} = \frac{1}{h\,a_{66}} \tag{3.8}$$

The out-of-plane bending stiffness of each leg about its transverse y axis, per unit width along the y axis, can be calculated as a function of the modified values of the laminate compliance matrix at the elevation of the flexural neutral axis e_{NAyy} (see equation (3.3)), as follows:

$$\frac{dEI_{yy}}{dy} = \frac{1}{d_{11NAyy}} = \frac{1}{d_{11}} \tag{3.9}$$

While the twisting stiffness of each leg can also be calculated in a similar fashion, the analytical model discussed in this dissertation treats twisting stiffness using a higher fidelity formulation that accounts for through-thickness shear effects, and is discussed in detail in Section 3.11.

While it would not be exceptionally difficult to employ the effects of non-zero values of e_{NAyy} and/or e_{npFT} when calculating the composite properties of a built-up beam comprising one or more legs having thin unbalanced and un-symmetric laminates, it will be shown in Section 3.19 that the present analytical model is simply not conducive to the analysis of such a beam due to its inability to fully account for all coupling effects that could potentially be exhibited (such as extensional-twisting coupling, bending-twisting coupling, and bending-shear coupling). Furthermore, the treatment of nodal areas discussed in Section 3.6 is not conducive for analyses that involve laminates having non-zero values of e_{NAyy} and/or e_{npFT}. Ultimately, the present analytical model is intended to serve as a means of approximating the behaviour of laminated composite members using methodologies that would be familiar to stress analysts that are well-versed in the analysis of conventional metallic structures. It is for this reason that the majority of the present analytical model was formulated in a manner that is limited to the analysis of members that comprise balanced symmetric laminates and/or balanced anti-symmetric laminates having a large number of laminae (plies), such that most of the coupling phenomena discussed in Section 1.2.9 can be largely ignored. As such, for the purposes of all subsequent discussions pertaining to the present analytical method (with the exception of torsional stiffness calculations discussed in Section 3.11), the values of e_{NAyy} and e_{npFT} shall be taken as zero, the centroid of each leg shall be assumed to be located on its mid-plane, and the values of E_{xx}, G_{xy}, and $dEI_{yy}\big/dy$ shall be calculated in accordance with equations (3.6), (3.8), and (3.9), respectively.

3.6 Distribution of Cross-Sectional Areas and Mechanical Properties

3.6.1 General

Although Figure 3.1 clearly illustrates the intended cross-sectional geometry that would result from a user-stipulated system of leg lengths and leg thicknesses, it is not always obvious how the mechanical properties should be defined within the nodal regions where two or more legs intersect. In sections that only comprise very thin legs, this concern is of little significance in the context of the entire cross-sectional geometry; however, in the more general case of a member that features thick legs that differ substantially in their mechanical properties, the aforementioned concern may have greater significance. The analytical model discussed in this dissertation makes an important distinction between structural phenomena that relate to the development of normal stresses parallel to the longitudinal X axis of the member (such as axial compression, axial tension, and bending moments), and structural phenomena that relate to the development of shear stresses within the x-y plane of each leg of the member (such as torsion moments, warping bi-moments, and transverse shear forces). It is interesting to note that the presence of warping bi-moments is dependent upon a combination of longitudinal normal stresses and in-plane shear stresses; however, it will be shown in Section 3.12 that the total twisting moment that results from warping is calculated merely by integrating the shear stresses within the x-y plane of each leg of the member.

3.6.2 Treatment of Nodal Regions for Axial and Flexural Phenomena

When investigating structural phenomena that relate to the development of normal stresses parallel to the longitudinal X axis of the member, it is important that any region having a given set of mechanical properties is given an accurately modelled cross-sectional area and an accurately modelled position with respect to the elastic centroid of the member's cross-section. Overlapping cross-sectional areas at the intersection of perpendicular legs would not be acceptable under any circumstances because this could lead to a re-distribution of material with respect to the elastic centroid of the section, thus altering the net bending stiffness of the member. As such, for the purposes of calculations that are dependent upon the development of longitudinal X stresses, rectangular regions are defined at the intersection of any two or more legs, as shown by the shaded regions in Figure 3.2.

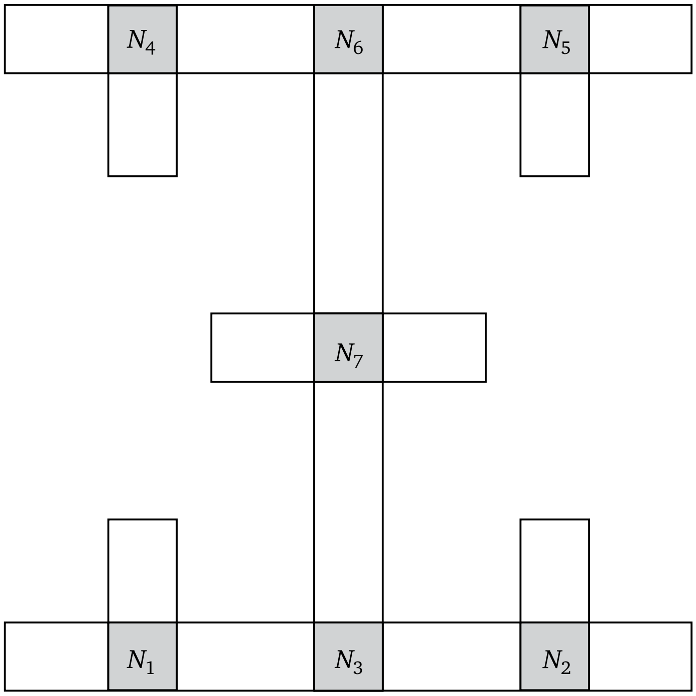

Figure 3.2: Treatment of nodal regions within cross-sectional geometry for the purposes of modelling phenomena that are dependent upon normal stresses along the longitudinal X axis of the member.

The dimensions of each of these shaded nodal regions are calculated as a function of the thicknesses of each of the surrounding legs. In the case of a node that is surrounded by two perpendicularly oriented legs, the Y dimension of the node is set equal to the thickness of the leg that is parallel to the Z axis, and the Z dimension of the node is set equal to the thickness of the leg that is parallel to the Y axis. In the case of a node that is surrounded by more than two legs, each dimension of the node is set equal to the average of the thicknesses of the surrounding legs that are oriented perpendicular to the dimension of interest.

In general, the mechanical properties that are assigned to each node are calculated as a weighted average of the mechanical properties of each of the surrounding legs. The bulk modulus values of each leg are calculated as discussed in Section 3.5. The bulk modulus properties of each node are then calculated as follows:

$$P_{node} = \frac{1}{2}\left[\left(\frac{P_{LY1}h_{LY1} + P_{LY2}h_{LY2}}{h_{LY1} + h_{LY2}}\right) + \left(\frac{P_{LZ1}h_{LZ1} + P_{LZ2}h_{LZ2}}{h_{LZ1} + h_{LZ2}}\right)\right] \tag{3.10}$$

where P_{LY1} and P_{LY2} are the relevant bulk modulus values within the two intersecting legs that are oriented parallel to the Y axis, h_{LY1} and h_{LY2} are the thicknesses of the two intersecting legs that are oriented parallel to the Y axis, P_{LZ1} and P_{LZ2} are the relevant bulk modulus values within the two intersecting legs that are oriented parallel to the Z axis, and h_{LZ1} and h_{LZ2} are the thicknesses of the two intersecting legs that are oriented parallel to the Z axis. Equation (3.10) will provide erroneous bulk modulus values for nodes that are only surrounded by two parallel legs; however, in such a scenario, the nodal region will have zero cross-sectional area, thus rendering the bulk modulus value irrelevant.

As a bi-product of creating these nodal regions, it is necessary to trim the length of each leg such that it does not protrude into the nodal regions. As such, for the purposes of calculations that are dependent upon the development of longitudinal X stresses, the length of each leg is defined as shown by the white (unshaded) regions in Figure 3.10.

3.6.3 Treatment of Nodal Regions for Shear Phenomena

When investigating structural phenomena that relate to the development of shear stresses within the x-y plane of each leg of the member, it is important that the total shear strain energy within each leg is calculated accurately; as such, the length of each leg must be modelled accurately, whereas overlapping areas within the nodal regions are of somewhat lesser concern provided that the total area of the cross-section is modelled accurately. Furthermore, it is important that all shear strain energy is calculated using the exact mechanical properties present within each of the legs of the section; hence, it would not be acceptable to generate nodal regions having averaged (smeared) mechanical properties for the purpose of calculations that depend upon the development of shear stresses within the x-y plane of each leg of the member.

In the case of a node that is situated between two legs that intersect at a right angle, the length of each leg shall terminate at the intersection point of the mid-planes of these two legs; hence, each leg shall penetrate half way through the nodal region, as illustrated in Figure 3.3.

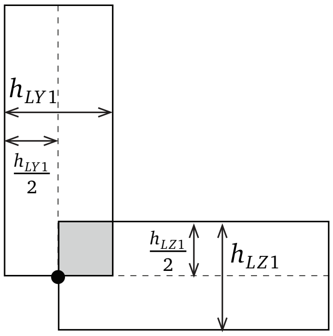

Figure 3.3: Treatment of nodal regions at the intersection of two legs for the purposes of modelling phenomena that are dependent upon x-y shear stresses within the plane of each leg of the member.

It is evident from Figure 3.3 that some material from each leg is overlapped within the shaded area of this nodal region; however, an equal sized area also exists within this nodal region where there is no material present from either of the two legs. As such, the total cross-sectional area of the member is accurately modelled at this node despite the presence of an overlapped region.

In the case of a node that is situated at the intersection of three orthogonal legs, the two parallel legs (on opposing sides of the nodal region) shall each penetrate one quarter of the way through the nodal region. Conversely, the length of the third leg (perpendicular to the aforementioned two parallel legs) shall be set such that it penetrates half way through the nodal region. This treatment of nodal regions at the intersection of three orthogonal legs is illustrated in Figure 3.4.

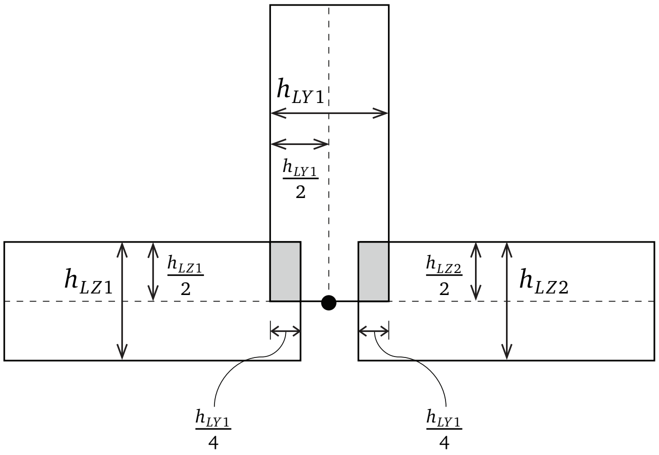

Figure 3.4: Treatment of nodal regions at the intersection of three legs for the purposes of modelling phenomena that are dependent upon x-y shear stresses within the plane of each leg of the member.

It is evident from Figure 3.4 that the two cross-sectional areas where material from more than one leg is overlapped (shown as shaded regions) are balanced by two additional areas of equal size where no material from any leg is present. As such, the total cross-sectional area of the member is accurately modelled at this node despite the presence of two overlapped regions.

In the case of a node that is situated at the intersection of four orthogonal legs, each of these four legs shall penetrate one quarter of the way through the nodal region, as illustrated in Figure 3.5.

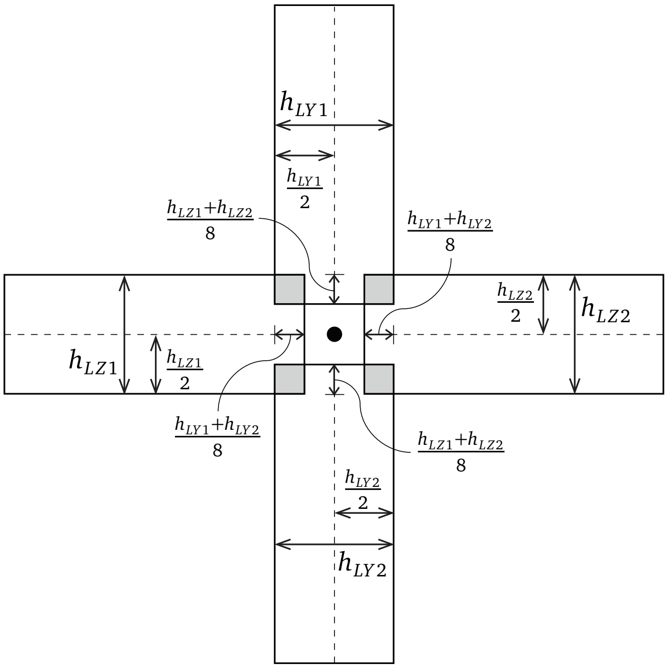

Figure 3.5: Treatment of nodal regions at the intersection of four legs for the purposes of modelling phenomena that are dependent upon x-y shear stresses within the plane of each leg of the member.

It is evident from Figure 3.5 that the four cross-sectional areas (at the four corners of the nodal region) where material from more than one leg is overlapped (shown as shaded regions) are balanced by four additional areas of equal size (near the centre of the nodal region) where no material from any of the four legs is present. As such, the total cross-sectional area of the member is accurately modelled at this node despite the presence of four overlapped regions.

3.6.4 Nominal Material Properties

Although the mechanical properties may vary dramatically within the cross-sectional area of a composite member, it is often convenient to define nominal mechanical properties that can be used as smeared values over the entire cross-sectional area of the member. As such, E_{XX} shall be defined as the nominal normal elastic modulus along the longitudinal X axis of the member. Since the exact value of E_{XX} is unimportant (it is simply used as a weighting function), it will simply be defined here as the mean value of E_{xx} (see Section 3.5) for all of the legs of the cross-sectional geometry. Similarly, G_{XY} and G_{XZ} shall be defined as the nominal out-of-plane shear moduli of the section within the X-Y and X-Z planes, respectively. The values of G_{XY} and G_{XZ} may be taken equal to each other, and may be calculated as the mean value of G_{xy} (see Section 3.5) for all of the legs of the cross-sectional geometry. In general, the nominal shear modulus values G_{XY} and G_{XZ} can be used for any application where a transverse nominal shear modulus value is required. Some of the subsequent sections in this dissertation will include discussions that refer to values of $G_{XY'}$ and $G_{XZ'}$; these values may also be set equal to G_{XY} and G_{XZ}.

It is also convenient to define nominal cross-sectional areas that are normalized with respect to the aforementioned nominal elastic modulus values. As such, A_E shall be defined as the nominal cross-sectional area that has been normalized with respect to the nominal normal elastic modulus along the longitudinal X axis of the member. The value of A_E is calculated as follows:

$$A_E = \frac{\sum_{j=1}^{N_L} A_j\, E_{xx\,j}}{E_{XX}} + \frac{\sum_{i=1}^{N_N} A_i\, E_{xx\,i}}{E_{XX}} \tag{3.11}$$

where A_j is the cross-sectional area of the j^{th} leg of the section, A_i is the cross-sectional area of the i^{th} nodal region of the section, $E_{xx\,j}$ is the value of E_{xx} within the j^{th} leg of the section, $E_{xx\,i}$ is the value of E_{xx} within the i^{th} nodal region of the section, N_L is the total number of legs within the section, and N_N is the total number of nodal regions within the section. Similarly, A_G shall be defined as the nominal cross-sectional area that has been normalized with respect to the nominal transverse shear modulus of the member. The value of A_G is calculated as follows:

$$A_G = \frac{\sum_{j=1}^{N_L} A_j\, G_{xy\,j}}{G_{XY}} + \frac{\sum_{i=1}^{N_N} A_i\, G_{xy\,i}}{G_{XY}} = \frac{\sum_{j=1}^{N_L} A_j\, G_{xy\,j}}{G_{XZ}} + \frac{\sum_{i=1}^{N_N} A_i\, G_{xy\,i}}{G_{XZ}} \tag{3.12}$$

where $G_{xy\,j}$ is the value of G_{xy} within the j^{th} leg of the section, and $G_{xy\,i}$ is the value of G_{xy} within the i^{th} nodal region of the section.

The elevation of the Z-Z flexural neutral axis (measured parallel to the Y axis) can be calculated with respect to the origin of the section, as follows:

$$Y_{NA\,ZZ} = \frac{\sum_{j=1}^{N_L} \left(A_j\, E_{xx\,j}\, Y_j\right) + \sum_{i=1}^{N_N} \left(A_i\, E_{xx\,i}\, Y_i\right)}{A_E\, E_{XX}} \tag{3.13}$$

where Y_j is the Y coordinate of the centroid of the j^{th} leg of the section (measured with respect to the origin of the section), and Y_i is the Y coordinate of the centroid of the i^{th} nodal region of the section (measured with respect to the origin of the section). Similarly, the elevation of the Y-Y flexural neutral axis (measured parallel to the Z axis) can be calculated with respect to the origin of the section, as follows:

$$Z_{NA\,YY} = \frac{\sum_{j=1}^{N_L}\left(A_j\,E_{xx\,j}\,Z_j\right) + \sum_{i=1}^{N_N}\left(A_i\,E_{xx\,i}\,Z_i\right)}{A_E\,E_{XX}} \tag{3.14}$$

where Z_j is the Z coordinate of the centroid of the j^{th} leg of the section (measured with respect to the origin of the section), and Z_i is the Z coordinate of the centroid of the i^{th} nodal region of the section (measured with respect to the origin of the section).

3.7 Bending Stiffness

3.7.1 General

The bending moment in a beam can be calculated, in accordance with Euler-Bernoulli beam theory, as the product of its bending stiffness and a bending curvature imposed upon the beam. In the case of bending moments and curvatures induced about the Y-Y axis of a beam, this relationship can be written as follows:

$$M_{YY} = -E_{XX}\,I_{YY}\,\frac{d\Phi_{YY}}{dX} \tag{3.15}$$

where M_{YY} is the bending moment about the Y-Y axis, E_{XX} is the nominal longitudinal composite elastic modulus of the section (see Section 3.6.4), I_{YY} is the second area moment of inertia of the section about its Y-Y axis, and Φ_{YY} is the angle of rotation of the cross-section at position X about its Y-Y axis relative to the initial undeformed shape of the member.

The bending stiffness of a beam is a function of the distribution of elastic material within the cross-section of the beam. More specifically, bending stiffness can be calculated as the integral of the second moment of the longitudinal axial stiffness of all material in the cross-section about the relevant neutral axis about which bending curvatures are generated.

The local bending stiffness of each leg must first be converted to the global X-Y-Z coordinate system. The total bending stiffness of a built-up section can then be expressed as the summation of the local bending stiffness of each component (leg) and the second moment of axial stiffnesses (product of areas and longitudinal elastic moduli) of each leg about the relevant bending axis of the section. This treatment is known as the “parallel axis theorem”, and is discussed in most introductory structural analysis texts [10].

3.7.2 Local Bending Stiffness

The Y-Y bending stiffness per unit length of a leg that is oriented parallel to the Y axis can simply be taken as the local bending stiffness of that leg about its own y-y axis $dEI_{yy}\big/dy$, as discussed in Section 3.5. Similarly, the Z-Z bending stiffness per unit length of a leg that is oriented parallel to the Z axis can simply be taken as the local bending stiffness of that leg about its y-y axis. As such, the total Y-Y bending stiffness of a leg (leg j) that is oriented parallel to the Y axis can calculated as follows:

$$EI_{YY\,par\,j} = b_j \frac{dEI_{yy}}{dy} = \frac{b_j}{d_{11\,j}} \tag{3.16}$$

where b_j is the effective width of leg j for bending applications (see Section 3.6.2 and Figure 3.2), and $d_{11\,j}$ is the value of the d_{11} term from the bending compliance matrix $\mathbf{d}$ of the laminate present within leg j. Similarly, the total Z-Z bending stiffness of a leg (leg j) that is oriented parallel to the Z axis can calculated as follows:

$$EI_{ZZ\,par\,j} = b_j \frac{dEI_{yy}}{dy} = \frac{b_j}{d_{11\,j}} \tag{3.17}$$

In the case of legs that are oriented perpendicular to the axis about which bending is taking place, bending stiffness must be calculated as the product of the longitudinal elastic modulus of the laminate present within the leg, and the integral of the second moment of areas about the mid-width of the leg. As such, the Y-Y bending stiffness of a leg (leg j) that is oriented perpendicular to the Y axis can be calculated as follows:

$$EI_{YY\,perp\,j} = E_{xx\,j} \frac{h_j\, b_j^3}{12} = \frac{b_j^3}{12\, a_{11\,j}} \tag{3.18}$$

where h_j is the thickness of leg j, $E_{xx\,j}$ is the longitudinal elastic modulus of the laminate present within leg j, and $a_{11\,j}$ is the value of the a_{11} term from the extensional compliance matrix $\mathbf{a}$ of the laminate present within leg j. Similarly, the Z-Z bending stiffness of a leg (leg j) that is oriented perpendicular to the Z axis can be calculated as follows:

$$EI_{ZZ\,perp\,j} = E_{xx\,j} \frac{h_j\, b_j^3}{12} = \frac{b_j^3}{12\, a_{11\,j}} \tag{3.19}$$

The Y-Y bending stiffness of each nodal region can be calculated as a function of the surrounding legs, as follows:

$$EI_{YY\,node\,i} = \frac{1}{2}\left[N_{Y\,i} \left(\frac{d_{11\,Y1}^{-1} + d_{11\,Y2}^{-1}}{NZ_{LY1} + NZ_{LY2}} \right) + \frac{N_{Z\,i}^3}{12} \left(\frac{a_{11\,Z1}^{-1} + a_{11\,Z2}^{-1}}{NZ_{LZ1} + NZ_{LZ2}} \right) \right] \tag{3.20}$$

where $N_{Y\,i}$ is the Y dimension of the i^{th} nodal region of the section (see Section 3.6.2 and Figure 3.2), $N_{Z\,i}$ is the Z dimension of the i^{th} nodal region of the section (see Section 3.6.2 and Figure 3.2), $d_{11\,Y1}$ and $d_{11\,Y2}$ are the relevant values of the d_{11} term from the bending compliance matrix $\mathbf{d}$ of the laminates present within the two intersecting legs that are oriented parallel to the Y axis, and $a_{11\,Z1}$ and $a_{11\,Z2}$ are the relevant values of the a_{11} term from the extensional compliance matrix $\mathbf{a}$ of the laminates present within the two intersecting legs that are oriented parallel to the Z axis. In addition,

NZ_{LY1} and NZ_{LY2} are binary values representing the presence of each of the two intersecting legs that are oriented parallel to the Y axis (set to unity if the relevant leg exists, or zero if it does not), and NZ_{LZ1} and NZ_{LZ2} are binary values representing the presence of each of the two intersecting legs that are oriented parallel to the Z axis (set to unity if the relevant leg exists, or zero if it does not). Similarly, the Z-Z bending stiffness of each nodal region can be calculated as a function of the surrounding legs, as follows:

$$EI_{ZZ\,node\,i} = \frac{1}{2}\left[N_{Z\,i}\left(\frac{d^{-1}_{11\,Z1} + d^{-1}_{11\,Z2}}{NZ_{LZ1} + NZ_{LZ2}}\right) + \frac{N^3_{Y\,i}}{12}\left(\frac{a^{-1}_{11\,Y1} + a^{-1}_{11\,Y2}}{NZ_{LY1} + NZ_{LY2}}\right)\right] \tag{3.21}$$

where $d_{11\,Z1}$ and $d_{11\,Z2}$ are the relevant values of the d_{11} term from the bending compliance matrix $\mathbf{d}$ of the laminates present within the two intersecting legs that are oriented parallel to the Z axis, and $a_{11\,Y1}$ and $a_{11\,Y2}$ are the relevant values of the a_{11} term from the extensional compliance matrix $\mathbf{a}$ of the laminates present within the two intersecting legs that are oriented parallel to the Y axis. Equations (3.20) and (3.21) will provide erroneous bending stiffness values for nodes that are only surrounded by two parallel legs; however, in such a scenario, the nodal region will have zero cross-sectional area, thus rendering the bending stiffness value irrelevant.

3.7.3 Global Bending Stiffness

As mentioned in Section 3.7.1, the total global bending stiffness of the built-up beam can be calculated as the sum of the local stiffnesses of each leg (see Section 3.7.2) and the second moment of axial stiffnesses (product of areas and longitudinal elastic moduli) of each leg about the relevant bending axis of the section. As such, the total Y-Y bending stiffness of the built-up beam can be calculated as follows:

$$EI_{YY\,total} = \sum_{j=1}^{N_L}\left(EI_{YY\,leg\,j} + \frac{b_j}{a_{11\,j}}\bar{Z}_j^2\right) + \sum_{i=1}^{N_N}\left(EI_{YY\,node\,i} + E_{xx\,i}A_i\,\bar{Z}_i^2\right) \tag{3.22}$$

where N_L is the total number of legs in the built-up section, $EI_{YY\,leg\,j}$ is the local Y-Y bending stiffness of leg j (calculated using equation (3.16) for legs that are oriented parallel to the Y axis, or equation (3.18) for legs that are oriented perpendicular to the Y axis), b_j is the effective width of leg j for bending applications (see Section 3.6.2 and Figure 3.2), $a_{11\,j}$ is the value of the a_{11} term from the extensional compliance matrix $\mathbf{a}$ of the laminate present within leg j, and $\bar{Z}_j$ is the perpendicular distance from the Y-Y neutral axis of the section to the centroid of leg j (measured parallel to the Z axis of the section). In addition, N_N is the total number of nodes in the built-up section, $EI_{YY\,node\,i}$ is the local Y-Y bending stiffness of node i, A_i is the cross-sectional area of the i^{th} nodal region of the section (see Section 3.6.2 and Figure 3.2), $E_{xx\,i}$ is the effective longitudinal elastic modulus of the i^{th} nodal region of the section (see equation (3.10)), and $\bar{Z}_i$ is the perpendicular distance from the Y-Y neutral axis of the section to the centroid of the i^{th} nodal region of the section (measured parallel to the Z axis of the section). Similarly, the total Z-Z bending stiffness of the built-up beam can be calculated as follows:

$$EI_{ZZ\,total} = \sum_{j=1}^{N_L}\left(EI_{ZZ\,leg\,j} + \frac{b_j}{a_{11\,j}}\,\bar{Y}_j^2\right) + \sum_{i=1}^{N_N}\left(EI_{ZZ\,node\,i} + E_{xx\,i}A_i\,\bar{Y}_i^2\right) \tag{3.23}$$

where $EI_{ZZ\,leg\,j}$ is the local Z-Z bending stiffness of leg j (calculated using equation (3.17) for legs that are oriented parallel to the Z axis, or equation (3.19) for legs that are oriented perpendicular to the Z axis), $\bar{Y}_j$ is the perpendicular distance from the Z-Z neutral axis of the section to the centroid of leg j (measured parallel to the Y axis of the section), $EI_{ZZ\,node\,i}$ is the local Z-Z bending stiffness of the i^{th} nodal region of the section, and $\bar{Y}_i$ is the perpendicular distance from the Z-Z neutral axis of the section to the centroid of the i^{th} nodal region of the section (measured parallel to the Y axis of the section).

In members having unsymmetrical cross-sections, the Y-Z stiffness product of inertia may be non-zero, and can be calculated as follows:

$$EI_{YZ\,total} = \sum_{j=1}^{N_L}\left(\frac{b_j}{a_{11\,j}}\,\bar{Y}_j\,\bar{Z}_j\right) + \sum_{i=1}^{N_N}\left(E_{xx\,i}A_i\,\bar{Y}_i\,\bar{Z}_i\right) \tag{3.24}$$

Ultimately, an effective moment of inertia for flexure about the global Y or Z axes can be calculated by dividing the aforementioned bending stiffness values by the nominal longitudinal elastic modulus of the section. As such, the Y-Y second area moment of inertia of the entire section can be calculated as follows:

$$I_{YY} = \frac{EI_{YY\,total}}{E_{XX}} \tag{3.25}$$

where is E_{XX} is the nominal longitudinal elastic modulus of the section, as defined in Section 3.6.4. Similarly, the Z-Z second area moment of inertia of the entire section can be calculated as follows:

$$I_{ZZ} = \frac{EI_{ZZ\,total}}{E_{XX}} \tag{3.26}$$

Finally, the Y-Z area product of inertia of the entire section can be calculated as follows:

$$I_{YZ} = \frac{EI_{YZ\,total}}{E_{XX}} \tag{3.27}$$

3.7.4 Principal Axes of Flexure

The principal axes of flexure for a given section can be defined as the axes about which the maximum and minimum values of second area moment of inertia will exist; hence, they are also the axes about which the maximum and minimum values of bending stiffness will exist. In the case of members having doubly symmetric cross-sections that comprise orthogonally oriented legs (webs and flanges), the principal axes of flexure will be oriented parallel and/or perpendicular to the axes of symmetry, which will also be parallel and/or perpendicular to the orientations of the legs of the section. This orientation (parallel and/or perpendicular to the orientations of the legs of the section) shall be denoted as the global coordinate system (see Sections 3.3 and 3.4). In the case of members having singly symmetric cross-sections that comprise orthogonally oriented legs (webs and flanges), the principal axes of flexure will be oriented parallel and/or perpendicular to the axis of symmetry. Conversely, in the case of a member that has a completely unsymmetrical cross-section, the principal axes of flexure may exist at some angle $\phi_{principal}$ measured counter-clockwise relative to the Y and Z axes of the global coordinate system. The value of this angle $\phi_{principal}$ may be calculated as follows [10]:

$$\phi_{principal} = \frac{1}{2} \arctan\left(\frac{2\, I_{YZ}}{I_{ZZ} - I_{YY}} \right) \tag{3.28}$$

The principal axis that is oriented at a counter-clockwise angle of $\phi_{principal}$ relative to the global Y axis will be denoted here as the Y' axis. The second area moment of inertia of the section about this Y' axis can be calculated as follows [10]:

$$I_{Y'Y'} = \frac{I_{YY} + I_{ZZ}}{2} + \frac{I_{YY} - I_{ZZ}}{2} \cos\left(2\, \phi_{principal}\right) - I_{YZ} \sin\left(2\, \phi_{principal}\right) \tag{3.29}$$

The principal axis that is oriented at a counter-clockwise angle of $\phi_{principal}$ relative to the global Z axis will be denoted here as the Z' axis. The second area moment of inertia of the section about this Z' axis can be calculated as follows [10]:

$$I_{Z'Z'} = \frac{I_{YY} + I_{ZZ}}{2} - \frac{I_{YY} - I_{ZZ}}{2} \cos\left(2\, \phi_{principal}\right) + I_{YZ} \sin\left(2\, \phi_{principal}\right) \tag{3.30}$$

Finally, the area product of inertia of the section within its principal Y'-Z' coordinate system can be shown to be equal to zero, as follows [10]:

$$I_{Y'Z'} = \frac{I_{YY} - I_{ZZ}}{2} \sin\left(2\, \phi_{principal}\right) + I_{YZ} \cos\left(2\, \phi_{principal}\right) = 0 \tag{3.31}$$

3.8 Shear-Centre Location

In the case of a structural member having a doubly-symmetric cross-section composed of a single isotropic material, any transverse load applied through the centroid of the section and in a direction parallel to the major or minor axis of the section will result in a lateral deflection that is parallel to the direction of loading, with no coupled torsional response. Conversely, in a member having a cross-section that is only singly symmetric or completely unsymmetric, any transverse load applied parallel to an axis about which the section is unsymmetric will cause shear-flow through the walls of the section that will sum to a net twisting moment about the longitudinal axis of the member. As such, there exists a point known as the shear-centre O, through which transverse forces may be applied without causing the development of these twisting moments. In essence, the distance between the centroid and shear-centre of a section must be defined such that a transverse force that acts through the shear-centre of the section will generate a moment about the centroid of the section that is exactly equal and opposite to the twisting moment that is generated by the total shear flow within the walls of the section due to that very same transverse load (see Figure 3.6).

In order to locate the shear-centre of an arbitrary section, it is necessary to perform calculations in the context of the principal Y' and Z' axes of the section (see Section 3.7) such that no bending moment is generated about the axis of a transversely applied load. It is useful to denote s as a coordinate along a curvilinear path defined by the mid-plane of the system of thin-shell legs that make up the cross-section of the structural member of interest. At any given position S (along the s coordinate system) within the cross-section of a transversely loaded thin-walled member, it can be shown that the magnitude of the in-plane x-y shear stresses within the walls of the member can be found as a function of some transverse force applied in the Z' direction, as follows:

$$\tau_{xy\,S} = \frac{V_{Z'}\, EQ_{Y'Y'S}}{E_{XX}\, I_{Y'Y'}\, h_S} \tag{3.32}$$

where $V_{Z'}$ is a transverse shear force applied parallel to the Z' principal axis of the member, E_{XX} is the nominal longitudinal composite elastic modulus of the section (see Section 3.6.4), $I_{Y'Y'}$ is the second area moment of inertia of the section about its Y'-Y' axis (see Section 3.7), h_S is the total thickness of the laminate at position S, and $EQ_{Y'Y'S}$ is the integral of the first moment of the product of areas and local E_{xx} longitudinal elastic moduli about the Y'-Y' principal axis of the member, for all material situated on one side of coordinate S of the cross-sectional geometry of the member. The value of $EQ_{Y'Y'S}$ can be found at any position S on the member's cross-section, as follows:

$$EQ_{Y'Y'S} = \int_{0}^{S} E_{xx\,s}\, \bar{Z}'_s\, h_s ds = \int_{S}^{m} E_{xx\,s}\, \bar{Z}'_s\, h_s ds \tag{3.33}$$

where m is the entire length over which the coordinate s is defined, $E_{xx\,s}$ is the longitudinal elastic modulus of the relevant leg of the cross-section at coordinate s (see equation (3.6) in Section 3.5), h_s is the total thickness of the laminate at position s, and $\bar{Z}'_s$ is the perpendicular distance from the Y'-Y' neutral axis of the section to coordinate s (measured parallel to the Z' axis of the section). In the context of a stringer made up of legs that each comprise unique composite laminates, the value of $E_{xx\,s}$ in equation (3.33) shall be taken as $1\big/\!\left(h\, a_{11}\right)$, where h is the total thickness of the laminate, and a_{11} is taken from the laminate extensional compliance matrix $\mathbf{a}$ of the relevant leg, calculated from Classical Laminated Plate Theory. The net torsion moment caused by in-plane shear flows can be calculated by integrating the first moment of in-plane x-y shear flows about the centroid of the section; a useful equation of equilibrium can then be established by equating this value to the first moment of the applied transverse force $V_{Z'}$ (assumed to have been applied through the shear-centre of the section) about the centroid of the section, as follows:

$$V_{Z'}\, e_{Y'} = \int_{0}^{m} \tau_{xy\,S}\, h_S\, r_{perp\,C\,S}\, dS = \frac{V_{Z'}}{E_{XX}\, I_{Y'Y'}} \int_{0}^{m} \int_{0}^{S} E_{xx\,s}\, \bar{Z}'_s\, h_s ds\; r_{perp\,C\,S}\, dS \qquad (3.34)$$

where $e_{Y'}$ is the distance between the centroid and shear-centre of the section measured parallel to the Y' axis, and $r_{perp\,C\,S}$ is the moment arm of the S coordinate on the mid-plane of the relevant leg of the cross-section about the centroid of the entire section, measured perpendicular to the surface of the relevant leg at coordinate S. Figure 3.6 helps to illustrate the aforementioned equilibrium relationship in the context of a C-channel cross-sectional geometry, and also shows some of the geometric dimensions that are relevant to this calculation.

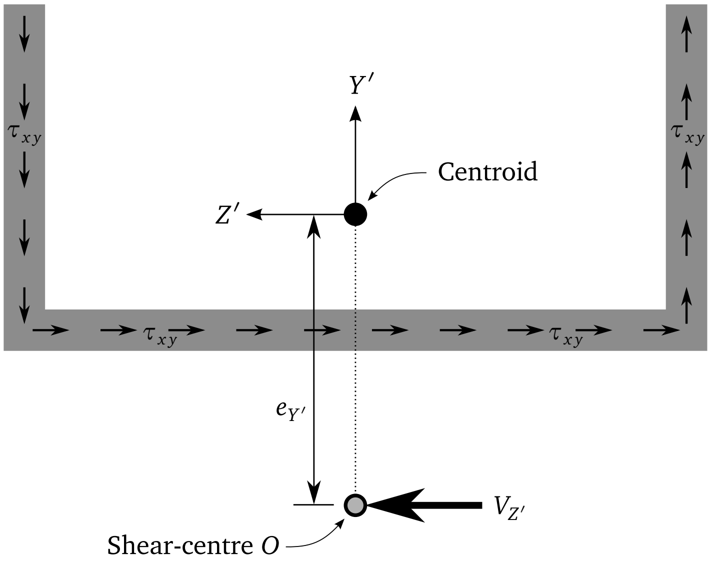

Figure 3.6: Cross-sectional drawing of a C-channel member, illustrating the equilibrium relationship that is used to find the shear-centre of such a member. Note that τ_{xy} represents mid-plane shear stresses within the x-y plane of each leg of the cross-sectional geometry.

Solving for $e_{Y'}$, the Y' component of the distance from the centroid of the section to the shear-centre O of the section can be found as follows:

$$e_{Y'} = \frac{1}{E_{XX}\, I_{Y'Y'}} \int_{0}^{m} \int_{0}^{S} E_{xx\,s}\, \bar{Z}'_s\, h_s ds\; r_{perp\,C\,S}\, dS \qquad (3.35)$$

Similarly, the Z' component of the distance from the centroid of the section to the shear-centre O of the section can be found as follows:

$$e_{Z'} = \frac{1}{E_{XX}\, I_{Z'Z'}} \int\limits_{0}^{m} \int\limits_{0}^{S} E_{xx\,s}\, \bar{Y}'_s\, h_s ds\; r_{perp\,C\,S}\, dS \tag{3.36}$$

where $I_{Z'Z'}$ is the second area moment of inertia of the section about its Z'-Z' axis (see Section 3.7), and $\bar{Y}'_s$ is the perpendicular distance from the Z'-Z' neutral axis of the section to coordinate s (measured parallel to the Y' axis of the section).

3.9 Polar Moment of Inertia

The area polar moment of inertia of a cross-section is an important characteristic when calculating its torsional buckling load, as will be discussed in Section 3.15. The area polar moment of inertia of a section about its centroid I_C can be calculated as the sum of the major and minor second area moments of inertia of the section (see Section 3.7.4), as follows:

$$I_C = I_{Y'Y'} + I_{Z'Z'} \tag{3.37}$$

The area polar moment of inertia of the section about its shear-centre I_O can then be calculated by augmenting the aforementioned value of I_C using the parallel axis theorem, as follows:

$$I_O = I_C + A_E \left(e_{Y'}^2 + e_{Z'}^2 \right) \tag{3.38}$$

where A_E is the nominal cross-sectional area that has been normalized with respect to the nominal normal elastic modulus along the longitudinal X axis of the member (see Section 3.6.4), and $e_{Y'}$ and $e_{Z'}$ are the Y' and Z' components of the distance between the centroid and the shear-centre of the section, respectively (see Section 3.8).

3.10 Transverse Shear Stiffness

Euler-Bernoulli beam theory assumes a relationship between an applied transverse load and the resulting deflection which, through successive differentiation, dictates a direct relationship between the applied bending moment, the flexural stiffness of the beam, and the resultant curvature exhibited by the beam. Timoshenko beam theory [76][77] improves upon this relationship a by adding provisions to account for additional transverse compliance caused by shear deformations. Ultimately, Timoshenko beam theory manifests itself as the super-position of bending deflection and shear deflection, and is dependent upon knowledge of material and geometric properties including: longitudinal elastic modulus, shear modulus, second area moment of inertia, cross-sectional area, and Timoshenko shear correction factor. Barbero, Lopez-Anido, and Davalos demonstrated [5] an elegant application of Timoshenko beam theory for the analysis of pultruded FRP composite beams having constant cross-sectional geometries.

While Timoshenko beam theory is applicable to any direction of transverse loading, in the interest of clarity, the author has elected to derive Timoshenko beam theory in the context of a transverse shear force applied in the Z' direction, coupled with a bending moment about the Y'-Y' axis. The Y'-Y' bending moment in a member at any given position X along its length can be defined as follows:

$$M_{Y'Y'} = -E_{XX}\, I_{Y'Y'}\, \frac{d\Phi_{Y'Y'}}{dX} \tag{3.39}$$

where $M_{Y'Y'}$ is the bending moment about the Y'-Y' axis, E_{XX} is the nominal longitudinal composite elastic modulus of the section (see Section 3.6.4), $I_{Y'Y'}$ is the second area moment of inertia of the section about its Y'-Y' axis (see Section 3.7), and $\Phi_{Y'Y'}$ is the angle of rotation of the cross-section at position X about its Y'-Y' axis relative to the initial undeformed shape of the member. The lateral deflection of the beam in the Z' direction at any position X along its length can be defined as a function of the applied transverse shear force, as follows:

$$\frac{dw}{dX} = \Phi_{Y'Y'} - \frac{V_{Z'}}{\beta_{Y'Y'} A_G\, G_{XZ'}} = \Phi_{Y'Y'} - \frac{1}{\beta_{Y'Y'} A_G\, G_{XZ'}} \frac{dM_{Y'Y'}}{dX} \tag{3.40}$$

where $V_{Z'}$ is a transverse shear force applied in the Z' direction, w is the lateral deflection of the cross-section in the Z' direction relative to the initial undeformed shape of the member, A_G is the cross-sectional area of the beam normalized with respect to the nominal transverse shear modulus (see Section 3.6.4), $G_{XZ'}$ is the nominal X-Z' shear modulus of the entire section (see Section 3.6.4), and $\beta_{Y'Y'}$ is the Timoshenko shear correction factor for use with transverse shear forces applied in the Z' direction of the section. Since $\Phi_{Y'Y'}$ represents the true angle of rotation of the cross-section at position X, whereas dw/dX represents the slope of the longitudinal axis of the deformed member at position X, any difference between these values represents a shear strain angle in the X-Z' plane of the member. Figure 3.7 shows the deformed shape of a transversely loaded beam, and helps to illustrate some of the geometric dimensions that are relevant to the present formulation for Timoshenko beam theory.

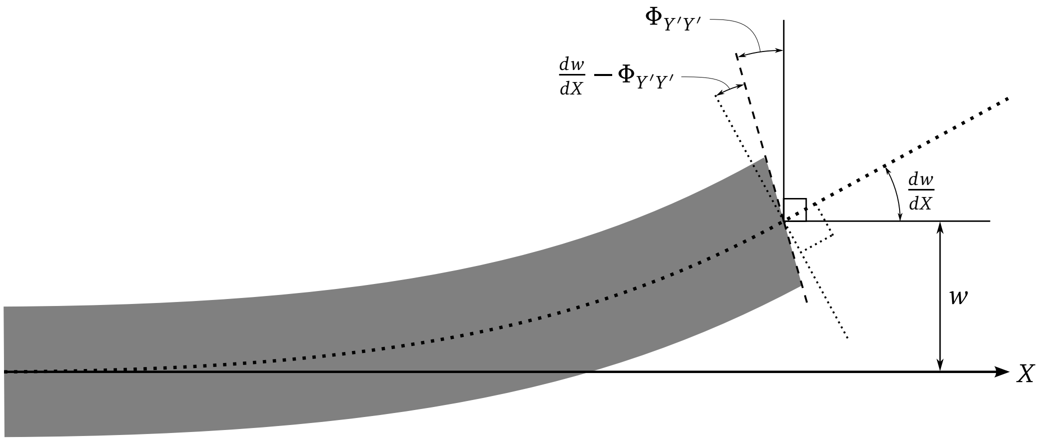

Figure 3.7: Deformed shape of a transversely loaded beam, illustrating some of the geometric dimensions that are relevant to the present formulation for Timoshenko beam theory.

Substituting equation (3.39) into equation (3.40) gives the following differential equation relating the angle of rotation of the beam's cross-section to the transverse Z' deflection of the beam:

$$\frac{dw}{dX} = \Phi_{Y'Y'} - \frac{E_{XX}\, I_{Y'Y'}}{\beta_{Y'Y'}\, A_G\, G_{XZ'}} \frac{d^2\Phi_{Y'Y'}}{dX^2} \tag{3.41}$$

While there has been some dispute as to the most accurate method of calculating the Timoshenko shear correction factor $\beta_{Y'Y'}$ for a member having an arbitrary cross-section, its seems that most authors agree upon methodologies that are based upon classical work-energy theorems. As such, the present analytical method employs a Timoshenko shear correction factor that is calculated by equating total internal shear strain energy to external work done by a transverse shear force. Recall from equations (3.32) and (3.33) that the x-y shear stress within the plane of each leg in a thin-walled beam's cross-section can be calculated as a function of a transversely applied force in the Z' direction, as follows:

$$\tau_{xyS} = \frac{V_{Z'}}{E_{XX}\, I_{Y'Y'}\, h_S} \int_0^S E_{xxs}\, \bar{Z}'_s\, h_s ds \tag{3.42}$$

where $V_{Z'}$ is a transverse shear force applied parallel to the Z' principal axis of the member, $I_{Y'Y'}$ is the second area moment of inertia of the section about its Y'-Y' axis (see Section 3.7), h_S is the total thickness of the laminate at positions S on the beam's cross-section, h_s is the total thickness of the laminate at positions s on the beam's cross-section, E_{xxs} is the longitudinal elastic modulus of the relevant leg of the cross-section at coordinate s (see equation (3.6) in Section 3.5), and $\bar{Z}'_s$ is the perpendicular distance from the Y'-Y' neutral axis of the section to coordinate s (measured parallel to the Z' axis of the section). In the context of a stringer made up of legs that each comprise unique composite laminates, the value of E_{xxs} in equation (3.42) shall be taken as $1 \big/ \left(h\, a_{11}\right)$, where h is the total thickness of the laminate, and a_{11} is taken from the laminate extensional compliance matrix **a** of the relevant leg, calculated from Classical Laminated Plate Theory. Dividing equation (3.42) by the x-y shear modulus of the laminate at position S, it is possible to calculate the x-y shear strain at position S as follows:

$$\gamma_{xy\,S} = \frac{V_{Z'}}{E_{XX}\, I_{Y'Y'}\, h_S\, G_{xy\,S}} \int_0^S E_{xx\,s}\, \bar{Z}'_s\, h_s ds \tag{3.43}$$

where $G_{xy\,S}$ is the x-y shear modulus of the laminate at position S (see equation (3.8) in Section 3.5). In the context of a stringer made up of legs that each comprise unique composite laminates, the value of $G_{xy\,S}$ in equation (3.43) shall be taken as $1 \big/ \left(h\, a_{66}\right)$, where h is the total thickness of the laminate, and a_{66} is taken from the laminate extensional compliance matrix **a** of the relevant leg, calculated from Classical Laminated Plate Theory. The total x-y shear strain energy caused by a transverse shear force applied in the Z' direction can be calculated within an infinitesimal length of the structural member, dX, as follows:

$$\mathrm{U}_{int\,xy\,VZ'} = \frac{V_{Z'}^2}{2\left(E_{XX}\, I_{Y'Y'}\right)^2}\, dX \int_0^m \frac{\left(\int_0^S E_{xx\,s}\, \bar{Z}'_s\, h_s ds\right)^2}{h_S\, G_{xy\,S}}\, dS \tag{3.44}$$

where m is the entire length over which the coordinate s is defined. The external work that is done by a transverse load applied in the Z' direction can be calculated as follows:

$$\mathrm{U}_{ext\,VZ'} = \frac{V_{Z'}^2}{2\,\beta_{Y'Y'}\, A_G\, G_{XZ'}}\, dX \tag{3.45}$$

Finally, the value of the Timoshenko shear correction factor, $\beta_{Y'Y'}$ can be calculated by combining equations (3.44) and (3.45), equating internal strain energy to external work, and isolating for $\beta_{Y'Y'}$, as follows:

$$\beta_{Y'Y'} = \left[\frac{A_G\, G_{XZ'}}{\left(E_{XX}\, I_{Y'Y'}\right)^2} \int_0^m \frac{\left(\int_0^S E_{xx\,s}\, \bar{Z}'_s\, h_s ds\right)^2}{h_S\, G_{xy\,S}}\, dS \right]^{-1} \tag{3.46}$$

In a similar fashion, the Timoshenko shear correction can be calculated for use with transverse shear loads applied in the Y' direction, as follows:

$$\beta_{Z'Z'} = \left[\frac{A_G\, G_{XY'}}{\left(E_{XX}\, I_{Z'Z'}\right)^2} \int_0^m \frac{\left(\int_0^S E_{xx\,s}\, \bar{Y}'_s\, h_s ds\right)^2}{h_S\, G_{xy\,S}}\, dS \right]^{-1} \tag{3.47}$$

where $I_{Z'Z'}$ is the second area moment of inertia of the section about its Z'-Z' axis (see Section 3.7), $G_{XY'}$ is the nominal X-Y' shear modulus of the entire section, and $\bar{Y}'_s$ is the perpendicular distance from the Z'-Z' neutral axis of the section to coordinate s (measured parallel to the Y' axis of the section).

3.11 Torsional Stiffness

This section includes work that was reproduced and adapted from [34], which is a published manuscript for which the author retains copyright ownership (see Appendix G). In addition, the author has obtained explicit permission from the relevant parties for the reproduction of this manuscript in the present dissertation (see Appendix G). The final definitive version of [34] has been published in the Journal of Composite Materials, by SAGE Publications Ltd, All rights reserved. ©

3.11.1 General

Much of the existing engineering science for the analysis of laminated composites is focused on shell-type laminated structures that are thin relative to their breadth, whereby it can be assumed that all stresses act parallel to the plane of the laminate. Conversely, thick laminates tend to necessitate more complex analytical methods due to the presence of non-trivial through-thickness stresses near their free edges. These through-thickness stresses become particularly relevant in the analysis of thick laminated rectangular plates of finite width that are subjected to torsional loadings applied about a single longitudinal axis.

When warping deformations are unconstrained, the uniform torsional response of a member having a constant cross-section along its length can be defined in accordance with the following linear function:

$$T_{SV} = C \frac{d\phi}{dx} \tag{3.48}$$

where T_{SV} is the Saint-Venant torsion moment applied about the longitudinal x axis of the member, ϕ is the angle of twist about the longitudinal x axis of the member, and C is the Saint-Venant's torsional stiffness of the member [68]. The purpose of the following section is to develop an accurate and pragmatic method of calculating such a torsional stiffness value for thick laminated rectangular plates of finite width, comprising an arbitrary number of plies arranged in any laminate stacking sequence. The goal is to do so in a manner that is conducive for practical engineering applications (e.g. in industry). By virtue of the aforementioned Saint-Venant torsion theory, it is assumed that the laminated plate of interest is long in relation to its width, and that the long edges (which are parallel to the axis of the applied torsion moment) are free of any applied tractions or moments (see Figure 3.8).

The present methodology is intended for use with laminates having plies composed of continuous unidirectional fibre reinforced polymer composites that can each be modelled as orthotropic or transversely isotropic materials. Two coordinate systems shall be defined for use in all subsequent discussions in this section. A 1-2-3 lamina coordinate system (see Figure 3.8) shall be defined at the mid-thickness of each lamina (ply) whereby the 1 direction is parallel to the fibre orientation, the 2 direction is in the plane of each lamina and oriented perpendicular to the fibres, and the 3 direction is oriented normal to the plane of the lamina. An x-y-z global laminate coordinate system (see Figure 3.8) shall be defined at the mid-thickness of the complete laminate whereby the x direction is parallel to the axis of the applied torsion moment, the y direction is in the plane of the laminate and oriented perpendicular to the axis of the applied torsion moment, and the z direction is oriented normal to the plane of the laminate. For the purposes of the present analytical methodology, the material model within each ply shall be orthotropic within its lamina 1-2-3 coordinate system, but may behave as an anisotropic material within the laminate's global x-y-z coordinate system. Figure 3.8 illustrates the aforementioned lamina and global laminate coordinate systems, the axis of the applied torsion moment, and some of the basic geometric dimensions of the laminated plate.

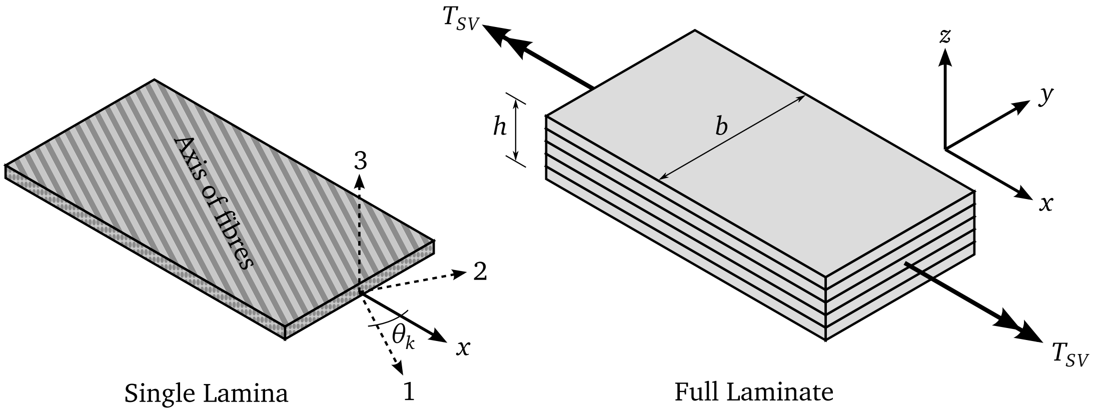

Figure 3.8: Lamina and laminate coordinate systems

3.11.2 Isotropic Homogeneous Plates Subjected to Torsion

In general, the torsional stiffness of any member of a continuous cross-section that is composed of a single homogeneous and isotropic material can be found as a product of the shear modulus of the material G and a geometric property (torsion constant) of the section J, as shown in the following equation:

$$C = JG \tag{3.49}$$

While the value of J is relatively easy to find for circular cross-sections, more complex analyses are necessary for most other cross-sectional geometries. The Prandtl Stress Function [63] is a means of calculating the shear stress field present in a member of constant arbitrary cross-sectional geometry that is undergoing a torsional loading; hence, it can also be used to determine the geometric torsion constant, J, of such a member [10][79]. In the case of thin and broad rectangular plates having widths much greater than their thicknesses, the Prandtl Stress Function yields a geometric torsion constant formulation that simplifies to the following form:

For high aspect ratio rectangular plates ($b/h > 10$):

$$J_{thin} = \frac{1}{3} b h^3 \tag{3.50}$$

where b is the width of the plate along the y axis, and h is the thickness of the plate along the z axis (see Figure 3.8). This aforementioned equation for broad thin plates is derived based upon the assumption that all of the shear stresses that are contributing to the net torsion moment are acting parallel to the broad surfaces of the plate. In reality, these shear stresses traverse through the thickness of the plate near the free edges of the plate; however, if the width-to-thickness aspect ratio of the plate is very high, then the distribution of these through-thickness shear stresses is relatively unimportant. Conversely, in thick plates having lower width-to-thickness aspect ratios, it is no longer reasonable to neglect the distribution of these through-thickness shear stresses, and a higher fidelity application of the Prandtl Stress Function becomes necessary. Unfortunately, in the case of thick rectangular plates, the solution to the Prandtl Stress Function involves an infinite series for which an exact solution can be difficult and impractical to find [10][79]. Fortunately, there exists an approximate solution (within 4% of the exact solution) to this function which takes the following form [95]:

For low aspect ratio rectangular plates ($b/h \leq 10$):

$$J_{thick} = \frac{b h^3}{16} \left[\frac{16}{3} - 3.36 \frac{h}{b} \left(1 - \frac{h^4}{12 b^4} \right) \right] \tag{3.51}$$

This method of calculating torsional stiffness by finding the geometric property J, and multiplying this value by the shear modulus G is only applicable to plates composed of a single homogeneous and isotropic material. As such, this method is not directly applicable to laminated composite plates. It is interesting to note that, as expected, the values of J_{thin} and J_{thick} begin to converge at high width-to-thickness aspect ratios. However, at low width-to-thickness aspect ratios, the value of J_{thin}

will tend to be higher than the value of J_{thick}; as such, the use of J_{thin} in torsion calculations will result in an over-estimate of torsional stiffness. The term $\aleph_{geom}$ shall now be introduced as a new geometric adjustment factor, as follows:

$$\aleph_{geom} = \frac{J_{thick}}{J_{thin}} = \frac{3}{16}\left[\frac{16}{3} - 3.36\frac{h}{b}\left(1 - \frac{h^4}{12\,b^4}\right)\right] \tag{3.52}$$

If η_{geom} is denoted as the geometric width-to-thickness aspect ratio of the plate, then the expression for $\aleph_{geom}$ can be simplified as follows:

$$\aleph_{geom} = 1 - \frac{0.63}{\eta_{geom}}\left(1 - \frac{1}{12\,\eta_{geom}^4}\right) \qquad \text{where:} \qquad \eta_{geom} = \frac{b}{h} \tag{3.53}$$

The value of $\aleph_{geom}$ is always less than unity, and helps to illustrate the amount by which J_{thin} overestimates the geometric torsion constant of an isotropic rectangular plate of a given geometric width-to-thickness aspect ratio, η_{geom}. As such, it can be said that $J_{thick} = \aleph_{geom} J_{thin}$. While $\aleph_{geom}$ has minimal practical applications in the analysis of isotropic plates in torsion, it will be shown to have great value in the analysis of thick composite laminated plates that are subjected to torsional loadings.

3.11.3 Thin Laminated Plates Subjected to Torsion

To calculate the torsional stiffness of a laminated plate, it is first necessary to characterize the type of torsion that is taking place; as such, an important distinction must be made between pure torsion and free torsion. Pure torsion is defined as a state of constrained torsion whereby all other degrees of freedom are restrained. Consequently, in pure torsion, any form of coupling exhibited by the laminate may cause additional internal stresses, but ultimately only twisting deformations will be permitted in the laminated plate. In essence, pure torsion is relevant when a specific angle of twist is to be imposed about the longitudinal axis of the member while all other degrees of freedom are restrained (set to zero). Conversely, free torsion may be defined as a state of unconstrained torsion whereby the only induced load is a torsion moment, and all other degrees of freedom are unrestrained. As such, in free torsion, any form of coupling exhibited by the laminate may manifest itself as flexural, shear, or extensional deformations that occur as a bi-product of the applied twisting moment. In essence, free torsion is relevant when a specific torsion moment is to be imposed about the longitudinal axis of the member while all other forces and moments are set to zero.

The simplest and most direct method of finding the torsional stiffness of a laminated plate is to utilize the terms of the stiffness matrix calculated from Classical Laminated Plate Theory (CLPT). Detailed explanations of the derivation and use of CLPT can be found in many composites texts [39][54], and is summarized briefly in Section 1.2.8. It is important to note that the derivation of CLPT is based upon the assumption that twisting moments are applied to all four edges of a rectangular element, whereas the more conventional definition of uniaxial torsion (and that which would be relevant in the context of equation (3.48)) is represented by only a pair of equal and opposite torques that act about a single longitudinal axis. As such, the value of M_{xy} that is used in CLPT (see Section 1.2.8) is analogous to only half of the uniaxial torsion moment that was defined in equation (3.48). The cause of this apparent discrepancy is the presence of through-thickness shear stresses in the case of uniaxial torsion, which may be justifiably neglected when twisting moments are evenly distributed over all four edges of a rectangular element (as in the case of CLPT), as shown by Whitney in 1991 [92]. Figure 3.9 illustrates this relationship between the uniaxial torsion moment T_{SV} defined in equation (3.48) and the twisting moments M_{xy} that are applied in CLPT, as well as the in-plane shear stresses τ_{xy} and through-thickness shear stresses τ_{xz} that are present during each type of loading.

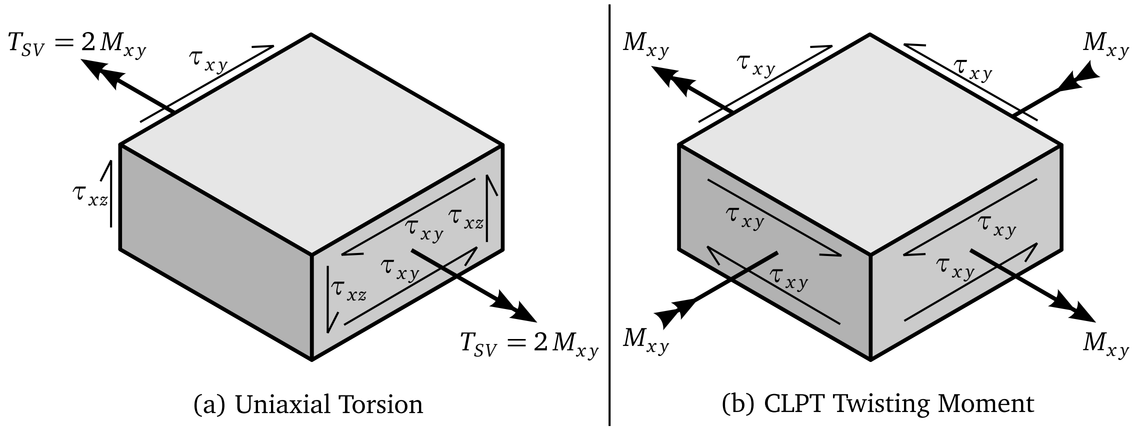

(a) Uniaxial Torsion (b) CLPT Twisting Moment

Figure 3.9: Shear stresses present during the case of (a) uniaxial torsion and (b) twisting moments applied in accordance with CLPT

In addition, twisting curvatures that are used in CLPT are based upon out-of-plane displacement partial derivatives that are ultimately analogous to double of what is typically defined as a torsional rotation angle in cases of uniaxial torsion. This discrepancy (a factor of 2) emerges during the derivation of CLPT (see equations (1.26) and (1.27) in Section 1.2.8), and can be attributed to the use of engineering shear strains (rather than tensorial shear strains). Furthermore, it is important to recognize that the terms of the laminate stiffness and compliance matrices in CLPT are defined per unit width of laminate.

The C_{66} term of the laminate stiffness matrix relates twisting moments to twisting curvatures. However, using this term directly would fail to account for bending-twisting, extensional-twisting, or shear-twisting coupling phenomena. As such, in the case of free torsion, it is necessary to instead calculate the inverse of the laminate stiffness matrix to arrive upon the laminate compliance matrix, and then use the S_{66} term of this compliance matrix (which is equal to the d_{66} term of the laminate bending compliance matrix) for the purposes of calculating the torsional stiffness of the laminated plate. Ultimately, the free torsional stiffness for a laminated plate having a finite width, b, may be found from CLPT as follows:

$$C_{lamFT} = \frac{4b}{S_{66}} = \frac{4b}{d_{66}} \tag{3.54}$$

Since this torsional stiffness is based upon the compliance matrix of the laminate, it shall only be applied in cases of free torsion. In cases of pure torsion, it would be necessary to instead derive the torsional stiffness from the C_{66} term of the laminate stiffness matrix (which is equal to the D_{66} term of the laminate bending stiffness matrix), as follows:

$$C_{lamPT} = 4b\,C_{66} = 4b\,D_{66} \tag{3.55}$$

It is of critical importance to recognize that the aforementioned CLPT based torsional stiffness values are dependent upon Kirchhoff-Love thin plate assumptions [43][53], and therefore are only applicable to laminated plates having very high width-to-thickness aspect ratios ($b >> h$). CLPT assumes that all stresses in a laminated plate act parallel to the surfaces of the laminate. As such, in the case of torsion, CLPT neglects to account for the development of through-thickness shear stresses near the free edges of the laminated plate. Therefore, by virtue of these thin-plate assumptions, it is not surprising that the aforementioned use of CLPT for a single plate composed entirely of a single isotropic material will result in a torsional stiffness that is identical to that which would be calculated using equation (3.49) and the aforementioned equation for J_{thin} (equation 3.50). As such, for any laminated plate analyzed using CLPT, there exists an equivalent smeared shear modulus that can be used in conjunction with J_{thin} to calculate the aforementioned torsional stiffness values. This effective shear modulus, G_{effFT} or G_{effPT}, may be found for cases of free torsion or pure torsion, respectively, as follows:

$$\begin{aligned} G_{effFT} &= \frac{C_{lamFT}}{J_{thin}} = \frac{12}{h^3\,S_{66}} = \frac{12}{h^3\,d_{66}} \\ G_{effPT} &= \frac{C_{lamPT}}{J_{thin}} = \frac{12\,C_{66}}{h^3} = \frac{12\,D_{66}}{h^3} \end{aligned} \tag{3.56}$$

To facilitate higher fidelity torsional analyses, it is necessary to determine the effective in-plane x-y shear modulus of each ply of the laminate. However, the value of this effective in-plane shear modulus for angled anisotropic plies is dependent upon the type of torsional loading that is present. As such, using the constitutive relationships included in Sections 1.2.7 and 1.2.8, the following criteria defining pure torsion of laminated plates can be established:

$$\begin{aligned} \text{At the laminate mid-plane:} \quad \varepsilon^0_{xx} &= \varepsilon^0_{yy} = \gamma^0_{xy} = 0 \\ k_{xx} &= k_{yy} = 0 \\ M_{xy} &= D_{66}\, k_{xy} \end{aligned} \tag{3.57}$$

The in-plane x-y shear stress in lamina k can be defined using the constitutive relationship of the lamina (see Section 1.2.7) as follows:

$$\tau_{xy\,k} = \bar{Q}_{61\,k}\, \varepsilon_{xx\,k} + \bar{Q}_{62\,k}\, \varepsilon_{yy\,k} + \bar{Q}_{66\,k}\, \gamma_{xy\,k} \tag{3.58}$$

Recognizing that $\varepsilon_{xx\,k} = \varepsilon_{yy\,k} = 0$ for pure torsion, and that in general $\tau_{xy} = G_{xy}\gamma_{xy}$, the effective in-plane shear modulus of lamina k can be defined for cases of pure torsion as follows:

$$G_{xyPT\,k} = \bar{Q}_{66\,k} \tag{3.59}$$

Similarly, the following criteria that define free torsion of laminated plates can be established:

$$\begin{aligned} N_{xx} = N_{yy} = N_{xy} = M_{xx} &= M_{yy} = 0 \\ k_{xx} &= d_{16}\, M_{xy} \\ k_{yy} &= d_{26}\, M_{xy} \\ k_{xy} &= d_{66}\, M_{xy} \end{aligned} \tag{3.60}$$

The in-plane strains in lamina k can be calculated for free torsion, and substituted into the constitutive relationship of the lamina as follows:

$$\begin{aligned} \varepsilon_{xx\,k} &= b_{16}\, M_{xy} + z_{mid\,k}\, d_{16}\, M_{xy} \\ \varepsilon_{yy\,k} &= b_{26}\, M_{xy} + z_{mid\,k}\, d_{26}\, M_{xy} \\ \gamma_{xy\,k} &= b_{66}\, M_{xy} + z_{mid\,k}\, d_{66}\, M_{xy} \quad \rightarrow \quad M_{xy} = \frac{\gamma_{xy\,k}}{b_{66} + z_{mid\,k}\, d_{66}} \\ \tau_{xy\,k} &= \bar{Q}_{61\,k}\, \varepsilon_{xx\,k} + \bar{Q}_{62\,k}\, \varepsilon_{yy\,k} + \bar{Q}_{66\,k}\, \gamma_{xy\,k} \\ \tau_{xy\,k} &= \frac{\bar{Q}_{61\,k}\left(z_{mid\,k}\, d_{16} + b_{16}\right)}{b_{66} + z_{mid\,k}\, d_{66}} \gamma_{xy\,k} + \frac{\bar{Q}_{62\,k}\left(z_{mid\,k}\, d_{26} + b_{26}\right)}{b_{66} + z_{mid\,k}\, d_{66}} \gamma_{xy\,k} + \bar{Q}_{66\,k}\, \gamma_{xy\,k} \end{aligned} \tag{3.61}$$

where $z_{mid\,k}$ is the elevation of the mid-plane of lamina k relative to the mid-plane of the laminate. Recognizing in general that $\tau_{xy} = G_{xy}\gamma_{xy}$, the effective in-plane shear modulus of lamina k can be defined for cases of free torsion as follows:

$$G_{xyFT\,k} = \frac{\bar{Q}_{61\,k}\left(z_{mid\,k}\, d_{16} + b_{16}\right)}{b_{66} + z_{mid\,k}\, d_{66}} + \frac{\bar{Q}_{62\,k}\left(z_{mid\,k}\, d_{26} + b_{26}\right)}{b_{66} + z_{mid\,k}\, d_{66}} + \bar{Q}_{66\,k} \tag{3.62}$$

In either case of pure or free torsion, an elevation exists within the laminate at which in-plane x-y shear strains are equal to zero. This plane shall be denoted as the “twisting neutral plane” (see Section 3.5). In cases of pure torsion, the twisting neutral plane is simply coincident with the mid-plane of the laminate; this is because, in pure torsion, only twisting deformations about the laminate mid-plane are permitted, and all other deformations are restrained. Conversely, in cases of free torsion, the twisting neutral plane may be at some elevation e_{npT} above the mid-plane of the laminate. Using the aforementioned constitutive relationships and setting in-plane x-y shear strains to zero, the elevation of the twisting neutral plane can be found with respect to the laminate mid-plane, denoted by e_{npPT} or e_{npFT} for cases of pure torsion or free torsion, respectively, as follows:

$$\begin{aligned} e_{npPT} &= 0 \\ e_{npFT} &= -\frac{b_{66}}{d_{66}} \end{aligned} \tag{3.63}$$

The values of these elevations will be positive when the twisting neutral plane falls above the mid-plane of the laminate, and negative when the twisting neutral plane falls below the mid-plane of the laminate.

3.11.4 Torsional Stiffness of Thick Laminated Plates

The following derivation serves to establish a correction factor that is capable of modifying the aforementioned pure torsional stiffness C_{lamPT} and free torsional stiffness C_{lamFT} for thin laminated plates, such that they account for the presence of through-thickness shear stresses near the laminate’s free edges, and can therefore be used for the torsional analysis of thick laminated plates of finite width.

In the interest of clarity, this derivation will be performed in a general sense that may be applied to cases of either pure torsion or free torsion. As such, the in-plane shear modulus of ply k will be denoted here as $G_{xyT\,k}$, which shall be taken as $G_{xyPT\,k}$ for cases of pure torsion, or $G_{xyFT\,k}$ for cases of free torsion. Similarly, the in-plane shear modulus of ply i will be denoted here as $G_{xyT\,i}$, which shall be calculated in a manner analogous to $G_{xyT\,k}$. The effective smeared shear modulus for torsion will be denoted here as G_{effT}, which shall be taken as G_{effPT} for cases of pure torsion, or G_{effFT} for cases of free torsion. The elevation of the twisting neutral plane will be denoted here as e_{npT}, which shall be taken as e_{npPT} for cases of pure torsion, or e_{npFT} for cases of free torsion. Finally, the laminate torsional stiffness values from CLPT will be denoted here as C_{lam}, which shall be taken as C_{lamPT} for cases of pure torsion, or C_{lamFT} for cases of free torsion.

In order to proceed with this derivation, it is necessary to assume that the through-thickness distribution of in-plane x-y shear strains (γ_{xy}) is linear, which is a reasonable assumption in the context of all previously discussed theorems for both laminated and homogeneous plates. As such, a new term ψ shall be defined to represent the slope of this linear through-thickness gradient of x-y shear strains, as follows:

$$\psi = \frac{\partial \gamma_{xy}}{\partial z} \tag{3.64}$$

It is noted that all in-plane x-y shear stresses must tend to zero at the free edges of the laminated plate, assuming that no shear tractions are applied to the free edges. In the case of torsional loadings, this attenuation of in-plane x-y shear stresses is primarily accomplished through the generation of through-thickness x-z shear stresses. As such, in the case of torsional loadings, the through-thickness x-z shear stress at a given elevation has a magnitude that is equal to the through-thickness integral of the transverse (y direction) rate-of-change of in-plane x-y shear stresses in all of the material above or below the elevation of interest, as shown in the following equation:

$$\tau_{xz\,W} = \int_{z=0}^{W} \frac{\partial \tau_{xy\,z}}{\partial y} dz \tag{3.65}$$

where $\tau_{xz\,W}$ is the x-z shear stress at elevation W (the elevation of interest), and $\tau_{xy\,z}$ is the x-y shear stress at elevation z.

In order to calculate the magnitude of the through-thickness x-z shear stresses due to torsion of a laminated plate, it would be necessary to know the rate of change of in-plane x-y shear stresses along the transverse y axis of the plate, which constitutes a highly indeterminate problem of many dependent partial differential equations [61][64][55]. However, in the absence of this information, a nominal distribution of through-thickness x-z shear strains through the depth of the laminated plate can be determined as a function of a nominal rate of change of the slope of the through-thickness distribution of in-plane x-y shear strains. In order to achieve this, is useful to define a new term $Q_{yT\,k}$ as the integral of the first moment of x-y shear moduli ($G_{xyT\,i}$ in lamina i and $G_{xyT\,k}$ in lamina k) about the twisting neutral plane of the laminate, for all material below the elevation of interest. The value of $Q_{yT\,k}$ may be evaluated at any elevation within each lamina k as follows:

$$Q_{yT\,k} = \int_{\alpha_k=0}^{z_{ply\,k}} \left[\left(z_{botNP\,k} + \alpha_k\right) G_{xyT\,k}\right] d\alpha_k + \sum_{i=1}^{k-1} \int_{\alpha_i=0}^{t_{ply\,i}} \left[\left(z_{botNP\,i} + \alpha_i\right) G_{xyT\,i}\right] d\alpha_i \tag{3.66}$$

where $z_{botNP\,k}$ is the elevation of the bottom of lamina k relative to the twisting neutral plane of the laminate, $z_{botNP\,i}$ is the elevation of the bottom of lamina i relative to the twisting neutral plane of the laminate, and $t_{ply\,i}$ is the total thickness of lamina i. The variables α_k and α_i represent elevations within laminae k and i, measured with respect to $z_{botNP\,k}$ and $z_{botNP\,i}$, respectively. Similarly, the upper integration bound $z_{ply\,k}$ is the specific elevation of interest where $Q_{yT\,k}$ is to be evaluated (within lamina k), measured with respect to $z_{botNP\,k}$. Figure 3.10 shows a cross-sectional view of the laminate, and helps to illustrate the aforementioned geometric variables that are relevant to the calculation of $Q_{yT\,k}$.

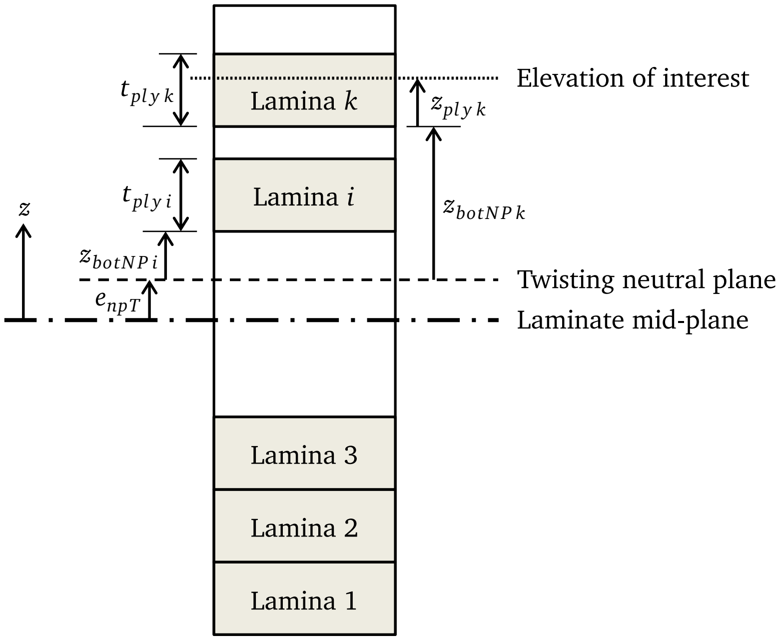

Figure 3.10: Geometric variables relevant to the calculation of $Q_{yT\,k}$

It is worth nothing that the present definition for $Q_{yT\,k}$ is somewhat reminiscent of a variational through-thickness shear formulation developed by Cosentino and Weaver in 2010 [21]; however, that particular work was intended for general-case computational modelling of thick laminated plates, whereas the present work is intended as a pragmatic approximate analysis technique to quickly ascertain the torsional stiffness of thick laminated plates. The definite integrals for $Q_{yT\,k}$ can be solved within their integration bounds as follows:

$$Q_{yT\,k} = \left(z_{botNP\,k}\, z_{ply\,k} + \frac{z_{ply\,k}^2}{2} \right) G_{xyT\,k} + \sum_{i=1}^{k-1} \left[\left(z_{botNP\,i}\, t_{ply\,i} + \frac{t_{ply\,i}^2}{2} \right) G_{xyT\,i} \right] \tag{3.67}$$

It should be noted that the value of $Q_{yT\,k}$ can be evaluated at any elevation within the thickness of lamina k; however, the equations describing $Q_{yT\,k}$ are unique within each lamina. As such, $Q_{yT\,k}$ is calculated as a piece-wise summation of the definite continuous integrals though the thicknesses of each lamina below the elevation of interest, and up to the exact elevation of interest, $z_{ply\,k}$, which resides somewhere within the thickness of lamina k. For practical purposes, it is more convenient to expand $Q_{yT\,k}$ into the following polynomial:

$$Q_{yT\,k} = A_{QC\,k} + A_{Q1\,k}\, z_{ply\,k} + A_{Q2\,k}\, z_{ply\,k}^2 \tag{3.68}$$

where:

$$A_{QC\,k} = A_{QC\,k-1} + A_{Q1\,k-1}\, t_{ply\,k-1} + A_{Q2\,k-1}\, t_{ply\,k-1}^2$$

$$A_{Q1\,k} = z_{botNP\,k}\; G_{xyT\,k}$$

$$A_{Q2\,k} = \left(\frac{1}{2}\right) G_{xyT\,k}$$

$$t_{ply\,k-1} = \text{ Thickness of lamina } k-1$$

$A_{QC\,k-1}$ is analogous to $A_{QC\,k}$ but evaluated within lamina $k-1$

$A_{Q1\,k-1}$ is analogous to $A_{Q1\,k}$ but evaluated within lamina $k-1$

$A_{Q2\,k-1}$ is analogous to $A_{Q2\,k}$ but evaluated within lamina $k-1$

At this point, the coefficient $Q_{yT\,k}$ can be assembled along with a nominal value of ψ to arrive upon the nominal through-thickness distribution of x-z shear stresses that will arise as a result of some unknown nominal change in the slope of the through-thickness distribution of in-plane x-y shear strains. This nominal x-z shear stress distribution through the thickness of the laminate can be expressed as follows:

$$\tau_{xzNOM\,k} = \left(\frac{d\psi_{Lam}}{dy}\right) Q_{yT\,k} \tag{3.69}$$

where ψ_{Lam} is the assumed value of ψ within the laminate of interest. It is now possible to calculate the rate of accumulation of through-thickness x-z shear strain energy in each ply along the y axis, as a function of some unknown nominal change in the slope of the through-thickness distribution of in-plane x-y shear strains. This rate of accumulation of x-z shear strain energy can be expressed within lamina k as follows:

$$\frac{dU_{xzNOM\,k}}{dy} = \int_0^{t_{ply\,k}} \left[\left(\frac{d\psi_{Lam}}{dy}\right)^2 \frac{Q_{yT\,k}^2}{2\,G_{xz\,k}} dx \right] dz_{ply\,k} \tag{3.70}$$

where $G_{xz\,k}$ is the through-thickness x-z shear modulus of lamina k. The value of $G_{xz\,k}$ within each lamina k can be calculated as follows:

$$G_{xz\,k} = G_{13\,k}\cos^2\theta_k + G_{23\,k}\sin^2\theta_k \tag{3.71}$$

where $G_{13\,k}$ is the 1-3 shear modulus of lamina k, $G_{23\,k}$ is the 2-3 shear modulus of lamina k, and θ_k is the angle measured between the 1 axis of the lamina coordinate system (fibre axis) of lamina k and the x axis of the global laminate coordinate system (see Figure 3.8). Strictly speaking, the development of x-z shear strains is potentially dependent upon the presence of both x-z shear stresses and y-z shear stresses [90]. The constitutive coupling terms that relate y-z and x-z shear behaviours emerge upon transformation of the 3-dimensional orthotropic compliance matrix of lamina k (see equation (1.1) in Section 1.2.6) for an angular rotation θ_k about the lamina 3 axis. However, these constitutive coupling terms relating y-z and x-z shear behaviours will tend to approach zero when the values of $G_{13\,k}$ and $G_{23\,k}$ are similar, as is the case here (see equations (1.4), (1.8), and (1.11) in Section 1.2.6). Furthermore, since no appreciable y-z shear stresses are developed under the given uniaxial Saint-Venant torsional loading conditions (see Figure 3.9), the aforementioned y-z to x-z constitutive coupling terms bear little relevance here. As such, for the purposes of this derivation, it is reasonable to calculate the value of $G_{xz\,k}$ using equation (3.71).

Once again, Equation (3.70) cannot be used to calculate the actual x-z shear strain energy within the lamina; however, it does represent the nominal rate of accumulation of x-z shear strain energy within each lamina along the y axis. If this formula were integrated over the entire thickness of the laminate, the resultant value would represent the nominal rate at which the total through-thickness x-z shear strain energy accumulates as a function of the rate of change of the slope of the through-thickness distribution of in-plane x-y shear strains, $d\psi_{Lam}\big/dy$. This rate of x-z shear strain energy accumulation is not necessarily the same for all laminates of the same thickness; it is dependent upon the through-thickness distribution of x-y and x-z shear moduli. As such, it is useful to equate the rate of x-z shear strain energy accumulation for the laminate of interest to that of a homogeneous isotropic plate having the same thickness and a nominal smeared shear modulus of $G_{eff\,T}$ in both the x-y and x-z directions, as follows:

$$\frac{1}{2}\sum_{k=1}^{n}\int_{0}^{t_{ply\,k}}\left[\left(\frac{d\psi_{Lam}}{dy}\right)^2\frac{Q_{yT\,k}^2}{G_{xz\,k}}dx\right]dz_{ply\,k}=\frac{1}{2}\left(\frac{d\psi_{Hom}}{dy}\right)^2\frac{h^5\,G_{eff\,T}}{120}\,dx \tag{3.72}$$

where n is the total number of plies in the laminate, and ψ_{Hom} is the assumed value of ψ within a homogeneous isotropic plate having the same thickness and nominal smeared shear modulus as the laminated plate of interest. This expression can be rearranged, and a new coefficient, κ, can be introduced as follows:

$$\kappa=\frac{\left(\frac{d\psi_{Hom}}{dy}\right)^2}{\left(\frac{d\psi_{Lam}}{dy}\right)^2}=\frac{120}{h^5\,G_{eff\,T}}\left[\sum_{k=1}^{n}\int_{0}^{t_{ply\,k}}\left(\frac{Q_{yT\,k}^2}{G_{xz\,k}}\right)dz_{ply\,k}\right] \tag{3.73}$$

where:

$$\int_{0}^{t_{ply\,k}} \left(\frac{Q_{yT\,k}^2}{G_{xz\,k}} \right) dz_{ply\,k} = A_{U1\,k}\, t_{ply\,k} + A_{U2\,k}\, t_{ply\,k}^2 + A_{U3\,k}\, t_{ply\,k}^3 + A_{U4\,k}\, t_{ply\,k}^4 + A_{U5\,k}\, t_{ply\,k}^5$$

$$A_{U1\,k} = \frac{A_{QC\,k}^2}{G_{xz\,k}}$$

$$A_{U2\,k} = \left(\frac{1}{2}\right) \frac{2\,A_{QC\,k} A_{Q1\,k}}{G_{xz\,k}}$$

$$A_{U3\,k} = \left(\frac{1}{3}\right) \frac{\left(2\,A_{QC\,k} A_{Q2\,k}\right) + A_{Q1\,k}^2}{G_{xz\,k}}$$

$$A_{U4\,k} = \left(\frac{1}{4}\right) \frac{2\,A_{Q1\,k} A_{Q2\,k}}{G_{xz\,k}}$$

$$A_{U5\,k} = \left(\frac{1}{5}\right) \frac{A_{Q2\,k}^2}{G_{xz\,k}}$$

$$t_{ply\,k} = \text{ Thickness of lamina } k$$

The value of κ describes the square of the relative rate at which the through-thickness gradient of x-y shear strains is attenuated near the free edges of a laminated plate undergoing torsion. It is a value that compares this rate in a given laminate with that which would be expected in an isotropic homogeneous plate having the same thickness and nominal smeared shear modulus, $G_{eff\,T}$, assuming that the rate of accumulation of through-thickness x-z shear strain energy is set equal in the laminated plate and the homogeneous isotropic plate. The square root of κ will serve to directly describe the relative rate at which the slope of the through-thickness distribution of in-plane x-y shear strains is attenuated near the free edges of the laminate, which is directly proportional to the relative rate at which through-thickness x-z shear stresses are developed near the free edges of the laminate. These relationships are made with respect to an isotropic plate having the same thickness as the laminated plate of interest. In such an isotropic plate, the rate of development of total through-thickness shear force is directly proportional to the thickness of the plate, and the rate of change of the through-thickness gradient of x-y shear strains. As such, an isotropic plate having a thickness of $h\sqrt{\kappa}$ and a shear modulus of $G_{eff\,T}$ would exhibit the same rate of development of total through-thickness shear force per unit width as the laminated composite plate of interest, and would simultaneously exhibit the same rate of attenuation of in-plane x-y shear strains as the laminated composite plate of interest. By extension, it can be said that the laminated composite plate of interest would exhibit an overall proportion of x-y and x-z shear stresses over its y-z cross-section that is comparable to an isotropic plate having an effective width-to-thickness aspect ratio, $\eta_{eff\,T}$, defined as follows:

$$\eta_{eff\,T} = \frac{b}{h\sqrt{\kappa}} = \frac{\eta_{geom}}{\sqrt{\kappa}} \tag{3.74}$$

This does not mean that an isotropic plate having a width of b, a thickness of $h\sqrt{\kappa}$, and a shear modulus of G_{effT} will have the same torsional stiffness as the laminate of interest; it simply means that the percentage by which J_{thin} will overestimate the geometric torsion constant of an isotropic plate having a width-to-thickness aspect ratio of η_{effT} is approximately equal to the percentage by which C_{lamPT} or C_{lamFT} will tend to overestimate the torsional stiffness of the laminated composite plate of interest under the relevant torsional loading conditions. As such, it is logical to introduce a new effective torsional stiffness correction factor $\aleph_{effT}$, which is defined in a manner that is analogous to equation (3.53), but is based upon the effective aspect ratio η_{effT}, as follows:

$$\aleph_{effT} = 1 - \frac{0.63}{\eta_{effT}} \left(1 - \frac{1}{12\,\eta_{effT}^4} \right) \tag{3.75}$$

This correction factor serves to modify the torsional stiffness for thin laminated plates in order to account for the presence of through-thickness shear stresses near the free edges of the plate. Recall that the value of κ may be evaluated for cases of either pure torsion or free torsion, denoted by κ_{FT} and κ_{PT}, respectively. The quantities η_{effT} and $\aleph_{effT}$ can now be re-defined for the case of pure torsion, as follows:

$$\begin{aligned} \eta_{effPT} &= \frac{b}{h\sqrt{\kappa_{PT}}} = \frac{\eta_{geom}}{\sqrt{\kappa_{PT}}} \\ \aleph_{effPT} &= 1 - \frac{0.63}{\eta_{effPT}} \left(1 - \frac{1}{12\,\eta_{effPT}^4} \right) \end{aligned} \tag{3.76}$$

Similarly, the quantities η_{effT} and $\aleph_{effT}$ can be re-defined for the case of free torsion, as follows:

$$\begin{aligned} \eta_{effFT} &= \frac{b}{h\sqrt{\kappa_{FT}}} = \frac{\eta_{geom}}{\sqrt{\kappa_{FT}}} \\ \aleph_{effFT} &= 1 - \frac{0.63}{\eta_{effFT}} \left(1 - \frac{1}{12\,\eta_{effFT}^4} \right) \end{aligned} \tag{3.77}$$

It is now possible to calculate the corrected torsional stiffness of a thick laminated composite plate subjected to pure torsion, as follows:

$$C_{lamThickPT} = \aleph_{effPT} C_{lamPT} = \aleph_{effPT} 4b\, C_{66} = \aleph_{effPT} 4b\, D_{66} \tag{3.78}$$

Similarly, the corrected torsional stiffness of a thick laminated composite plate subjected to free torsion can be calculated as follows:

$$C_{lamThickFT} = \aleph_{effFT} C_{lamFT} = \aleph_{effFT} \frac{4b}{S_{66}} = \aleph_{effFT} \frac{4b}{d_{66}} \tag{3.79}$$

This analysis technique serves to illustrate that the accuracy with which C_{lamPT} or C_{lamFT} model the torsional stiffness of a laminated plate is not a function of its true geometric width-to-thickness aspect ratio; on the contrary, it is a function of its effective aspect ratio, η_{effPT} or η_{effFT}. While it is a common engineering practice to assume that a plate having a geometric width-to-thickness aspect ratio greater than 10 justifies the use of Kirchhoff-Love thin plate assumptions, this assumption may not hold true for laminated composite plates. In fact, a laminated composite plate is quite likely to have an effective aspect ratio that is considerably lower than its true geometric width-to-thickness aspect ratio; hence, the values of $\aleph_{effPT}$ and $\aleph_{effFT}$for such a laminated plate would be considerably lower than the value of $\aleph_{geom}$ for that same laminated plate.

3.11.5 Practical Application of the Present Analytical Method

While its derivation may seem somewhat cumbersome, the present analytical model can be employed for practical engineering applications by following a relatively simple set of steps, as follows:

1. Calculate the values of η_{geom} and $\aleph_{geom}$ using equation (3.53).
2. Find the constitutive stiffness matrix of each lamina within the laminate x-y-z coordinate system.
3. Calculate the value of $G_{xz\,k}$ within each lamina (ply) using equation (3.71).
4. Carry out Classical Laminated Plate Theory to find the laminate stiffness matrix
5. Invert the laminate stiffness matrix to find the laminate compliance matrix
6. Calculate the values of G_{effFT} and G_{effPT} using equation (3.56).
7. Calculate the values of $G_{xyPT\,k}$ and $G_{xyFT\,k}$ within each lamina (ply) using equations (3.59) and (3.62), respectively.
8. Calculate the values of e_{npPT} and e_{npFT} using equation (3.63).
9. Calculate the values of the constant terms present within the polynomial shown in equation (3.68) for each lamina (ply) of the laminate.
10. Substitute the aforementioned constant values from equation (3.68) into equation (3.73) to find the values of κ_{PT} and κ_{FT}.
11. Substitute the values of κ_{PT} and κ_{FT} into equations (3.76) and (3.77), respectively, to find the torsional stiffness correction factors $\aleph_{effPT}$ and $\aleph_{effFT}$, respectively.
12. Substitute the values of $\aleph_{effPT}$ and $\aleph_{effFT}$ into equations (3.78) and (3.79) to find the corrected torsional stiffness values for cases of pure torsion and free torsion, respectively.

The present analytical model can easily be integrated into any existing computer program that includes an algorithm for CLPT. The authors were able to add the necessary calculations for $\sqrt{\kappa_{PT}}$ and $\sqrt{\kappa_{FT}}$ to an existing MathWorks® MATLAB® based subroutine for CLPT with only 48 additional lines of code. Subsequent calculations of torsional stiffness values would only require three to four additional lines of code for each case of pure torsion or free torsion. The present analytical method could also be easily integrated into spreadsheet based CLPT analyses.

Although equation (3.51) serves as an approximate closed-form solution to the Prandtl Stress Function for isotropic and homogeneous rectangular plates, its formulation is limited to applications in which the width of the plate b is greater than its thickness h. By extension, applications of the present analytical method should likely limited to analyses of laminates having effective width-to-thickness aspect ratios η_{effPT} and η_{effFT} that are greater than unity.

3.11.6 Computational Validation

Validation Cases

The present analytical method has been computationally validated against seven different laminates (laminates “a” through “g”), each tested at two different geometric aspect ratios. Each of these test laminates comprised a 3 mm thick core, and five 0.4 mm thick plies laminated above and below the core, for a total laminate thickness of 7 mm. All plies comprised either an isotropic aluminium material, or a unidirectional continuous filament carbon fibre reinforced polymer (CFRP) composite material. The mechanical properties of these two materials in their lamina 1-2-3 coordinate systems are shown in Table 3.1:

Table 3.1: Mechanical properties of aluminium and CFRP materials used in torsion validation study, within their lamina 1-2-3 coordinate systems.

	Aluminium	**CFRP**
E_{11} (GPa)	75.22	183.14
E_{22} (GPa)	75.22	9.09
E_{33} (GPa)	75.22	9.09
G_{12} (GPa)	28.28	3.30
G_{23} (GPa)	28.28	3.30
G_{31} (GPa)	28.28	3.30
ν_{12}	0.330	0.276
ν_{23}	0.330	0.376
ν_{31}	0.330	0.0137

Table 3.2 illustrates the material type and orientation (measured between the material 1 axis and the laminate x axis) within each ply of each of the seven laminates tested. The CFRP material defined in Table 3.1 is denoted in Table 3.2 as “CC” (representing “carbon composite”), and the aluminium material defined in Table 3.1 is denoted in Table 3.2 as “Al”.

Table 3.2: Material type, orientation, and lamina thickness in each ply of the laminates tested. In this table, the CFRP material is denoted here as “CC” (representing “carbon composite”), and the aluminium material is denoted here as “AL”.

Lamina Thickness (mm)	**Laminate Type**						
	a	**b**	**c**	**d**	**e**	**f**	**g**
0.4	+45° CC	+45° CC	Al	0° CC	±45° CC	+45° CC	+30° CC
0.4	−45° CC	−45° CC	Al	0° CC	±45° CC	+45° CC	+30° CC
0.4	0° CC	Al	Al	0° CC	±45° CC	0° CC	0° CC
0.4	−45° CC	−45° CC	Al	0° CC	±45° CC	−45° CC	−60° CC
0.4	+45° CC	+45° CC	Al	0° CC	±45° CC	−45° CC	−60° CC
3.0	Al	0° CC	0° CC	Al	±45° CC	Al	Al
0.4	+45° CC	+45° CC	Al	0° CC	±45° CC	0° CC	Al
0.4	−45° CC	−45° CC	Al	0° CC	±45° CC	0° CC	Al
0.4	0° CC	Al	Al	0° CC	±45° CC	0° CC	Al
0.4	−45° CC	−45° CC	Al	0° CC	±45° CC	0° CC	Al
0.4	+45° CC	+45° CC	Al	0° CC	±45° CC	0° CC	Al

“CC” = CFRP material “Al” = Aluminium material

It is clear from Table 3.2 that laminates “a” through “e” are balanced and symmetric, laminate “f” is balanced and un-symmetric, and laminate “g” is unbalanced and un-symmetric. Laminates “c”, “d”, and “e” are specially orthotropic laminates within the laminate x-y-z coordinate system, and as such, they exhibit no coupling of any sort; hence, free torsion and pure torsion produce identical results for these laminates. Laminates “a” and “b” exhibit bending-twisting coupling; thus, a distinction between free torsion and pure torsion must be made for these laminates. The asymmetry of laminates “f” and “g” dictates that the distinction between free torsion and pure torsion is of critical importance when analyzing these laminates. Due to its unbalanced and un-symmetric laminate architecture, laminate “g” exhibits a fully populated stiffness matrix, and is potentially susceptible to all forms of coupling.

Each of these laminates was used to construct two virtual strips having widths b (perpendicular to the torsion axis) of 30 mm and 45 mm, respectively. The total length of each strip L_{total} (parallel to the torsion axis) was 120 mm; this length was selected to allow for a 30 mm long torsional gauge region (L_g = 30 mm) to be used for data collection near the mid-span of each specimen, while ensuring that no torsional data would be collected within 45 mm (the maximum width b of any specimen) of the load application zone. Figure 3.11 illustrates the geometric configuration of these virtual specimens.

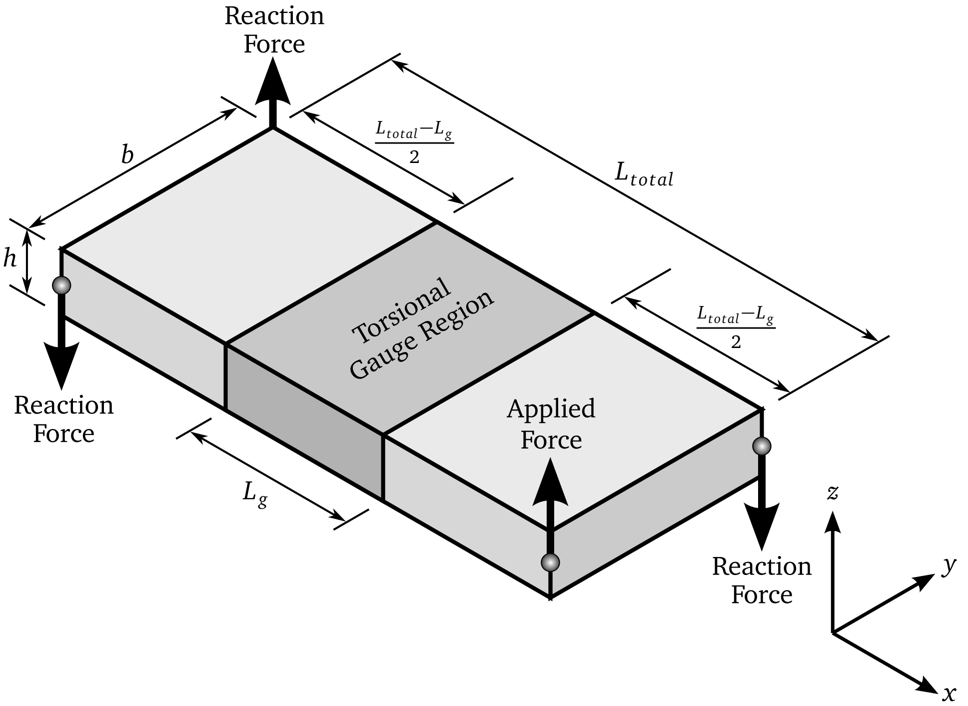

Figure 3.11: Geometry and loading configuration of virtual specimens used for torsional validation study.

Methodology Employed for Finite Element Analyses

A finite element (FE) model of each virtual specimen was built and analyzed using MARC® (a product of the MSC™ Software Corporation). These models comprised one layer of eight-noded first-order isoparametric solid elements per ply (MARC® element formulation 7 [57]), with the exception that the 3 mm thick core received six layers of these same solid elements. Each of these solid elements featured three global translational degrees of freedom per node, and eight Gaussian integration points. The aluminium material was modelled as a linear elastic homogeneous isotropic material. The CFRP material was modelled as a linear elastic homogeneous orthotropic material with nine constitutive properties. In the case of laminates “c” and “d”, this orthotropic model was aligned with the laminate x-y-z coordinate system for all plies. For laminates “f” and “g”, the layer of elements representing each ply was given a material coordinate system that was aligned with the fibres present within that ply. For laminate “e”, a new global orthotropic material model was formulated to have the same constitutive properties as a balanced symmetric laminate having a very large number of +45° and −45° laminae, and was modelled within the laminate x-y-z coordinate system. Laminates “a” and “b” were modelled using two different techniques. To model the behaviour of laminates “a” and “b” in free torsion, the layer of elements representing each ply was given a material coordinate system that was aligned with the fibres present within that ply, in much the same way that laminates “f” and “g” were modelled. This technique ensured that all coupling phenomena would be properly represented. To model the behaviour of laminates “a” and “b” in pure torsion, the material in each ply was modelled using a global orthotropic material model aligned with the global laminate x-y-z coordinate system, and given mechanical properties derived directly from the relevant terms of the $\bar{\mathbf{Q}}_{\mathbf{k}}$ stiffness matrix of that ply within the global laminate x-y-z coordinate system (see Section 1.2.7). This modelling technique was used to suppress all coupling phenomena and ensure a state of pure torsion.

Torsion was imposed upon each of these FE models by minimally constraining the mid-plane nodes at three of the four corners bounding each virtual specimen, and stipulating a vertical (z direction) translation of the node located at the mid-plane of the fourth corner. Torsion moments were then calculated from the reaction forces at each of these four nodes (see Figure 3.11). Torsional rotation angles were then calculated from the measured nodal displacements of four mid-plane nodes located at the corners of the aforementioned 30 mm long gauge region near the mid-span of each virtual specimen. Finally, the torsional stiffness of each virtual specimen was back-calculated from the aforementioned FE output data using the following equation:

$$C_{FE} = \frac{T_{SV}\, L_g}{\phi_g} \tag{3.80}$$

where T_{SV} is the calculated torque, L_g is the length of the torsional gauge region (30 mm for all virtual FE specimens), and ϕ_g is the angle of rotation observed over this torsional gauge length. Although not every possible combination of laminate architectures, geometric aspect ratios, and loading conditions (free torsion versus pure torsion) could be modelled using the available resources (limited computing time and power), the majority of these scenarios were tested.

Results of the Validation Study

Table 3.3 compares the FE results with the present analytical method for the 30 mm wide specimens tested in pure torsion:

Table 3.3: Comparison between analytical and FE results for 30 mm wide specimens tested in pure torsion. Note that the tabulated % difference values were calculated as $100\left(C_{lamThickPT} - C_{FE}\right)/C_{FE}$.

Laminate	**Width of specimen** b **(mm)**	**Loading**	**Analytical Torsional Stiffness** $C_{lamThickPT}$ **(GPa mm^4)**	**FE Torsional Stiffness** C_{FE} **(GPa mm^4)**	**% Difference**
a	30	Pure Torsion	90409	91021	-0.672
b	30	Pure Torsion	72472	72952	-0.657
c	30	Pure Torsion	59603	59990	-0.644
d	30	Pure Torsion	16391	16303	0.538
e	30	Pure Torsion	76262	76674	-0.537

Table 3.4 compares the FE results with the present analytical method for the 45 mm wide specimens tested in pure torsion:

Table 3.4: Comparison between analytical and FE results for 45 mm wide specimens tested in pure torsion. Note that the tabulated % difference values were calculated as $100\left(C_{lamThickPT} - C_{FE}\right)/C_{FE}$.

Laminate	**Width of specimen** b **(mm)**	**Loading**	**Analytical Torsional Stiffness** $C_{lamThickPT}$ **(GPa mm^4)**	**FE Torsional Stiffness** C_{FE} **(GPa mm^4)**	**% Difference**
a	45	Pure Torsion	155178	155654	-0.306
b	45	Pure Torsion	139865	140252	-0.276
c	45	Pure Torsion	104549	104331	0.209
d	45	Pure Torsion	25424	25202	0.881
e	45	Pure Torsion	153248	153539	-0.190

Table 3.5 compares the FE results with the present analytical method for the 30 mm wide specimens tested in free torsion:

Table 3.5: Comparison between analytical and FE results for 30 mm wide specimens tested in free torsion. Note that the tabulated % difference values were calculated as $100\left(C_{lamThickFT} - C_{FE}\right)/C_{FE}$.

Laminate	**Width of specimen** b **(mm)**	**Loading**	**Analytical Torsional Stiffness** $C_{lamThickFT}$ **(GPa mm^4)**	**FE Torsional Stiffness** C_{FE} **(GPa mm^4)**	**% Difference**
c	30	Free Torsion	59603	59990	-0.644
d	30	Free Torsion	16391	16303	0.538
e	30	Free Torsion	76262	76674	-0.537
f	30	Free Torsion	38680	38224	1.192
g	30	Free Torsion	69822	70591	-1.089

Table 3.6 compares the FE results with the present analytical method for the 45 mm wide specimens tested in free torsion:

Table 3.6: Comparison between analytical and FE results for 45 mm wide specimens tested in free torsion. Note that the tabulated % difference values were calculated as $100\left(C_{lamThickFT} - C_{FE}\right)/C_{FE}$.

Laminate	**Width of specimen** b **(mm)**	**Loading**	**Analytical Torsional Stiffness** $C_{lamThickFT}$ **(GPa mm^4)**	**FE Torsional Stiffness** C_{FE} **(GPa mm^4)**	**% Difference**
a	45	Free Torsion	155043	155020	0.015
b	45	Free Torsion	139740	139762	-0.016
c	45	Free Torsion	104549	104331	0.209
d	45	Free Torsion	25424	25202	0.881
e	45	Free Torsion	153248	153539	-0.190
f	45	Free Torsion	62772	61957	1.315
g	45	Free Torsion	112961	113580	-0.545

Figure 3.12 summarizes the results of the aforementioned computational validation by plotting the torsional stiffness values calculated using the present analytical method ($C_{lamThickPT}$ or

$C_{lamThickFT}$) against the relevant torsional stiffness values calculated from the FE analyses (C_{FE}) for each of the 22 test cases. Hypothetically, if every one of these data points exhibited perfect correlation (zero discrepancy between the results of the present analytical method and the FE results), then all of the data points would be scattered along a diagonal line having a 1:1 slope. For the convenience of the reader, this "line of zero discrepancy" has been included in Figure 3.12; any data point that falls directly on this line represents a case of perfect correlation between the present analytical method and the relevant FE analysis.

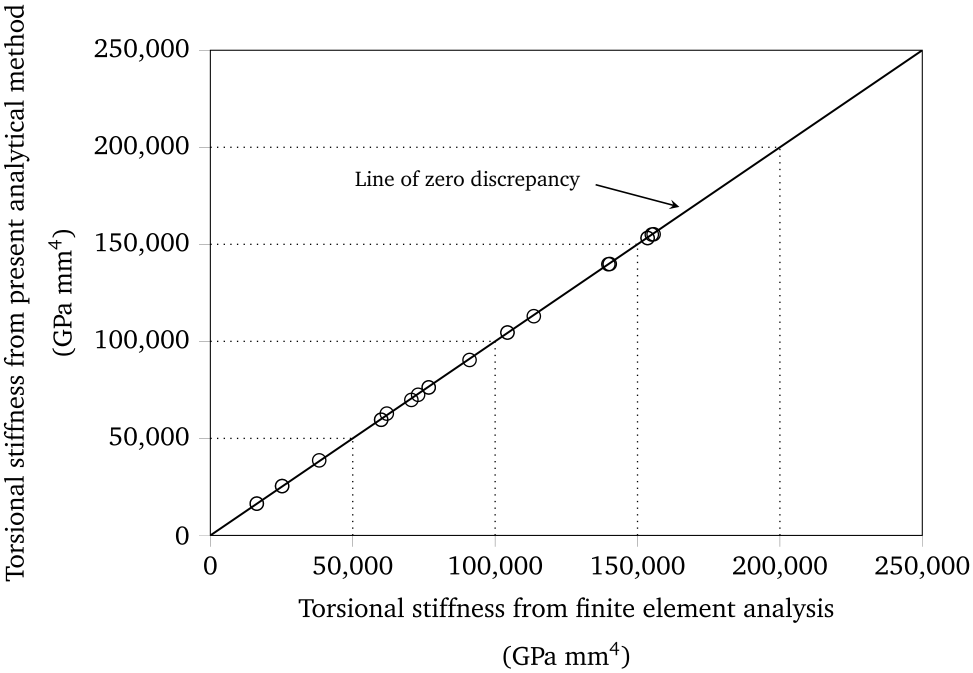

Figure 3.12: Comparison between torsional stiffness values calculated using the present analytical method ($C_{lamThickPT}$ or $C_{lamThickFT}$) and the relevant torsional stiffness values calculated from the FE analyses (C_{FE})

Figure 3.13 illustrates the lack of analytical fidelity afforded by conventional CLPT based analytical methods by plotting the torsional stiffness values calculated using conventional CLPT based analytical methods (C_{lamPT} or C_{lamFT}) against the relevant torsional stiffness values calculated from the FE analyses (C_{FE}) for each of the 22 test cases. As such, Figure 3.13 is similar to Figure 3.12, but has been modified to neglect the improvements in analytical fidelity that would have been afforded by the inclusion of $\aleph_{effPT}$ or $\aleph_{effFT}$ in equations (3.55) or (3.54), respectively.

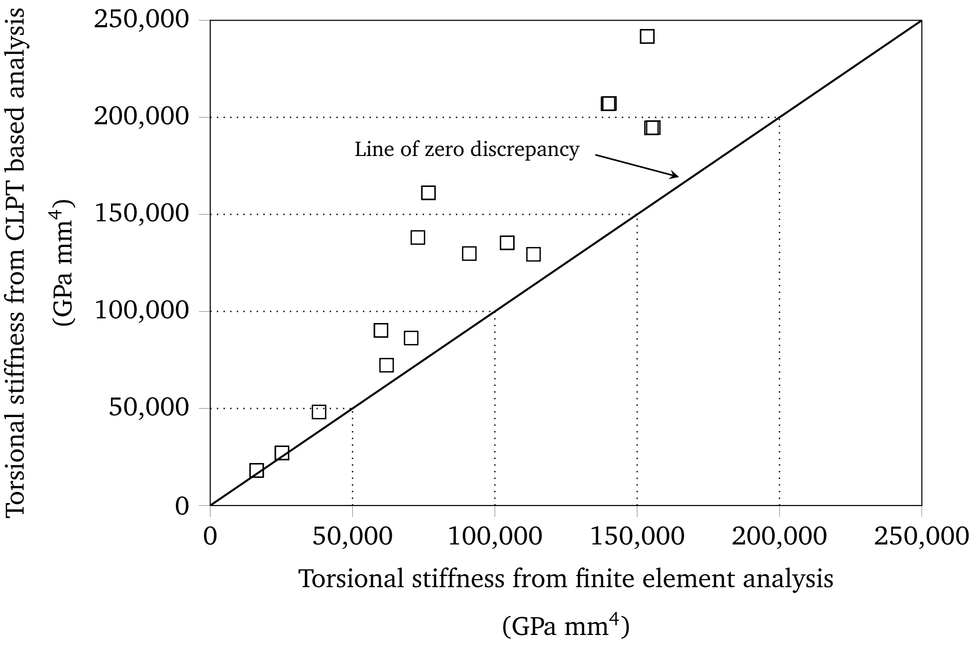

Figure 3.13: Comparison between torsional stiffness values calculated using conventional CLPT based analytical methods (C_{lamPT} or C_{lamFT}) and the relevant torsional stiffness values calculated from the FE analyses (C_{FE})

Convergence Study for Finite Element Analyses

Although the aforementioned computational validation appears to have conclusively illustrated the accuracy of the present torsional analysis methodology, it is prudent to confirm that the finite element analyses used for this validation were conducted in a reliable manner. Ordinarily, convergence of FEA computational models is checked by beginning with a relatively coarse finite element (FE) mesh of the structure of interest, and then iteratively repeating the same structural analysis using increasingly refined (fine) FE meshes; once it has been observed that two successive iterations yield extremely similar structural responses, the engineer may conclude that a sufficiently refined FE mesh has been created. Such a convergence study is typically carried out prior to proceeding with a comprehensive validation program. Unfortunately, the very nature of laminated plates presents unique challenges when carrying out a conventional convergence study. In order to capture the unique mechanical properties of each lamina (ply) within the laminate, it was necessary to model each lamina (ply) using a discrete layer of solid elements; this dictated that the through-thickness dimension of each element was quite small (0.4 mm) relative to the overall thickness of the laminated plate (7 mm). The other two dimensions of each element were limited in the interest of maintaining acceptable element aspect ratios (the longest element dimension was 1.5 mm, measured parallel to the axis of the applied uniaxial torsion loading), which resulted in a relatively large number of elements.

Ultimately, the FE mesh that was used for the aforementioned validation study contained 57600 elements and 67758 nodes, with three degrees of freedom per node. Each analysis was carried out using a DELL™ Precision™ T3500 computer that had 12 GB of RAM, an Intel® Xeon® W3540 quadruple-core processor running at 2.93 GHz per core, a math coprocessor, and a Red Hat® Linux® operating system; this resulted in typical computing times of approximately 40 minutes per analysis. While it would not be possible to increase the size of each element due to the aforementioned geometric limitations, it might have been possible to use more than one layer of solid elements within the thickness of each lamina (ply); however, doing so would have dramatically increased the number of degrees of freedom of the model, thus severely increasing computing time. While 40 minutes is not an unreasonable amount of computing time for high fidelity FE analyses, the present validation program necessitated the analysis of 22 unique scenarios, which would each require approximately 40 minutes of computing time. As such, it was decided that it would have been impractical to deviate from the aforementioned FE mesh geometry.

It became evident that the accuracy of these FE analyses was heavily dependent upon the length of the virtual specimens (parallel to the axis of the applied uniaxial torsion loading) used for this validation study. Specifically, in the vicinity of the transverse loads that were applied to generate a state of uniaxial torsion (near both ends of each virtual specimen), it was observed that the laminated plates did not respond in a uniform fashion that was consistent with Saint-Venant's torsion theory. As such, while it was impractical to deviate from the already refined FE mesh that was used for the computational validation study, it was decided that a geometric convergence study should be carried out in order to ascertain that each virtual specimen was sufficiently long (parallel to the axis of the applied uniaxial torsion loading) to ensure that accurate torsional data could be obtained from within the 30 mm long torsional gauge region located near the mid-span of each virtual specimen. In order to ascertain that a state of Saint-Venant uniaxial torsion exists throughout the entire torsional gauge region, it is useful to verify that the cross-sectional distribution of strain energy is constant over the entire length (x direction) of said torsional gauge region. Von Mises stresses are proportional to strain energy, and can therefore be used for the aforementioned assessment. Figure 3.14 illustrates the equivalent von Mises stress distribution within the top lamina (ply) of the 45 mm wide virtual specimen comprising laminate "e".

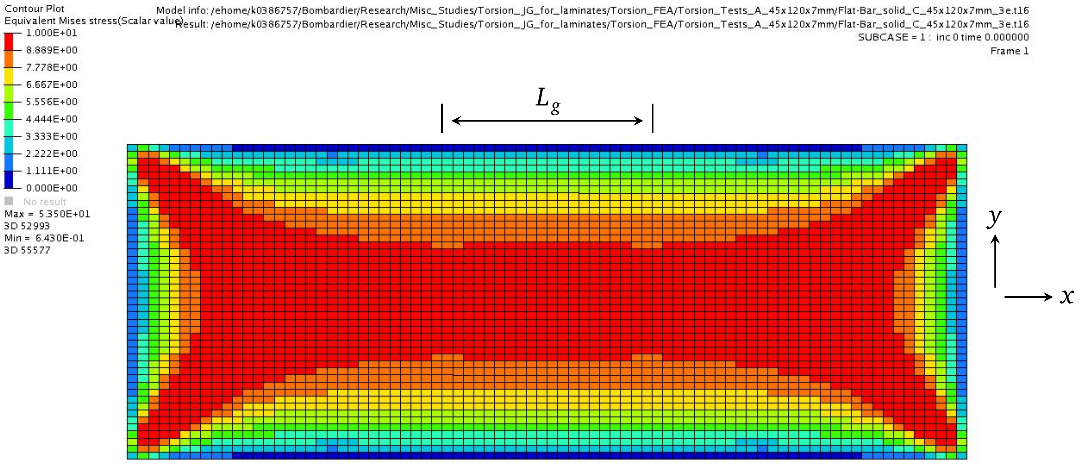

Figure 3.14: Equivalent von Mises stress distribution within the top lamina (ply) of the virtual specimen comprising laminate "e", and having a width of 45 mm and a length of 120 mm. Note that L_g represents the length of the torsional gauge region, which in this particular case has a length of 30 mm.

It is evident from Figure 3.14 that the von Mises stress distribution over the width (y direction) of this virtual specimen is relatively constant over the 30 mm length of its torsional gauge region L_g, but varies dramatically closer to the ends of this virtual specimen (where transverse loads were applied to generate a state of uniaxial torsion). As such, it is likely that a state of pure Saint-Venant uniaxial torsion exists within the torsional gauge region of this virtual specimen; hence, it is not surprising that good correlation was found between the present analytical method and this FE analysis (see results for Laminate "e" in Tables 3.4 and 3.6).

While the aforementioned preliminary assessment of the von Mises stress distribution does help to support the validity of the FE analyses, it remains to be conclusively demonstrated that the virtual specimens were sufficiently long that, within their torsional gauge regions, they were behaving as infinitely long torsion members in accordance with Saint-Venant's torsion principal. As such, a geometric convergence study was carried out to ensure that the behaviour of a virtual specimen within its torsional gauge region is insensitive to a change in the length of the specimen outside of its torsional gauge region, thus demonstrating that a state of Saint-Venant uniaxial torsion did, in fact, exist within the torsional gauge region.

The virtual specimen that was selected for this convergence study was that which had a width b of 45 mm, and comprised laminate "e". The FE mesh for this virtual specimen was scaled along its longitudinal x axis to create five additional FE meshes of varying lengths L_{total}: 64 mm, 108 mm, 114 mm, 126 mm, and 132 mm. In some cases, it was necessary to increase or decrease the mesh density along the x axis in order to ensure that the element aspect ratio was not changed significantly.

Care was also taken to ensure that the length of the torsional gauge region L_g remained similar to the 30 mm length used in the validation cases. Table 3.7 summarizes the geometry and torsional stiffness observed from each of the virtual specimens utilized in this convergence study.

Table 3.7: Geometries and torsional stiffnesses observed in torsional convergence study of the virtual specimen comprising laminate “e” and having a width b of 45 mm. Note that data pertaining to the specimen used for validation purposes (L_{total} = 120 mm) is written here in bold font.

Total length L_{total} **(mm)**	**Length of torsional gauge region** L_g **(mm)**	**Length of each end beyond torsional gauge region** $\frac{L_{total}-L_g}{2}$ **(mm)**	**FE Torsional stiffness** C_{FE} **(GPa mm^4)**
64	32	16	164300
108	27	40.5	154343
114	28.5	42.75	153860
120	**30**	**45**	**153539**
126	31.5	47.25	153342
132	33	49.5	153235

In order to more directly assess the validity of the FE mesh used for the validation study, it is useful to calculate the ratio between the structural responses observed from of each of the modified FE meshes and the structural response observed from the mesh that was ultimately used for the validation study. As such, Figure 3.15 includes a plot of the torsional stiffness values C_{FE} obtained from each of the modified FE meshes created for the convergence study, normalized with respect to the C_{FE} value obtained from the FE mesh that was ultimately used for the validation study (L_{total} = 120 mm & L_g = 30 mm).

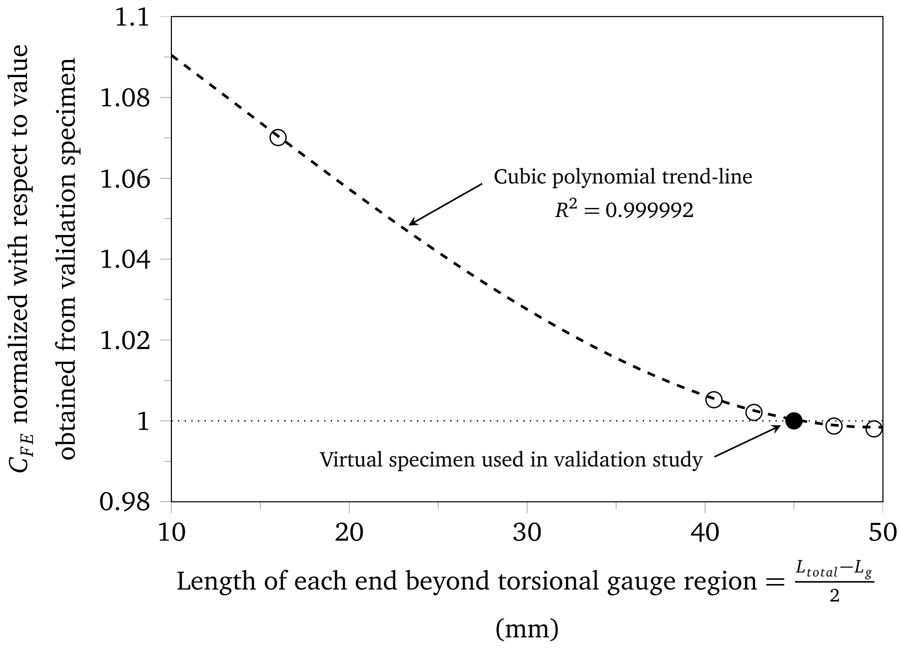

Figure 3.15: Convergence of torsional stiffness values C_{FE} as virtual specimen length is varied.

It is evident from Figure 3.15 that the FE mesh that was used for the validation study is very near convergence. Judging by the slope of the cubic polynomial trend-line that is included in Figure 3.15, it appears as though the trend has essentially converged upon reaching the final data point of the plot (slope of -3.698E-5, which is very nearly zero). The torsional stiffness value C_{FE} measured from the FE mesh represented by this final data point ($L_{total} = 132$ mm & $L_g = 33$ mm) is only 0.198% lower that that which was measured from the FE mesh that was ultimately used for the validation study ($L_{total} = 120$ mm & $L_g = 30$ mm). As such, it may be concluded that the FE mesh that was selected for the aforementioned validation study is acceptable for the purposes of approximating Stain-Venant uniaxial torsion behaviour within the torsional gauge region of each virtual specimen.

It is worth noting that the aforementioned -0.198% discrepancy observed at the final data point of the convergence study is very similar to the -0.190% discrepancy that was noted between the torsional stiffness calculated using the present analytical model ($C_{lamThickPT}$ and/or $C_{lamThickFT}$) and that which was observed during the validation study C_{FE} (see results for Laminate "e" in Tables 3.4 and 3.6). In fact, there is only a 0.008% difference between the torsional stiffness value calculated using the present analytical model ($C_{lamThickPT}$ and/or $C_{lamThickFT}$) and that which was observed from the FE analysis that was used for the final data point of the convergence study ($L_{total} = 132$ mm & $L_g = 33$ mm). This substantiates the notion that any further refinement or lengthening of the FE mesh that was used for the validation study would only serve to improve upon the already acceptable validation that was demonstrated in Figure 3.12, and Tables 3.3, 3.4, 3.5, and 3.6.

In addition to the previous discussions regarding convergence and FE mesh sensitivity, it is also worth noting that all 22 of the FE analyses that were used to validate the present torsion model (see Tables 3.3, 3.4, 3.5, and 3.6) exhibited excellent energy balance characteristics. In fact, within the scope of the output precision of the MARC® FE solver that was used (six significant figures of precision for both external work and internal strain energy), every one of these 22 FE simulations exhibited exact equality of external work and internal strain energy. This correlation between external work and internal strain energy helps to confirm that no numerical anomalies or excessive round-off errors were generated during the FE solution.

3.11.7 Discussion

The previous section on computational validation (Section 3.11.6) has illustrated the accuracy and versatility of the present analytical model. In addition to the accuracy of its torsional stiffness predictions, the present methodology employs intermediate steps which can help to illustrate the severity of the through-thickness shear effects in a given laminated plate, and can help the engineer to gauge the importance of employing analytical techniques that are beyond the complexity of a simple planar CLPT based analysis. Table 3.8 shows the calculated values of $\sqrt{\kappa_{PT}}$ and $\sqrt{\kappa_{FT}}$ for each of the laminates discussed in Section 3.11.6, as well as the calculated values of $\aleph_{effPT}$ and $\aleph_{effFT}$ for each of these laminates when a laminate width b of either 30 mm or 45 mm is used.

Table 3.8: Calculated values of $\sqrt{\kappa_{PT}}$, $\sqrt{\kappa_{FT}}$, $\aleph_{effPT}$, and $\aleph_{effFT}$ for each laminate

Laminate	$\sqrt{\kappa_{PT}}$	$\sqrt{\kappa_{FT}}$	$\aleph_{effPT}$ $b = 30$**mm**	$\aleph_{effFT}$ $b = 30$**mm**	$\aleph_{effPT}$ $b = 45$**mm**	$\aleph_{effFT}$ $b = 45$**mm**
a	2.0750	2.0756	0.6964	0.6963	0.7968	0.7968
b	3.3347	3.3362	0.5248	0.5246	0.6752	0.6750
c	2.3270	2.3270	0.6604	0.6604	0.7723	0.7723
d	0.6316	0.6316	0.9072	0.9072	0.9381	0.9381
e	3.7718	3.7718	0.4733	0.4733	0.6340	0.6340
f	3.3728	1.3442	0.5200	0.8026	0.6716	0.8683
g	1.4921	1.2996	0.7809	0.8091	0.8538	0.8727

It is evident from Table 3.8 that laminate “e” exhibits the highest values of $\sqrt{\kappa_{PT}}$ and $\sqrt{\kappa_{FT}}$, which therefore yields the lowest values of $\aleph_{effPT}$ and $\aleph_{effFT}$. This is not surprising since its composition of entirely ±45° CFRP plies yields relatively high in-plane x-y shear moduli in conjunction with relatively low through-thickness x-z shear moduli. Also, because laminate “e” was modelled as having a very large number of thin ±45° CFRP plies, it behaves as though it is balanced, symmetric, and specially orthotropic; hence, its values of $\sqrt{\kappa_{PT}}$ and $\sqrt{\kappa_{FT}}$ are identical. Laminate “d” has a through-thickness distribution of plies arranged such that its core material has a very high in-plane x-y shear modulus in comparison with its skin material; this causes laminate “d” to behave in torsion as though it has a much higher width-to-thickness aspect ratio than its physical geometry would suggest, which is reflected by its very low values of $\sqrt{\kappa_{PT}}$ and $\sqrt{\kappa_{FT}}$. Therefore, in the context of through-thickness shear effects, laminate “d” behaves as though it is not as thick as it appears. Laminates “f” and “g” both feature un-symmetric stacking sequences; this causes discrepancies in their responses to pure torsion and free torsion, which is reflected by their dissimilar values of $\sqrt{\kappa_{PT}}$ and $\sqrt{\kappa_{FT}}$. Similarly, laminates “a” and “b” both exhibit slightly dissimilar values of $\sqrt{\kappa_{PT}}$ and $\sqrt{\kappa_{FT}}$, which is due to the bending-twisting coupling that is inherent from their balanced symmetric laminate architectures. Conversely, laminates “c”, “d”, and “e” all feature specially orthotropic laminates that are completely free from any torsional coupling phenomena; hence, these laminates each exhibit identical values of $\sqrt{\kappa_{PT}}$ and $\sqrt{\kappa_{FT}}$.

The importance of accounting for through-thickness shear effects is made most evident when examining laminate “e”, which exhibits $\sqrt{\kappa_{PT}}$ and $\sqrt{\kappa_{FT}}$ values that are both equal to 3.7718. In the case of the rectangular plate having a width b of 30 mm, the geometric width-to-thickness aspect ratio η_{geom} is equal to 4.2857; however, the relatively high values of $\sqrt{\kappa_{PT}}$ and $\sqrt{\kappa_{FT}}$ for laminated “e” dictate effective width-to-thickness aspect ratios η_{effPT} and η_{effFT} of only 1.1363 (for both pure torsion and free torsion), thus yielding $\aleph_{effPT}$ and $\aleph_{effFT}$ values of only 0.4733 (for both pure torsion and free torsion). In this particular case, the use of conventional CLPT based analysis techniques (ignoring through-thickness shear effects) would tend to over-predict torsional stiffness by 111.30%. In fairness, this particular example utilized a geometric width-to-thickness aspect ratio that is considerably less than what would typically be considered conducive for the use of CLPT (a width-to-thickness aspect ratio of 10 is often considered to be the practical lower limit for the use of Kirchhoff-Love thin plate assumptions). However, if a rectangular plate were to be fabricated using laminate “e” with a true geometric width-to-thickness aspect ratio of $b/h = 10$, this laminated plate would behave as though it had an effective width-to-thickness aspect ratio of only 2.6513. As such, even when a geometric width-to-thickness aspect ratio of 10 is employed, the use of conventional CLPT based analysis techniques (ignoring through-thickness shear effects) for laminate “e” would still tend to over-predict torsional stiffness by 31.10%. Figure 3.16 illustrates the amount by which analysis techniques that ignore through-thickness shear effects (Kirchhoff-Love thin plate assumptions) will tend to over-predict torsional stiffness as a function of geometric width-to-thickness aspect ratio; it demonstrates this for the case of laminate "e", as well as for the case of a homogeneous isotropic rectangular plate.

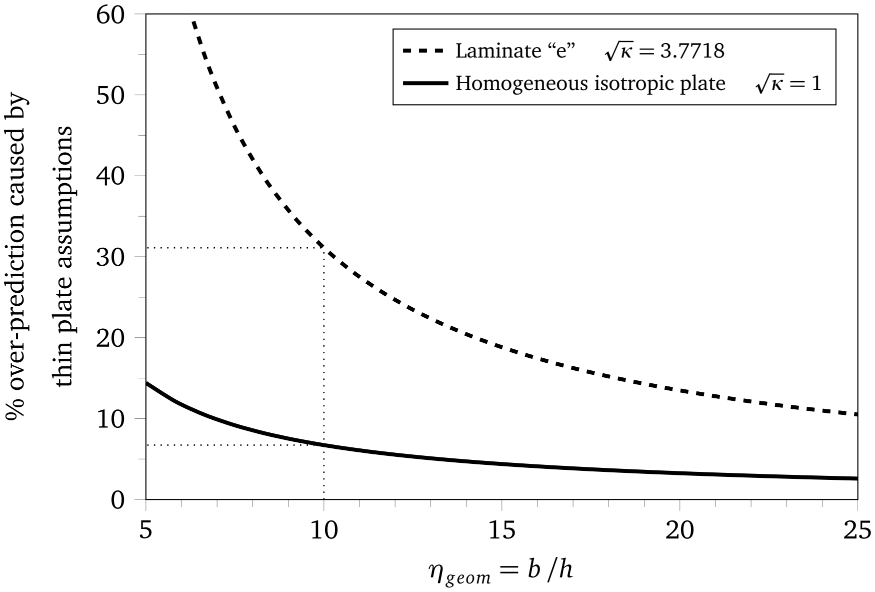

Figure 3.16: Percent over-prediction of torsional stiffness caused by ignoring through-thickness shear effects, as a function of geometric width-to-thickness aspect ratio ($\sqrt{\kappa}$ is defined in Equation (3.73))

3.11.8 Conclusions Regarding the Present Formulation for Torsional Stiffness

An analytical method was developed for the calculation of the torsional stiffness of thick laminated plates, and was validated through comparison with the results of a multitude of FE analyses. The following conclusions have been drawn:

1. Of the 22 test cases that were explored, the largest discrepancy between the FE results and the results of the present analytical method was 1.315%.

2. The present analytical method necessitates the calculation of intermediate coefficients $\sqrt{\kappa_{PT}}$ and $\sqrt{\kappa_{FT}}$, which may be used to communicate meaningful information regarding the effective width-to-thickness aspect ratio of a laminated plate, as well as the amount by which conventional Classical Laminated Plate Theory (CLPT) based analysis techniques (ignoring through-thickness shear effects) will tend to over predict the torsional stiffness of a given laminated plate.

3. The values of $\sqrt{\kappa_{PT}}$ and $\sqrt{\kappa_{FT}}$ may be calculated for a laminate without having any information regarding the geometric width-to-thickness aspect ratio of the finished product. As such, it would be convenient, for the purpose of practical applications, to keep tabulated values of $\sqrt{\kappa_{PT}}$ and $\sqrt{\kappa_{FT}}$ for laminates that are frequently used in design.

4. The geometric width-to-thickness aspect ratio η_{geom} is not directly relevant to determining the validity of Kirchhoff-Love thin plate assumptions; on the contrary, the effective width-to-thickness aspect ratios η_{effPT} and η_{effFT} should be used for this determination.

5. The present analytical model can easily be integrated into an existing computer algorithm for CLPT, or any spreadsheet based CLPT analyses.

6. Use of the present analytical method shall be limited to the analyses of laminates having effective width-to-thickness aspect ratios η_{effPT} and η_{effFT} that are greater than unity. It is likely that additional limitations exist for this analytical method; as such, it is recommended that additional research is carried out in order to further validate this work, and quantify its limitations.

3.11.9 Implementation into the Present Analytical Method for Built-Up Thin-Walled Open Sections

The aforementioned derivation for the torsional stiffness of thick laminated plates (Sections 3.11.1 through 3.11.8) was focused on the analysis of a single planar laminate undergoing torsion. Some adjustments must be made to this analytical model in order to apply it to built-up thin-walled open sections comprising multiple laminated plates. Specifically, provisions must be made in order to differentiate between legs of the section that have fewer than two free edges that are parallel to the axis of the applied torsional loading.

The torsional stiffness model that was derived in Sections 3.11.1 through 3.11.8 was dependent upon the assumption that both of the edges of the laminated plate that are parallel to the axis of the applied torsional loading may be considered as free edges; hence, it was assumed that these edges are not attached to any adjacent structure, and are not subjected to any applied tractions or moments. This assumption implies that all x-y shear stresses within the plane of the laminate must tend to zero at these free edges in order to satisfy equilibrium requirements. Conversely, in the case of built-up thin-walled open sections comprising multiple laminated plates, each leg of the section is in direct contact with at least one adjacent leg; hence, the x-y shear stresses within the plane of each leg will not necessarily tend to zero at these intersections. Figures 3.17, 3.18, and 3.19 illustrate the shear stress distribution over the cross-section of plates subjected to uniaxial torsion, for the case of plates that have two, one, and zero free edges, respectively.

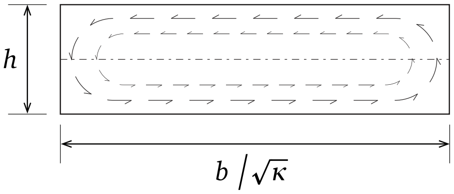

Figure 3.17: Shear stress distribution over the cross-section of a plate subjected to uniaxial torsion, for the case of a plate that has two free edges.

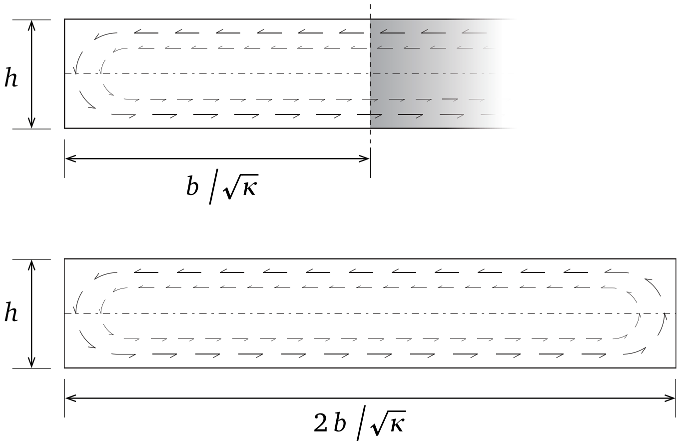

Figure 3.18: Shear stress distribution over the cross-section of a plate subjected to uniaxial torsion, for the case of a plate that has one free edge.

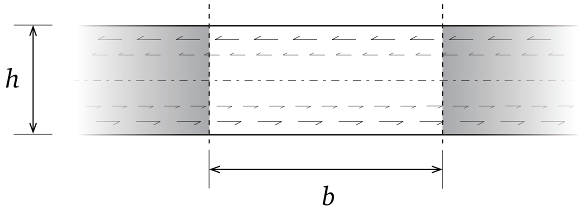

Figure 3.19: Shear stress distribution over the cross-section of a plate subjected to uniaxial torsion, for the case of a plate that has no free edges.

In the case of a section wall (leg) that has two free edges that are parallel to the axis of the applied torsional loading, torsional stiffness can simply be calculated by directly applying the procedure outlined in Section 3.11.5.

In the case of a section wall (leg) that has only one free edge that is parallel to the axis of the applied torsional loading, the cross-sectional shear stress distribution is similar to half of the shear stress distribution that would be exhibited by a similar plate having two free edges and double the effective width-to-thickness aspect ratio (η_{effPT} or η_{effFT}) of the plate of interest (see Figure 3.18). As such, in this case, torsional stiffness can be calculated using the following procedure:

1. Double the effective aspect ratio (η_{effPT} or η_{effFT}) calculated in equation (3.74).
2. Substitute this modified effective aspect ratio into equation (3.75) to calculate the torsional stiffness correction factor ($\aleph_{effPT}$ or $\aleph_{effFT}$).
3. Calculate the torsional stiffness of the section wall (leg) by substituting the aforementioned torsional stiffness correction factor into equation (3.78) and/or (3.79), while being sure to use the actual width b of the leg in this calculation.

In the case of a section wall (leg) that has no free edges that are parallel to the axis of the applied torsional loading, it is reasonable to assume that all shear stresses are parallel to the mid-plane of the section wall (see Figure 3.19). As such, in this case, torsional stiffness can simply be calculated using equation (3.54) or (3.55).

It is worth noting that free torsional stiffness is of far greater importance than pure torsional stiffness for most practical purposes. As such, any subsequent mention of torsional stiffness in this dissertation will refer to free torsional stiffness.

3.12 Warping Stiffness

3.12.1 Conventional Vlasov Primary Warping

The presence of warping restraints at the ends of a member undergoing twisting deformations will generate longitudinal stresses, which will tend to increase the apparent torsional stiffness of the structural member. This combination of torsion and warping is often referred to as "non-uniform torsion" or "restrained torsion", since torsion and warping deformations are not constant over the length of a member when warping restraints are employed. The engineering principals used to calculate the warping stiffness of thin-walled structural members were developed by Vlasov [85], and the derivation of the relevant formulae [78] have been reproduced here for the convenience of the reader, and adapted to the context of members built up of legs comprising composite laminates.

It is useful to denote s as a coordinate along a curvilinear path defined by the mid-plane of the system of thin-shell legs that make up the cross-section of the structural member of interest. This coordinate shall begin with a value of zero at one of the free edges of the section. The term ω shall be denoted as the warping displacements generated by pure torsion, assuming that the member possesses zero warping stiffness. If a member is to be represented by an infinite number of infinitesimally thin fibres parallel to the longitudinal axis of the member, then any rotation of one end of the member about its shear-centre will require some or all of these fibres to become inclined relative to the longitudinal axis of the member; this inclination in turn leads to longitudinal displacements. These longitudinal displacements are referred to as warping displacements, and are ultimately responsible for the increase in torsional stiffness exhibited by a member whose ends have been restrained against such longitudinal (warping) displacements.

The term ω_s shall be defined as twice the sectorial area swept by a radial line that spans between the shear-centre of the section and the mid-plane of the section walls (legs of the section), and migrates along the mid-planes of these section walls from one of the free edges of the section to the s coordinate of interest (see Figure 3.20). As such, the value of ω_s can be evaluated as follows:

$$\omega_s = \int_0^s r_{perp\,Os}\, ds \tag{3.81}$$

where $r_{perp\,Os}$ is the moment arm of the s coordinate on the mid-plane of the relevant leg of the cross-section about the shear-centre (see Section 3.8) of the entire section, measured perpendicular to the surface of the relevant leg at coordinate s (see Figure 3.20). It should be noted that this sectorial area ω_s is taken as positive when the angular propagation of the sweeping radial line occurs in the counter-clockwise direction. Figure 3.20 employs the example of an S-shaped cross-sectional geometry to illustrate the aforementioned geometric dimensions.

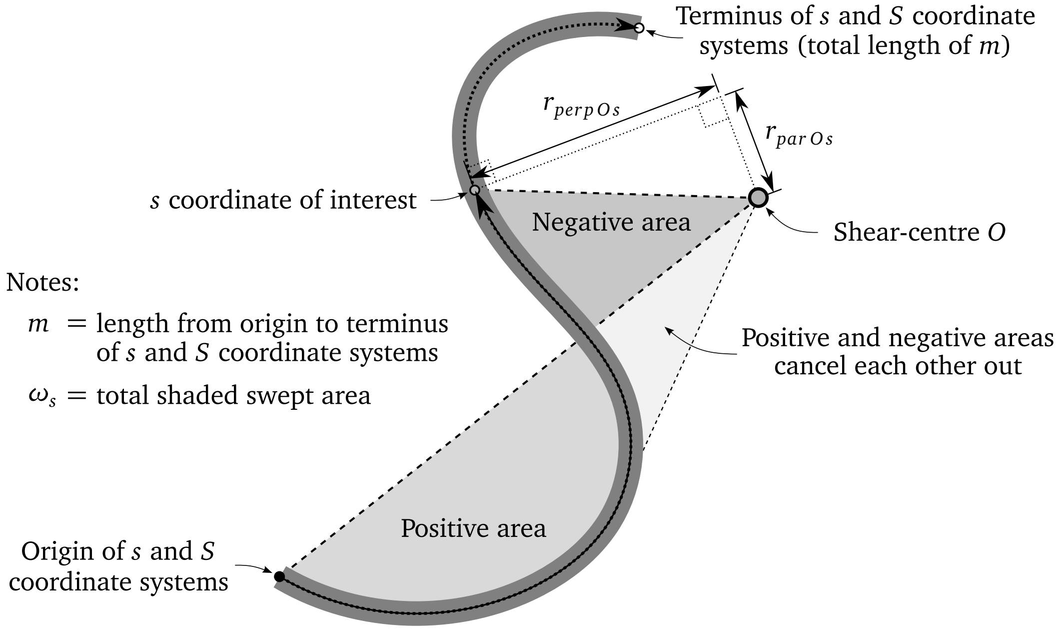

Figure 3.20: Cross-sectional drawing of an S-section member, showing geometric dimensions relevant to the calculation of various warping coefficients, such as ω_s, $\bar{\omega}_s$, and C_{1B2}.

It is now possible to calculate the average value of ω_s over the cross-section of the member, as follows:

$$\bar{\omega}_s = \frac{1}{m} \int_0^m \omega_s \, ds \tag{3.82}$$

where m is the entire length over which the coordinate s is defined (scalar displacement between origin and terminus of s coordinate system, as shown in Figure 3.20). It is now possible to calculate the warping displacement at any point on the cross-section as follows:

$$\omega = \frac{d\phi}{dX} \left(\bar{\omega}_s - \omega_s \right) \tag{3.83}$$

where ϕ is the angle of rotation of the cross-section about its shear-centre. Since ω represents a longitudinal displacement, equation (3.83) can be differentiated with respect to the longitudinal X coordinate to find the normal strain caused by warping, which can then be multiplied by the local longitudinal Young's elastic modulus to obtain the normal stress caused by warping, as follows:

$$\sigma_{xx\,s} = \frac{d^2\phi}{dX^2} \left(\bar{\omega}_s - \omega_s \right) E_{xx\,s} \tag{3.84}$$

where $E_{xx\,s}$ is the longitudinal elastic modulus of the relevant leg of the cross-section at coordinate s (see equation (3.6) in Section 3.5). In the context of a stringer made up of legs that each comprise unique composite laminates, the value of E_{xxs} in equation (3.84) shall be taken as $1\big/\big(h\,a_{11}\big)$, where h is the total thickness of the laminate, and a_{11} is taken from the laminate extensional compliance matrix **a** of the relevant leg, calculated from Classical Laminated Plate Theory. It is important to note that the value of σ_{xxs} here represents the average composite normal stress over the entire thickness of the laminate at position s, and is not necessarily indicative of the normal stress present within any one of the plies of the laminate. It can be shown that the rate of change of σ_{xxs} with respect to the s coordinate is equal to the rate of change of the average x-y shear stress within the plane of the laminate at position s with respect to the X coordinate [78]. As such, the x-y shear flow within the plane of the laminate at position S (along the s coordinate system) can be calculated as follows:

$$q_S = -\frac{d^3\phi}{dX^3}\int_0^S \left(\bar{\omega}_s - \omega_s\right) E_{xxs} h_s \, ds \tag{3.85}$$

where h_s is the total thickness of the laminate at position s. In order to evaluate equation (3.85) as an indefinite integral, the integration constant shall be set such that the value of q_S tends to zero at all free edges of the cross-section. Integrating the first moment of shear flows (equation (3.85)) about the shear-centre of the section, it is possible to calculate the total torque about the longitudinal X axis caused exclusively by primary warping stresses, as follows:

$$T_{\omega 1} = -\frac{d^3\phi}{dX^3}\int_0^m \left(\bar{\omega}_s - \omega_s\right)^2 E_{xxs} h_s \, ds \tag{3.86}$$

A primary warping constant shall be defined as follows:

$$C_{1B1} = \int_0^m \left(\bar{\omega}_s - \omega_s\right)^2 E_{xxs} h_s \, ds \tag{3.87}$$

Rewriting equation (3.86) using the newly defined warping constant C_{1B1} results in a simplified expression for the primary warping moment, as follows:

$$T_{\omega 1} = -C_{1B1}\frac{d^3\phi}{dX^3} \tag{3.88}$$

3.12.2 Secondary Warping

The aforementioned primary warping moment can generally be treated as the total warping moment in the context of most structural members comprising thin shells. However, employing only primary warping moments will tend to under-predict the total warping moment in a member when the legs making up the cross-section are relatively thick, or in members having cross-sectional geometries that inherently exhibit zero or near-zero primary warping stiffness, such as T-sections or cruciform sections. In such cases, it is necessary to account for the secondary warping stiffness, which is a phenomenon that can be attributed to the out-of-plane bending stiffness of each of the legs making up an open section. As such, the secondary warping stiffness shall be defined as the integral of the second moment of out-of-plane bending stiffnesses of each leg, taken about the shear-centre of the member, as follows:

$$C_{1B2} = \int_{0}^{m} \left(\frac{dEI_{yys}}{dy} \, r_{par\,Os}^{2} \right) ds \tag{3.89}$$

where $dEI_{yys} \big/ dy$ is the local out-of-plane y-y bending stiffness per unit width dy of the relevant leg at the s coordinate of the cross-section (see equation (3.9) in Section 3.5), and $r_{par\,Os}$ is the moment arm of the s coordinate on the mid-plane of the relevant leg about the shear-centre (see Section 3.8) of the entire section, measured parallel to the surface of the relevant leg at coordinate s (see Figure 3.20). In this case, the value of $dEI_{yys} \big/ dy$ may be taken as $1 \big/ d_{11}$, where d_{11} is taken from the laminate bending compliance matrix **d** of the relevant leg, calculated from Classical Laminated Plate Theory. This secondary warping stiffness can be combined with the primary warping stiffness of the member, and the total warping moment can be calculated as follows:

$$T_{\omega} = T_{\omega 1} + T_{\omega 2} = -\left(C_{1B1} + C_{1B2} \right) \frac{d^{3}\phi}{dX^{3}} \tag{3.90}$$

where $T_{\omega 1}$ is the primary warping moment, $T_{\omega 2}$ is the secondary warping moment, and C_{1B1} is the primary warping stiffness (defined in equation (3.87) of Section 3.12.1). Equation (3.90) can be simplified by combining the primary and secondary warping stiffness terms into a single total warping stiffness term, C_{1B}, as follows:

$$T_{\omega} = -C_{1B} \frac{d^{3}\phi}{dX^{3}} \qquad \text{where:} \qquad C_{1B} = C_{1B1} + C_{1B2} \tag{3.91}$$

3.12.3 Additional Warping Compliance due to Mid-Plane In-Plane Shear Strains

Recall from equation (3.85) that the existence of non-zero warping moments depends upon the presence of shear flow within the plane of each leg of the section. By extension, it can therefore be assumed that mid-plane in-plane shear strains are present within each leg of the section, which will in turn lead to some additional torsional compliance of the entire member. In all subsequent discussions on this matter, the term “warping-shear” will refer to mid-plane in-plane shear stresses and strains that are caused by warping deformations, which generally occur during a state of restrained non-uniform torsion. In addition, the term “warping-shear compliance” will refer to shear deformations that develop within the plane of the walls (legs) of a member having a thin-walled open cross-section, due to the presence of non-trivial warping-shear strains. In structural members composed of conventional metallic engineering materials, the additional torsional compliance due to warping-shear strains can often be neglected. Conversely, structural members composed of continuous-fibre reinforced polymers often exhibit relatively low in-plane shear moduli relative to their longitudinal normal elastic moduli; therefore, it is often unreasonable to ignore the effects of warping-shear compliance in such composite structural members. While numerous methods of modelling the additional torsional compliance due to warping-shear strains have been presented in some recent publications (see Section 1.4.2), to the knowledge of the author, there is no unanimously accepted analytical method of calculating this additional compliance. As such, the author has undertaken to derive an analytical model to predict the additional torsional compliance that can be expected as a result of warping-shear strains.

It is first necessary to re-assign the angle of rotation due to conventional torsion and warping theory as ϕ_1, and assign any additional angle of rotation due to warping-shear compliance as ϕ_2. Recall from equation (3.85) that the shear flow within the plane of the laminate at position S (along the s coordinate system) can be calculated as follows:

$$q_S = \frac{d^3\phi_1}{dX^3} \int\limits_0^S \left(\bar{\omega}_s - \omega_s\right) E_{xx\,s} h_s \, ds \tag{3.92}$$

As such, the shear strain within the plane of the laminate at position S can be calculated as follows:

$$\gamma_{xy\,S} = \frac{q_S}{h_S\, G_{xy\,S}} = \frac{d^3\phi_1}{dX^3} \frac{\int_0^S \left(\bar{\omega}_s - \omega_s\right) E_{xx\,s} h_s \, ds}{h_S\, G_{xy\,S}} \tag{3.93}$$

where $G_{xy\,S}$ is the in-plane x-y shear modulus of the relevant leg of the cross-section at position S (see equation (3.8) in Section 3.5), and h_S the total thickness of the laminate at position S. In the context of a stringer made up of legs that each comprise unique composite laminates, the value of $G_{xy\,S}$ in equation (3.93) shall be taken as $1\big/\!\left(h\, a_{66}\right)$, where h is the total thickness of the laminate, and a_{66} is taken from the laminate extensional compliance matrix $\mathbf{a}$ of the relevant leg, calculated from Classical Laminated Plate Theory. It is important to note that shear flows must tend to zero at all free edges of the section, and hence, in-plane shear strains must also tend to zero at the free edges of the section. As such, the integration constants that are necessary for the evaluation of the indefinite integrals defined in equations (3.92) and (3.93) shall be set such that shear flow and shear strains tend to zero at all free edges of the section. The very presence of these shear strains indicates that there exists some total amount of shear strain energy per unit length of the structural member that is caused exclusively by warping-shear strains; this shear strain energy can be calculated as follows:

$$\mathrm{U}_{int\,xy\,ws} = \int_0^m \left[\frac{q_S^2}{2\,h_S\,G_{xy\,S}} dX \right] dS = \int_0^m \frac{\left[\frac{d^3\phi_1}{dX^3} \int_0^S \left(\bar{\omega}_s - \omega_s \right) E_{xx\,s} h_s \, ds \right]^2}{2\,h_S\,G_{xy\,S}} dX \, dS \tag{3.94}$$

The amount of external work that must be done in order to generate the aforementioned shear strain energy can be calculated as a function of the applied warping moment and some additional angle of rotation ϕ_2, as follows:

$$\mathrm{U}_{ext\,ws} = \frac{1}{2}\,T_\omega\,\frac{d\phi_2}{dX} dX = \frac{1}{2}\,C_{1B}\,\frac{d^3\phi_1}{dX^3}\,\frac{d\phi_2}{dX} dX \tag{3.95}$$

Setting external work equal to internal strain energy from equations (3.94) and (3.95), respectively, the following relationship is found:

$$\frac{d^3\phi_1}{dX^3} \int_0^m \frac{\left[\int_0^S \left(\bar{\omega}_s - \omega_s \right) E_{xx\,s} h_s \, ds \right]^2}{h_S\,G_{xy\,S}} dS = \frac{d\phi_2}{dX} C_{1B} \tag{3.96}$$

A new coefficient C_{1S} can now be introduced, which will help to simplify the aforementioned expressions, as follows:

$$C_{1S} = \int_0^m \frac{\left[\int_0^S \left(\bar{\omega}_s - \omega_s \right) E_{xx\,s} h_s \, ds \right]^2}{h_S\,G_{xy\,S}} dS \tag{3.97}$$

Rearranging equation (3.96) and substituting in the new coefficient C_{1S} defined in equation (3.97), it is now possible to express the additional torsional compliance due to warping-shear strains ϕ_2 in terms of conventionally calculated torsional rotations ϕ_1, as follows:

$$\frac{d\phi_2}{dX} = \frac{C_{1S}}{C_{1B}}\,\frac{d^3\phi_1}{dX^3} \tag{3.98}$$

Assigning a new term, C_{TS}, equation (3.98) can be rewritten as follows:

$$\frac{d\phi_2}{dX} = \frac{C_{1B}}{C_{TS}}\,\frac{d^3\phi_1}{dX^3} \qquad \text{where:} \qquad C_{TS} = \frac{C_{1B}^2}{C_{1S}} \tag{3.99}$$

Incidentally, the aforementioned derivation of the equations that define $d\phi_2\,/dX$ is nearly identical to the 2012 work of Wang, Zhao, Zhang, and Gong [89] which, given its time of publication, was likely developed prior to the completion of the presently described methodology. While this realization certainly detracts from the significance and novelty of the present author's contribution to this particular subject matter, the similarity of these independently and nearly simultaneously developed analytical models serves to substantiate the validity of both works.

3.13 Overall Response to Restrained Torsion

The total twisting moment T_{XX} imposed upon a structural member can be calculated as the sum of the Saint-Venant torque T_{SV} (see Section 3.11) and the warping moment T_{ω} (see Section 3.12), as follows:

$$T_{XX} = T_{SV} + T_{\omega} = C \frac{d\phi_1}{dX} - C_{1B} \frac{d^3\phi_1}{dX^3} \tag{3.100}$$

where C is the Saint-Venant torsional stiffness discussed in Section 3.11, and C_{1B} is the warping constant discussed in Sections 3.12.1 and 3.12.2. The total angle of twist due to all torsion and warping effects can now be expressed as follows:

$$\frac{d\phi}{dX} = \frac{d\phi_1}{dX} + \frac{d\phi_2}{dX} \tag{3.101}$$

where ϕ is the total angle of twist, ϕ_1 is the angle of twist due to conventional torsion and warping analyses (ignoring warping-shear compliance), and ϕ_2 is the additional angle of twist caused by warping-shear strains. Recall from equation (3.99) that the value of ϕ_2 can be calculated in terms of ϕ_1 as follows:

$$\frac{d\phi_2}{dX} = \frac{C_{1B}}{C_{TS}} \frac{d^3\phi_1}{dX^3} \qquad \text{where:} \qquad C_{TS} = \frac{C_{1B}^2}{C_{1S}} \tag{3.102}$$

where C_{1S} is the warping-shear compliance coefficient defined in equation (3.97) of Section 3.12.3. Ultimately, the total torsional response of a member having non-trivial warping-shear compliance can be calculated by solving the system of differential equations defined by equations (3.100), (3.101), and (3.102).

The torsional response of a member having non-trivial warping stiffness is highly dependent upon its boundary conditions. The presence of warping restraints at one or both ends of a member can greatly increase its torsional stiffness. For the case of a member that is twisted about its longitudinal axis while both ends are restrained against warping deformations (see Figure 4.19), the solution to equation (3.100) can be found as follows:

$$\phi_1(X) = \frac{T_{XX}}{C_{1B}\Gamma^3} \left[\sinh(\Gamma X) + \Gamma(L - X) - (1 + \cosh(\Gamma X)) \tanh\left(\frac{\Gamma L}{2}\right) \right] \tag{3.103}$$

where:

$$\Gamma = \sqrt{\frac{C}{C_{1B}}}$$

Therefore:

$$\phi_{1\,\text{Total}} = \frac{T_{XX}}{C_{1B}\Gamma^3} \left[\Gamma L - 2\tanh\left(\frac{\Gamma L}{2}\right) \right] \tag{3.104}$$

where L is the total twisted length of the member, T_{XX} is the twisting moment applied to the member, $\phi_1(X)$ is the angle of rotation measured at position X (ignoring warping-shear compliance), and $\phi_{1\,\text{Total}}$ is the total angle of rotation measured between the two ends of the member (ignoring warping-shear compliance). Since equation (3.104) was derived from equation (3.100), it represents only the torsional rotation that results when warping-shear compliance is neglected. The additional torsional compliance caused by warping-shear strains can be calculated by integrating equation (3.102) over the total twisted length of the member, as follows:

$$\phi_{2\,\text{Total}} = \frac{C_{1B}}{C_{TS}} \int_0^L \frac{d^3\phi_1}{dX^3}\, dX = \frac{C_{1B}}{C_{TS}} \left[\frac{d^2\phi_1}{dX^2} \right] \Bigg|_{X=0}^{X=L} \tag{3.105}$$

For the case of a member that is twisted about its longitudinal axis while both ends are restrained against warping deformations (see Figure 4.19), the second derivative of ϕ_1 with respect to X can be evaluated at position X, as follows:

$$\frac{d^2\phi_1}{dX^2}(X) = \frac{T_{XX}}{C_{1B}\,\Gamma} \left[\sinh(\Gamma X) - \cosh(\Gamma X) \tanh\left(\frac{\Gamma L}{2} \right) \right] \tag{3.106}$$

As such, for the case of a member that is twisted about its longitudinal axis while both ends are restrained against warping deformations (see Figure 4.19), equation (3.105) can be evaluated as follows:

$$\phi_{2\,\text{Total}} = 2 \frac{T_{XX}}{C_{TS}\,\Gamma} \left[\tanh\left(\frac{\Gamma L}{2} \right) \right] \tag{3.107}$$

Summing equations (3.104) and (3.107), the entire angle of twist can be found for a member that is twisted about its longitudinal axis while both ends are restrained against warping deformations (see Figure 4.19), as follows:

$$\phi_{\text{Total}} = T_{XX} \left[\frac{\Gamma L - 2\tanh\left(\frac{\Gamma L}{2}\right)}{C_{1B}\,\Gamma^3} + \frac{2\tanh\left(\frac{\Gamma L}{2}\right)}{C_{TS}\,\Gamma} \right] \tag{3.108}$$

In a manner that is similar to the aforementioned derivation, the entire angle of twist can also be found for a member that is twisted about its longitudinal axis while one end is restrained against warping deformations and the other end is completely free to warp, as follows:

$$\phi_{\text{Total}} = T_{XX} \left[\frac{\Gamma L - \tanh(\Gamma L)}{C_{1B}\,\Gamma^3} + \frac{\tanh(\Gamma L)}{C_{TS}\,\Gamma} \right] \tag{3.109}$$

In addition to the aforementioned 2012 work of Wang, Zhao, Zhang, and Gong [89], it is worth noting that a plethora of other similar works have been recently developed to predict the restrained torsional response (warping) of open sections having non-trivial warping-shear compliance (see Section 1.4.2). However, while many of these works were computationally validated using the finite element method, the present author is not aware of any published works that provide experimental validation of a similar analytical method for the prediction of the restrained torsional response (warping) of open sections having non-trivial warping-shear compliance. Chapter 4 presents an experimental program that was carried out by the author to validate the derivations presented in Sections 3.12.3 and 3.13.

3.14 Flexural Buckling

3.14.1 General

Flexural buckling is a phenomenon whereby a column becomes unstable and deflects laterally in a predominantly flexural mode as a result of an applied axial compression force. The direction of this lateral deflection is dependent upon the cross-sectional geometry of the column, and the manner in which the column is restrained at its ends and along its length. A minimally constrained column will typically exhibit its critical (lowest) flexural buckling load about its minor flexural axis; however, if such a column is braced in a manner that restricts bucking about this axis, it may be forced to buckle about an alternative axis at a higher load. As such, it is generally necessary to check the critical buckling load of a column about numerous potential buckling axes. In the following section, flexural buckling will be discussed in the context of buckling about the Y'-Y' principal axis of the column of interest, whereby lateral deflections occur in the global Z' direction. These derivations can be adapted for the analysis of flexural buckling about any other axis of the column.

Conventional Euler buckling theory is derived on the basis of the elastic stability of an axially loaded column that has experienced some infinitesimal lateral perturbation. The critical Euler buckling load of a long column about its Y'-Y' axis can be found as follows:

$$P_{cr\,Eu\,Y'Y'} = \frac{\pi^2 n^2 E_{XX} I_{Y'Y'}}{L^2} \tag{3.110}$$

where E_{XX} is the nominal longitudinal composite elastic modulus of the section (see Section 3.6.4), $I_{Y'Y'}$ is the second area moment of inertia of the section about its Y'-Y' axis (see Section 3.7), L is the total buckling length between the supported ends of the column, and n is an integer value representing the number of half-sin curves within the buckled shape of the column. Similarly, the critical Euler buckling load of a long column about its Z'-Z' axis can be found as follows:

$$P_{cr\,Eu\,Z'Z'} = \frac{\pi^2 n^2 E_{XX} I_{Z'Z'}}{L^2} \tag{3.111}$$

where $I_{Z'Z'}$ is the second area moment of inertia of the section about its Z'-Z' axis (see Section 3.7). Since Euler-Bernoulli beam theory is employed, Euler buckling ignores the effects of transverse shear deformations; hence, the relevant equilibrium equations employed in the derivation of Euler buckling focus strictly upon the relationship between axial loads, bending moments, bending stiffness, and lateral perturbation of the column. The effect that transverse shear compliance has upon the compression buckling load of a column is most pronounced when the column is relatively short in comparison with its radius of gyration. When columns are composed of conventional metallic engineering materials, short-column failure modes such as yielding and local crippling generally become prevalent prior to the exhibition of any significant transverse shear effects. As such, in many cases, the implementation of a more rigorous buckling theory that accounts for transverse shear effects would be needlessly complex.

In comparison with conventional metallic engineering materials, unidirectional continuous-fibre reinforced polymer composite materials generally exhibit extremely low ratios of transverse shear modulus to longitudinal normal elastic modulus. While the exact relationship between these moduli is highly dependent upon the type and orientation of the fibres and the type of resin matrix that is used, these FRP materials will generally exhibit far more pronounced shear effects than their metallic counterparts. As such, conventional Euler buckling theory will often significantly over-predict the elastic buckling load of columns composed of unidirectional continuous-fibre reinforced polymers. The magnitude of this over-prediction is dependent upon many factors such as composition, fibre orientation, cross-sectional geometry, and the ratio of length to radius of gyration; the most severe over-prediction would occur in the case of a short column composed of longitudinally oriented fibres that have a high elastic modulus, and a resin matrix that has a very low shear modulus. Since the severity of this over-prediction is so varied and difficult to predict, as a general rule, it is unconservative to utilize conventional Euler buckling theory for the analysis of columns composed of continuous-fibre reinforced polymers; as such, a more rigorous buckling theory that accounts for transverse shear effects should be employed for the analysis of such fibre composite columns.

3.14.2 Elastic Flexural Buckling of Straight Columns with Transverse Shear Effects

The two most commonly utilized formulations for the elastic buckling load of columns with transverse shear effects are those presented by Engesser [26][27] and Haringx [30][31]. Although these two formulations may at first appear to be paradoxically different, it has been shown [6][7] that careful application of the relevant constitutive relationships in each of these formulations will yield identical results. As such, the author has elected to employ Engesser's formulation, which is derived in the following section of this dissertation, and adapted for applications in which laminated composite materials are employed.

As illustrated in Figure 3.21, the Y'-Y' bending moment at position X along the length of a column due to an axial compression force and some infinitesimal lateral perturbation in the Z' direction can be expressed as follows:

$$M_{Y'Y'} = E_{XX}\, I_{Y'Y'}\, \frac{d\Phi_{Y'Y'}}{dX} = Pw \tag{3.112}$$

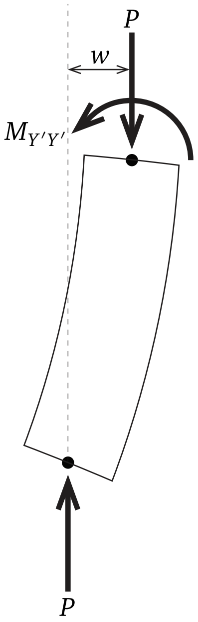

Figure 3.21: Free-body diagram illustrating the net bending moment about the Y'-Y' axis of the column as a function of $\Phi_{Y'Y'}$, P, and w.

where E_{XX} is the nominal longitudinal composite elastic modulus of the section (see Section 3.6.4), $I_{Y'Y'}$ is the second area moment of inertia of the section about its Y'-Y' axis (see Section 3.7), $\Phi_{Y'Y'}$ is the angle of rotation of the cross-section at position X about its Y'-Y' axis relative to the initial undeformed shape of the member, P is the applied axial compression force, and w is the lateral deflection of the cross-section in the Z' direction relative to the initial undeformed shape of the member. Since $\Phi_{Y'Y'}$ represents the true angle of rotation of the cross-section at position X, whereas dw/dX represents the slope of the longitudinal axis of the deformed member at position X, any difference between these values constitutes a shear strain angle in the X-Z' plane of the member, as shown in Figure 3.22 (see Figure 3.7 for further clarification of this geometric relationship). As such, the transverse shear force in the Z' direction at position X of the member can be calculated as a function of the X-Z' shear strain angle in the member as follows:

$$V_{Z'} = \beta_{Y'Y'} A_G\, G_{XZ'} \left(\Phi_{Y'Y'} + \frac{dw}{dX} \right) \tag{3.113}$$

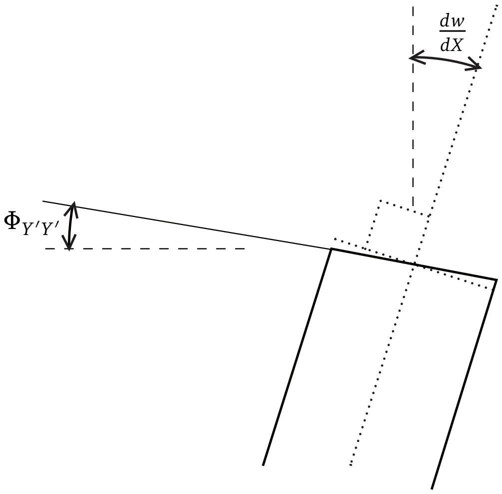

Figure 3.22: Engesser's model [26][27] of the net transverse shear strain in a column as a function of $\Phi_{Y'Y'}$ and dw/dX (see Figure 3.7 for further clarification of this geometric relationship).

where $\beta_{Y'Y'}$ is the Timoshenko shear correction factor for use with shear forces applied in the Z' direction (see Section 3.10), A_G is the cross-sectional area of the beam normalized with respect to the nominal transverse shear modulus (see Section 3.6.4), and $G_{XZ'}$ is the nominal composite X-Z' shear modulus of the section (see Section 3.6.4). Differentiating equation (3.112) with respect to X results in another expression for $V_{Z'}$, which can be substituted into equation (3.113) as follows:

$$E_{XX}\, I_{Y'Y'}\, \frac{d^2\Phi_{Y'Y'}}{dX^2} = P\frac{dw}{dX} = \beta_{Y'Y'} A_G\, G_{XZ'} \left(\Phi_{Y'Y'} + \frac{dw}{dX}\right) \tag{3.114}$$

Differentiating equation (3.112) twice with respect to X yields the following useful relationship between w and $\Phi_{Y'Y'}$:

$$E_{XX}\, I_{Y'Y'}\, \frac{d^3\Phi_{Y'Y'}}{dX^3} = P\frac{d^2w}{dX^2} \tag{3.115}$$

Differentiating equation (3.114) with respect to X yields the following expression:

$$P\frac{d^2w}{dX^2} = \beta_{Y'Y'} A_G\, G_{XZ'} \left(\frac{d\Phi_{Y'Y'}}{dX} + \frac{d^2w}{dX^2}\right) \tag{3.116}$$

Rearranging equation (3.116), differentiating once more with respect to X, and substituting in equation (3.115), the following expression is found:

$$-\left(1 - \frac{P}{\beta_{Y'Y'} A_G\, G_{XZ'}}\right)\frac{d^4w}{dX^4} = \frac{d^3\Phi_{Y'Y'}}{dX^3} = \frac{P}{E_{XX}\, I_{Y'Y'}}\frac{d^2w}{dX^2} \tag{3.117}$$

Finally, equation (3.117) can be rearranged in order to arrive upon the differential equation that governs flexural buckling of columns with transverse shear effects, as follows:

$$\frac{d^4w}{dX^4}+\left(\frac{\left(\frac{P}{E_{XX}\,I_{Y'Y'}}\right)}{\left(1-\frac{P}{\beta_{Y'Y'}\,A_G\,G_{XZ'}}\right)}\right)\frac{d^2w}{dX^2}=0 \tag{3.118}$$

The solution to this differential equation (3.118) can be found as follows:

$$w\left(X\right)=C_1\sin\left(X\sqrt{\frac{\left(\frac{P}{E_{XX}\,I_{Y'Y'}}\right)}{\left(1-\frac{P}{\beta_{Y'Y'}\,A_G\,G_{XZ'}}\right)}}\right)+C_2\cos\left(X\sqrt{\frac{\left(\frac{P}{E_{XX}\,I_{Y'Y'}}\right)}{\left(1-\frac{P}{\beta_{Y'Y'}\,A_G\,G_{XZ'}}\right)}}\right) \tag{3.119}$$

where $w\left(X\right)$ is the lateral Z' deflection of the column at position X, and C_1 and C_2 are integration constants. For a simply supported column (pin constraints at both ends of the column), the value of C_2 must be zero. Additionally, by inspection of equation (3.119), it is evident that the following equality must be true for a simply supported column:

$$\frac{\left(\frac{P}{E_{XX}\,I_{Y'Y'}}\right)}{\left(1-\frac{P}{\beta_{Y'Y'}\,A_G\,G_{XZ'}}\right)}L^2=\pi^2n^2 \tag{3.120}$$

where L is the total buckling length between the two pin-supported ends of the column, and n is an integer value representing the number of half-sin curves describing the buckled shape of the column. Rearranging equation (3.120) and isolating for the applied axial compression force P results in an equation for the critical axial compression load at which an infinitesimal lateral perturbation in the Z' direction will cause elastic buckling of the column about its Y'-Y' axis, as follows:

$$P_{cr\,En\,Y'Y'}=\frac{\left(\frac{\pi^2n^2}{L^2}\right)}{\left(\frac{1}{E_{XX}\,I_{Y'Y'}}\right)+\left(\frac{\pi^2n^2}{L^2\beta_{Y'Y'}\,A_G\,G_{XZ'}}\right)}=\frac{1}{\frac{L^2}{\pi^2n^2\,E_{XX}\,I_{Y'Y'}}+\frac{1}{\beta_{Y'Y'}\,A_G\,G_{XZ'}}} \tag{3.121}$$

For simply supported pin-pin columns, the value of n shall be taken as unity since the elastically deformed shape of the column can take the form of a single half-sin wave. Conversely, in the case of a fixed-fixed column in which both ends are restrained against all rotations and lateral translations, the value of n shall be taken as 2 since the elastically deformed shape of the column must pass through a minimum of two half-sin waves in this case. Similarly, the following expression can be used to find the critical axial compression load at which an infinitesimal lateral perturbation in the Y' direction will cause elastic buckling of the column about its Z'-Z' axis:

$$P_{cr\,En\,Z'Z'}=\frac{1}{\frac{L^2}{\pi^2n^2\,E_{XX}\,I_{Z'Z'}}+\frac{1}{\beta_{Z'Z'}\,A_G\,G_{XY'}}} \tag{3.122}$$

where $I_{Z'Z'}$ is the second area moment of inertia of the section about its Z'-Z' axis (see Section 3.7), $\beta_{Z'Z'}$ is the Timoshenko shear correction factor for use with shear forces applied in the Y' direction (see Section 3.10), and $G_{XY'}$ is the nominal composite X-Y' shear modulus of the section (see Section

3.6.4). It is interesting to note that equation (3.121) becomes equal to equation (3.110) if the value of $G_{XZ'}$ is set to infinity, and that equation (3.122) becomes equal to equation (3.111) if the value of $G_{XY'}$ is set to infinity.

Although the preceding derivation was based upon Engesser's formulation, it is interesting to note that equations (3.121) and (3.122) are quite similar to the relationships that were presented in the 2001 work of Kollár [44] and the 2009 work of Vo and Lee [86]. This similarity serves to substantiate the applicability of Engesser's flexural buckling model for applications pertaining to thin-walled open sections comprising laminated composite walls.

3.14.3 Elastic Flexural Buckling of Initially Curved Columns with Transverse Shear Effects

While the previous section discussed the critical buckling load of initially straight columns, in practice, columns are rarely perfectly straight in their initial unloaded form. As such, it is useful to understand the structural response of initially curved columns that are subjected to axial compression loadings. The behaviour of initially curved columns has long been understood in the context of the assumptions that are implicit in Euler buckling theory [78][70] (see equation (3.137) later in this section); however, at the time that the present analytical model was developed, the author was not aware of any previous attempts to understand this behaviour in a manner that accounts for the effects of transverse shear compliance. As such, the author has undertaken to derive a formula, based upon Engesser buckling theory [26][27], to calculate the lateral deflection of an axially loaded column that had some initial curved shape prior to the application of the axial compression force.

In a manner that is similar to equation (3.112), the Y'-Y' bending moment at position X due to an axial compression force, an initial lateral displacement of the undeformed column in the Z' direction, and some additional lateral perturbation in the Z' direction, can be expressed as follows:

$$M_{Y'Y'} = E_{XX}\, I_{Y'Y'}\, \frac{d\Phi_{Y'Y'}}{dX} = P\left(w + w_o\right) \tag{3.123}$$

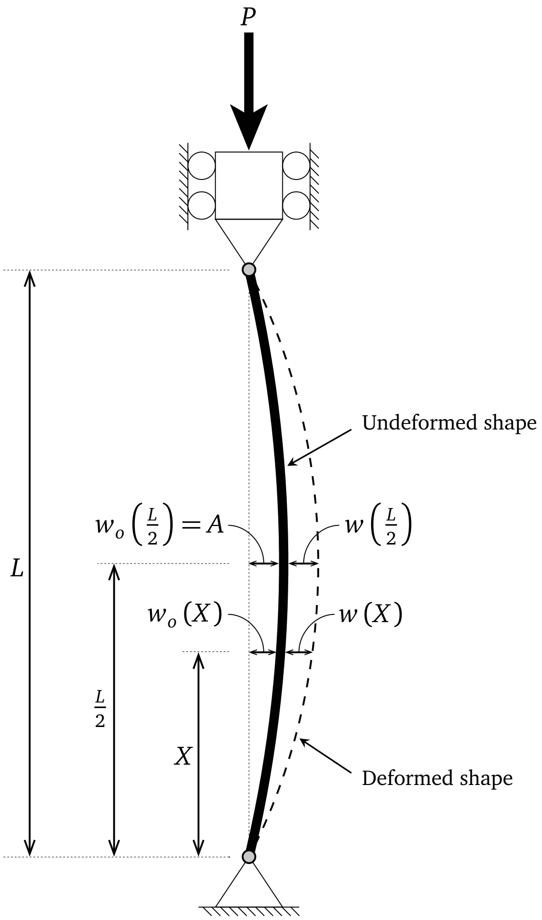

Figure 3.23: Undeformed and deformed shape of an initially curved column subjected to an axial compression force.

where w_o is the initial lateral Z' position of the undeformed member's cross-section at position X along its length (see Figure 3.23). It is interesting to note that equation (3.123) becomes identical to equation (3.112) when the value of w_o is zero, which is logical since equation (3.112) is intended for use with columns that are initially straight. As shown in equation (3.113), the transverse shear force in the Z' direction at position X of the member can be calculated as follows:

$$V_{Z'} = \beta_{Y'Y'} A_G \, G_{XZ'} \left(\Phi_{Y'Y'} + \frac{dw}{dX} \right) \tag{3.124}$$

Differentiating equation (3.123) respect to X and substituting the result into equation (3.124) yields the following expression:

$$V_{Z'} = \frac{dM_{Y'Y'}}{dX} = P\left(\frac{dw}{dX} + \frac{dw_o}{dX} \right) = \beta_{Y'Y'} A_G \, G_{XZ'} \left(\Phi_{Y'Y'} + \frac{dw}{dX} \right) \tag{3.125}$$

Differentiating equation (3.125) with respect to X and rearranging the resulting expression yields the following relationship:

$$\frac{P}{\beta_{Y'Y'} A_G \, G_{XZ'}} \left(\frac{d^2 w}{dX^2} + \frac{d^2 w_o}{dX^2} \right) = \frac{d\Phi_{Y'Y'}}{dX} + \frac{d^2 w}{dX^2} \tag{3.126}$$

Substituting equation (3.123) into equation (3.126) and differentiating the result twice with respect to X results in the following governing differential equation for the behaviour of an initially curved column that is subjected to an axial compression force:

$$\left(\frac{P}{\beta_{Y'Y'} A_G \, G_{XZ'}} - 1 \right) \frac{d^4 w}{dX^4} - \left(\frac{P}{E_{XX} \, I_{Y'Y'}} \right) \frac{d^2 w}{dX^2} = \left(\frac{P}{E_{XX} \, I_{Y'Y'}} \right) \frac{d^2 w_o}{dX^2} - \left(\frac{P}{\beta_{Y'Y'} A_G \, G_{XZ'}} \right) \frac{d^4 w_o}{dX^4} \tag{3.127}$$

In order to proceed with solving this differential equation, it is necessary to assign a mathematical function to represent the value of w_o at any given position X along the length of the column. It is useful to assume that the initially curved shape of the undeformed column is sinusoidal in nature. As such, the value of w_o at any position X along the length of the column can be defined by the following function, and its respective derivatives:

$$\begin{aligned} w_o &= A \sin\left(\frac{i_s \pi X}{L} \right) \\ \frac{d^2 w_o}{dX^2} &= -\frac{i_s^2 \pi^2}{L^2} A \sin\left(\frac{i_s \pi X}{L} \right) \\ \frac{d^4 w_o}{dX^4} &= \frac{i_s^4 \pi^4}{L^4} A \sin\left(\frac{i_s \pi X}{L} \right) \end{aligned} \tag{3.128}$$

where A is the amplitude of the sin wave that describes the initial curved shape of the undeformed column, and i_s is the number of half-sin waves present over the length of the column. When the value of i_s is set to unity, it is assumed that only a single half-sin wave represents the undeformed shape of the column; in such a scenario, the maximum value of w_o would occur at the mid-span ($X = L/2$) of the column, and would be equal to the aforementioned amplitude A (see Figure 3.23).

It is possible to replace equation (3.128) with a Fourier series that would theoretically be capable of representing a column having any initially curved undeformed shape, as follows:

$$w_o = \sum_{i_s=1}^{\infty} A_{i_s} \sin\left(\frac{i_s \pi X}{L} \right) \tag{3.129}$$

where A_{i_s} is the amplitude of the $i_s{}^{\text{th}}$ sin wave of the Fourier series, which has a wavelength of $2L / i_s$. However, in the interest of minimizing the complexity of the solution to equation (3.127), it will be assumed here that the column of interest has an initial undeformed shape that can be represented by a single sin wave, thus facilitating the use of equation (3.128). Substituting equation (3.128) into equation (3.127) results in the following differential equation:

$$\frac{d^4w}{dX^4}+\left(\frac{\left(\frac{P}{E_{XX}\,I_{Y'Y'}}\right)}{\left(1-\frac{P}{\beta_{Y'Y'}\,A_G\,G_{XZ'}}\right)}\right)\frac{d^2w}{dX^2}=\left(\frac{\left(\frac{P}{E_{XX}\,I_{Y'Y'}}\right)+\left(\frac{i_s^2\,\pi^2\,P}{L^2\,\beta_{Y'Y'}\,A_G\,G_{XZ'}}\right)}{\left(1-\frac{P}{\beta_{Y'Y'}\,A_G\,G_{XZ'}}\right)}\right)\frac{i_s^2\,\pi^2}{L^2}A\sin\left(\frac{i_s\pi X}{L}\right) \tag{3.130}$$

Assigning new coefficients F_1 and F_2, equation (3.130) can be rewritten as follows:

$$\frac{d^4w}{dX^4}+F_2\frac{d^2w}{dX^2}=F_1\sin\left(\frac{i_s\pi X}{L}\right) \tag{3.131}$$

where:

$$F_1=\frac{i_s^2\,\pi^2}{L^2}A\left(\frac{\left(\frac{P}{E_{XX}\,I_{Y'Y'}}\right)+\left(\frac{i_s^2\,\pi^2\,P}{L^2\,\beta_{Y'Y'}\,A_G\,G_{XZ'}}\right)}{\left(1-\frac{P}{\beta_{Y'Y'}\,A_G\,G_{XZ'}}\right)}\right) \qquad F_2=\left(\frac{\left(\frac{P}{E_{XX}\,I_{Y'Y'}}\right)}{\left(1-\frac{P}{\beta_{Y'Y'}\,A_G\,G_{XZ'}}\right)}\right)$$

The solution to this differential equation (3.131) can be found as follows:

$$w\left(X\right)=\frac{L^4\,F_1\sin\left(\frac{i_s\pi X}{L}\right)}{i_s^4\pi^4-L^2i_s^2\pi^2F_2}+C_1\frac{\left(i_s^2\pi^2-L^2F_2\right)\cos\left(X\sqrt{F_2}\right)}{i_s^2\pi^2F_2-L^2{F_2}^2}+C_2\frac{\left(i_s^2\pi^2-L^2F_2\right)\sin\left(X\sqrt{F_2}\right)}{i_s^2\pi^2F_2-L^2{F_2}^2}+C_3X+C_4 \tag{3.132}$$

where C_1, C_2, C_3, and C_4 are constants of integration that can be found in accordance with the relevant boundary conditions. If it is assumed that the deformed shape of the loaded column follows a sinusoidal shape having the same wavelength as the initial undeformed curved shape of the column, then the values of all four of these integration constants can be set to zero, and equation (3.132) can be rewritten as follows:

$$w\left(X\right)=\frac{L^4\,F_1\sin\left(\frac{i_s\pi X}{L}\right)}{i_s^4\pi^4-L^2i_s^2\pi^2F_2} \tag{3.133}$$

Substituting the definitions of F_1 and F_2 into equation (3.133) gives the following expression for the lateral deflection of the column at a given position X along its length:

$$w\left(X\right)=\frac{\left(\frac{P}{\beta_{Y'Y'}\,A_G\,G_{XZ'}}+\frac{L^2\,P}{n^2\,\pi^2\,E_{XX}\,I_{Y'Y'}}\right)}{\left(1-\frac{P}{\beta_{Y'Y'}\,A_G\,G_{XZ'}}-\frac{L^2\,P}{n^2\,\pi^2\,E_{XX}\,I_{Y'Y'}}\right)}A\sin\left(\frac{n\pi X}{L}\right) \tag{3.134}$$

where n is an integer value representing the number of half-sin waves that describe both the deformed and undeformed shapes of the column (assumed to be equal). By inspection of equations (3.134) and (3.121), it is evident that equation (3.134) can be rewritten as follows:

$$w\left(X\right)=\left(\frac{\left(\frac{P}{P_{cr\,En\,Y'Y'}}\right)}{1-\left(\frac{P}{P_{cr\,En\,Y'Y'}}\right)}\right)A\sin\left(\frac{n\pi X}{L}\right) \tag{3.135}$$

It is likely that the maximum lateral deflection of a simply supported (pin constraints at both ends of the column) axially loaded column will generally occur at its mid-span; as such, it is convenient to substitute the values $n = 1$ and $X = L/2$ into equation (3.135) in order to yield the following expression for the mid-span lateral deflection of a simply supported (pin constraints at both ends of the column) column that had an initial undeformed curved shape than can be represented by a single half-sin wave:

$$w(L/2) = A\left(\frac{\left(\frac{P}{P_{cr\,En\,Y'Y'}}\right)}{1-\left(\frac{P}{P_{cr\,En\,Y'Y'}}\right)}\right) \tag{3.136}$$

where A is the lateral eccentricity of the column at its mid-height ($X = L/2$) due to its initial undeformed sinusoidal shape.

In the context of conventional Euler buckling analysis (ignoring the effects of transverse shear compliance), it has been shown [78][70] that the following expression can be used to calculate the lateral deflection of an axially loaded column that had some initial sinusoidal shape prior to the application of the compression load:

$$w(L/2) = A\left(\frac{\left(\frac{P}{P_{cr\,Eu\,Y'Y'}}\right)}{1-\left(\frac{P}{P_{cr\,Eu\,Y'Y'}}\right)}\right) \tag{3.137}$$

It is interesting to note that equation (3.137) is nearly identical to equation (3.136), with the exception that the Euler critical buckling load $P_{cr\,Eu\,Y'Y'}$ is used in equation (3.137), whereas the Engesser critical buckling load $P_{cr\,En\,Y'Y'}$ is used in equation (3.136). The similarity of these two formulae serves to substantiate the validity of the aforementioned derivation for equation (3.136).

Coincidentally, several months after the present author completed the aforementioned derivation of equation (3.136), a nearly identical derivation was published in a journal article [9] written by Bonab, Hashemi, and Hosseini. This journal article [9] was not published until the present dissertation was already in its final stages of preparation and review; as such, although the novelty of the presently discussed formulation was somewhat attenuated by the work of Bonab et al 2013 [9], it was decided that the present author's work on this derivation was novel at its time of completion, and it therefore retained valid cause for inclusion in the present dissertation.

3.15 Torsional Buckling

In some cases, a column having a thin-walled open section may buckle torsionally about a straight longitudinal axis when subjected to a concentrically applied axial load. Typically, the axis about which this torsional buckling will occur is coincident with the shear-centre of the section.

When calculating the critical elastic flexural buckling load of an initially straight column subjected to a concentrically applied axial load, it is necessary to assume an initial infinitesimal lateral perturbation of the column such that the necessary equilibrium equations can be assembled, manipulated, and resolved into a useful expression for the critical flexural buckling load. In a similar fashion, the derivation of the critical torsional buckling load of a column (which can be found in many texts on advanced mechanics and/or elastic stability [78]) is based upon the assumption of an initial infinitesimal torsional rotation angle, which is subsequently used to assemble the equations of equilibrium of the column in this perturbed state. This equilibrium expression takes the form of a differential equation, which can be manipulated and solved to yield an expression for the critical elastic torsional buckling load of a column, as follows [78]:

$$P_{cr\,V\,\phi} = \frac{A_E}{I_O}\left[C + \left(C_{1B}\frac{\pi^2 n^2}{L^2}\right)\right] \tag{3.138}$$

where I_O is the area polar moment of inertia of the section about its shear-centre (see Section 3.9), A_E is the nominal cross-sectional area that has been normalized with respect to the nominal normal elastic modulus along the longitudinal X axis of the member (see equation (3.11) in Section 3.6.4), C is the Saint-Venant torsional stiffness (see Section 3.11), C_{1B} is the warping constant (see Sections 3.12.1 and 3.12.2), and n is an integer value representing the number of half-sin curves that describe the phase of the warped shape of the column over its length.

It was explained in Section 3.12 that conventional Vlasov warping analysis will tend to over-predict the restrained torsional stiffness (warping stiffness) of a beam that comprises legs having non-trivial warping-shear compliance. By extension, is can be expected that equation (3.138) will tend to over-predict the critical elastic torsional buckling load of a column that has a thin-walled open section comprising legs having non-trivial in-plane shear compliance. The additional warping compliance caused by these warping-shear strains can be added in series to equation (3.138) to yield the following improved expression for the critical elastic torsional-shear buckling load of a column [44][86]:

$$P_{cr\,S\,\phi} = \frac{A_E}{I_O}\left[C + \left(\frac{L^2}{C_{1B}\,\pi^2 n^2} + \frac{1}{C_{TS}}\right)^{-1}\right] \tag{3.139}$$

where C_{TS} is a stiffness term that accounts for additional warping compliance caused by warping-shear strains (see equation (3.99) in Section 3.12.3).

3.16 Flexural-Torsional-Shear Buckling

The most general case of long column buckling (global buckling that ignores local effects) is that which accounts for flexural, torsional, and shear modes of deformation. Many text books on advanced mechanics and/or elastic stability include detailed derivations for the calculation of coupled flexural-torsional buckling of long columns [78]. Such derivations typically result in the following cubic expression, which can be used to find the critical elastic flexural-torsional buckling load $P_{cr\,FT}$ of long simply supported (pin constraints at both ends of the column) columns subjected to concentric axial compression loadings [78]:

$$\Omega_{FT\,3}\,P_{cr\,FT}^{3}+\Omega_{FT\,2}\,P_{cr\,FT}^{2}+\Omega_{FT\,1}\,P_{cr\,FT}+\Omega_{FT\,0}=0 \tag{3.140}$$

where:

$$\Omega_{FT\,3}=\frac{I_C}{I_O}$$

$$\Omega_{FT\,2}=\frac{A_E}{I_O}\left(P_{cr\,Eu\,Y'Y'}\,e_{Z'}^{2}+P_{cr\,Eu\,Z'Z'}\,e_{Y'}^{2}\right)-\left(P_{cr\,Eu\,Y'Y'}+P_{cr\,Eu\,Z'Z'}+P_{cr\,V\,\phi}\right)$$

$$\Omega_{FT\,1}=P_{cr\,Eu\,Y'Y'}\,P_{cr\,Eu\,Z'Z'}+P_{cr\,Eu\,Y'Y'}\,P_{cr\,V\,\phi}+P_{cr\,Eu\,Z'Z'}\,P_{cr\,V\,\phi}$$

$$\Omega_{FT\,0}=-P_{cr\,Eu\,Y'Y'}\,P_{cr\,Eu\,Z'Z'}\,P_{cr\,V\,\phi}$$

where A_E is the nominal cross-sectional area that has been normalized with respect to the nominal normal elastic modulus along the longitudinal X axis of the member (see equation (3.11) in Section 3.6.4), I_C and I_O are the polar moments of inertia of the column about its centroid and shear-centre, respectively (see Section 3.9), $P_{cr\,Eu\,Y'Y'}$ and $P_{cr\,Eu\,Z'Z'}$ are the Euler buckling loads of the column about it's Y'-Y' and Z'-Z' axes, respectively (see equations (3.110) and (3.111) in Section 3.14), and $P_{cr\,V\,\phi}$ is the torsional buckling load of the column (see equation (3.138) in Section 3.15). Upon finding the roots of this expression, is can be seen that $P_{cr\,FT}$ has three possible values representing the lowest buckling load that corresponds with each of the three possible elastic flexural-torsional mode shapes of the column. It should be noted that each of these mode shapes can also exist as integer multiples of themselves; such an occurrence can sometimes be caused by structural bracing, which may prohibit the formation of lower harmonics of a given mode shape, but allow for the formation of higher harmonics. As such, care must be taken when determining which mode shapes govern the elastic stability of the column.

Although equation (3.140) can be used to find the critical elastic flexural-torsional buckling load of a long column, it was suggested in Sections 3.14 and 3.15 that both flexural and torsional buckling load calculations for FRP composite columns are potentially susceptible to over-prediction if the effects of in-plane shear compliance are ignored. As such, it is necessary to account for flexural, torsional, and shear modes of deformation when determining the critical buckling load of FRP composite columns. However, rather than treat shear as a completely independent mode of deformation, it is convenient to recognize that shear phenomena generally occur as a function of bending phenomena, and can therefore be coupled to said bending phenomena. As such, it is possible to evaluate the critical elastic flexural-torsional-shear buckling load $P_{cr\,FTS}$ of long simply supported (pin constraints at both ends of the column) columns by simply re-writing equation (3.140) with torsional and flexural buckling load values that account for the effects of shear compliance, as follows:

$$\Omega_{FTS\,3}\,P^3_{cr\,FTS}+\Omega_{FTS\,2}\,P^2_{cr\,FTS}+\Omega_{FTS\,1}\,P_{cr\,FTS}+\Omega_{FTS\,0}=0 \tag{3.141}$$

where:

$$\Omega_{FTS\,3}=\frac{I_C}{I_O}$$

$$\Omega_{FTS\,2}=\frac{A_E}{I_O}\left(P_{cr\,En\,Y'Y'}\,e^2_{Z'}+P_{cr\,En\,Z'Z'}\,e^2_{Y'}\right)-\left(P_{cr\,En\,Y'Y'}+P_{cr\,En\,Z'Z'}+P_{cr\,S\,\phi}\right)$$

$$\Omega_{FTS\,1}=P_{cr\,En\,Y'Y'}\,P_{cr\,En\,Z'Z'}+P_{cr\,En\,Y'Y'}\,P_{cr\,S\,\phi}+P_{cr\,En\,Z'Z'}\,P_{cr\,S\,\phi}$$

$$\Omega_{FTS\,0}=-P_{cr\,En\,Y'Y'}\,P_{cr\,En\,Z'Z'}\,P_{cr\,S\,\phi}$$

where $P_{cr\,En\,Y'Y'}$ and $P_{cr\,En\,Z'Z'}$ are the flexural-shear buckling loads of the column about it's Y'-Y' and Z'-Z' axes, respectively (see equations (3.121) and (3.122) in Section 3.14), and $P_{cr\,S\,\phi}$ is the torsional-shear buckling load of the column (see equation (3.139) in Section 3.15). Upon finding the roots of this expression, is can be seen that $P_{cr\,FTS}$ has three possible values representing the lowest buckling load that corresponds with each of the three possible elastic flexural-torsional-shear mode shapes of the column.

3.17 Analytical Modelling Computer Program

Each of the analytical procedures presented in the previous sections of this chapter can be used individually, or together, to assess the structural response of a beam or stringer of constant open cross-sectional geometry, that is built-up of legs composed of laminated composite materials. The goal of this chapter was to provide a sufficiently broad suite of analytical procedures such that a complete flexural-torsional-shear buckling analysis could be carried out on such a structural member.

While the author's intention was to do so in a manner that is conducive for the use of "hand-calculation" type analytical methods (see Section 3.1), it is evident that the aforementioned analytical procedures are of sufficient complexity to necessitate the aid of a computer program. As such, the author has developed such a computer program using MathWorks® MATLAB®. This computer program was written in such a manner that each of the aforementioned analytical procedures is carried out by its own subroutine, and the results of all of these subroutines are compiled by the main program to ultimately yield output for the user. This programming architecture is efficient, and it also enables the user to easily navigate the programming code and retain an understanding of the analytical methodologies that are involved.

The user provides input data to the computer program in the form of a series of Microsoft® Excel® spreadsheets. Each of these spreadsheets contain data pertaining to one leg of the cross-sectional geometry (see Figure 3.1); these data include: the laminate stacking sequence, material properties, and dimensions of the relevant leg of the cross-sectional geometry. The MATLAB® computer program reads these data into a series of arrays, and then commences processing.

This computer program provides the user with a full suite of engineering section constants that can be employed in many of the classical beam analysis calculations that would be familiar to any structural engineer who is well versed in the design and analysis of metallic structural members. The computer program then utilizes these section constants to assess the flexural-torsional-shear buckling response (see Section 3.16) of the structural member of interest. The output from this buckling analysis includes: flexural buckling loads about each of the principal flexural axes of the member, the torsional buckling load of the member, and the full flexural-torsional-shear interaction buckling loads associated with the first three buckling mode shapes of the member. These outputs are calculated at a series of effective buckling lengths, and plots are generated to illustrate the expected critical buckling load of the member as a function of its effective buckling length.

In addition, the program was written in such a way that the user is able to intentionally neglect the structural phenomena captured by some of the analytical procedures discussed in this chapter. This is useful when assessing the importance of these individual structural phenomena to the overall structural response of the member, and helps to demonstrate the potential dangers of utilizing low fidelity classical analytical methods to assess the performance of structural members that comprise laminated FRP composite materials. In particular, the user may choose to either include or exclude the following structural phenomena from a buckling analysis: the effect that transverse shear compliance has upon the flexural buckling load, the effect that through-thickness shear effects has upon Saint-Venant torsional stiffness, and the effect that warping-shear strains have upon the restrained torsion (warping) response.

The aforementioned computer program was developed using a Lenovo® ThinkPad® T430 computer that had 8 GB of RAM, an Intel® Core™ i7-3520M dual-core processor running at 2.90 GHz per core, and a Microsoft® Windows® 7 Professional operating system. When run on this computer, the aforementioned MATLAB® based computer program typically required a processing time of approximately 62 seconds; however, it is worth noting that a significant proportion of that time was devoted to read and write operations, whereby MATLAB® was required to communicate with a Microsoft® Excel® spreadsheet program. As such, it is likely that processing time could be significantly reduced if the present computer program were modified to interface with input data stored in text files, as opposed to the aforementioned Microsoft® Excel® spreadsheet based input structure.

3.18 Computational Validation of the Present Analytical Model

3.18.1 General

This chapter has described a comprehensive analytical model that comprises a plethora of smaller analytical procedures. Many of these procedures are based upon existing engineering science that has been proven reliable over many years of use in the academic and engineering communities. Conversely, some of the procedures discussed in this chapter are either completely new contributions, or based upon relatively new and unproven state-of-the-art engineering science. In such cases, the author has undertaken to demonstrate the validity of these unproven analytical methods using either computational or experimental methods (see Section 3.11.6 and Chapter 4). However, due to the breadth and complexity of the overall analytical method presented in this chapter, the author has decided to carry out a computational validation of this entire analytical model in such a way that every one of the smaller analytical procedures would be assessed simultaneously.

3.18.2 Virtual Test Set-Up

General

It was discussed in Section 1.5 that the present analytical method was initially developed for the purpose of predicting the elastic buckling load of aircraft wing stringers. Section 3.16 introduced a cubic expression (equation (3.141)) whose roots represent the critical buckling loads associated with each of the first three global flexural-torsional-shear mode shapes of a column. Upon examining the coefficients present in equation (3.141), and exploring the subordinate equations upon which each of these coefficients are dependent (presented in various sections throughout Chapter 3), it is made evident that elastic flexural-torsional-shear buckling is, in fact, dependent upon every one of the analytical procedures discussed in this chapter, with the exception of the analytical procedure presented in Section 3.14.3. For this reason, elastic flexural-torsional-shear buckling was elected as the structural test case that would be used to validate the present analytical method.

Cross-Sectional Geometry

Although elastic flexural-torsional-shear buckling is potentially dependent upon all of the analytical procedures discussed in this chapter, some of these analytical procedures only bear significant relevance in the case of members having particular cross-sectional attributes. In particular, it is desirable to select a cross-sectional geometry that will tend to couple the effects of flexure and torsion, such that both of these states of deformation will be well represented during an elastic buckling analysis. Under the right circumstances, a member of any cross-sectional geometry can potentially buckle as a result of flexural, torsional, and/or shear modes of deformation; however, if one of these mode shapes were to become excited at a much lower critical buckling load than the others, it would be difficult to evaluate the validity of the present analytical model for the prediction of the other two types of deformation. Conversely, the use of a member that exhibits substantial flexural-torsional coupling will ensure that both modes of deformation will occur simultaneously, and will therefore be well represented in the validation program.

In order to ensure that flexural-torsional coupling will occur, it is necessary to employ a cross-sectional geometry that exhibits a shear-centre location that is distant from the centroid of the section, and is not coincident with the mid-plane of any of the walls of the section. In fact, the severity of flexural-torsional interaction will generally be greatest in cases where the shear-centre location is distant from the geometric bounds of the cross-section. In addition, it is desirably to employ a cross-sectional geometry that is completely un-symmetric (does not exhibit symmetry about any axes) such that some degree of flexural-torsional coupling is likely to be exhibited in all mode shapes of the member. Conversely, a singly symmetric section (a section that is symmetric about only one of its principal axes) will only exhibit flexural-torsional coupling when the excited mode shape involves flexure about the symmetric axis of the section, and a doubly symmetric section (a section that is symmetric about both of its principal axes) will exhibit no flexural-torsional coupling at all since its shear-centre is coincident with its centroid.

Ultimately, it was decided that a carefully designed J-section would best satisfy the aforementioned criteria necessary to ensure that the full suite of analytical procedures included in the present analytical method would be assessed during this validation study. Figure 3.24 illustrates the dimensions of the selected cross-sectional geometry.

It is evident in Figure 3.24 that the cross-sectional geometry has been segregated into regions designated as “core” and “skin”. This was done to allow for the use of unique material models and local material coordinate systems within each these regions, as will be discussed below. The skin regions were each given a thickness of 2 mm per skin, measured with respect to the through-thickness dimension (laminate z axis) of the relevant leg of the section. As such, in order to achieve the dimensions shown in Figure 3.24, the core regions were each given a thickness of either 3 mm or 5 mm, measured with respect to the through-thickness dimension of the relevant leg of the section. Figure 3.24 also illustrates the orientation of the global X-Y-Z coordinate system used to define the geometry of these virtual specimens.

It is worth noting that aircraft wing stringers often feature J-section type cross-sectional geometries; as such, this validation study is directly relevant to the initial intended purpose of the present analytical model. In fact, the dimensions of the selected cross-sectional geometry shown in Figure 3.24 are quite typical of aluminium upper wing stringers used in large commercial aircraft.

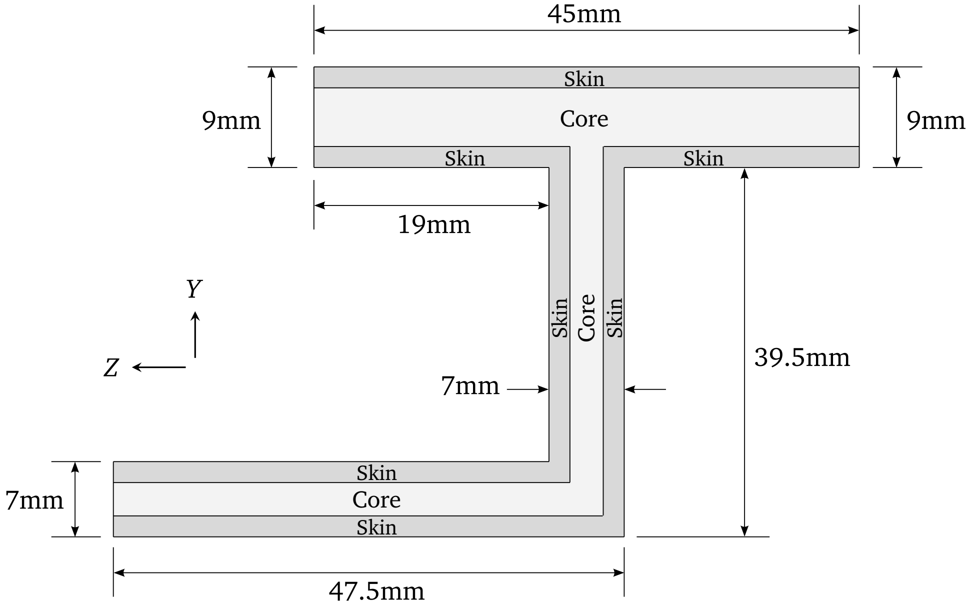

Figure 3.24: Cross-sectional geometry of virtual specimens used for validation of complete analytical model under elastic flexural-torsional-shear buckling conditions.

Material Composition

Two types of materials were employed in the virtual specimens used for the present validation study: a homogeneous and isotropic 6061-T6 aluminium material, and an orthotropic unidirectional continuous-fibre carbon FRP (CFRP) material. The mechanical properties of these two materials in their local 1-2-3 coordinate systems are shown in Table 3.9:

Table 3.9: Mechanical properties of aluminium and CFRP materials used in buckling validation study, within their local 1-2-3 coordinate systems.

	Aluminium	**CFRP**
E_{11} (GPa)	68.900	182.875
E_{22} (GPa)	68.900	7.026
E_{33} (GPa)	68.900	7.026
G_{12} (GPa)	25.900	2.550
G_{23} (GPa)	25.900	2.551
G_{31} (GPa)	25.900	2.550
ν_{12}	0.330	0.276
ν_{23}	0.330	0.276
ν_{31}	0.330	0.0106

Three types of virtual specimens were formulated from the aforementioned cross-sectional geometry and material constituents (see Figure 3.24 and Table 3.9).

The first type of virtual specimen, designated here as “AL”, was simply composed entirely (both skin and core regions) of the aluminium material shown in Table 3.9. Although this aluminium material model is isotropic in nature and its orientation is unimportant, for the purposes of clarity, the 1 axis of the material coordinate system was aligned with the longitudinal X axis of the member, and the 2 axis of the material coordinate system was aligned with the global Y axis of the member.

The second type of virtual specimen, designated here as “C-0-0”, was simply composed entirely (both skin and core regions) of the CFRP material shown in Table 3.9. Once again, the 1 axis of the material coordinate system was aligned with the longitudinal X axis of the member, and the 2 axis of the material coordinate system was aligned with the global Y axis of the member.

The third type of virtual specimen, designated here as “C-0-45”, was designed as a laminated beam, whereby the core material was oriented differently than the skin material. The core regions of virtual specimen C-0-45 were composed of the CFRP material shown in Table 3.9, with the 1 axis of the material coordinate system aligned with the longitudinal X axis of the member, and the 2 axis of the material coordinate system was aligned with the global Y axis of the member. Conversely, the skin regions (each having a thickness of 2 mm) were modelled as ±45° laminates having a very large number of laminae, each composed of the CFRP material shown in Table 3.9. As such, a CLPT analysis was carried out to determine the orthotropic mechanical properties of a balanced and symmetric laminate of a large number of CFRP plies oriented at alternating angles of $+45°$ and $-45°$; Table 3.10 summarizes the mechanical properties that were found for such a laminate within its x-y-z laminate coordinate system.

Table 3.10: Mechanical properties of ±45° CFRP laminate used in buckling validation study, within its laminate x-y-z coordinate system.

	±45° **CFRP**
E_{xx} (GPa)	9.694
E_{yy} (GPa)	9.694
E_{zz} (GPa)	7.026
G_{xy} (GPa)	46.642
G_{yz} (GPa)	2.551
G_{zx} (GPa)	2.551
ν_{xy}	0.900
ν_{yz}	0.276
ν_{zx}	0.0106

The skin regions of virtual specimen C-0-45 were composed of the laminated ±45° CFRP material shown in Table 3.10, with the x axis of the laminate coordinate system aligned with the longitudinal X axis of the member, and the y axis of the laminate coordinate system oriented parallel to the mid-plane of each leg of the cross-sectional geometry.

Effective Buckling Length

Effective buckling length is perhaps one of the most important parameters to define when carrying out an elastic buckling analysis. In general, flexural modes of deformation will tend to be dominant when very long effecting buckling lengths are employed; therefore, torsion and shear effects will bear relatively little effect upon the resulting critical buckling loads. Conversely, when very short effective buckling lengths are employed, local buckling and crippling phenomena (such as crippling of individual legs of the cross-section) will tend to dominate the critical mode shapes; therefore, the aforementioned elastic flexural-torsional-shear buckling analysis (see Section 3.16) will fail to capture the highly complex mode shapes that will tend to occur at very short effective buckling lengths. As such, for the present computational validation, it is important that the selected effective buckling length is long enough to ensure that local effects are unimportant, while simultaneously being short enough that torsion and shear effects both bear significant contributions to the overall critical buckling mode shape.

It was decided that four different effective buckling lengths would be employed for the present validation study: 300 mm, 450 mm, 525 mm, and 600 mm. Utilizing more than one effective buckling length would serve to illustrate the validity of the present analytical method over a broad range of effective buckling lengths. In addition, this range of buckling lengths was selected in order to increase the likelihood that at least one of these buckling lengths would yield a desirable elastic buckling mode shape that exhibited fully coupled flexure, torsion, and shear, while being free of local modes of deformation (such as crippling of individual legs of the cross-section) that could not be captured by the present analytical method. It was expected that one or more of the buckling mode shapes exhibited by virtual specimens of the shortest effective buckling lengths might include local deformations; these particular analysis cases would be disqualified from this validation study since the present analytical method is not formulated to capture such local effects.

Virtual Specimen Designations

At each of the aforementioned four effective buckling lengths, three unique virtual specimens were formulated having each of the aforementioned material compositions, resulting in a total of 12 virtual specimens. Table 3.11 defines the designations that will be used to describe each of these virtual specimens in all subsequent discussions.

Table 3.11: Designations used to define each of the virtual specimens used in buckling validation study.

Effective Buckling Length	**Material Composition Designation**		
	AL	**C-0-0**	**C-0-45**
300mm	AL-300	C-0-0-300	C-0-45-300
450mm	AL-450	C-0-0-450	C-0-45-450
525mm	AL-525	C-0-0-525	C-0-45-525
600mm	AL-600	C-0-0-600	C-0-45-600

3.18.3 Methodology Employed for Finite Element Analyses

General

A finite element (FE) model of each of the 12 virtual specimens defined in Table 3.11 was built and analyzed using MARC® (a product of the MSC™ Software Corporation). These models comprised eight-noded first-order isoparametric solid elements (MARC® element formulation 7 [57]), having three global translational degrees of freedom per node, and eight Gaussian integration points. Each analysis was carried out using a DELL™ Precision™ T3500 computer that had 12 GB of RAM, an

Intel® Xeon® W3540 quadruple-core processor running at 2.93 GHz per core, a math coprocessor, and a Red Hat® Linux® operating system.

Material Models

The aluminium material present within virtual specimens having the AL composition was modelled as a linear elastic homogeneous isotropic material. The mechanical properties defined for this material model are those shown for the aluminium material in Table 3.9. Since an isotropic model was used for this material, it was only necessary to stipulate one elastic modulus and one Poisson's Ratio, and it was unnecessary to define a bespoke material coordinate system for any of the specimens having the AL material composition. This material model was assigned to both core and skin regions of virtual specimens having the AL composition.

The unidirectional continuous CFRP material present within virtual specimens having the C-0-0 and C-0-45 compositions was modelled as a linear elastic homogeneous orthotropic material. The nine constitutive mechanical properties defined for this material model are those shown for the CFRP material in Table 3.9. A 1-2-3 material coordinate system was defined for this material, whereby the 1 axis was aligned with the X axis (longitudinal axis) of the member's global coordinate system, and the 2 axis was aligned with the Y axis of the member's global coordinate system. This material model and material coordinate system was assigned to all core regions of virtual specimens having the C-0-45 composition, and to both core and skin regions of virtual specimens having the C-0-0 composition.

The ±45° CFRP laminate present within the skin regions of virtual specimens having the C-0-45 composition was modelled as a linear elastic homogeneous orthotropic material. The nine constitutive mechanical properties defined for this material model are those shown for the ±45° CFRP material in Table 3.10. The x-y-z laminate coordinate system of this material was oriented such that the x axis of the laminate coordinate system was aligned with the X axis (longitudinal axis) of the member's global coordinate system, and the y axis of the laminate coordinate system was oriented parallel to the mid-plane of each leg of the cross-sectional geometry. In order to achieve this, it was necessary to define two unique x-y-z laminate coordinate systems. In the skin regions of legs having mid-planes oriented parallel to the global Y axis of the virtual specimen, the y axis of laminate coordinate system was aligned with Y axis of global coordinate system. Conversely, in the skin regions of legs having mid-planes oriented parallel to the global Z axis of the virtual specimen, the y axis of laminate coordinate system was aligned with Z axis of global coordinate system.

Boundary Conditions

While the four effective buckling lengths used in the present validation study have already been defined in Section 3.18.2, there are numerous combinations of total member length and end-constraints that could be employed to create the desired effective buckling lengths.

In the case of a simply supported column having pin boundary conditions at each end (designated as “pin-pin” boundary conditions), the effective flexural buckling length is equal to the total length of the member. Unfortunately, it can be quite difficult to impose pin-pin boundary conditions in FE analyses due to the generation of local stress concentrations in regions near the pin constraints. In addition, the imposition of a pin constraint results in a stipulated axis about which rotations are allowed, which can potentially alter some of the modes of deformation that the member might otherwise have assumed. For example, although a pin-pin column does have an effective buckling length equal to its total length for the case of flexural buckling about the axis of the pin supports, the effective buckling length of such a column is equal to half of its total length for torsional buckling and/or for flexural buckling about an axis that is perpendicular to the axis of the pin supports. Furthermore, pin-pin buckling tests are highly sensitive to the position of the pin axis relative to the cross-sectional geometry of the member; in order to prevent beam-column effects caused by loading eccentricity, it is critical that the axis of the pin supports pass through the elastic centroid of the section such that the pin axis is coincident with one of the flexural neutral axes of the section. Ultimately, the perceived elegance of pin-pin buckling is limited to analyses that involve flexural buckling about the axis of the pins, whereby no other modes of deformation are to be expected.

In the case of a column that has fixed boundary conditions at each end (designated as “fixed-fixed” boundary conditions), the effective buckling length is equal to half of the total length of the member; this is the case for torsional buckling, as well as for flexural buckling about all possible axes of flexure. Fixed-fixed boundary conditions allow a member to bend about any axes, and assume completely natural modes of deformation. Prior to lateral perturbation at the critical buckling load, axial loading of a fixed-fixed column may be assumed perfectly concentric and the positions of the flexural neutral axes need-not be considered. In addition, the use of fixed boundary constraints do not generally lead to inclement local stress concentrations unless materials having very high Poisson’s Ratios are present. Unfortunately, because the effective buckling length of a fixed-fixed column is equal to half of the total length of the member, to model the elastic buckling of such a column using FEA techniques would require an FE mesh having approximately double the number of elements that would be needed if this same column were to be modelled using pin-pin boundary conditions, an equal mesh density, and the same effective buckling length.

Ultimately, it was decided that the FEA simulations used for the present validation study would be carried out in a manner that takes advantage of the symmetry present within the flexural-torsional-shear modes that are possible during fixed-fixed column buckling analyses. As such, at one end of the member (the loaded end), all nodes within the cross-sectional area were restrained against translation in the global Y axis and global Z axis, and a translation was imposed along the global X axis to simulate a longitudinal compression displacement. At the opposite end of the member (the plane of symmetry representing the mid-span of a fixed-fixed column), all nodes within the cross-sectional area were free to translate along the global Y axis and global Z axis, and were restrained against translation along the global X axis. As such, one end of the column was restrained against all rotations and lateral translations, and was loaded (displaced) along the longitudinal axis of the member; the opposite end of the column was free to translate laterally and rotate about the longitudinal axis of the member, but was restrained against longitudinal displacements and against rotations about all transverse axes of the member. This system of boundary conditions offers all of the aforementioned benefits present in fixed-fixed buckling analyses, but results in an effective buckling length that is equal to the total length of the member, thus enabling the use of an FE mesh having half of the elements that are necessary for fixed-fixed buckling analyses.

Solution Type

The FE models discussed in this section were analyzed using MARC® (a product of the MSC™ Software Corporation). The analysis of each virtual specimen was carried out using a two step process: a linear static analysis, and a modal analysis [56].

A linear static FE analysis was used to assess the initial axial compression stiffness of each virtual specimen. This linear analysis employed a single load increment to impose a small axial compression displacement upon each specimen, in accordance with the aforementioned boundary conditions.

Modal analyses were carried out to determine the mode shapes (eigenvectors) of each virtual specimen under the given compression loading environments that were generated during the aforementioned linear elastic static analyses. The estimated linear buckling collapse loads of each virtual specimen were then calculated by finding the eigenvalues associated with each of the aforementioned mode shapes of the virtual specimen, and then multiplying these eigenvalues by the magnitude of the axial load that was initially applied during the aforementioned linear static analysis for that specimen. In the MARC® input structure, the “BUCKLE” history definition is used to stipulate the desired method of eigenvalue extraction [58]; the Lanczos method was used for the present validation study, as it tends to yield fast and reliable convergence [56]. The critical buckling loads predicted by this linear modal analysis technique served as the source of FE data for the present validation study, and it is these values that are represented in all of the tabulated and plotted data included in Section 3.18.4.

Convergence Study and Mesh Definition

When designing the FE mesh that was to be used for this validation study, it was first necessary to establish the distribution of finite elements over the cross-sectional area of the virtual specimens (see Figure 3.24). It was necessary to represent the skin regions of the cross-section using at least one layer of elements. It could be argued that more than one layer of elements would better represent these skin regions; however, this would result in very thin elements, thus severely limiting all other dimensions of the elements if concerns regarding element aspect ratio are to be observed. As such, as a base-line, it was decided that a single layer of elements would be used to represent the skin regions of the cross-section. These elements were made to be approximately square within the cross-sectional plane of the virtual specimens, and the resulting nodal positions from these elements then dictated the size and dimensions of the elements representing the core regions of the cross-section. The elements within the core regions of the cross-section were also made to be approximately square within the cross-sectional plane of the virtual specimens. Ultimately, the cross-sectional FE mesh geometry shown in Figure 3.25 was selected as a baseline for all virtual specimens used in the present validation study.

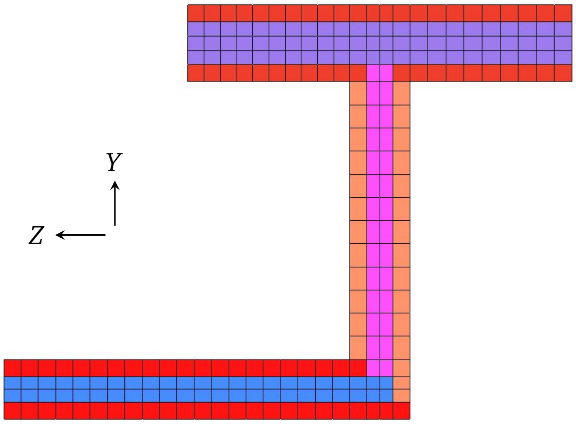

Figure 3.25: Cross-sectional geometry of base-line FE mesh used for buckling validation study.

The cross-sectional discretization illustrated in Figure 3.25 was lofted along the X axis of the member to create a single layer of three dimensional elements, which will be denoted here as a "cross-sectional element set". This element set was then replicated and stacked along the X axis of the member until the desired total length of the virtual specimen was achieved. The thickness of each cross-sectional element set is equal to the length of each element L_{EX}, measured along the X axis of the member (see Figure 3.26). This L_{EX} dimension is governed by the quotient of the total length of the virtual specimen and the number of cross-sectional element sets present over the length of the relevant virtual specimen.

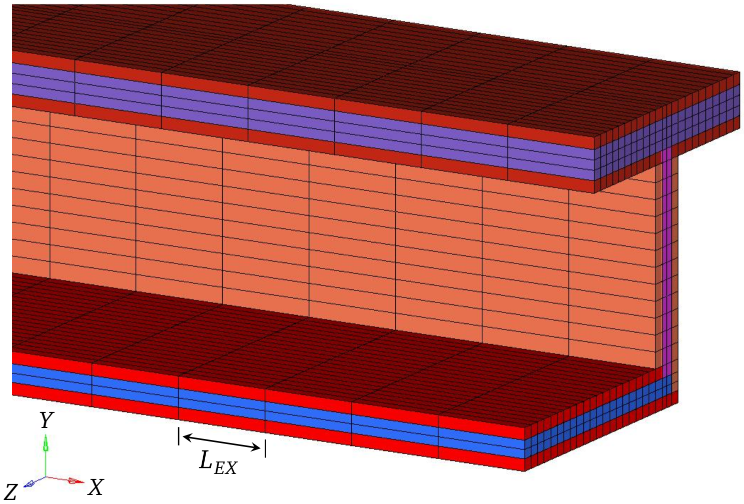

Figure 3.26: Length of each element L_{EX} used for buckling validation study, measured along the Z axis of the member.

A convergence study was carried to aid in establishing the FE mesh density that should be used along the longitudinal axis (X axis) of each specimen. This convergence study was carried out in the context of the C-0-45-525 virtual specimen, since the specimens having the C-0-45 composition are the most complex virtual specimens incorporated in the present validation study. While retaining all of the aforementioned geometric and material parameters possessed by virtual specimen C-0-45-525, the number of cross-sectional element sets over the length of this virtual specimen was varied, and the resulting critical buckling loads (first mode) were recorded. Table 3.12 shows the results of this convergence study.

Table 3.12: Longitudinal FE mesh convergence study results for buckling validation study.

Trial #	**Element Length L_{EX} (mm)**	**Maximum Element Aspect Ratio**	**Critical Buckling Load (N)**
1	15.44	10.29	372573
2	10.10	6.73	366703
3	8.61	5.74	365530
4	7.72	5.15	364908
5	7.00	4.67	364412
6	**6.40**	**4.27**	**364035**
7	4.95	3.30	363341

It is evident from Table 3.12 that, within the range of convergence trials that were attempted, this type of elastic buckling analysis is relatively insensitive to the number of cross-sectional element sets over the length of the virtual specimen. It is likely that FE meshes employing much greater values of L_{EX} would have yielded far more divergent results than those tabulated in Table 3.12; however, in the interest of maintaining reasonable element aspect ratios (any aspect ratio less than five is generally considered reasonable), it seemed appropriate to limit the present convergence study to its current maximum element aspect ratio of 10.29.

Although trial # 7 yielded a slightly different (and likely more accurate) critical buckling load than trial # 6, there was only a 0.19% difference between the buckling loads predicted by these two trials. Conversely, the greater longitudinal FE mesh density employed in trial # 7 necessitated 29.2% more elements than the FE mesh used for trial # 6, which resulted in 24.5% greater computing time to be required by trial # 7. As such, the longitudinal FE mesh density of convergence trial # 6 (tabulated in bold font in Table 3.12) was selected as a base-line to be used for all virtual specimens in the present validation study. This particular FE mesh featured a maximum element aspect ratio of 4.27, and a total of 82 cross-sectional element sets over the length (X axis) of the specimen. It was not possible to maintain this exact configuration for all virtual specimens, since the total length of each virtual specimen in this validation study varied between 300 mm and 600 mm; however, the longitudinal mesh density of each virtual specimen was adjusted such that the maximum element aspect ratio never exceeded 4.27, and there were no fewer than 82 cross-sectional element sets over the length (X axis) of each virtual specimen.

The reasons for the designed cross-sectional mesh discretization shown in Figure 3.25 have been explained from a pragmatic standpoint; however, it remains to be demonstrated that this mesh is sufficiently refined to guarantee accurate predictions of critical buckling loads for the virtual specimens in the present validation study. Unfortunately, the very same reasons cited for the selection of this designed cross-sectional mesh discretization rendered it difficult to experiment with alternative cross-sectional mesh discretization schemes. In particular, it would have been challenging to deviate from the decision to represent the skin regions using a single layer of elements. Nevertheless, the author was able to produce a cross-sectional mesh discretization scheme featuring a lesser mesh density than that shown in Figure 3.25 by representing the core regions with only a single layer of elements. This coarse cross-sectional mesh discretization is illustrated in Figure 3.27.

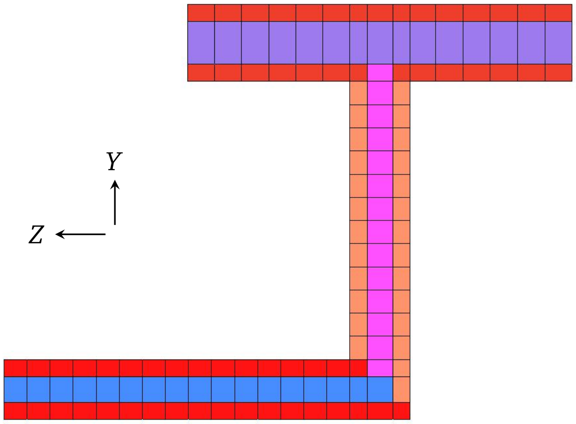

Figure 3.27: Cross-sectional geometry of coarse FE mesh used for buckling mesh sensitivity study.

While a single additional cross-sectional mesh discretization scheme does not facilitate a convergence study, it does allow for a sensitivity study to be performed, which can help to illustrate whether or not the behaviour of the FE model of virtual specimen C-0-45-525 is sensitive to a change of its cross-sectional mesh discretization scheme. As such, two FE meshes of virtual specimen C-0-45-525 were created; one employed the cross-sectional mesh discretization scheme shown in Figure 3.25, and the other employed the cross-sectional mesh discretization scheme shown in Figure 3.27. Both of these FE meshes used the selected longitudinal mesh density shown in trial # 6 of Table 3.12. The results of these two FE analyses are shown in Table 3.13.

Table 3.13: Cross-sectional FE mesh sensitivity study results for buckling validation study.

Cross-Sectional Mesh Type	**Critical Buckling Load (N)**
Base-line (see Figure 3.25)	364035
Coarse (see Figure 3.27)	365158

It is evident from Table 3.13 that the coarse cross-sectional mesh discretization scheme shown in Figure 3.27 resulted in only a 0.31% difference in predicted critical buckling load relative to that predicted using the base-line cross-sectional mesh discretization scheme shown in Figure 3.25. As such, it can be reasonably concluded that the present validation study is relatively insensitive to the cross-sectional mesh discretization scheme that is used; therefore, the selected cross-sectional mesh discretization scheme shown in Figure 3.25 was used for all virtual specimens employed in the present validation study.

In addition to the previous discussions regarding convergence and FE mesh sensitivity, it is also worth noting that all of the FE analyses that were carried out during the present validation study exhibited excellent energy balance characteristics. In fact, of the 12 validation cases that were simulated (see Table 3.11), the maximum discrepancy between external work and internal strain energy was less than 0.05%. This correlation between external work and internal strain energy helps to confirm that no large numerical anomalies or excessive round-off errors were generated during the FE solution.

3.18.4 Results of the Buckling Validations Study

Tables 3.14, 3.15, and 3.16 show the collapse loads associated with the first three modes of buckling, for each of the virtual specimens tested during the present computational validation study. In addition, these tables describe the general type of mode shape that was observed from the post-processed deformation plots from each of these FE simulations. The nomenclature “F-T-S” is used to describe a mode shape that appeared to encompass flexural, torsional, and shear effects, with no significant bias toward any one of these types of deformation. Conversely, the term “flex” is sometimes added in brackets to indicate that a F-T-S buckling mode exhibited some bias toward flexural deformation. The term “Local” signifies a mode shape that included local deformations, such as crippling or local buckling of individual legs of the cross-section.

Table 3.14: FEA predicted buckling loads for each mode shape of AL virtual specimens. Mode shapes that appear to encompass flexural, torsional, and shear effects, are designated here as “F-T-S”. Mode shapes that appear to include local deformations are designated here as “Local”. The term “flex” in brackets indicates an abundance of flexural deformations in a F-T-S regime.

Virtual Specimen		**Mode 1**	**Mode 2**	**Mode 3**
AL-300	Collapse Load (N)	741233	1099469	1369036
	Mode Shape	F-T-S (flex)	F-T-S	Local
AL-450	Collapse Load (N)	373012	695617	1080726
	Mode Shape	F-T-S (flex)	F-T-S	Local
AL-525	Collapse Load (N)	280592	590812	901334
	Mode Shape	F-T-S (flex)	F-T-S	Local
AL-600	Collapse Load (N)	217006	507291	743750
	Mode Shape	F-T-S (flex)	F-T-S	Local

Table 3.15: FEA predicted buckling loads for each mode shape of C-0-0 virtual specimens. Mode shapes that appear to encompass flexural, torsional, and shear effects, are designated here as "F-T-S". Mode shapes that appear to include local deformations are designated here as "Local". The term "flex" in brackets indicates an abundance of flexural deformations in a F-T-S regime.

Virtual Specimen		**Mode 1**	**Mode 2**	**Mode 3**
C-0-0-300	Collapse Load (N)	410967	509255	660190
	Mode Shape	Local	Local	Local
C-0-0-450	Collapse Load (N)	343018	410661	484041
	Mode Shape	F-T-S	Local	Local
C-0-0-525	Collapse Load (N)	302456	397481	445393
	Mode Shape	F-T-S	Local	Local
C-0-0-600	Collapse Load (N)	265130	390991	418005
	Mode Shape	F-T-S	Local	Local

Table 3.16: FEA predicted buckling loads for each mode shape of C-0-45 virtual specimens. Mode shapes that appear to encompass flexural, torsional, and shear effects, are designated here as "F-T-S". Mode shapes that appear to include local deformations are designated here as "Local". The term "flex" in brackets indicates an abundance of flexural deformations in a F-T-S regime.

Virtual Specimen		**Mode 1**	**Mode 2**	**Mode 3**
C-0-45-300	Collapse Load (N)	886745	1054700	1072523
	Mode Shape	Local	Local	Local
C-0-45-450	Collapse Load (N)	477960	869272	1058335
	Mode Shape	F-T-S (flex)	F-T-S	Local
C-0-45-525	Collapse Load (N)	364035	738708	1020206
	Mode Shape	F-T-S (flex)	F-T-S	Local
C-0-45-600	Collapse Load (N)	284448	637682	882301
	Mode Shape	F-T-S (flex)	F-T-S	Local

Figures 3.28, 3.29, 3.30, and 3.31 have been included to illustrate what is meant when the terms "F-T-S", "F-T-S (flex)", and "Local" are used to describe the modes of deformation exhibited by each of the virtual specimens. Figure 3.28 shows the first buckling mode shape of virtual specimen C-0-0-300, which serves as an example of a "Local" buckling mode. It is evident from this figure

that the cross-sectional geometry of pictured virtual specimen has clearly deviated from its original orthogonal state.

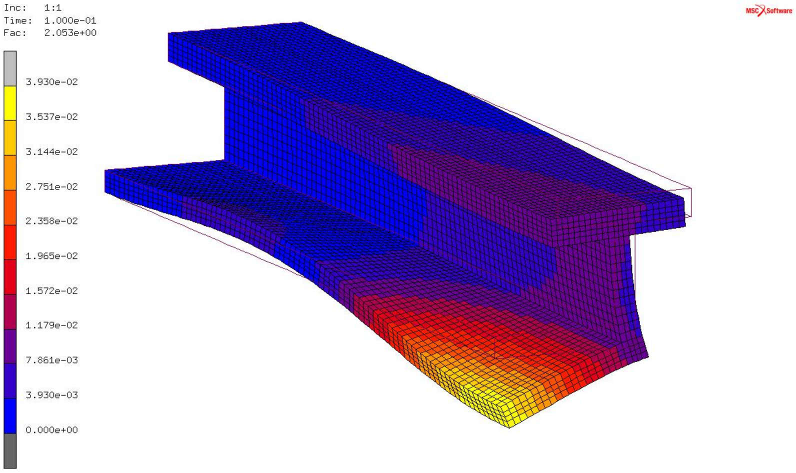

Figure 3.28: Mode shape 1 of virtual specimen C-0-0-300, illustrating “Local” deformation.

Figure 3.29 shows the third buckling mode shape of virtual specimen C-0-0-300, which also exhibited a “Local” buckling mode. While Figure 3.28 does illustrate a type of “Local” mode shape that was exhibited by many of the virtual specimens in the present validation study, the author has elected to also include Figure 3.29 in order to illustrate an example of a “Local” mode shape that includes more severe and obvious local effects.

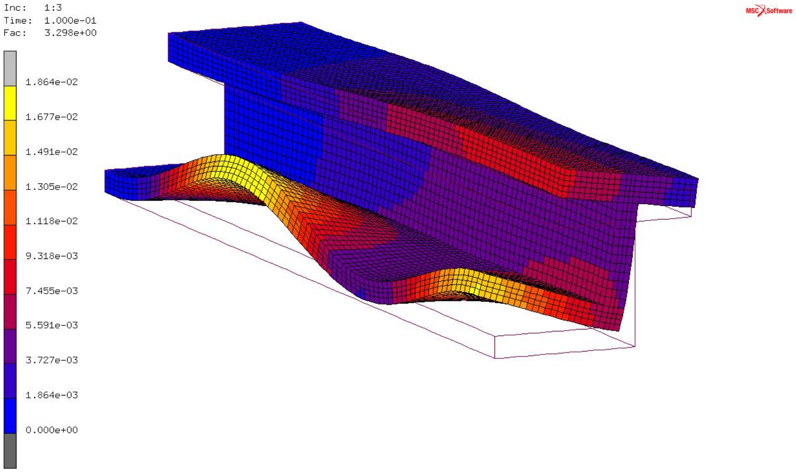

Figure 3.29: Mode shape 3 of virtual specimen C-0-0-300, illustrating “Local” deformation.

Figure 3.30 shows the first buckling mode shape of virtual specimen C-0-0-525, which serves as an example of a “F-T-S” buckling mode. It is evident that flexural, torsional, and shear deformations are all well represented by the buckling mode shape that is exhibited in this figure.

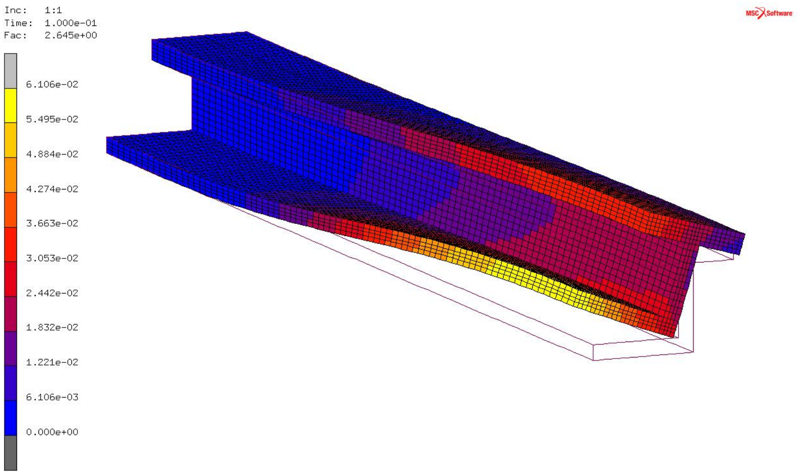

Figure 3.30: Mode shape 1 of virtual specimen C-0-0-525, illustrating “F-T-S” deformation.

Figure 3.31 shows the first buckling mode shape of virtual specimen C-0-45-525, which serves as an example of a “F-T-S (flex)” buckling mode. Although flexural, torsional, and shear deformations are all represented by the buckling mode shape that is exhibited in this figure, it is evident that flexural deformation is more dominant that torsional and/or shear deformations in this particular validation case.

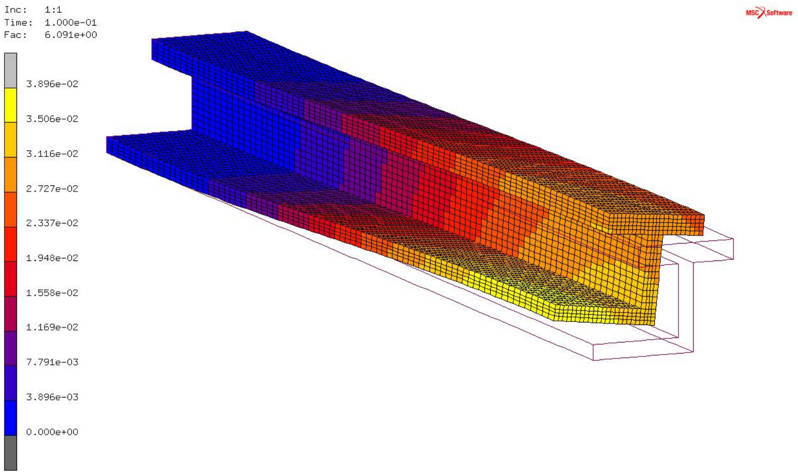

Figure 3.31: Mode shape 1 of virtual specimen C-0-45-525, illustrating “F-T-S (flex)” deformation.

Ultimately, the purpose of this computational validation study was to compare the FEA results presented in Tables 3.14, 3.15, and 3.16 with the buckling response predicted by the present analytical model discussed in the previous sections of this chapter. As such, input files were created to represent each of the virtual specimens presented in Table 3.11, and analytical simulations were run for each of these input files using the MathWorks® MATLAB® based analytical modelling computer program that was discussed in Section 3.17. This analytical modelling computer program was used to generate plots of critical buckling load (buckling load associated with the first mode shape) versus effective buckling length for each of the virtual specimen types (AL, C-0-0, and C-0-45); the critical buckling loads predicted by the aforementioned FE analyses for each of the relevant virtual specimens were over-laid on these plots in order to clearly illustrate correlation between these two very different analysis techniques. The first of these plots, which was created for the four virtual specimens featuring the AL composition, is shown in Figure 3.32. In addition, the numerical data pertaining to this particular comparison has been summarized in Table 3.17.

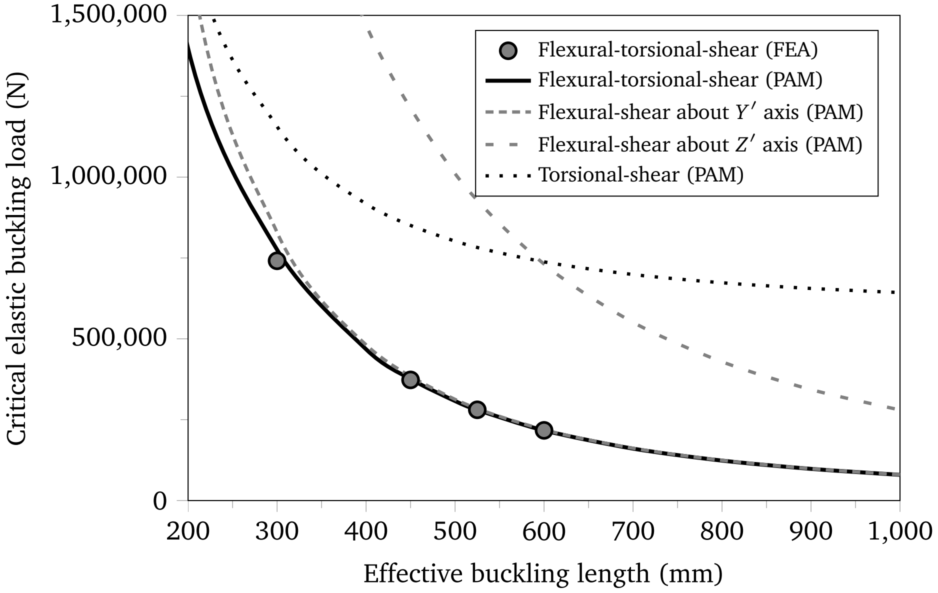

Figure 3.32: Validation results for flexural-torsional-shear buckling of AL virtual specimens. Legend entries designated as “FEA” represent results of the FE analyses, and legend entries designated as “PAM” represent results of the present MATLAB® based analytical modelling computer program.

Table 3.17: Comparison between critical buckling loads predicted by present analytical model and FEA simulations for AL virtual specimens. Note that the tabulated % difference values were calculated with respect to the FEA MARC® data points.

Virtual Specimen	Critical Buckling Load of 1st Mode (N)		% Difference
	FEA MARC®	Analytical Model MATLAB®	
AL-300	741233	775630	4.64
AL-450	373012	375770	0.74
AL-525	280592	280390	-0.07
AL-600	217006	216750	-0.12

Figure 3.33 compares the critical buckling loads predicted by the FE analyses with those of the MATLAB® based analytical modelling computer program, for each of the virtual specimens featuring the C-0-0 composition. The critical buckling load predicted by the FE analysis of virtual specimen C-0-0-300 has been intentionally omitted from this plot since it exhibited local deformations in its critical buckling mode shape ("Local" buckling mode shape). In addition, the numerical data pertaining to this comparison has been summarized in Table 3.18.

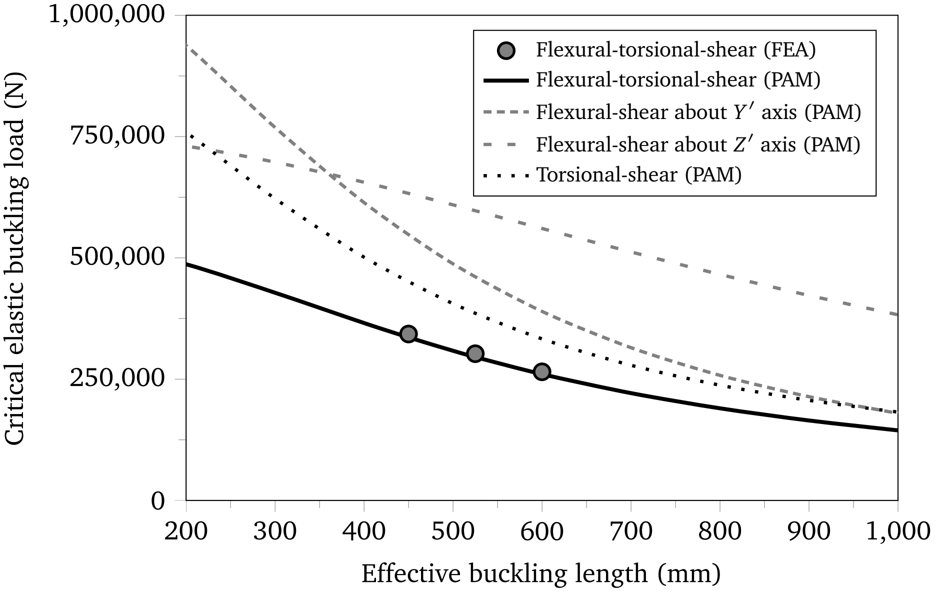

Figure 3.33: Validation results for flexural-torsional-shear buckling of C-0-0 virtual specimens. Legend entries designated as "FEA" represent results of the FE analyses, and legend entries designated as "PAM" represent results of the present MATLAB® based analytical modelling computer program.

Table 3.18: Comparison between critical buckling loads predicted by present analytical model and FEA simulations for C-0-0 virtual specimens. Note that the tabulated % difference values were calculated with respect to the FEA MARC® data points.

Virtual Specimen	Critical Buckling Load of 1st Mode (N)		% Difference
	FEA MARC®	Analytical Model MATLAB®	
C-0-0-450	343018	336120	-2.01
C-0-0-525	302456	295580	-2.27
C-0-0-600	265130	260300	-1.82

Figure 3.34 compares the critical buckling loads predicted by the FE analyses with those of the MATLAB® based analytical modelling computer program, for each of the virtual specimens featuring the C-0-45 composition. The critical buckling load predicted by the FE analysis of virtual specimen C-0-45-300 has been intentionally omitted from this plot since it exhibited local deformations in its critical buckling mode shape ("Local" buckling mode shape). In addition, the numerical data pertaining to this comparison has been summarized in Table 3.19.

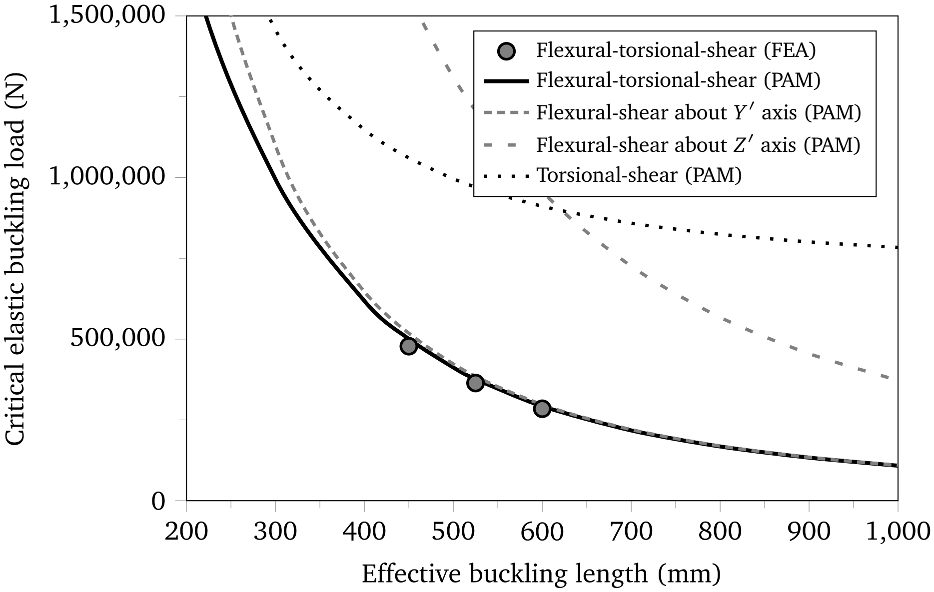

Figure 3.34: Validation results for flexural-torsional-shear buckling of C-0-45 virtual specimens. Legend entries designated as "FEA" represent results of the FE analyses, and legend entries designated as "PAM" represent results of the present MATLAB® based analytical modelling computer program.

Table 3.19: Comparison between critical buckling loads predicted by present analytical model and FEA simulations for C-0-45 virtual specimens. Note that the tabulated % difference values were calculated with respect to the FEA MARC® data points.

Virtual Specimen	Critical Buckling Load of 1st Mode (N)		% Difference
	FEA MARC®	Analytical Model MATLAB®	
C-0-45-450	477960	500550	4.73
C-0-45-525	364035	376380	3.39
C-0-45-600	284448	292360	2.78

3.18.5 Discussion

The buckling plots shown in Figures 3.32, 3.33, and 3.34 offer some insight regarding the cause of the various mode shapes that are tabulated in Tables 3.14, 3.15, and 3.16. The critical buckling modes of all of the AL and C-0-45 specimens were dominated by flexural deformations (see Figure 3.31); this is consistent with the observation that the Y' axis flexural-shear buckling curves shown in Figures 3.32 and 3.34 are considerably lower that the torsional-shear buckling curves shown in each of these figures. In fact, the Y' axis flexural-shear buckling curves are only marginally above the overall flexural-torsional-shear interaction buckling curves shown in Figures 3.32 and 3.34. Conversely, the critical buckling modes of all of the C-0-0 specimens were fairly balanced in their flexural-torsional-shear interaction, with only a slight bias toward torsional deformations (see Figure 3.30); this is consistent with the observation that the torsional-shear buckling curve shown in Figures 3.33 is slightly lower that either of the flexural-shear buckling curves shown in this figure, but still considerably higher than the overall flexural-torsional-shear interaction buckling curve.

It was mentioned previously that the present MATLAB® based analytical modelling computer program is capable of excluding various analytical procedures when calculating the overall flexural-torsional-shear interaction buckling response of a member. Many of the classical analytical calculations that are commonly employed for the analysis of beams composed of conventional metallic engineering materials tend to neglect the effects of transverse shear compliance. As such, the aforementioned utility in the present MATLAB® based analytical modelling computer program can be used to demonstrate the potential consequences of employing such classical calculation techniques for the analysis of structural members composed of FRP composite materials, or any other anisotropic and/or orthotropic materials that exhibit relatively low shear moduli in comparison with their longitudinal elastic moduli. Figure 3.35 is a reproduction of Figure 3.33 that has been modified to neglect the effects of transverse shear compliance within the flexural buckling analyses; as such, this plot utilizes conventional Euler flexural buckling analysis (see equation (3.110) in Section 3.14) in place of higher fidelity Engesser buckling analysis (see equation (3.121) in Section 3.14).

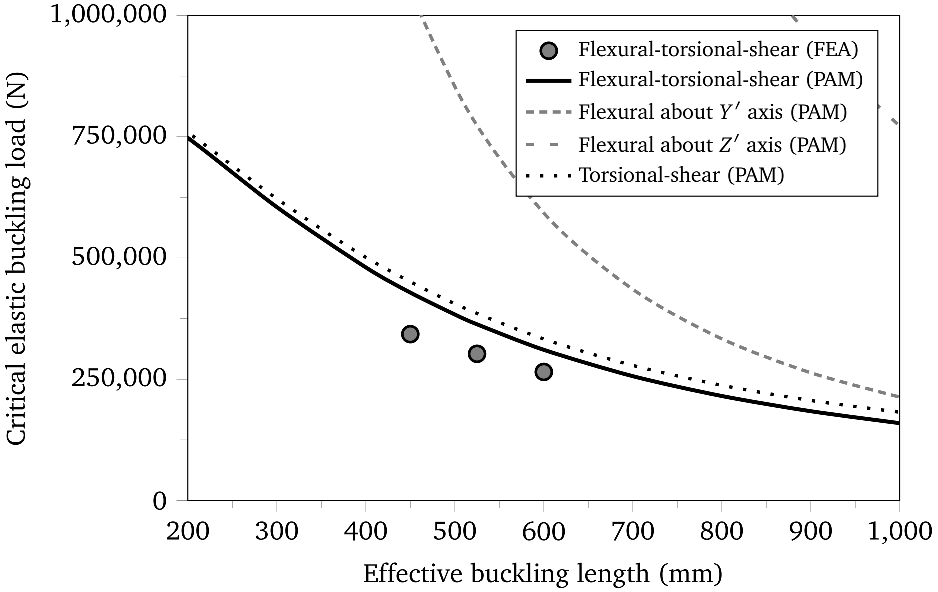

Figure 3.35: Validation results for flexural-torsional-shear buckling of C-0-0 virtual specimens, ignoring the effects of transverse shear compliance. Legend entries designated as "FEA" represent results of the FE analyses, and legend entries designated as "PAM" represent results of the present MATLAB® based analytical modelling computer program.

It is evident from Figure 3.35 that failure to account for transverse shear effects caused the MATLAB® based analytical modelling computer program to significantly over-predict the critical buckling loads exhibited by the FE analyses of the C-0-0 virtual specimens. In fact, in the case of specimen C-0-0-450, a 24.98% over-prediction was observed as a result of the exclusion of this particular mechanical phenomenon.

Figure 3.36 is a reproduction of Figure 3.33 that has been modified to neglect the effects of warping-shear compliance within the restrained torsional (warping) buckling analyses; as such, this plot utilizes a torsional buckling load calculation that is based upon conventional Vlasov warping theory (see equation (3.138) in Section 3.15) in place of a higher fidelity warping theory that accounts for the effects of warping-shear strains (see equation (3.139) in Section 3.15).

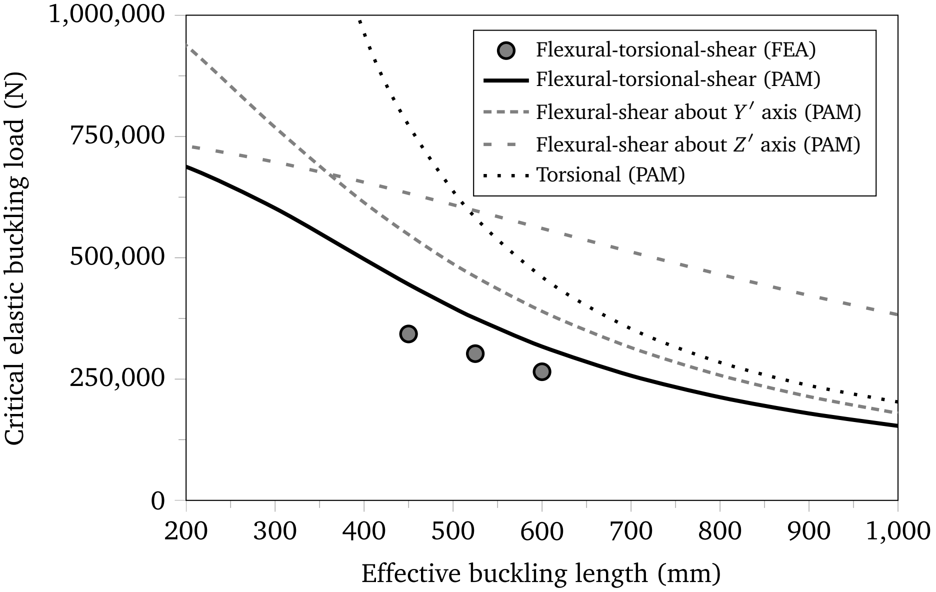

Figure 3.36: Validation results for flexural-torsional-shear buckling of C-0-0 virtual specimens, ignoring effects of warping-shear compliance in restrained torsion (warping) analyses. Legend entries designated as "FEA" represent results of the FE analyses, and legend entries designated as "PAM" represent results of the present MATLAB® based analytical modelling computer program.

It is evident from Figure 3.36 that failure to account for warping-shear compliance in the torsional buckling analyses caused the MATLAB® based analytical modelling computer program to significantly over-predict the critical buckling loads exhibited by the FE analyses of the C-0-0 virtual specimens. In fact, in the case of specimen C-0-0-450, a 29.82% over-prediction was observed as a result of the exclusion of this particular mechanical phenomenon. Furthermore, it is interesting to note that the exclusion of warping-shear compliance in the torsional buckling analyses has caused such a dramatic increase in the predicted torsional buckling loads, that that the Y' axis flexural-shear buckling buckling curve now falls below the torsional buckling curve. As such, this exclusion has, in fact, altered the overall buckling mode shape that is expected to govern the critical buckling load of this virtual specimen. This observation serves to illustrate the severity of the consequences that could result from employing conventional classical analytical methods to predict the performance of composite structures having relatively low transverse shear moduli in comparison with their longitudinal elastic moduli.

Figure 3.37 is a reproduction of Figure 3.33 that has been modified to neglect all mid-plane in-plane shear effects; as such, this plot utilizes a flexural buckling load calculation that is based upon conventional Euler buckling theory (see equation (3.110) in Section 3.14), and a torsional buckling load calculation that is based upon conventional Vlasov warping theory (see equation (3.138) in Section 3.15).

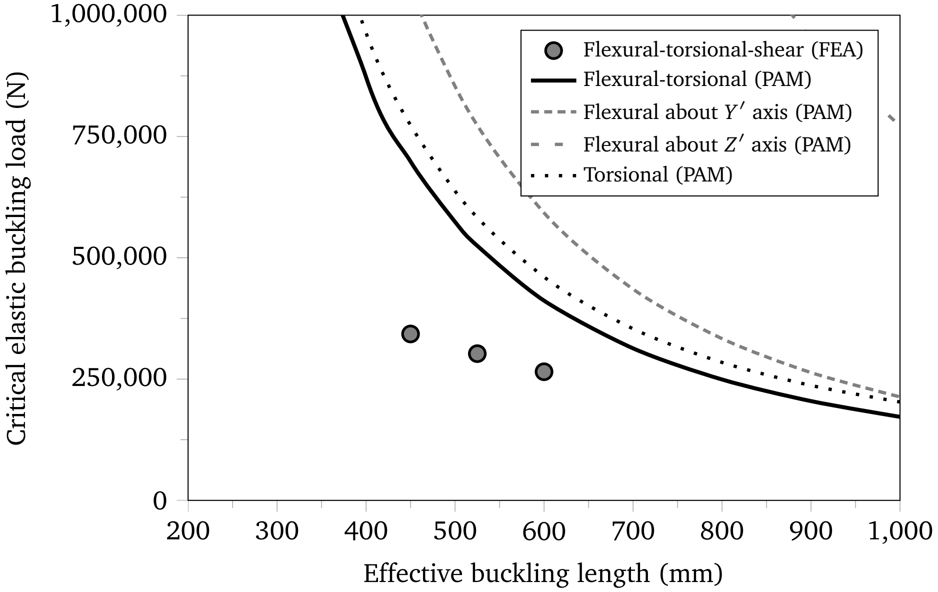

Figure 3.37: Validation results for flexural-torsional-shear buckling of C-0-0 virtual specimens, ignoring all effects of mid-plane in-plane shear compliance. Legend entries designated as "FEA" represent results of the FE analyses, and legend entries designated as "PAM" represent results of the present MATLAB® based analytical modelling computer program.

It is evident from Figure 3.37 that failure to account for mid-plane in-plane shear compliance caused the MATLAB® based analytical modelling computer program to significantly over-predict the critical buckling loads exhibited by the FE analyses of the C-0-0 virtual specimens. In fact, in the case of specimen C-0-0-450, a 103.63% over-prediction was observed as a result of the exclusion of these mechanical phenomena. This severe over-prediction is, once again, indicative of the potential dangers of employing conventional classical analytical methods to predict the performance of composite structures having relatively low transverse shear moduli in comparison with their longitudinal elastic moduli.

Although the primary purpose of the aforementioned computational validation study was to assess the validity of the present analytical model, the results of this study can also be used to demonstrate the light-weighting benefits of FRP structural systems. Recall from Tables 3.17 and 3.19 that specimens AL-450 and C-0-45-450 exhibited critical buckling loads (predicted by the present analytical model) of approximately 376 kN and 501 kN, respectively. Each of these specimens features a length of 450 mm, a cross-sectional area of 965 mm^2, and a total volume of 434250 mm^3. The aluminium and CFRP material models described in Tables 3.9 and 3.10 would likely have densities of approximately 0.0027 g/mm^3 and 0.0016 g/mm^3, respectively. As such, the mass of specimen AL-450 is found to be approximately 1.172 kg, and the mass of specimen C-0-45-450 is found to be approximately 0.695 kg. Normalizing the buckling load of each specimen with respect to its mass, the specific buckling loads of specimens AL-450 and C-0-45-450 are found to be approximately 321 kN/kg and 721 kN/kg, respectively. As such, it is evident that the column buckling strength per unit weight exhibited by specimen C-0-45-450 is more than double of that exhibited by specimen AL-450, which is illustrative of the considerable light-weighting benefits that can potentially be afforded by CFRP structural systems. If a similar J-section stringer were to be designed as a hybrid composite co-pultruded member comprising predominantly CFRP laminates with an aluminium strip embedded within one of the legs of the section, it is likely that only some of the aforementioned light-weighting benefits would be lost. Consider a specimen that is nearly identical to specimen C-0-45-450, with the exception that the material within the core region of its lower 47.5 mm by 7 mm flange (see Figure 3.24) has been replaced by the aluminium material model shown in Table 3.9. This hypothetical hybrid composite co-pultruded stringer specimen would have a critical buckling load (predicted by the present analytical model) of approximately 440 kN and a mass of approximately 0.760 kg, resulting in a specific buckling load of approximately 579 kN/kg. As such, the column buckling strength per unit weight exhibited by this hypothetical hybrid composite co-pultruded stringer would be approximately 80% greater than that exhibited by specimen AL-450. This simple numerical study has illustrated that the proposed hybrid composite co-pultruded aircraft stringer technology (see Section 2.2) is likely capable of offering most of the light-weighting benefits afforded by the current state-of-the-art CFRP aircraft structural systems, while simultaneously retaining the manufacturability and serviceability that previously could only be afforded by conventional metallic (aluminium) aircraft structural systems constructed using mechanical fasteners.

3.19 Limitations of the Present Analytical Model

3.19.1 General

While the present analytical method has been developed to be robust within the context of its intended application, it is not without limitations. The following section highlights some of the most severe limitations of the present analytical method. Although this section has been completed to the best of the author's ability, the reader must recognize that it would have been unreasonable to attempt to include every potential limitation of the present analytical method within this section. Nevertheless, the author has attempted to identify the most significant of these limitations.

3.19.2 Local Effects and Material Non-Linearity

The present analytical method has no provisions to account for the effects of material non-linearities, such as post-yield plasticity. While it would not have been impossible to account for such effects, doing so would have necessitated an iterative non-linear analysis technique, which would have severely complicated the model.

In addition, the present analytical method has no provisions to account for the effects of local buckling or crippling of individual legs of the member's cross-section. Such local deformations can often govern the critical buckling loads of columns having thin section walls, and very short effective buckling lengths. While these effects could certainly have been added to the present analytical model (various analytical procedures for doing so are readily available in the literature), this was deemed unnecessary for the intended purposes of the present analytical method.

Ultimately, in order to bound the breadth of this dissertation, any local buckling and/or crippling effects, as well as geometric and/or material non-linearities were all deemed to be beyond the scope and intended purpose of the present analytical model. As such, care must be taken when utilizing the present analytical method to predict the buckling loads of columns having very short effective buckling lengths, whereby material plasticity and/or local buckling modes could potentially govern the critical buckling load.

3.19.3 Coupling Effects

It was briefly mentioned in Section 3.5 that the present analytical model has not been formulated to account for all of the laminate coupling effects that were discussed in Section 1.2.9. While it would likely have been possible to account for such coupling effects within many of the analytical procedures discussed in this chapter, not all of these analytical procedures were formulated in a manner that can facilitate the inclusion of these coupling effects. The treatment of nodal regions of the cross-sectional geometry (see Sections 3.6.2 and 3.6.3) was formulated in a manner that assumes that the elastic centroid of each leg is coincident with its geometric centroid; conversely, a laminate that is susceptible to coupling between in-plane and out-of-plane behaviours will generally exhibit an elastic centroid that is located at a different through-thickness elevation than its geometric centroid (see Section 3.5).

Although a simpler treatment of the nodal regions might have facilitated the implementation of provisions to account for some of the more complex laminate coupling effects, this would likely have negated the present analytical model's unique ability to accurately predict the bending stiffness of sections having legs of "moderate thickness" (see Section 3.2). Since the present analytical model was originally formulated for the purpose of predicting the elastic stability of aircraft wing stringers (which often exhibit open cross-sections of somewhat bulky dimensions), the author felt that it was important for the present model to be formulated in a manner that is not limited to analyses of sections having extremely thin walls. In addition, it was noted by the author that, at the present time, many aircraft manufacturers have a tendency to make a concerted effort to utilize FRP composite laminates that are balanced and symmetric in as many applications as is practicable; this is done primarily for the purpose of simplifying engineering analyses by eliminating all coupling effects except for bending-twisting coupling. As such, the additional analytical complexity that would result from the inclusion of provisions for all laminate coupling effects would not be warranted for many of the analyses that would be common in the aerospace industry.

Ultimately, the present analytical model was formulated in a manner that is generally limited to analyses of sections comprising balanced and symmetric or balanced and anti-symmetric laminates having a large number of layers such that these laminates can essentially be modelled as homogeneous and orthotropic within the laminate x-y-z coordinate system. It is worth noting that the torsional stiffness analytical procedure discussed in Section 3.11 is, in fact, capable of predicting the fully coupled torsional response of any laminate; however, most of the other analytical procedures discussed in this chapter do exhibit the aforementioned limitation.

3.19.4 Thickness of Individual Legs of the Cross-Section

It was previously mentioned that the present analytical model includes provisions to account for cross-sectional geometries that include legs of “moderate thickness” (see Section 3.2). However, it should be noted that not all analytical procedures in this model received such provisions. Calculations for bending stiffness and torsional stiffness were both formulated in a manner that accounts for cross-sectional dimensions that would not be conducive for the use of thin plate assumptions. Conversely, such provisions were not included in the analytical procedures used to calculate the shear-centre location and Timoshenko shear correction factor. On the contrary, the calculations of the shear-centre location and Timoshenko shear correction factor were both formulated in a manner that neglects the presence of x-z shear stresses acting through the thickness of each leg of the section. While this exclusion may seem to be inconsistent with the aforementioned efforts to account for cross-sectional geometries that include legs of “moderate thickness”, the consequences of such an exclusion in the context of calculations of the shear-centre location and Timoshenko shear correction factor would be far less severe than a similar exclusion made in the context of the bending stiffness or torsional stiffness.

The inclusion of shear effects in the present analytical model constitutes improved analytical fidelity that only becomes significant in the context of structural members composed of orthotropic materials that have very low shear moduli in comparison with their longitudinal elastic moduli (such as laminated FRP composites). While this improved analytical fidelity is certainly warranted for inclusion in the present analytical model, it is doubtful that a significant further increase in fidelity would be afforded by accounting for the presence of x-z shear stresses acting through the thickness of each leg of the section. It is evident from Figure 3.35 that the severity of the consequences of ignoring the effects of transverse shear compliance in a column buckling analysis is inversely proportional to the effective buckling length of the column, and hence, the slenderness ratio of the column. Similarly, in the context of flexural buckling with provisions for transverse shear compliance (see discussion on Engesser buckling in Section 3.14.2), the severity of the consequences of ignoring the effects of x-z shear stresses acting through the thickness of each individual leg of the section would likely be inversely proportional to the slenderness ratio of each individual leg of the column's cross-section. As such, the consequences of ignoring the effects of x-z shear stresses acting through the thickness of each individual leg of the section would likely only become significant in the context of columns having extremely short effective buckling lengths. When such short effective buckling lengths are employed, it is likely that the effects of local buckling and crippling of individual legs of the cross-section would govern the critical buckling load of the member (see Section 3.19.2), thus negating the benefits of including provisions to account for the effects of x-z shear stresses acting through the thickness of each individual leg of the section. As such, it is unlikely that a tangible improvement in analytical fidelity would result from the inclusion of the effects of x-z shear stresses acting through the thickness of each individual leg of the section. Nevertheless, this shortcoming does help to explain why the present analytical model will tend to slightly over-predict the flexural-shear buckling loads of short beams and columns that comprise legs having very low through-thickness x-z shear moduli and relatively high in-plane x-y shear moduli (see Figure 3.34 and Table 3.19).

Ultimately, in the interest of achieving a reasonable balance between analytical fidelity and simplicity, it was decided that the analytical procedures employed for the calculations of the shear-centre location and Timoshenko shear correction factor shall both be formulated in a manner that neglects the presence of x-z shear stresses acting through the thickness of each leg of the section.

3.19.5 Boundary Conditions

The present analytical model does not enable user stipulated shear deformation restraints; as such, it is incapable of predicting a fully restrained end whereby cross-sections are required to remain planar. The analytical procedures discussed in Sections 3.10 and 3.12.3 calculate cross-sectional distributions of shear stresses and strains based upon the assumption that the member is very long, and its cross-section is free to deviate from its initial planar state due to the presence of shear strains. Conversely, in the vicinity of a rigid support at the fixed end of a structural member, the member might be restrained such that its cross-section must remain planar. As such, the assumptions employed in the present analytical model will tend to result in a slight under-prediction of shear stiffness in the vicinity of a fixed support. This phenomenon is briefly discussed in Section 1.2.4 of Michael David Hayes's Ph.D. dissertation [32]. Although this discrepancy is really only relevant in the context of very short beams and columns, it does help to explain why the present analytical model will tend to slightly under-predict the flexural-shear buckling loads of short beams and columns that comprise legs having very low in-plane x-y shear moduli (see Figure 3.33 and Table 3.18).

3.19.6 Discretization of Cross-Sectional Geometry

In Section 3.11.4, a novel analytical modelling procedure was presented to predict the torsional stiffness of thick rectangular laminated plates of finite width. Although this torsion model does account for the distribution of both x-y and x-z stresses over the cross-sectional area of thick rectangular laminated plates, it was formulated in a manner that assumes that only a single rectangular plate is to be modelled, and that this rectangular plate comprises only a single laminate. Strictly speaking, the torsion model presented in Section 3.11.4 is not capable of correctly modelling the stress distribution over the cross-section of a member comprising more than one leg; however, the methodology described in Section 3.11.9 was developed to utilize the present torsion model in a piece-wise fashion to approximate the torsional stiffness of beams and/or stringers having open sections built up of multiple legs comprising FRP composite laminates. This expands considerably upon the breadth of applications afforded to the present torsional stiffness formulation; however, it is important that the engineer is aware of the limitations of the methodology described in Section 3.11.9.

In essence, the methodology described in Section 3.11.9 assumes that any given leg of the cross-section (segment of laminated material) has either two free edges, one free edge, or is very distant from any free edges (see Figures 3.17, 3.18, and 3.19 in Section 3.11.9). This final stipulation is significant because it implies that, if a leg of the section has no free edges (meaning that it is surrounded by two or more other legs), then all of the shear stresses that are generated by a torsion moment will occur parallel to the mid-plane of the laminate (within the x-y plane), and there will be no through-thickness x-z shear stresses present within this leg. In addition, this assumption implies that, in the case of a leg of the section that has only one free edge, the state of stress at the opposite edge of the leg (which is in contact with one or more adjacent legs of the section) will comprise exclusively in-plane x-y shear stresses, and there will be no through-thickness x-z shear stresses present at this non-free (shared) edge of the leg. These assumptions are of little concern in the case of members that are designed such that any leg of the section that terminates in a free edge is relatively long in comparison with the total sum of the lengths of all of the legs of the section. Conversely, the present torsion model will tend to over-predict the torsional stiffness of a member that has been designed such that it includes relatively short legs that terminate in free edges, and longer intermediate legs in between these terminus legs.

The severity of the aforementioned shortcoming is dependent upon a variety of factors, including: the number of free edges in the section, the thickness of the legs that feature free edges, and the through-thickness x-z shear modulus of the legs that feature free edges. However, under all circumstances, the present torsion model will yield more accurate and more conservative predictions of torsional stiffness than more conventional analysis techniques that are purely based upon CLPT and ignore the effects of through-thickness x-z shear stresses. This is because the present torsion model will always make at least some provisions to account for the effects of through-thickness x-z shear stresses, thus improving upon the fidelity of the analysis.

Chapter 4

Experimental Validation of Analytical Restrained Torsion Model

4.1 Purpose and Scope

Section 3.12.3 presented a novel means of augmenting classical Vlasov warping analysis such that it accounts for the effects of warping-shear strains, and Section 3.13 explained how this model can be employed in a unidimensional beam-type analytical model. It was mentioned in these sections that other researchers have produced similar models in recent years. Much of these similar works have been computationally validated using the FE method (see Section 1.4.2); however, the author is not aware of any similar restrained torsion (warping) analytical models that have been validated using experimental methods.

The following chapter details an experimental program that was formulated to validate the complete analytical model for restrained torsion that was described in Sections 3.12 and 3.13. Slotted tube specimens were prepared to function as beams having thin-walled open sections (see Section 4.2). These specimens were experimentally tested under restrained torsion conditions (see Section 4.6), and the stiffness of each specimen was monitored and recorded (see Section 4.7). The mechanical properties of these tube specimens were experimentally quantified (see Section 4.4), and the relevant engineering section constants were calculated (see Section 4.5). These section constants were then used to carry out the analytical method described in Sections 3.12 and 3.13, and the results of these analyses were compared with the results of the aforementioned experimental restrained warping tests (see Section 4.7).

4.2 Specimens

Since this experimental program was intended for validation purposes, it was decided that the experimental specimens should comprise mass-produced materials having highly repeatable mechanical properties and cross-sectional geometries. In addition, to maximize the effect that warping-shear strains have upon the restrained torsional (warping) stiffness, it was decided that the selected experimental test specimens should have a relatively high longitudinal elastic modulus in conjunction with a relatively low in-plane shear modulus. Perhaps the most extreme example of mass-produced structural members having the aforementioned desired properties is pultruded CFRP members comprising epoxy resin and continuous longitudinally oriented unidirectional fibres.

Pultruded CFRP members are commercially available in a wide variety cross-sectional geometries and sizes. For the present investigation, it was desirable to select a member having a thin-walled open cross-sectional geometry; however, it was also necessary to ensure that the specimens could undergo some sort of preliminary testing to ascertain the mechanical properties of the materials of which they are composed. As such, it was decided that the experimental specimens would have thin-walled hollow round tube sections. Such a tubular specimen geometry would be ideal to facilitate testing to determine the mechanical properties of the materials present in the specimens. In addition, a thin longitudinal slot could be machined through the wall of each of these tube specimens, thus yielding a thin-walled open cross-sectional geometry that would be appropriate for experimental testing of restrained torsion (warping).

Thin-walled pultruded CFRP tubes comprising epoxy resin and continuous longitudinally oriented unidirectional carbon fibres were sourced from Goodwinds LLC of Mount Vernon, Washington, USA. These tubes were found to have an outside diameter of 19.0467 ± 0.0071 mm, and a wall thickness of 2.6067 ± 0.0644 mm (see Table A.1 in Appendix A). These tubes were used for the majority of the structural tests described in this chapter. In addition, it was decided that the present experimental investigation should also include some control specimens comprising a conventional homogeneous and isotropic metallic engineering material, and having a cross-sectional geometry that is similar to the aforementioned CFRP specimens. As such, the author sourced generic hardware-grade extruded aluminium tubes having an outside diameter of 19.0878 ± 0.0618 mm, and a wall thickness of 1.2700 ± 0.0574 mm (see Table A.2 in Appendix A).

To ascertain the mechanical properties of the materials of which each type of specimen was composed, it was necessary to conduct a series of structural tests on the tubes in their original unaltered condition (prior to creating a longitudinal slot in each specimen). Conversely, all restrained torsion (warping) tests were conducted using slotted tube specimens in order to ensure that the warped specimens were of open cross-sectional geometry. As such, a single slot was cut parallel to the longitudinal axis of each warping specimen using a carbide end-mill bit. These slots were measured to have a width of 1.4555 ± 0.0403 mm in the CFRP tube specimens, and a width of 1.5822 ± 0.0286 mm in the aluminium tube specimens. A more detailed explanation of the geometry of these warping specimens is included in Section 4.6. Table 4.1 summarizes the cross-sectional dimensions of each type of tube specimen included in the present experimental validation program.

Table 4.1: Measured cross-sectional geometry of tube specimens used in experimental validation of analytical model for restrained torsion (see Appendix A).

Dimension	CFRP Tubes	Aluminium Tubes
Outside Diameter (mm)	19.05 ± 0.007	19.09 ± 0.062
Wall Thickness (mm)	2.61 ± 0.064	1.27 ± 0.057
Width of Slot (mm)	1.46 ± 0.040	1.58 ± 0.029

4.3 Apparatus

4.3.1 General

The following experimental validation program necessitated the use of both torsional and flexural testing procedures. Sections 4.3.2 and 4.3.3 detail the apparatus that were necessary to complete each of these torsional and flexural tests, respectively. In particular, these apparatus include: structural loading equipment, instrumentation, data acquisition equipment, and any other miscellaneous hardware that were necessary to carry out each of these experimental structural tests.

4.3.2 Apparatus for Torsion Tests

Torsion Testing Machine

Unfortunately, the author did not have access to a torsion testing apparatus that was appropriate for the present experimental investigation. The experimental torsion tests described in Sections 4.4.2 and 4.6 necessitated a machine that would be capable of imposing torque upon specimens of varying lengths, while accurately and precisely measuring torque and torsional rotation angles. As such, a bespoke torsion testing machine was designed by the author and one of his colleagues, and was subsequently manufactured by a local fabrication shop called REKO International Group Inc. This bespoke torsion testing machine is shown in Figure 4.1.

Figure 4.1: Photograph of bespoke torsion testing machine.

The primary structure of this torsion testing machine comprises a 1.6 m long blanchard-ground steel table, which was designed to have a torsional stiffness that was a minimum of 100 times greater than the stiffest specimen ever expected to be tested using the machine. The stiffness of this table is of critical importance in order to prevent erroneous measurements of torsional rotation angles during a torsion test. It is estimated that this table has an end-to-end torsional stiffness of more than 22000 Nm/Degree (over a 1.4 m long torsional gauge length). This table rests upon four steel legs, which are securely anchored to the concrete floor of the laboratory in which it resides; this further increases the apparent stiffness of the table. The axis that is parallel to the 1.6 m long dimension of this table will subsequently be referred to as the “longitudinal axis” of the table.

A 19.05 mm thick rectangular steel vertical flange (referred to as the “dead flange”) is mounted atop one end of the table, and is fastened in such a manner that its position can be adjusted along the longitudinal axis of the table. Regardless of its position, the dead flange is always oriented such that its plane is perpendicular to the longitudinal axis of the table. This dead flange has a smooth milled surface, and features a circular bolt pattern to facilitate mechanical fastening of specimens or specimen mounting fixtures to the flange.

A steel box assembly is fastened atop the end of the table that is opposite the position of the aforementioned dead flange. This steel box houses a 50 mm diameter steel shaft (referred to as the “main shaft”) oriented parallel to the longitudinal axis of the table, which is supported by two large ball bearing assemblies mounted within the walls of the aforementioned steel box assembly. A 19.05 mm thick circular steel flange (referred to as the “live flange”) is welded to the end of this shaft that faces the dead flange at the opposite end of the table. This live flange also has a smooth milled surface, and features a circular bolt pattern matching that of the dead flange. The main shaft also supports a large sprocket having a pitch radius of 176.92 mm. A 530 motorcycle chain is engaged to this sprocket, and hangs down below either side of the sprocket. On one side of the sprocket, the motorcycle chain is fastened to a vertically oriented Acme threaded steel rod that hangs within a steel enclosure mounted beneath the table. By turning a nut that is threaded onto this Acme threaded rod below this enclosure, the entire Acme threaded rod is pulled downward through its enclosure, which pulls downward on the motorcycle chain, thus rotating the main shaft and, consequently, the live flange as well. On the other side of the sprocket, the motorcycle chain is fastened to a counter-weight, which balances the weight of the aforementioned Acme threaded rod assembly.

An experimental test specimen can be oriented parallel to the longitudinal axis of the table and fastened to the live and dead flanges located at each end of the torsion testing machine. When the Acme nut is turned and the threaded rod pulls downward on the motorcycle chain, the live flange turns about the axis of the main shaft while the dead flange remains in its original fixed orientation; this imposes a twisting deformation upon the experimental test specimen. Figure 4.2 is a simplified isometric line drawing illustrating the aforementioned architecture of this torsion testing machine; some details have been omitted from this drawing to help clarify the major components that were previously discussed in this section.

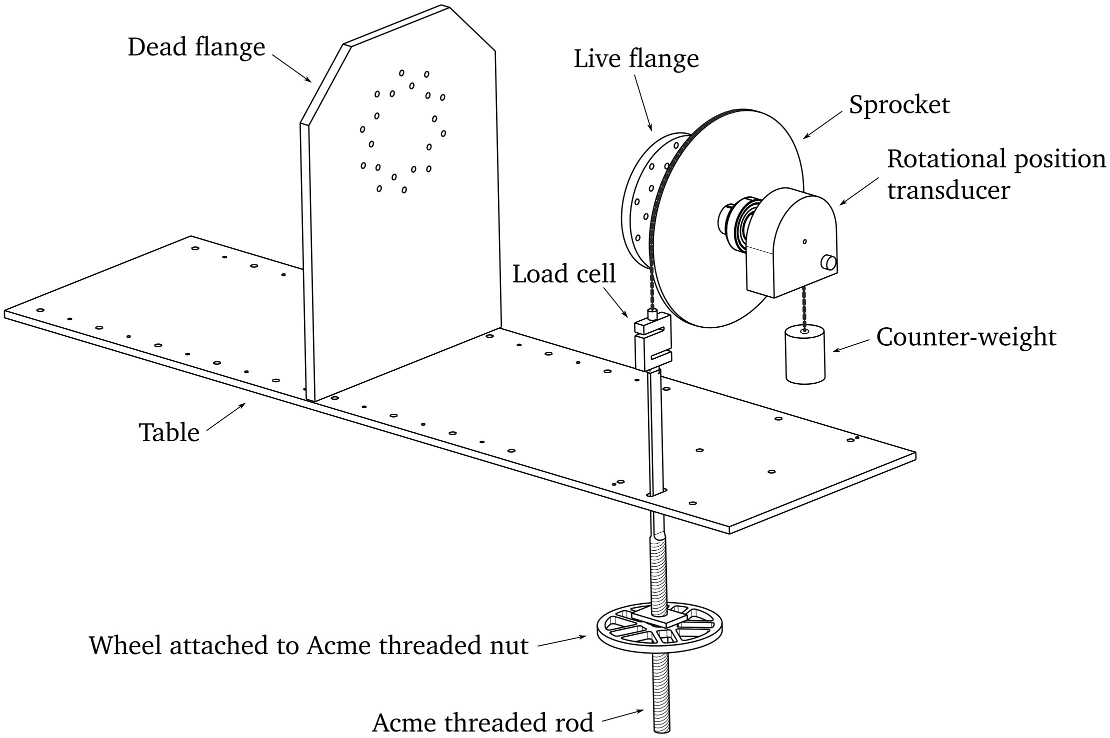

Figure 4.2: Isometric line drawing of torsion testing machine.

Torsion Testing Instrumentation

In order to determine the torsional stiffness of a specimen being tested using the torsion testing machine, it was necessary to simultaneously monitor the magnitude of the torque and angle of torsional rotation imposed upon the specimen. This was accomplishing by incorporating an S-Type load cell and a rotational position transducer in the design of the aforementioned torsion testing machine.

An S-Type load cell was installed at the connection point between the motorcycle chain and the Acme threaded rod (see Figure 4.2) such that the tension in the chain could be measured. The magnitude of this tension could then be multiplied by the pitch radius of the sprocket (176.92 mm) to arrive upon the torque imposed upon the specimen at any given time during a torsion test. The sensor that was selected for this purpose is a Model 60001A300-1000 S-Beam load cell, manufactured by Sensortronics™ of the Vishay® Precision Group. This axial tension-compression load cell has a maximum capacity of 1334.47 N (300 lbs), and a safe overload limit of 150% of this capacity. The calibration data that was provided with this sensor indicates that it has a full-scale output of 3.582 mV/V, an input resistance of 380 Ohms, an output resistance of 350 Ohms, and requires 10 V of DC excitation. The total manufacturer specified combined error for this instrument is reported as ±0.02% of the full-scale output (in accordance with NTEP® Class III specifications), which equates to an error of ±0.267 N of linear force. In the context of the torsion testing machine used in the present investigation, this equates to an error of ±47.22 N·mm of torque.

A rotational position transducer was installed at the free end of the main shaft of the torsion testing machine (see Figure 4.2). This rotational position transducer was positioned such that the axis of its shaft is coincident with the axis of the main shaft of the torsion testing machine. The shaft of the rotational position transducer was inserted into a small hole at the end of the main shaft of the torsion testing machine, and a set-screw was installed to ensure that both of these shafts rotate together. The enclosure of the rotational position transducer was held stationary by the surrounding structure of the torsion testing machine. As such, any rotation of the main shaft of the torsion testing machine (and hence, and rotation of the live flange) can be directly measured by the rotational position transducer. The sensor that was selected for this purpose is the Model RT9101-0001-131-4110 potentiometric rotational transducer, manufactured by Celesco™ Transducer Products Inc of Measurement Specialties™ Inc. This rotational sensor has a full stroke range of 360° (2π radians), and is reported to have infinite resolution. The calibration data that was provided with this sensor indicates that it has a full-scale output of 2.661 mV/V/degree. While this sensor is reported to accept a maximum of 30 V of AC or DC excitation, 10 V of DC excitation was supplied during the present investigation. The calibration error for this professionally calibrated instrument is reported as ±0.179% of the observed angle of rotation. In addition, the manufacturer reports a repeatability of ±0.02% of the full-scale output, which equates to a repeatability of ±0.072° (±0.00126 radians) of rotation angle.

Torsion Testing Data Acquisition Equipment

In order to excite, monitor, and record data from the aforementioned load cell and rotational position transducer, it was necessary to employ a data acquisition system and data acquisition software. The System 8000 data acquisition system, manufactured by Micro-Measurements® of the Vishay® Precision Group, was selected for this role.

The main hardware component of the System 8000 is the Model 8000-8-SM Scanner. This eight channel data acquisition scanner utilizes a built-in 32 bit floating point digital signal processor operating at 300 MHz, a 24 bit analogue-to-digital converter, and employs Finite Impulse Response multistage filtering to remove noise. It is capable of accepting inputs from a variety of sensors including: thermocouples, high-level voltage signal sensors, strain-gauge-based transducers, and strain-gauges. Each instrument, which in this case includes a load cell and a rotational position transducer, connects to the Model 8000-8-SM Scanner using conventional Ethernet cables with 8-pin TIA/EIA RJ45 connectors. Strain-gauge based millivolt-level sensors, such as the S-Type load cell used in this investigation, are monitored with a resolution of 0.25 μV, and amplified with a DC gain accuracy of ±0.05 %. High-level sensors, such as the rotational position transducer used in this investigation, are monitored with an effective resolution of 100 μV. The excitation voltage of the Model 8000-8-SM Scanner is ±10 mV, with a resolution of 3 mV.

The Model 8000-8-SM Scanner is connected to a host personal computer via an additional Ethernet cable. The Micro-Measurements® StrainSmart® data acquisition software operates on this host personal computer, and is responsible for configuring, controlling, and acquiring data from the Model 8000-8-SM Scanner. For all torsion tests carried out during the present experimental program, experimental data was acquired at a rate of 10 Hz.

Miscellaneous Materials Used for Torsion Testing

Fixtures were needed in order to fasten each experimental specimen to the live and dead flanges at each end of the torsion testing machine. These fixtures comprised 26 mm thick aluminium rectangular plates that were cut using a water-jet machine. Each fixture plate featured a hole near each of its four corners; these holes were used to mechanically fasten the plate to one of the flanges of the torsion testing machine. One or two larger holes were created near the centre of each plate; each experimental specimen was potted into to these larger holes using an epoxy resin adhesive. These aluminium end fixture plates are explained more thoroughly in Sections 4.4.2 and 4.6.

Henkel LePage® Gel Epoxy (Henkel product number 1165246) was selected as the epoxy resin adhesive that was employed to pot each specimen into the aluminium end fixture plates. The manufacturer of this expoy resin reports that it has a tensile shear strength of 13.355 ± 0.614 MPa when adhered to sandblasted aluminium and allowed to cure for 24 hours. In addition, the manufacturer reports that this epoxy resin exhibits a Shore D hardness of 81 ± 2, provided that it is allowed to cure for seven days, its surface is abraded, and then the hardness of this abraded surface is tested one day later.

Care was taken to ensure that a rigid potted joint was created at each end of each specimen. Prior to potting each specimen into its end fixture plates, both the specimen and its end fixture plates were thoroughly cleaned with isopropyl rubbing alcohol. A generous quantity of the epoxy resin was then applied, and was allowed a minimum of 24 hours to cure prior to each structural test.

4.3.3 Apparatus for Bending Tests

Flexural Testing Machine

The experimental flexural tests described in Section 4.4.3 required the use of a structural testing machine that could impose symmetric 3-point bending loadings on beam specimens. For this purpose, the author elected to utilize an MTS® Criterion™ Model 43 (C43.304) Universal Testing System, manufactured by the MTS® Systems Corporation. This electromechanical axial tension-compression structural testing machine comprises a screw-driven cross-head with two guide columns, and is actuated by an AC servo motor for precise stroke control. This machine is rated for a maximum allowable load of 50 kN, making it well suited for most small-scale structural tests involving tension, compression, direct shear, and/or bending. The machine also features an adjustable cross-head speed ranging between 0.005 mm/minute and 750 mm/minute, thus facilitating tests requiring a large range of strain rates.

Flexural Testing Instrumentation

The MTS® Criterion™ Model 43 (C43.304) Universal Testing System incorporates an integrated encoder system to monitor its cross-head position, which can be used to directly monitor the vertical displacement of the mid-span loading point during a 3-point bending test. The manufacturer reports that this cross-head position output has a resolution of 0.00006 mm, and is accurate to within ±0.5% of the true cross-head position.

The MTS® Criterion™ Model 43 (C43.304) Universal Testing System also incorporates a precise axial tension-compression load cell that features Transducer Electronic Data Sheet self-identification capabilities (in accordance with the IEEE 1451.4 standard), which enables the Criterion™ Model 43 loading machine to automatically download and apply the appropriate calibration information for the installed load cell. The manufacturer reports that this load cell has a force accuracy of ±1.0% of the applied force when the applied force is between 250 N and 500 N, and an accuracy of ±0.5% of the applied force when the applied force is between 500 N and 50 kN.

Flexural Testing Data Acquisition Equipment

The MTS® Criterion™ Model 43 Universal Testing System is designed to communicate with a personal computer running the MTS® TestSuite™ TW data acquisition software. This software is responsible for controlling the Criterion™ Model 43 loading machine throughout the duration of a structural test, and it simultaneously monitors and records all data acquired from the load cell and cross-head position encoder. The software is also fully configurable such that the user can define the parameters and sequencing of a structural test to suit the requirements of the experimental program. For all flexural tests carried out during the present experimental program, experimental data was acquired at a rate of 2 Hz.

Miscellaneous Materials Used for Flexural Testing

Strictly speaking, the MTS® Criterion™ Model 43 Universal Testing System is only capable of applying direct axial tension or compression forces. In order to utilize this machine for flexural tests, it was necessary to employ a symmetric 3-point bending set-up whereby the machine imposed a transverse vertical load upon each simply-supported beam specimen (see Section 4.4.3). As such, a stiff beam (known as a "spreader beam") was needed to serve as a support structure for each simply-supported beam specimen; the MTS® Model 642.25 Bend Fixture spreader beam was selected for this purpose, as it integrates well with the Criterion™ Model 43 loading machine. This spreader beam was mounted horizontally within the Criterion™ Model 43 loading machine, centred beneath the cross-head of the machine. Two precision-machined steel cylinders, measuring 40 mm in diameter, were fastened to the top surface of the spreader beam; these cylinders acted as roller-supports at each end of each simply-supported beam specimen. A similar steel cylinder was fastened to the cross-head of the Criterion™ Model 43 loading machine; this cylinder served as the load application point at the mid-span of each simply-supported beam specimen. Figure 4.3 shows the spreader beam, the two cylindrical roller supports atop each end of the spreader beam, and the cylindrical load application roller above the mid-span of the spreader beam.

Figure 4.3: Photograph of MTS® Model 642.25 spreader beam used during 3-point bending tests.

The spreader beam featured a ruled top surface with 0.5 mm graduations; this ruled surface facilitated precise positioning of the roller supports, such that the span of the simply-supported beam specimens could be measured with no more than ±0.25 mm of measurement error. Figure 4.4 is a photograph of one of the cylindrical roller supports mounted atop one end of the spreader beam; the aforementioned ruled top surface of the MTS® Model 642.25 spreader beam is also visible in this figure.

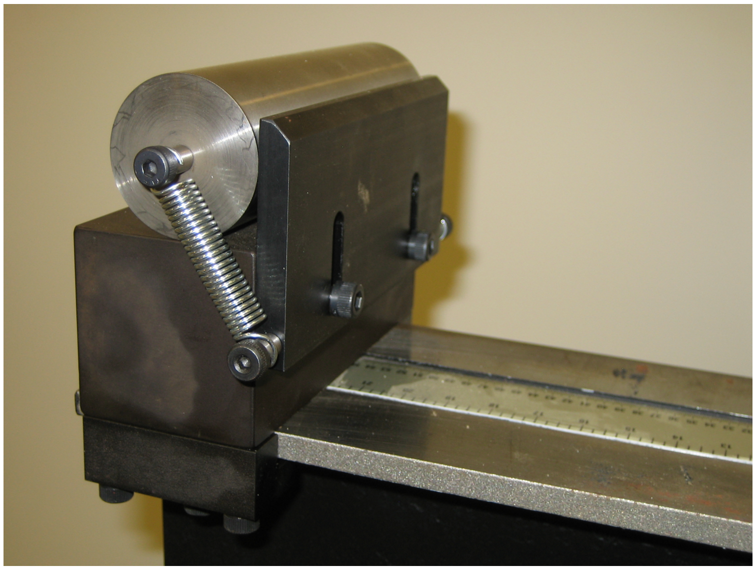

Figure 4.4: Photograph of a cylindrical roller support mounted atop one end of the spreader beam. This photograph also shows the ruled top surface of the MTS® Model 642.25 spreader beam, which helps to ensure precise positioning of the roller supports.

4.4 Determination of Mechanical Properties of Tube Specimens

4.4.1 General

Before any analyses could be carried out on the experimental specimens, it was first necessary to assess the mechanical properties of the materials that these specimens comprised. In particular, it was necessary to determine the value of the longitudinal elastic modulus E_{XX} (which in this case was the same as the local longitudinal elastic modulus E_{xx}), and the in-plane shear modulus G_{xy}. In the case of the tubes used for the present experimental validation study, the value of G_{xy} was the same as the global transverse shear moduli G_{XY} and G_{XZ}.

These mechanical properties were determined using a series of experimental tests that were carried out on the tube specimens in their virgin, un-slotted configurations. Figure 4.5 illustrates some of the cross-sectional geometric dimensions of these un-slotted tubes that will be referenced in subsequent discussions in this section (Section 4.4).

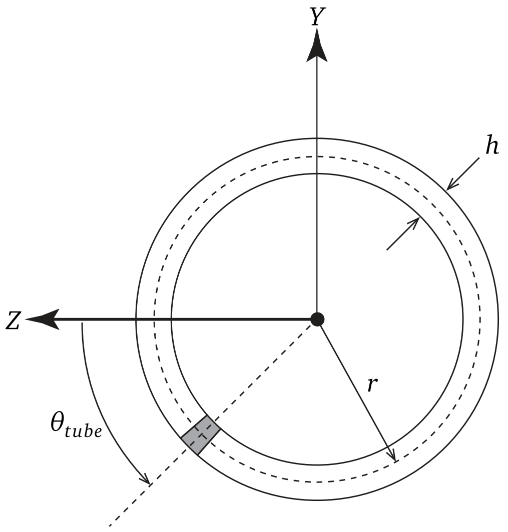

Figure 4.5: Cross-sectional geometry of un-slotted hollow tube.

It is evident from Figure 4.5 that the origin of the global X-Y-Z coordinate system is positioned at the centre of the tube, and the X axis is aligned with the longitudinal axis of the tube. It is also shown in Figure 4.5 that r represents the radius from the centre of the tube to the mid-plane of the tube wall, h represents the thickness of the tube wall, and θ_{tube} is an angular coordinate representing the swept angle between the Z axis and the position of interest (shaded region in Figure 4.5), measured about the longitudinal X axis of the tube. Table 4.2 was derived from Table 4.1 in order to summarize the cross-sectional dimensions of each type of tube specimen in the context of the geometric dimensions illustrated in Figure 4.5.

Table 4.2: Cross-sectional geometry of tube specimens, modified to reflect geometric dimensions shown in Figure 4.5. These dimensions were used for the assessment of the mechanical properties of which each specimen was composed.

Dimension	**CFRP Tubes**	**Aluminium Tubes**
r **(mm)**	8.22 ± 0.003	8.91 ± 0.029
h **(mm)**	2.61 ± 0.064	1.27 ± 0.057

4.4.2 Shear Modulus

Theory

Perhaps the simplest and most direct method of determining the shear modulus of a material is to form it into a tube of circular cross-section, and experimentally measure the torsional stiffness of this tube. In the case of a circular tube that is loaded in pure torsion in accordance with Saint-Venant's principal (the member must be sufficiently long such that local end conditions do not significantly affect the torsional response), the torsional stiffness will be entirely dependent upon the tube's cross-sectional dimensions and shear modulus; the normal elastic modulus of the tube has negligible significance under this loading condition. Recall from equations (3.48) and (3.49) of Section 3.11 that the Saint-Venant torsional response of a member of homogeneous and isotropic materials can be calculated as follows:

$$T_{SV} = J_{tube} G \frac{d\phi}{dX} \tag{4.1}$$

where T_{SV} is the torque applied about the longitudinal X axis of the member, ϕ is the angle of torsional rotation exhibited by the member, J_{tube} is a geometric property of the member (often referred to as the "torsion constant"), and G is the shear modulus of the isotropic material of which the member is composed. Although the CFRP tubes that were utilized in this experimental validation study do not comprise isotropic materials, it is expected that the CFRP can be modelled as transversely isotropic about the longitudinal X axis of the member. As such, equation (4.1) is, in fact, directly applicable to the presently discussed CFRP tubes (as well as the aluminium control specimens). The value of G in equation (4.1) will subsequently be referred to as G_{xy}. The value of J_{tube} for any circular tube of constant wall thickness h is equal to the second area polar moment of inertial of the tube about its longitudinal X axis, which can be calculated as follows:

$$J_{tube} = \frac{\pi}{2}\left(r + \frac{h}{2}\right)^4 - \frac{\pi}{2}\left(r - \frac{h}{2}\right)^4 \tag{4.2}$$

Integrating equation (4.1) over the total length of the tube and rearranging the resulting equation gives the following expression for G_{xy}:

$$G_{xy} = \frac{T_{SV}\, L_g}{\phi_g\, J_{tube}} \tag{4.3}$$

where L_g is the total gauge length of the tube over which the torsional rotation angle ϕ_g is to be measured. As such, the value of G_{xy} for each type of tube specimen employed in this experimental validation program (CFRP or aluminium) can be determined by experimentally measuring its torsional stiffness, and substituting the parameters and results of this experimental test into equation equation (4.3).

Experimental Procedure

Three CFRP tube specimens and one aluminium tube specimen were tested in pure torsion using the torsion testing apparatus described in Section 4.3.2. The length of these specimens was maximized in order to minimize the significance of any errors introduced at the ends of the specimens where the torsional loadings were applied. As such, each specimen was tested with an effective torsional gauge length of 682 ± 0.5 mm; this was the maximum torsion length that could be employed due to the initial length of the tube material from which the specimens were cut (812.8 mm), and the resolution of the torsion length adjustment graduations permitted by the torsion testing apparatus that was used (130 mm increments).

To restrain the ends of each specimen, a series of 26 mm thick aluminium plates were cut using a water-jet machine to create end fixture plates, as shown in Figure 4.6.

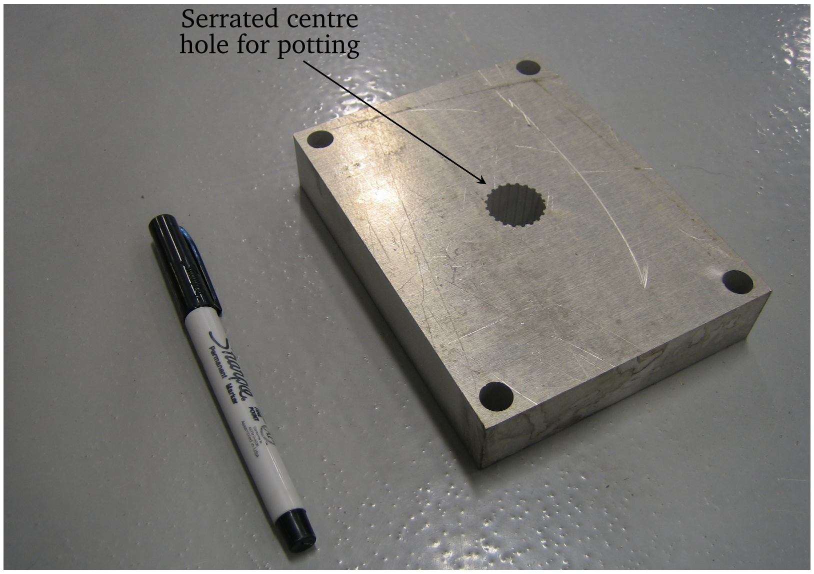

Figure 4.6: Aluminium end fixture plates used to restrain ends of tube specimens tested in pure torsion.

It is evident from Figure 4.6 that each of these end fixture plates was fabricated with a large serrated circular hole in the centre, and a smaller hole at each of the four corners of the plate. These smaller holes were used to mechanically fasten one of these end fixture plates to the flange at each end of the torsion testing apparatus; the bolt pattern was designed such that the centre of each end fixture plate was coincident with the axis of torsional rotation. Each end of each tube specimen was then potted into the large serrated circular hole in the centre of each end fixture plate using a generous quantity of the Henkel LePage® Gel Epoxy described in Section 4.3.2. This epoxy resin was allowed a minimum of 24 hours to cure prior to testing each specimen.

Figure 4.7 shows the aluminium tube specimen within the torsion testing apparatus described in Section 4.3.2, and ready to be tested in pure torsion.

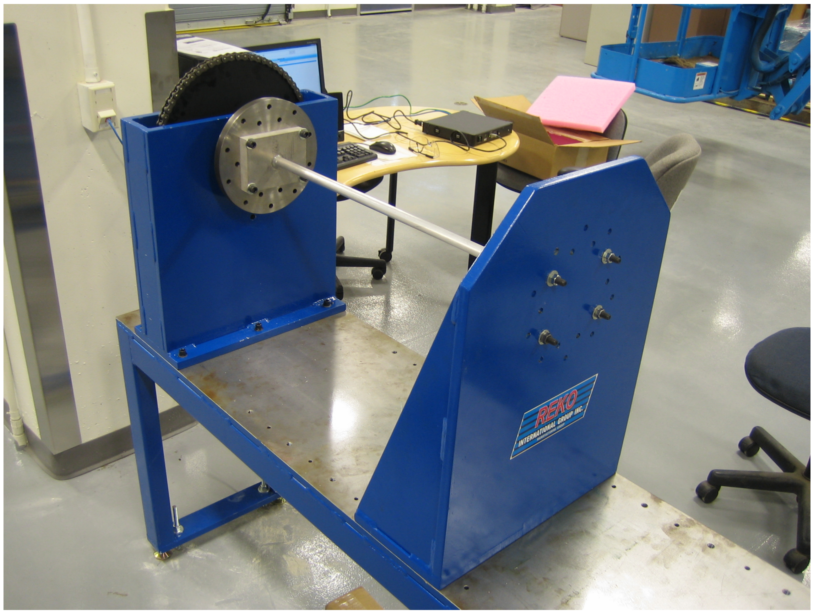

Figure 4.7: Experimental set-up for pure torsion tests used to determine shear modulus of tube specimens. This photograph shows the aluminium tube specimen within the torsion testing apparatus described in Section 4.3.2, and ready to be tested.

Figure 4.8 shows a close-up of one end of a CFRP tube specimen within the torsion testing apparatus described in Section 4.3.2, after some torsional rotation angle ϕ_g has been imposed upon the specimen.

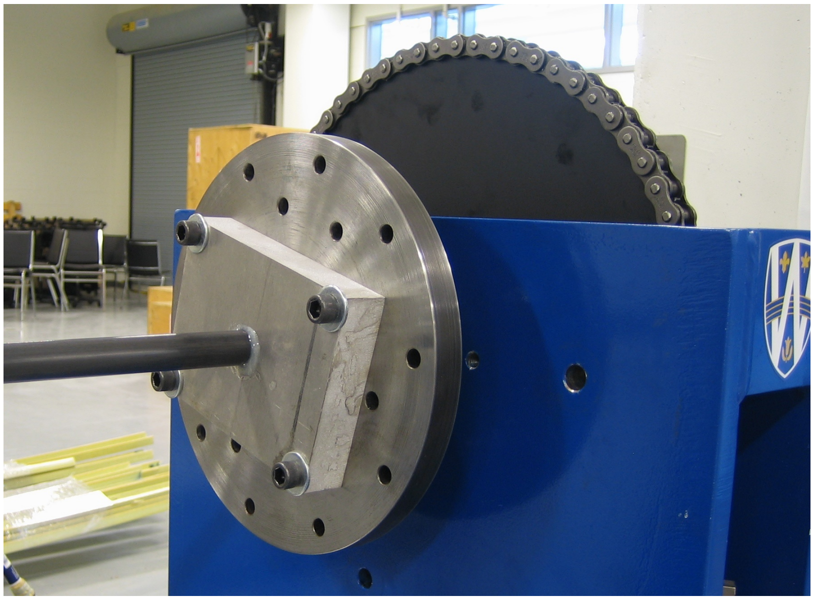

Figure 4.8: Experimental pure torsion test used to determine shear modulus of a CFRP tube specimens. This photograph shows a close-up of one end of a CFRP tube specimen within the torsion testing apparatus described in Section 4.3.2, after some torsional rotation angle ϕ_g has been imposed upon the specimen.

Results

A plot of torque T_{SV} versus torsional rotation angle ϕ_g was created using the data acquired from each torsion test, and a linear trend-line was fit through all data points up to a torsional rotation angle ϕ_g of 6° (see Appendix B). The slope of this linear trend-line represents the torsional stiffness of each specimen. Ultimately, the expected values of G_{xy} were calculated for both the CFRP and aluminium tube specimens by substituting the dimensional measurements from Table 4.2 and the measured torsional stiffness of each specimen into equations (4.2) and (4.3). In addition, upper and lower bound values of G_{xy} were calculated for each specimen by using the relevant upper and lower bound values associated with the dimensions of the specimen. The resulting torsional stiffness and G_{xy} values are summarized for the CFRP and aluminium tube specimens in Tables 4.3 and 4.4, respectively.

Table 4.3: Results of torsion tests used to determine shear modulus G_{xy} of CFRP tube specimens.

Test #	**Length (mm)**	**Torsional Stiffness (N·mm/Degree)**	G_{xy} **Expected (GPa)**	G_{xy} **Upper Bound (GPa)**	G_{xy} **Lower Bound (GPa)**
1	682 ± 0.5	882.0	3.696	3.801	3.596
2	682 ± 0.5	850.6	3.564	3.666	3.468
3	682 ± 0.5	846.5	3.547	3.648	3.451
		Average (mean)	3.602	3.705	3.505
		Standard Deviation	0.081	0.084	0.079

Table 4.4: Results of torsion test used to determine shear modulus G_{xy} of aluminium tube specimens.

Test #	**Length (mm)**	**Torsional Stiffness (N·mm/Degree)**	G_{xy} **Expected (GPa)**	G_{xy} **Upper Bound (GPa)**	G_{xy} **Lower Bound (GPa)**
1	682 ± 0.5	3886.6	26.781	28.356	25.345

The overall upper bound value of G_{xy} for the CFRP specimens was calculated as the sum of the mean and standard deviation of the upper bound values shown in Table 4.3. Similarly, the overall lower bound value of G_{xy} for the CFRP specimens was calculated as the difference between the mean and standard deviation of the lower bound values shown in Table 4.3. The final values of G_{xy} that are used in all subsequent analyses and discussions in this chapter are summarized in Table 4.5.

Table 4.5: Experimentally measured shear modulus G_{xy} of tube specimens.

Dimension	**CFRP Tubes**	**Aluminium Tubes**
G_{xy} **Expected (GPa)**	3.602	26.781
G_{xy} **Upper Bound (GPa)**	3.789	28.356
G_{xy} **Lower Bound (GPa)**	3.426	25.345

4.4.3 Longitudinal Elastic Modulus

Theory

The most direct method of determining the longitudinal elastic modulus E_{XX} of any material is to experimentally impose a tensile load upon a small sample ("coupon") of this material, and calculate the elastic modulus as a function of the observed tensile stiffness. Unfortunately, it can be quite challenging to effectively grip pultruded CFRP tube specimens for the purpose of imposing longitudinal tensile loadings. As such, the author decided that a more pragmatic approach to determine the value of E_{XX} for the present CFRP and aluminium experimental specimens would be to carry out symmetric 3-point bending tests on the specimens, and infer the relevant values of E_{XX} based upon the load versus deflection response observed during these tests. Figure 4.9 illustrates some of the geometric dimensions relevant to the analysis of symmetric 3-point bending tests.

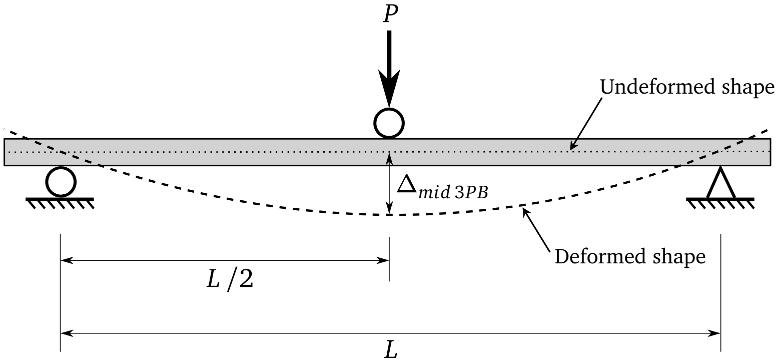

Figure 4.9: Geometric dimensions pertaining to a symmetric 3-point bending test.

It is evident from Figure 4.9 that the 3-point bending test is carried out in a manner whereby the specimen is simply supported (a roller support at one end, and a pin support at the other end) with a clear span of L, and a load P is applied at its mid-span via a roller. The mid-span deflection $\Delta_{mid\,3PB}$ is measured as the vertical displacement of the roller that is used to apply the mid-span loading. In accordance with Timoshenko beam theory [76][77], the mid-span deflection of a beam subjected to symmetric 3-point bending can be calculated as follows:

$$\Delta_{mid\,3PB} = \frac{P\,L^3}{48\,E_{XX}\,I_{YY}} + \frac{P\,L}{4\,\beta_{YY}\,A_G\,G_{XZ}} \tag{4.4}$$

where I_{YY} is the second area moment of inertia of the tube about its Y-Y axis, β_{YY} is the Timoshenko shear correction factor for transverse shear loads applied in the Z direction, G_{XZ} is the nominal X-Z shear modulus of the member, and A_G is the nominal cross-sectional area of the tube, normalized with respect to the transverse shear modulus. In the context of the tubes discussed in the present experimental validation, the value of G_{XZ} can be taken as G_{xy}, which was experimentally determined in Section 4.4.2. The second area moment of inertia of the tube about its Y-Y axis can be calculated as follows:

$$I_{YY} = \frac{\pi}{4}\left(r + \frac{h}{2}\right)^4 - \frac{\pi}{4}\left(r - \frac{h}{2}\right)^4 \tag{4.5}$$

Since the transverse shear modulus is constant over the entire cross-sectional area of the tube, the value of A_G can simply be taken as the the total cross-sectional area of the tube, which can be calculated as follows:

$$A_G = \pi\left(r + \frac{h}{2}\right)^2 - \pi\left(r - \frac{h}{2}\right)^2 \tag{4.6}$$

Recall from equation (3.46) that the Timoshenko shear correction factor can be calculated for a thin-walled section as follows:

$$\beta_{YY} = \left[\frac{A_G\, G_{XZ}}{\left(E_{XX}\, I_{YY}\right)^2} \int\limits_0^m \frac{\left(\int\limits_0^S E_{xx\,s}\, \bar{Z}_s\, h_s ds \right)^2}{h_S\, G_{xy\,S}}\, dS \right]^{-1} \tag{4.7}$$

where E_{xxs} is the longitudinal elastic modulus of the wall of the tube at coordinate s, G_{xys} is the x-y shear modulus within the plane of the wall of the tube at coordinate s, m is the entire length over which the coordinate s is defined, h_s is the wall thickness at coordinate s (taken here as a constant value h), and $\bar{Z}_s$ is the perpendicular distance from the Y-Y neutral axis of the section to coordinate s (measured parallel to the Z axis of the section). In a manner similar to $\bar{Z}_s$, the term $\bar{Z}_\theta$ will be defined here as the perpendicular distance from the Y-Y neutral axis of the section to coordinate θ_{tube} (measured parallel to the Z axis of the section). Upon inspection of Figure 4.5, it is evident that the value of $\bar{Z}_\theta$ at the relevant coordinate θ_{tube} can be calculated as follows:

$$\bar{Z}_\theta = r\, \cos\left(\theta_{tube}\right) \tag{4.8}$$

Recognizing that the values of G_{xys}, E_{xxs}, and h_s are all constant over the circumference of the tube, equation (4.7) can be evaluated for a hollow tube by replacing ds with $r\, d\theta_{tube}$, replacing h_s with h, substituting in $\bar{Z}_\theta$ from equation (4.8) for $\bar{Z}_s$, and integrating over the entire circumference of the tube, as follows:

$$\beta_{YY} = \frac{I_{YY}^2}{\pi A_G\, h\, r^5} \tag{4.9}$$

Utilizing the aforementioned section constants, the longitudinal elastic modulus E_{XX} can be recovered by rearranging equation (4.4) as follows:

$$E_{XX} = \frac{L^3}{48\,I_{YY}} \left(\frac{\Delta_{mid\,3PB}}{P} - \frac{L}{4\,\beta_{YY}\,A_G\,G_{xy}} \right)^{-1} \tag{4.10}$$

While equation (4.10) does account for the effects of transverse shear compliance, it fails to account for local transverse deformations at the supports and load application point. In the case of long solid beams comprising conventional metallic engineering materials, this concern of local effects would likely be insignificant. However, in the case of beams having thin-walled circular tube cross-sections, the transverse loads at the supports and loading point can result in local crushing and transverse deformations (ovalization) of the original circular cross-sectional geometry of the tube, which may constitute a non-trivial component of the total deflection $\Delta_{mid\,3PB}$ measured during the experimental 3-point bending tests. As such, in the interest of achieving the most accurate possible estimate of E_{XX}, equation (4.10) was modified to account for these local transverse compliances, as follows:

$$E_{XX} = \frac{L^3}{48\,I_{YY}} \left(\frac{\Delta_{mid\,3PB}}{P} - \frac{L}{4\,\beta_{YY}\,A_G\,G_{xy}} - C_{crush} \right)^{-1} \tag{4.11}$$

where C_{crush} is the total additional vertical compliance that results from the local transverse crushing and cross-sectional deformations that occur at each of the support points and load application point. The value of C_{crush} may be treated as a characteristic value that is associated with the cross-sectional geometry and material composition of each type of beam that is undergoing symmetric 3-point bending; it is generally independent of the span length L of the 3-point bending test, provided that L is significantly greater than the cross-sectional dimensions of the beam.

It would be quite difficult to reliably ascertain an accurate value of C_{crush} using any sort of a direct experimental test. However, since the value of C_{crush} is relatively insensitive to to the clear span L employed during a 3-point bending test, there exists a single value of C_{crush} for a given tube specimen such that it is possible to carry out multiple symmetric 3-point bending tests, each employing different clear span values L, and calculate the same value of E_{XX} by substituting the results of any one of these tests into equation (4.11). As such, by carrying out two symmetric 3-point bending tests having different clear spans L, the value of C_{crush} can be determined as that which will allow equation (4.11) to yield the same value of E_{XX} for both of these tests.

Experimental Procedure

Nine CFRP tube specimens and three aluminium tube specimens were tested in symmetric 3-point bending using the MTS® Criterion™ Model 43 Universal Testing System described in Section 4.3.3. Three different span lengths L were employed: 590 mm, 490 mm, and 440 mm. Three CFRP specimens and one aluminium specimen were tested at each of these three span lengths.

The use of multiple span lengths was necessary in order to facilitate the calculation of the value of C_{crush} for each type of specimen. Strictly speaking, only two unique span lengths would have been required to calculate the value of C_{crush} for each type of specimen; however, the inclusion of a third span length would enable verification of the aforementioned notion that the value of C_{crush} is not dependent upon span length L. If the value of C_{crush} were dependent upon span length, then a value of C_{crush} that yields the same value of E_{XX} when two different span lengths are used, would not necessarily yield the same value of E_{XX} when a third span length is used.

Figure 4.10 shows one of the CFRP tube specimens within the MTS® Criterion™ Model 43 Universal Testing System, and ready to undergo a symmetric 3-point bending test.

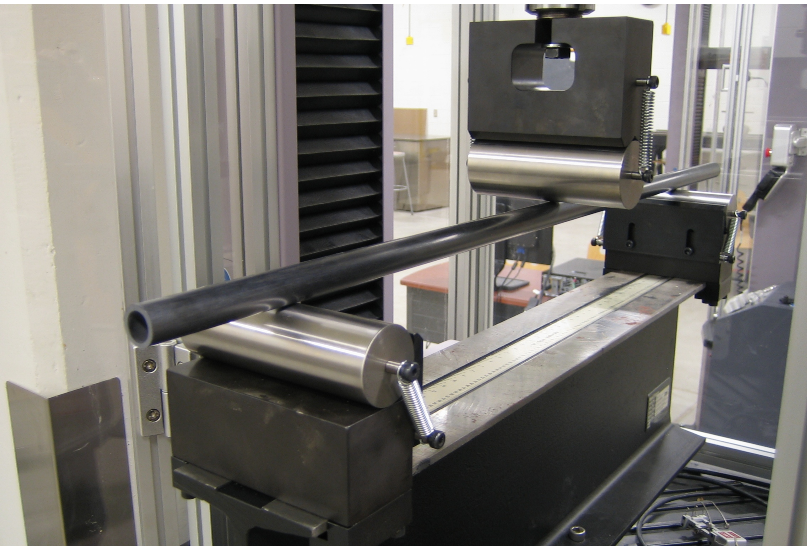

Figure 4.10: Experimental set-up for 3-point bending tests used to determine elastic modulus of tube specimens.

Results

A plot of load P versus mid-span deflection $\Delta_{mid\,3PB}$ was created using the data acquired from each 3-point bending test, and a linear trend-line was fit through all data points that reside within the linear regime of the test data (see Appendix C). In the case of all CFRP tube specimens, this linear regime included all data points up to a peak load P of 350 N. Conversely, in the case of the aluminium tube specimens, this linear regime included all data points up to a peak load P of 150 N, 200 N, and 250 N, for the case of bending tests having spans L of 590 mm, 490 mm, and 440 mm, respectively. The reciprocal of the slope of this linear trend-line represents the overall mid-span transverse compliance $(\Delta_{mid\,3PB}\ /P)$ of each specimen.

An initial value of C_{crush} was assumed for all specimens, and the necessary section constants of the tube were calculated using the dimensional data from Table 4.2 and equations (4.5), (4.6), and (4.9).

These section constants, in conjunction with the relevant values of G_{xy} determined in Section 4.4.2 and the overall mid-span transverse compliance values ($\Delta_{mid\,3PB}\ /\ P$) observed for each specimen, were then substituted into equation (4.11) to find a series of expected E_{XX} values based upon the results of each 3-point bending test. These calculations were carried out using a Microsoft® Excel® spreadsheet program.

For both the CFRP and aluminium specimens, the Microsoft® Excel® "Goal Seek" iterative solver function was used to determine the necessary values of C_{crush} that would yield identical predictions of E_{XX} based upon the results of bending tests having spans L of 590 mm and 440 mm. In the case of the CFRP tube specimens, it was necessary to base this "Goal Seek" iterative solution upon the average (mean) test results associated with the three bending tests carried out at each of these two span lengths. These iterative analyses yielded C_{crush} values of 0.0003145 mm/N and 0.0002184 mm/N for the CFRP and aluminium tube specimens, respectively. Finally, these values of C_{crush} were substituted back into equation (4.11) to again find the expected E_{XX} values based upon the results of each 3-point bending test. The results of these analyses are tabulated in Tables 4.6 and 4.7.

Table 4.6: Results of 3-point bending tests used to determine elastic modulus E_{XX} of CFRP tube specimens. These data were calculated based upon a C_{crush} value of 0.0003145 mm/N, which was selected in order to equate the average (mean) expected E_{XX} values determined based upon tests that utilized 590 mm and 440 mm span lengths.

Test #	**Span** L **(mm)**	**Mid-Span Compliance** $\Delta_{mid\,3PB}\ /\ P$ **(mm/N)**	E_{XX} **Expected (GPa)**	E_{XX} **Upper Bound (GPa)**	E_{XX} **Lower Bound (GPa)**
1	590 ± 0.25	0.00906	112.367	116.299	108.686
2	590 ± 0.25	0.00904	112.597	116.538	108.907
3	590 ± 0.25	0.00906	112.311	116.240	108.631
4	490 ± 0.25	0.00547	112.447	116.719	108.475
5	490 ± 0.25	0.00548	112.243	116.506	108.280
6	490 ± 0.25	0.00548	112.212	116.473	108.250
7	440 ± 0.25	0.00415	111.818	116.317	107.656
8	440 ± 0.25	0.00411	113.184	117.754	108.959
9	440 ± 0.25	0.00414	112.273	116.795	108.090
		Average (mean)	112.384	116.627	108.437
		Standard Deviation	0.367	0.462	0.416

$C_{crush} = 0.0003145$ mm/N

Table 4.7: Results of 3-point bending tests used to determine elastic modulus E_{XX} of aluminium tube specimens. These data were calculated based upon a C_{crush} value of 0.0002184 mm/N, which was selected in order to equate the expected E_{XX} values determined based upon tests that utilized 590 mm and 440 mm span lengths.

Test #	**Span** L **(mm)**	**Mid-Span Compliance** $\Delta_{mid\,3PB}\ /\ P$ **(mm/N)**	E_{XX} **Expected (GPa)**	E_{XX} **Upper Bound (GPa)**	E_{XX} **Lower Bound (GPa)**
1	590 ± 0.25	0.02197	69.864	74.073	66.036
2	490 ± 0.25	0.01276	69.657	73.899	65.802
3	440 ± 0.25	0.00929	69.864	74.152	65.970
		Average (mean)	69.795	74.042	65.936
		Standard Deviation	0.120	0.130	0.120

$C_{crush} = 0.0002184$ mm/N

It is evident from Tables 4.6 and 4.7 that bending tests having spans L of 490 mm yielded predictions of E_{XX} that are quite similar to the the predictions of E_{XX} that were based upon the results of bending tests having spans L of 590 mm and 440 mm (less than 0.30% discrepancy). This validates the aforementioned hypothesis that the value of C_{crush} is relatively insensitive to the span length L of each 3-point bending test, provided that L is significantly greater than the cross-sectional dimensions of the beam.

The overall upper bound value of E_{XX} for the CFRP specimens was calculated as the sum of the mean and standard deviation of the upper bound values shown in Table 4.6, and the overall upper bound value of E_{XX} for the aluminium specimens was calculated as the sum of the mean and standard deviation of the upper bound values shown in Table 4.7. Similarly, the overall lower bound value of E_{XX} for the CFRP specimens was calculated as the difference between the mean and standard deviation of the lower bound values shown in Table 4.6, and the overall the lower bound value of E_{XX} for the aluminium specimens was calculated as the difference between the mean and standard deviation of the lower bound values shown in Table 4.7. The final values of E_{XX} that are used in all subsequent analyses and discussions in this chapter are summarized in Table 4.8.

Table 4.8: Experimentally measured longitudinal elastic modulus E_{XX} of tube specimens.

Dimension	**CFRP Tubes**	**Aluminium Tubes**
E_{XX} **Expected (GPa)**	112.384	69.795
E_{XX} **Upper Bound (GPa)**	117.089	74.171
E_{XX} **Lower Bound (GPa)**	108.021	65.816

4.5 Analytical Modelling of Restrained Torsion of Open Slotted Tube Specimens

4.5.1 General

The following section applies some of the analytical procedures from Chapter 3 to assess the restrained torsional response (warping response) of a tube that has had a channel cut through its wall along its longitudinal X axis. Figure 4.11 illustrates some of the cross-sectional dimensions that will be used in the subsequent derivations discussed in this section.

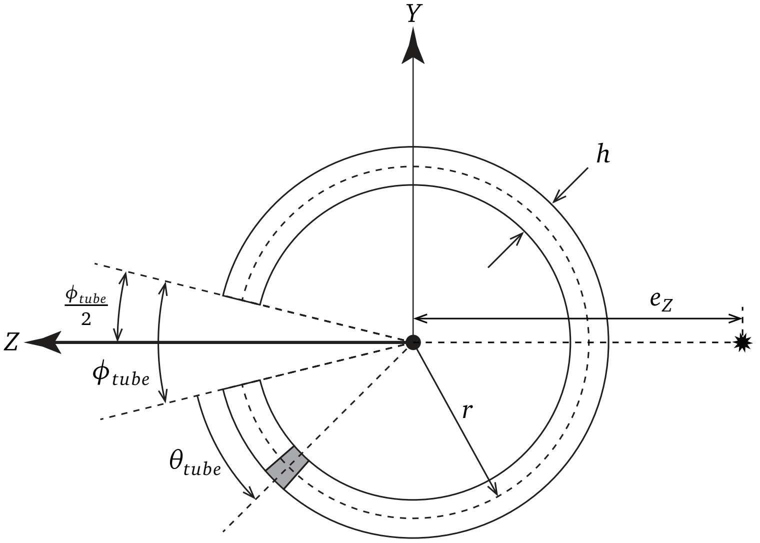

Figure 4.11: Cross-sectional geometry of thin-walled slotted tube.

It is evident from Figure 4.11 that the origin of the global X-Y-Z coordinate system is still taken about the centre of the original un-slotted tube's cross-sectional geometry, and the global X axis is aligned with the longitudinal axis of the tube. The dimension ϕ_{tube} represents the swept angle describing the width of the slot that has been cut into the tube, measured about the longitudinal X axis of the tube;

the position of this slot is assumed to be centred about the tube's Z axis. The dimension e_Z represents the distance between the tube's shear-centre and the longitudinal X axis of the tube; it is reasonable to assume that the dimension e_Z is parallel to the Z axis due to the singly-symmetric nature of the slotted tube's cross-sectional geometry. Also, it is evident from Figure 4.11 that, in all discussions pertaining to this slotted tube geometry, the dimension θ_{tube} is an angular coordinate representing the swept angle between the edge of the slot and the position of interest (shaded region in Figure 4.11), measured about the longitudinal X axis of the tube. Table 4.9 was derived from Table 4.1 in order to summarize the cross-sectional dimensions of each type of tube specimen in the context of the geometric dimensions illustrated in Figure 4.11.

Table 4.9: Cross-sectional geometry of slotted tube specimens, modified to reflect geometric dimensions shown in Figure 4.11.

Dimension	**CFRP Tubes**	**Aluminium Tubes**
r **(mm)**	8.22 ± 0.003	8.91 ± 0.029
h **(mm)**	2.61 ± 0.064	1.27 ± 0.057
ϕ_{tube} **(Radians)**	0.177 ± 0.005	0.178 ± 0.003

4.5.2 Location of Shear-Centre

Recall from Section 3.8 that $\bar{Y'}_s$ is defined as the perpendicular distance from the Z'-Z' neutral axis of the section to coordinate s (measured parallel to the Y' axis of the section). Similarly, the term $\bar{Y}_\theta$ shall be defined as the perpendicular distance from the Z-Z neutral axis of the section to coordinate θ_{tube} (measured parallel to the Y axis of the section). In the context of the present slotted tube specimens, inspection of Figure 4.11 reveals that $\bar{Y}_\theta$ can be calculated at coordinate θ_{tube} as follows:

$$\bar{Y}_\theta = -r\,\sin\left(\frac{\phi_{tube}}{2} + \theta_{tube}\right) \tag{4.12}$$

Using the aforementioned value of $\bar{Y}_\theta$, the second area moment of inertia about the Z-Z axis of the geometry shown in Figure 4.11 can be found as follows:

$$I_{ZZ} = \int_0^{2\pi-\phi_{tube}} \bar{Y}_\theta^2\,h\,r\,d\theta_{tube} = \int_0^{2\pi-\phi_{tube}} -hr^3\sin^2\left(\frac{\phi_{tube}}{2} + \theta_{tube}\right)d\theta_{tube} \tag{4.13}$$

In addition, the term Q_{ZZ} shall be defined as the integral of the first moment of areas about the Z-Z axis of the member, for all material situated on one side of the position of interest on the cross-sectional geometry of the member. In the context of the the geometry shown in Figure 4.11, the value of Q_{ZZ} can be found at coordinate θ_{tube} as follows:

$$Q_{ZZ} = \int_{0}^{\theta_{tube}} -h r^2 \sin\left(\frac{\phi_{tube}}{2} + \theta_{tube}\right) d\theta_{tube} \tag{4.14}$$

As such, the x-y shear flow within the tube wall that results from a transverse shear force V_Y in the Y direction can be calculated as follows:

$$q_{xy} = h\,\tau_{xy} = \frac{V_Y\,Q_{ZZ}}{I_{ZZ}} = V_Y \frac{\int_{0}^{\theta_{tube}} \sin\left(\frac{\phi_{tube}}{2} + \theta_{tube}\right) d\theta_{tube}}{r \int_{0}^{2\pi-\phi_{tube}} \sin^2\left(\frac{\phi_{tube}}{2} + \theta_{tube}\right) d\theta_{tube}} \tag{4.15}$$

where τ_{xy} is the average x-y shear stress within the plane of the tube wall. The total twisting moment M_c about the longitudinal X axis that is caused by this shear flow q_{xy} can be calculated by integrating the first moment of q_{xy} about the X axis for the entire cross-sectional area of the member, as follows:

$$M_c = \int_{0}^{2\pi-\phi_{tube}} q_{xy} r^2\, d\theta_{tube} = V_Y r \frac{\int_{0}^{2\pi-\phi_{tube}} \int_{0}^{\theta_{tube}} \sin\left(\frac{\phi_{tube}}{2} + \theta_{tube}\right) d\theta_{tube}\, d\theta_{tube}}{\int_{0}^{2\pi-\phi_{tube}} \sin^2\left(\frac{\phi_{tube}}{2} + \theta_{tube}\right) d\theta_{tube}} \tag{4.16}$$

Equation (4.16) can be equated to the product of the applied transverse shear force V_Y and the distance between the tube's shear-centre and the longitudinal X axis of the tube e_Z, as follows:

$$V_Y r \frac{\int_{0}^{2\pi-\phi_{tube}} \int_{0}^{\theta_{tube}} \sin\left(\frac{\phi_{tube}}{2} + \theta_{tube}\right) d\theta_{tube}\, d\theta_{tube}}{\int_{0}^{2\pi-\phi_{tube}} \sin^2\left(\frac{\phi_{tube}}{2} + \theta_{tube}\right) d\theta_{tube}} = V_Y e_Z \tag{4.17}$$

Solving for e_Z in equation (4.17) and carrying out the necessary integration yields the following expression for the distance between tube's shear-centre and the longitudinal X axis of the tube (measured parallel to the Z axis):

$$e_Z = r\left(\frac{2\sin\left(\frac{\phi_{tube}}{2}\right) + \left(2\pi + \phi_{tube}\right)\cos\left(\frac{\phi_{tube}}{2}\right)}{\pi + \frac{\sin\phi_{tube}}{2} - \frac{\phi_{tube}}{2}}\right) \tag{4.18}$$

It should be noted that the value of e_Z here does not represent the distance between the shear-centre and the centroid of the section as previously discussed in Section 3.8; on the contrary, the value of e_Z discussed in this section represents the distance between the shear-centre and the X axis of the tube, which is located at the centre of the original un-slotted tube's cross-sectional geometry.

The values of e_Z expected for both the CFRP and aluminium slotted tube specimens were calculated by substituting the dimensional measurements from Table 4.9 into equation (4.18). In addition, upper and lower bound values of e_Z were calculated using the relevant upper and lower bound values associated with the dimensions of the specimens. These expected, upper bound, and lower bound values of e_Z are tabulated in Table 4.10.

Table 4.10: Predicted shear-centre location e_Z in slotted tube specimens.

Dimension	**CFRP Tubes**	**Aluminium Tubes**
e_Z **Expected (mm)**	16.38	17.75
e_Z **Upper Bound (mm)**	16.39	17.81
e_Z **Lower Bound (mm)**	16.37	17.69

4.5.3 Saint-Venant Torsional Stiffness

Recall from Section 3.11.2 that the Saint-Venant torsional stiffness of a flat homogeneous and isotropic rectangular plate of finite width can be calculated as follows:

$$C_{flat} = G\,\frac{b\,h^3}{16}\left[\frac{16}{3} - 3.36\frac{h}{b}\left(1 - \frac{h^4}{12\,b^4}\right)\right] \tag{4.19}$$

where b is the width of the plate's cross-sectional geometry, h is the thickness of the plate's cross-sectional geometry, and G is the shear modulus of the isotropic material of which the plate is composed. Although the CFRP tubes that were utilized in this experimental validation study do not comprise isotropic materials, it is expected that the CFRP can be modelled as transversely isotropic about the longitudinal X axis of the member. As such, equation (4.19) can be modified for use with the presently discussed CFRP tubes (as well as the aluminium control specimens) by simply employing the necessary geometric relationships ($b = r\left(2\pi - \phi_{tube}\right)$) that can be ascertained from Figure 4.11, as follows:

$$C = G_{xy}\,\frac{r\,h^3\left(2\pi - \phi_{tube}\right)}{16}\left[\frac{16}{3} - 3.36\frac{h}{r\left(2\pi - \phi_{tube}\right)}\left(1 - \frac{h^4}{12\,r^4\left(2\pi - \phi_{tube}\right)^4}\right)\right] \tag{4.20}$$

where G_{xy} is the shear modulus that was experimentally determined in Section 4.4.2, and C is the Saint-Venant torsional stiffness of the slotted tube geometry shown in Figure 4.11.

The values of C expected for both the CFRP and aluminium slotted tube specimens were calculated by substituting the dimensional measurements from Table 4.9 and the shear moduli calculated in Section 4.4.2 into equation (4.20). In addition, upper and lower bound values of C were calculated using the relevant upper and lower bound values associated with the dimensions and mechanical properties of the specimens. These expected, upper bound, and lower bound values of C are tabulated in Table 4.11.

Table 4.11: Predicted Saint-Venant torsional stiffness C of slotted tube specimens.

Dimension	**CFRP Tubes**	**Aluminium Tubes**
C **Expected (GPa mm^4)**	1033	980.0
C **Upper Bound (GPa mm^4)**	1169	1189
C **Lower Bound (GPa mm^4)**	910.6	804.7

4.5.4 Primary Warping Constant

Recall from Section 3.12.1 that the calculation of the Vlasov primary warping constant is dependent upon the dimension r_{perpOs} (to be re-designated as r_{perp} in the present section), which is the moment arm of the position of interest (shaded region in Figure 4.11) about the shear-centre of the entire section, measured perpendicular to the mid-plane of the section wall at the position of interest. Utilizing the geometric schematic presented in Figure 4.12, the value of r_{perp} can be calculated at any position on the cross-section of the slotted tube geometry, as follows:

$$r_{perp} = r + e_Z \cos\left(\frac{\phi_{tube}}{2} + \theta_{tube}\right) \tag{4.21}$$

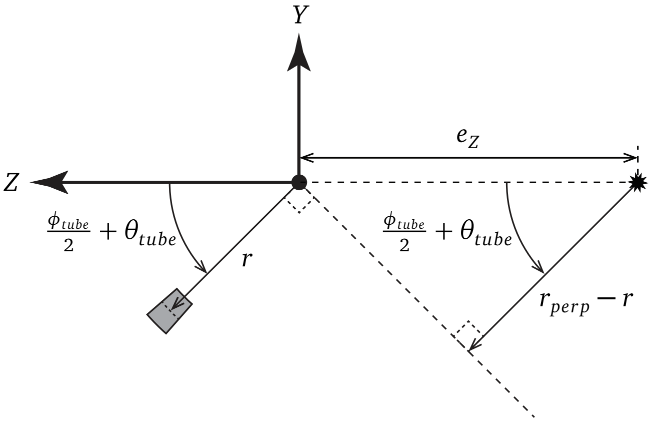

Figure 4.12: Geometric dimensions relevant to the calculation of r_{perp} for a slotted hollow tube. Note that the shaded region in this figure is analogous to the shaded region in Figure 4.11.

Adapting equation (3.81) from Section 3.12.1 for use with polar coordinates, and employing the aforementioned formulation for r_{perp} defined in equation (4.21), the quantity ω_θ can be evaluated at the position of interest as follows:

$$\omega_\theta = \int_0^{\theta_{tube}} r_{perp}\, r\, d\theta_{tube} = \int_0^{\theta_{tube}} r^2 + r\, e_Z\, \cos\left(\frac{\phi_{tube}}{2} + \theta_{tube}\right) d\theta_{tube} \tag{4.22}$$

where ω_θ is defined as twice the sectorial area swept by a radial line that spans between the shear-centre of the slotted tube section and the mid-plane of the slotted tube wall, and migrates along the mid-plane of slotted tube wall from one of its free edges to the position of interest. Evaluating the integral in equation (4.22) gives the following expression for ω_θ:

$$\omega_\theta = \theta_{tube}\, r^2 - r\, e_Z\, \sin\left(\frac{\phi_{tube}}{2}\right) + r\, e_Z\, \sin\left(\frac{\phi_{tube}}{2} + \theta_{tube}\right) \tag{4.23}$$

The average (mean) value of ω_θ over the entire cross-sectional area of the slotted tube can then be calculated as follows:

$$\bar{\omega}_\theta = \frac{1}{m} \int_0^{2\pi - \phi_{tube}} \omega_\theta\, r\, d\theta_{tube} \qquad \text{where:} \qquad m = r\,\left(2\pi - \phi_{tube}\right) \tag{4.24}$$

Substituting equation (4.23) into equation (4.24) gives the following expression:

$$\bar{\omega}_\theta = \frac{1}{2\pi - \phi_{tube}} \int_0^{2\pi - \phi_{tube}} \theta_{tube}\, r^2 - r\, e_Z\, \sin\left(\frac{\phi_{tube}}{2}\right) + r\, e_Z\, \sin\left(\frac{\phi_{tube}}{2} + \theta_{tube}\right) d\theta_{tube} \tag{4.25}$$

Evaluating the integral in equation (4.25) and simplifying the resulting equation give the following expression for $\bar{\omega}_\theta$:

$$\bar{\omega}_\theta = \pi\, r^2 - \frac{\phi_{tube}\, r^2}{2} - r\, e_Z\, \sin\left(\frac{\phi_{tube}}{2}\right) \tag{4.26}$$

Adapting equation (3.87) from Section 3.12.1 for use with polar coordinates, the Vlasov primary warping constant of the present slotted tube geometry can be calculated using the follows expression:

$$C_{1B1} = \int_0^{2\pi - \phi_{tube}} \left(\bar{\omega}_\theta - \omega_\theta\right)^2 E_{xx}\, h\, r\, d\theta_{tube} \tag{4.27}$$

where E_{xx} is the longitudinal elastic modulus of the material of which the tube is composed (taken here as the value of E_{XX} that was experimentally determined in Section 4.4.3). Substituting equations (4.23) and (4.26) into equation (4.27) gives the following expression for C_{1B1}:

$$C_{1B1} = r\, E_{xx}\, h \int_0^{2\pi - \phi_{tube}} \left(\pi\, r^2 - \frac{\phi_{tube}\, r^2}{2} - \theta_{tube}\, r^2 - r\, e_Z\, \sin\left(\frac{\phi_{tube}}{2} + \theta_{tube}\right)\right)^2 d\theta_{tube} \tag{4.28}$$

Upon solving the integral in equation (4.28) and simplifying the resulting expression, the Vlasov primary warping constant of the slotted tube geometry shown in Figure 4.11 can be expressed as follows:

$$C_{1B1} = E_{xx}\, h \left[r^5 \left(2\pi - \phi_{tube}\right) \Omega_{C1B11} + 2\, e_Z\, r^4\, \Omega_{C1B12} + \frac{e_z^2\, r^3}{2} \Omega_{C1B13} \right] \tag{4.29}$$

where:

$$\Omega_{C1B11} = \left(\frac{\phi_{tube}^2}{4} - \pi \phi_{tube} + \pi^2 \right) + \left(2\pi - \phi_{tube}\right) \left(\frac{\phi_{tube}}{2} - \pi \right) + \frac{1}{3} \left(2\pi - \phi_{tube}\right)^2$$

$$\Omega_{C1B12} = \left(\phi_{tube} - 2\pi\right) \cos\left(\frac{\phi_{tube}}{2} \right) - 2 \sin\left(\frac{\phi_{tube}}{2} \right)$$

$$\Omega_{C1B13} = 2\,\pi - \phi_{tube} + \sin\left(\phi_{tube}\right)$$

The values of C_{1B1} expected for both the CFRP and aluminium slotted tube specimens were calculated by substituting the dimensional measurements from Table 4.9 and the elastic moduli calculated in Section 4.4.3 into equation (4.29). In addition, upper and lower bound values of C_{1B1} were calculated using the relevant upper and lower bound values associated with the dimensions and mechanical properties of the specimens. These expected, upper bound, and lower bound values of C_{1B1} are tabulated in Table 4.12.

Table 4.12: Predicted primary warping stiffness C_{1B1} of slotted tube specimens.

Dimension	**CFRP Tubes**	**Aluminium Tubes**
C_{1B1} **Expected (GPa mm^6)**	71461622	32313440
C_{1B1} **Upper Bound (GPa mm^6)**	76914142	36626925
C_{1B1} **Lower Bound (GPa mm^6)**	66449253	28507791

4.5.5 Secondary Warping Constant

Recall from Section 3.12.2 that the calculation of the secondary warping constant is dependent upon the dimension $r_{par\,Os}$ (to be re-designated as r_{par} in the present section), which is the moment arm of the position of interest (shaded region in Figure 4.11) about the shear-centre of the entire section, measured parallel to the mid-plane of the section wall at the position of interest. Utilizing the geometric schematic presented in Figure 4.13, the value of r_{par} can be calculated at any position on the cross-section of the slotted tube geometry, as follows:

$$r_{par} = e_Z \sin\left(\frac{\phi_{tube}}{2} + \theta_{tube} \right) \tag{4.30}$$

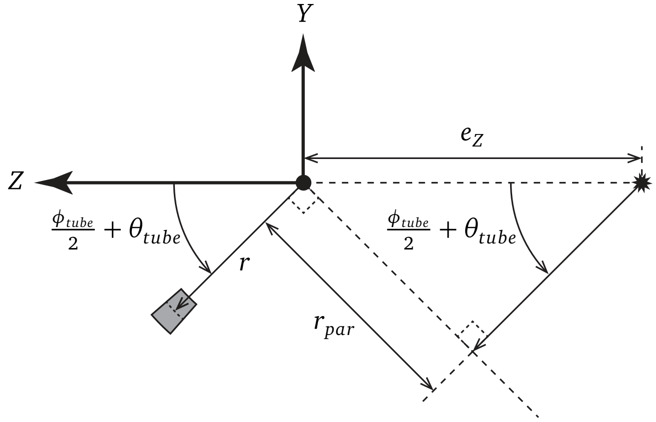

Figure 4.13: Geometric dimensions relevant to the calculation of r_{par} for a slotted hollow tube. Note that the shaded region in this figure is analogous to the shaded region in Figure 4.11.

It was also discussed in Section 3.12.2 that the calculation of the secondary warping constant is dependent upon the out-of-plane bending stiffness of the section walls $dEI_{yy}\big/dy$ at any given location of the cross-section. In the context of the slotted tubes relevant to the present experimental validation study, the value of $dEI_{yy}\big/dy$ can be calculated as follows:

$$\frac{dEI_{yy}}{dy}=E_{xx}\,\frac{h^3}{12} \tag{4.31}$$

where E_{xx} is the longitudinal elastic modulus of the material of which the tube is composed (taken here as the value of E_{XX} that was experimentally determined in Section 4.4.3).

Adapting equation (3.89) from Section 3.12.2 for use with polar coordinates, the secondary warping constant of the present slotted tube geometry can be calculated using the following expression:

$$C_{1B2}=\int_{0}^{2\pi-\phi_{tube}}\frac{dEI_{yy}}{dy}\,r_{par}^2\,r\,d\theta_{tube} \tag{4.32}$$

Substituting equations (4.30) and (4.31) into equation (4.32) gives the following expression for the secondary warping constant of the slotted tube geometry shown in Figure 4.11:

$$C_{1B2}=\frac{r\,E_{xx}\,e_Z^2\,h^3}{12}\left(\pi-\frac{\phi_{tube}}{2}+\frac{\sin\left(\phi_{tube}\right)}{2}\right) \tag{4.33}$$

The values of C_{1B2} expected for both the CFRP and aluminium slotted tube specimens were calculated by substituting the dimensional measurements from Table 4.9 and the elastic moduli calculated in Section 4.4.3 into equation (4.33). In addition, upper and lower bound values of C_{1B2} were calculated using the relevant upper and lower bound values associated with the dimensions and mechanical properties of the specimens. These expected, upper bound, and lower bound values of C_{1B2} are tabulated in Table 4.13.

Table 4.13: Predicted secondary warping stiffness C_{1B2} of slotted tube specimens.

Dimension	**CFRP Tubes**	**Aluminium Tubes**
C_{1B2} **Expected (GPa mm^6)**	1149006	105060
C_{1B2} **Upper Bound (GPa mm^6)**	1290037	128769
C_{1B2} **Lower Bound (GPa mm^6)**	1022966	85367

4.5.6 Total Warping Stiffness

Utilizing equation (3.91) of Section 3.12.2, the results from Tables 4.12 and 4.13 were combined to arrive upon the total warping stiffness values ($C_{1B} = C_{1B1} + C_{1B2}$) for both the CFRP and aluminium slotted tube specimens, which are tabulated in Table 4.14.

Table 4.14: Predicted total warping stiffness C_{1B} of slotted tube specimens, where: $C_{1B} = C_{1B1} + C_{1B2}$.

Dimension	**CFRP Tubes**	**Aluminium Tubes**
C_{1B} **Expected (GPa mm^6)**	72610628	32418500
C_{1B} **Upper Bound (GPa mm^6)**	78204178	36755694
C_{1B} **Lower Bound (GPa mm^6)**	67472218	28593158

4.5.7 Warping-Shear Compliance

Recall from Section 3.12.3 that the additional warping compliance due to warping-shear strains can be quantified using the newly introduced term C_{1S}. The value of C_{1S} was defined using equation (3.97) of Section 3.12.3, which can be modified for the case of the slotted tube geometry shown in Figure 4.11, as follows:

$$C_{1S} = \int_{0}^{2\pi-\phi_{tube}} \frac{\left[\int_{0}^{\theta_{tube}} \left(\bar{\omega}_{\theta} - \omega_{\theta}\right) E_{xx}\, h\, r\, d\theta_{tube} \right]^2}{h\, G_{xy}}\, r\, d\theta_{tube} \tag{4.34}$$

where E_{xx} is the longitudinal elastic modulus of the material of which the tube is composed (taken here as the value of E_{XX} that was experimentally determined in Section 4.4.3), and G_{xy} is the shear modulus that was experimentally determined in Section 4.4.2. Substituting equations (4.23) and (4.26) into equation (4.34) gives the following expression for C_{1S}:

$$C_{1S} = \frac{h\,E_{xx}^2\,r^3}{G_{xy}} \int_0^{2\pi-\phi_{tube}} \left[\int_0^{\theta_{tube}} \left(\pi\,r^2 - \frac{\phi_{tube}\,r^2}{2} - \theta_{tube}\,r^2 - r\,e_Z\,\sin\left(\frac{\phi_{tube}}{2} + \theta_{tube}\right)\right) d\theta_{tube} \right]^2 d\theta_{tube} \tag{4.35}$$

Upon solving the definite integrals in equation (4.35) and simplifying the resulting formula, the following expression is found to calculate the value of C_{1S} for the slotted tube geometry shown in Figure 4.11:

$$C_{1S} = \frac{h\,E_{xx}^2\,r^5}{4\,G_{xy}} \left[\Omega_{C1S1} + \Omega_{C1S2} + \Omega_{C1S3} + \Omega_{C1S4} + \Omega_{C1S5} + \Omega_{C1S6} + \Omega_{C1S7} + \Omega_{C1S8}\right] \tag{4.36}$$

where:

$$\begin{gathered}
\Omega_{C1S1} = \frac{1}{3}\,\phi_{tube}^2\,r^2\,\left(2\pi - \phi_{tube}\right)^3 + \frac{1}{2}\,\phi_{tube}\,r^2\,\left(2\pi - \phi_{tube}\right)^4 \\
\Omega_{C1S2} = -\frac{4}{3}\,\pi\,\phi_{tube}\,r^2\,\left(2\pi - \phi_{tube}\right)^3 \\
\Omega_{C1S3} = \frac{2}{3}\,r\,e_Z\,(2\pi - \phi_{tube})^2\,\left(\phi_{tube} - 2\pi\right)\cos\left(\frac{\phi_{tube}}{2}\right) \\
\Omega_{C1S4} = 2\,e_Z^2\,\sin\left(\phi_{tube}\right) - 16\,r\,e_Z\,\sin\left(\frac{\phi_{tube}}{2}\right) \\
\Omega_{C1S5} = -8\,r\,e_Z\,\left(2\pi - \phi_{tube}\right)\cos\left(2\pi - \frac{\phi_{tube}}{2}\right) \\
\Omega_{C1S6} = \frac{1}{5}\,r^2\,\left(2\,\pi - \phi_{tube}\right)^5 - \pi\,r^2\,\left(2\pi - \phi_{tube}\right)^4 \\
\Omega_{C1S7} = \frac{4}{3}\,\pi^2\,r^2\,\left(2\pi - \phi_{tube}\right)^3 + 4\,e_Z^2\,\left(2\pi - \phi_{tube}\right) \\
\Omega_{C1S8} = 2\,e_Z^2\,\left(2\pi - \phi_{tube}\right)\,\cos\left(\phi_{tube}\right) - 4\,e_Z^2\,\sin\left(2\pi - \phi_{tube}\right)
\end{gathered}$$

Finally, the more pragmatically configured warping-shear coefficient C_{TS} can be calculated using equation (3.99) of Section 3.12.3, as follows:

$$C_{TS} = \frac{C_{1B}^2}{C_{1S}} \tag{4.37}$$

The values of C_{TS} expected for both the CFRP and aluminium slotted tube specimens were calculated by substituting the dimensional measurements from Table 4.9, the elastic moduli calculated in Sections 4.4.2 and 4.4.3, and the warping stiffness values found in Section 4.5.6, into equations (4.36) and (4.37). In addition, upper and lower bound values of C_{TS} were calculated using the relevant upper and lower bound values associated with the dimensions and mechanical properties of the specimens. These expected, upper bound, and lower bound values of C_{TS} are tabulated in Table 4.15.

Table 4.15: Predicted warping-shear coefficient C_{TS} of slotted tube specimens.

Dimension	**CFRP Tubes**	**Aluminium Tubes**
C_{TS} **Expected (GPa mm^4)**	29519	132681
C_{TS} **Upper Bound (GPa mm^4)**	30886	147434
C_{TS} **Lower Bound (GPa mm^4)**	26455	117862

4.5.8 Overall Response to Restrained Torsion

In Section 3.13, a series of equations was derived to predict the overall restrained torsional stiffness of a thin-walled member that is restrained against warping at both ends. Equation (3.104) was presented for the purpose of predicting this restrained torsional response in accordance with conventional Vlasov warping theory, which neglects the effects of warping-shear compliance. Conversely, equation (3.108) was derived using the present analytical warping model, which accounts for the effects of warping-shear compliance using the C_{TS} coefficient that was found in Section 4.5.7. Both of these formulations were compared with the results of the experimental program in order to demonstrate the importance of accounting for warping-shear compliance, and to assess the improvement in fidelity afforded by the present analytical model in comparison with conventional Vlasov warping theory (see Section 4.7).

4.6 Experimental Testing of Restrained Torsion of Open Slotted Tube Specimens

4.6.1 Experimental Set-up and Procedure

It was decided that the slotted tube specimens would be tested in fixed-fixed restrained torsion, whereby a torsional rotation angle is imposed upon one end of the specimen while both ends are restrained against warping deformations. In order to achieve this, it was important that the ends of each specimen were very firmly held in some sort of a fixture, and that the shear-centre of each specimen's cross-section was coincident with the axis of torsional rotation. To achieve a symmetric loading environment, it was decided that each restrained torsion test would include a pair of slotted tube specimens, which would be positioned such that they were on opposing sides of a common shared shear-centre. In total, three pairs of CFRP slotted tube specimens and one pair of aluminium slotted tube specimens were created and tested using the torsion testing machine and apparatus described in Section 4.3.2.

As mentioned in Section 4.2, the slotted tube specimens were prepared by cutting the tube material to the necessary length, and then utilizing a carbide end-mill bit to cut a single slot parallel to the longitudinal axis of each warping specimen. These slots were measured to have a width of 1.4555 ± 0.0403 mm in the CFRP tube specimens, and a width of 1.5822 ± 0.0286 mm in the aluminium tube specimens (see Appendix A).

To restrain the ends of each pair of warping specimens, a series of 26 mm thick aluminium plates were cut using a water-jet machine to create end fixture plates, as shown in Figure 4.14.

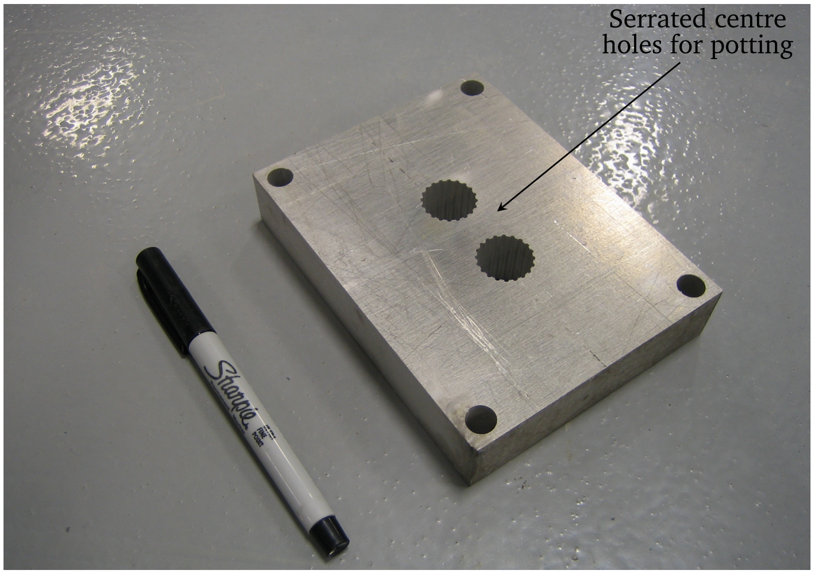

Figure 4.14: Aluminium end fixture plates used to restrain ends of tube specimens tested in restrained torsion (warping).

It is evident from Figure 4.14 that each of these end fixture plates was fabricated with a pair of large serrated circular holes near the centre of the plate, and a smaller hole at each of the four corners of the plate. These smaller holes were used to mechanically fasten one of these end fixture plates to the flange at each end of the torsion testing apparatus; the bolt pattern was designed such that the centre of each end fixture plate would be coincident with the axis of torsional rotation. The large serrated circular holes near the centre of each end fixture plate were each positioned such that their centres were a distance of e_Z from the centre of the end fixture plate; as such, it was necessary to fabricate a unique set of end fixture plates for use with the CFRP specimens and the aluminium specimens to accommodate their differing values of e_Z.

Using a generous quantity of the Henkel LePage® Gel Epoxy described in Section 4.3.2, each end of each slotted tube specimen was potted into one of the large serrated circular holes in the end fixture plates. Care was taken to ensure that the slotted tube specimens were potted in an orientation such that the slots of both tubes pointed away from the centres of the plates; this, in conjunction with the aforementioned positioning of the serrated holes, ensured that the shear-centres of both slotted tubes were coincident with the axis of torsional rotation. The epoxy resin was allowed a minimum of 24 hours to cure prior to testing each specimen assembly. Figure 4.15 is an illustration of the orientation of the cross-sections a pair of slotted tube specimens, as they would be potted into one of their end fixture plates.

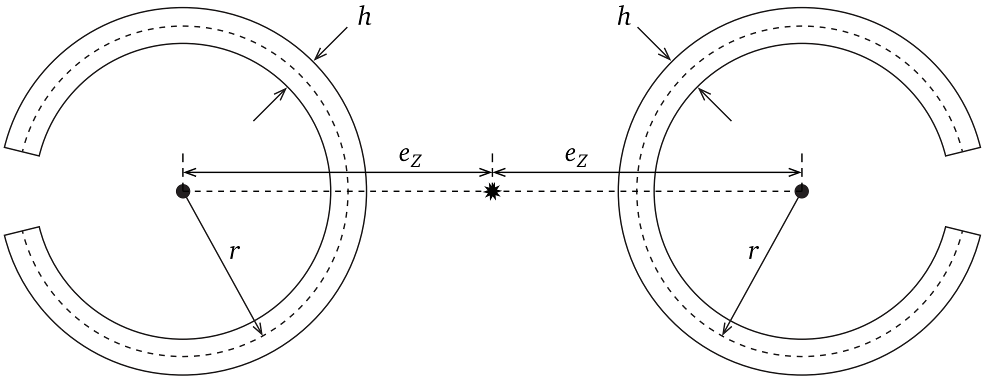

Figure 4.15: Orientation of a pair of slotted tube specimen cross-sections, as they would be potted into one of their end fixture plates for restrained torsion (warping) tests. This figure illustrates the necessary distance between these two specimens, and the required orientation of their slots such that they share a common shear-centre.

It was decided that the slots in the slotted tube specimens should not protrude into the potted ends of each tube specimen; this would help to ensure that warping was fully restrained at each end of the slotted tube specimens, without depending upon the stiffness of the epoxy potting resin to prevent such warping deformations from occurring. As such, the slots terminate 26 mm (the thickness of each of the aluminium end fixture plates) prior to reaching each end of the tube specimens.

Upon carrying out some preliminary analyses (see Section 4.5), it was decided that a total effective warping length (clear span between the inside faces of the two end fixture plates restraining each pair of specimens) of approximately 300 mm would result in a restrained torsional response that clearly illustrates the consequences of ignoring the effects of warping-shear compliance. As the effective warping length becomes significantly greater than this value, the consequence of ignoring the effects of warping-shear compliance would become far less significant (see Section 4.7). Conversely, if too short of an effective warping length were to be employed, the specimens would exhibit excessively stiff restrained torsional responses, thus limiting the torsional rotation angle that could be achieved prior to failure of each specimen. Due to the limited resolution of the torsion length adjustment graduations permitted by the torsion testing apparatus that was used (130 mm increments), a 292 mm effective warping length was selected for the present experimental validation study. As such, the slot that was cut into each specimen had a total length of 292 ± 0.5 mm, which meant that the total length of each specimen (including the un-slotted potted ends) was approximately 344 mm. Figure 4.16 is a schematic illustration showing a cross-sectional profile view of a slotted tube specimen potted into a pair of end fixture plates for restrained torsion (warping) tests. This figure shows the necessary dimensions of the tube specimen and its surrounding end fixture plates, such that the designed effective warping length of 292 ± 0.5 mm is achieved.

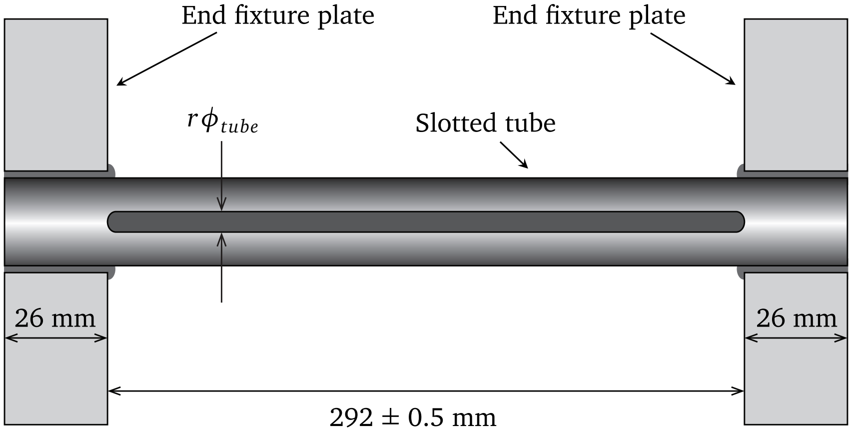

Figure 4.16: Cross-sectional profile view of a slotted tube specimen potted into a pair of end fixture plates for restrained torsion (warping) tests. This figure shows the relevant dimensions of the tube specimen and surrounding fixtures necessary to ensure that the designed effective warping length is achieved.

Figures 4.17 and 4.18 are photographs showing a pair of CFRP slotted tube specimens prior to being potted into an end fixture plate, and after being potted into an end fixture plate, respectively.

Figure 4.17: CFRP slotted tube specimens used for restrained torsion (warping) tests.

Figure 4.18: CFRP slotted tube specimens potted into aluminium end fixture plates used for restrained torsion (warping) tests.

4.6.2 Observations

In general, each pair of slotted tube warping specimens behaved as expected. All specimens appeared to warp about the axis of torsional rotation, which was designed to be coincident with the shear centre of each slotted tube specimen. With only one exception (described below), the ends of each warped slotted tube specimen appeared to remain normal to the surfaces of its end fixture plates, which indicates that the epoxy potted joints performed as intended to maintain fixed end-conditions, such that warping deformations were fully restrained. Figure 4.19 is a photograph showing a pair of CFRP slotted tube specimens undergoing a restrained torsion (warping) test.

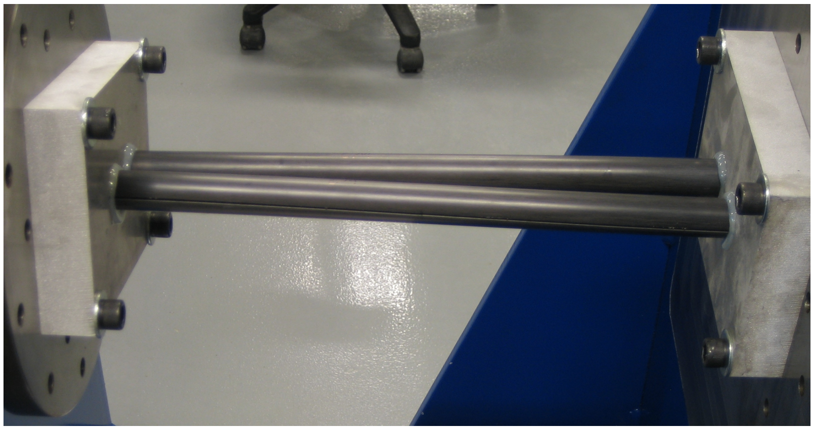

Figure 4.19: Experimental restrained torsion (warping) test of a pair of CFRP slotted tube specimens.

Although concerted efforts were made to ensure that the epoxy potting resin was fully cured prior to each experimental test (see Section 4.3.2), in the case of one of the pairs of CFRP slotted tube specimens, it was evident that the epoxy potting resin did not properly cure. This was likely caused by an improperly mixed batch of epoxy, which did not fully cross-link within the allotted 24 hour cure time. Consequently, at the time that these specimens were structurally tested under restrained torsion conditions, the epoxy potted joints securing this pair of specimens to their end fixture plates exhibited a soft and pliable consistency. As such, for this particular pair of CFRP slotted tube specimens, the epoxy potting resin was not capable of providing rigid potted joints that would restrain any significant rotations and/or warping displacements from occurring. On the contrary, it is likely that the soft and pliable nature of this improperly cured epoxy potting resin allowed significant rotations of the CFRP slotted tube specimens to occur within the potted joints. Ultimately, it is likely that this rotational compliance within the potted joints has lead to erroneously large measurements of restrained torsional rotation angles for this particular pair of CFRP slotted tube specimens (see CFRP warping test # 3 in Table 4.16). Figure 4.20 shows a cross-sectional profile view of a warped slotted tube specimen potted into a pair of end fixture plates, with potting resin that has not cured properly. This figure illustrates the source of the perceived additional warping compliance that can be caused by improperly cured potted joints.

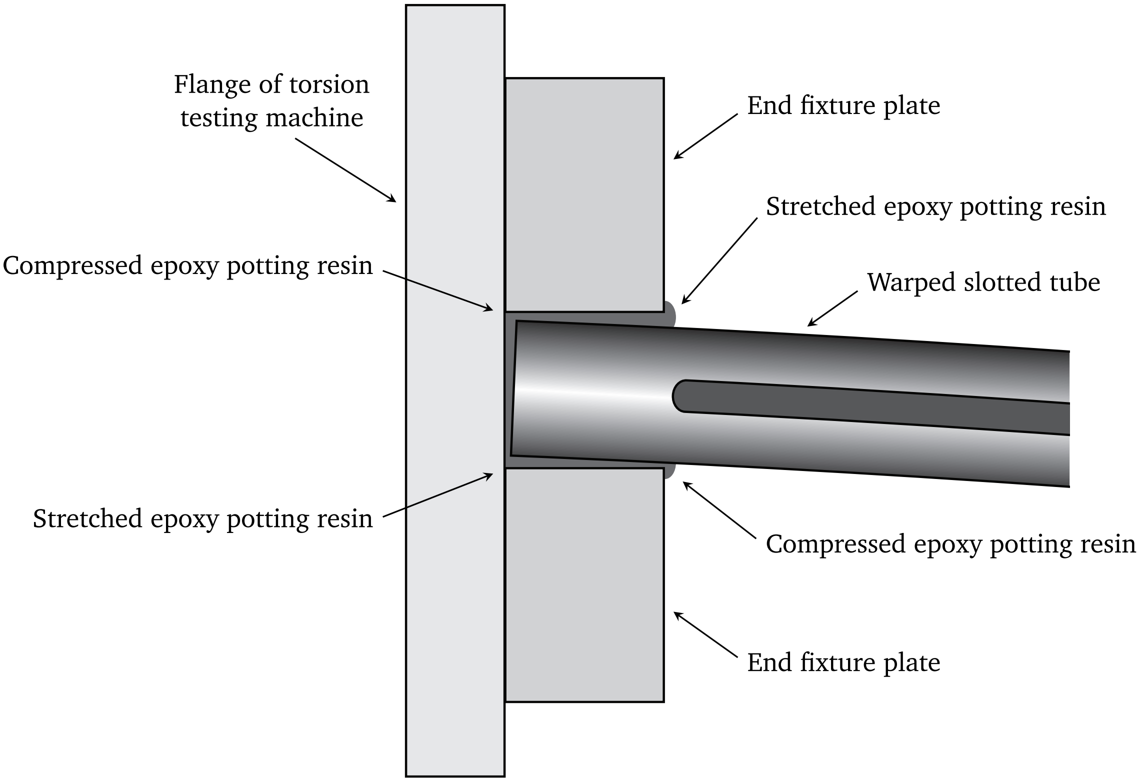

Figure 4.20: Cross-sectional illustration of a warped slotted tube specimen potted into a pair of end fixture plates, with potting resin that has not cured properly. This figure illustrates the source of the perceived additional warping compliance that can be caused by improperly cured potted joints.

4.7 Results and Discussion of the Restrained Torsion Experimental Program

Plots of measured torque (halved to account for the presence on two specimens in each test) versus angle of torsional rotation were created for each restrained torsion test that was carried out. Linear trend-lines were fitted through the linear regime of these plots, which was unanimously selected as the first 6° of rotation angle for all restrained torsion tests. The slope of these linear trend-lines represent the restrained torsional stiffness of each specimen. These plots and their accompanying linear trend-lines are included in Appendix D.

In order to quantify the error associated with each of the experimentally measured values of restrained torsional stiffness, it is necessary to recall from Section 4.3.2 the error and repeatability associated with each of the sensors employed in the torsion testing machine that was used. The total error associated with any torque measurement is simply equal to 47.22 N·mm, regardless of the magnitude of the torque measurement. Conversely, the error associated with a measurement of rotation angle has two components: a calibration error equal to 0.179 % of the observed rotation angle, and a repeatability error of 0.072°. Any error in the slope of the linear trend-line that was fit through the results of each restrained torsion test emerges as a function of the range of data through which this trend-line was fit. As such, the total error in the experimentally determined restrained torsional stiffness of each specimen can be calculated as follows:

$$\delta_{C_{RTS}} = C_{RTS}\sqrt{\left(\frac{\delta_T}{\Delta T}\right)^2 + \left(\frac{\delta_{\phi_g}}{\Delta \phi_g}\right)^2} \tag{4.38}$$

where C_{RTS} is the experimentally measured restrained torsional stiffness, $\Delta\phi_g$ is the total range of torsional rotations angles used to define the linear trend-line that was fit to the data (taken as 6°), ΔT is the total range of torques used to define the linear trend-line that was fit to the data (taken as $C_{RTS}\ \Delta\phi_g$), δ_T is the error associated with measurements of torque (taken as 47.22 N·mm), δ_{ϕ_g} is the error associated with measurements of torsional rotation angle, and $\delta_{C_{RTS}}$ is the total error associated with the experimentally measured value of restrained torsional stiffness. The calibration error associated with measurements of torsional rotation angle can be taken as 0.179 % of the aforementioned value of $\Delta\phi_g$, which yields a calibration error of 0.01074°. Combining this calibration error with the aforementioned repeatability error, the total value of δ_{ϕ_g} is then found to be 0.08274°.

Table 4.16 summarizes the experimentally measured values of restrained torsional stiffness, and the errors associated with each of these values, for each of the three pairs of CFRP slotted tube specimens that were tested in restrained torsion.

Table 4.16: Results of restrained torsion tests carried out on pairs of CFRP slotted tube specimens (see Appendix D).

Test #	**Restrained Torsional Stiffness (N·mm/Degree)**
1	488.2 ± 10.4
2	491.2 ± 10.4
3	429.7 ± 9.9

It is evident from Table 4.16 that the restrained torsional stiffness exhibited by the first two CFRP slotted tube specimens were quite similar (less than 0.6% discrepancy), whereas the third CFRP slotted tube specimen (test # 3) exhibited a considerably more compliant response to the imposed restrained torsional loading (14.3% more compliant than test # 2). This was likely caused by excessive compliance in the potted epoxy joints restraining each end of the CFRP slotted tubes used in test

3. It was explained in Section 4.6.2 that this particular pair of CFRP slotted tube specimens exhibited improperly cured epoxy potting resin, and that this could lead to erroneously high experimental measurements of restrained torsional compliance (see Figure 4.20). As such, the value of torsional stiffness associated with test # 3 in Table 4.16 was deemed as an outlier due to known causes, and was therefore omitted from any comparisons made with the present analytical method.

Table 4.17 summarizes the experimentally measured value of restrained torsional stiffness, and the error associated with this value, for the pair of aluminium slotted tube specimens that was tested in restrained torsion.

Table 4.17: Results of restrained torsion test carried out on the pair of aluminium slotted tube specimens (see Appendix D).

Test #	**Restrained Torsional Stiffness (N·mm/Degree)**
1	320.7 ± 9.0

Figures 4.21 and 4.22 show the torsional stiffnesses predicted by the present analytical method (see Section 4.5.8) as a function of the torsional gauge length, for the case of the CFRP and aluminimum slotted tube specimens studied in this investigation, respectively. Each of these figures includes a plot denoted as “PAM” that was generated using the present analytical formulation that accounts for the effects of warping-shear compliance (see equation (3.108) in Section 3.13), as well as a plot denoted as “Vlasov” that ignores the effects of warping-shear compliance (see equation (3.104) in Section 3.13). Upper bound and lower bound versions of each of these plots were generated (shown as fainter gray lines) by employing the upper bound and lower bound values of each of the relevant engineering section constants that were calculated in Section 4.5 for each type of slotted tube specimen. The experimental data points for test # 1 and test # 2 from Table 4.16 have been superimposed on Figure 4.21 to graphically illustrate the correlation of the present analytical model with the experimental results pertaining to the CFRP slotted tube specimens. Similarly, the experimental data point for test # 1 from Table 4.17 has been superimposed on Figure 4.22 to graphically illustrate the correlation of the present analytical model with the experimental result pertaining to the aluminium slotted tube specimens. Although experimental error values were calculated for each experimental data point (see Tables 4.16 and 4.17), the magnitude of these errors was small enough that the markers used to denote each experimental data point in Figures 4.21 and 4.22 are, in fact, larger than the span of the error bars that would be used to graphically illustrate these experimental errors.

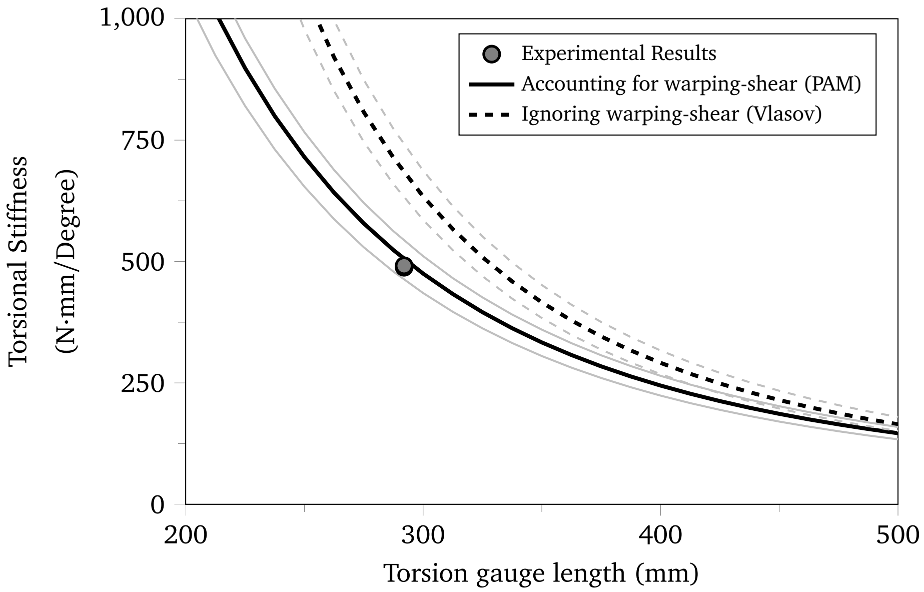

Figure 4.21: Validation results for restrained torsional (warping) stiffness of CFRP tube specimens. Legend entries designated as “PAM” represent results of the present analytical model, whereas “Vlasov” indicates the use of conventional Vlasov warping analysis (ignoring warping-shear compliance). Upper and lower bounds of the PAM and Vlasov predictions are represented by fainter gray variants of the lines used for these plots. The erroneous experimental results of CFRP warping test # 3 have been omitted from this figure.

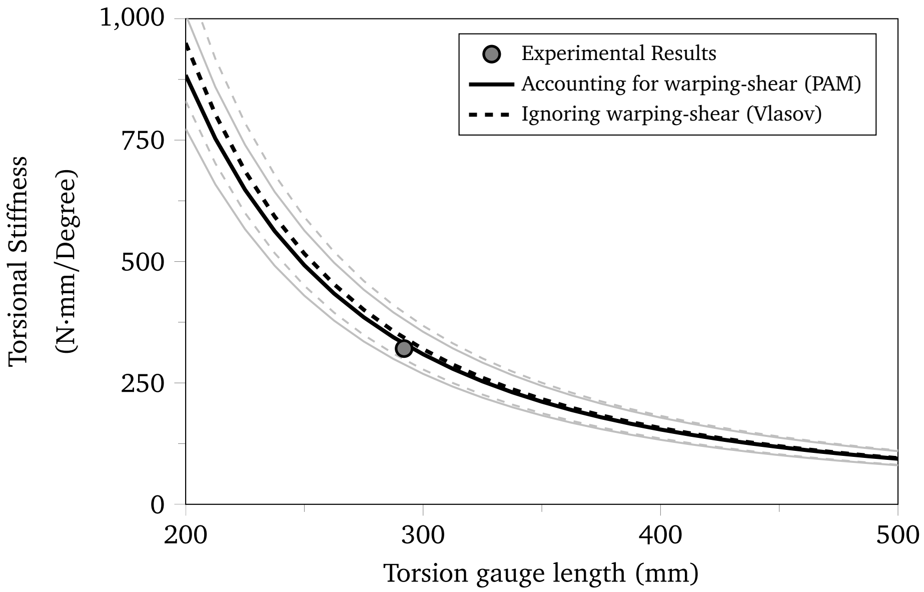

Figure 4.22: Validation results for restrained torsional (warping) stiffness of aluminium tube specimens. Legend entries designated as "PAM" represent results of the present analytical model, whereas "Vlasov" indicates the use of conventional Vlasov warping analysis (ignoring warping-shear compliance). Upper and lower bounds of the PAM and Vlasov predictions are represented by fainter gray variants of the lines used for these plots.

Figures 4.21 and 4.22 show good correlation between the present analytical model and the experimental results. All plotted experimental data points are well within the expected upper and lower bounds of the present analytical model that accounts for the effects of warping-shear compliance. In all cases, the present analytical model appears to have slightly over-predicted the value of torsional stiffness observed during the experimental tests. This can likely be attributed to a small amount of rotational compliance within the epoxy potted joints at the ends of each slotted tube specimen (see Figure 4.20 in Section 4.6.2). Although only one of the CFRP slotted tube specimens exhibited signs of improperly cured epoxy potted joints, the experimentally determined restrained torsional response of all of the slotted tube specimens was potentially susceptible to slight elastic deformations within the potted epoxy joints. As such, it is not surprising that the experimental tests consistently exhibited slightly more compliant restrained torsional responses than the theoretical restrained torsional responses predicted by the present analytical model. Table 4.18 summarizes the comparison between the three experimental data points included in Figures 4.21 and 4.22 and the relevant predictions of restrained torsional stiffness calculated using the present analytical model that accounts for the effects of warping-shear compliance (see equation (3.108) in Section 3.13).

Table 4.18: Comparison between restrained torsion tests and analytical predictions using present analytical model that accounts for the effects of warping-shear compliance. Note that the tabulated % discrepancy values were calculated with respect to the experimental data points.

Specimen Description	**Restrained Torsional Stiffness**		**Discrepancy (%)**
	Experimental Results (N·mm/Degree)	**Analytical Predictions (N·mm/Degree)**	
CFRP test # 1	488.2	506.1	3.7
CFRP test # 2	491.2	506.1	3.0
Aluminium test # 1	320.7	330.9	3.2

Analytical predictions were calculated using present analytical model that accounts for warping-shear compliance

It is interesting to note from Table 4.18 that the percent discrepancies between the experimental results and the present analytical model were quite similar for all three of the specimens included in this table; this supports the previously suggested notion that the discrepancy was caused by rotational compliance in the epoxy potted joints, since all three of these specimens employed the same epoxy potting resin.

Table 4.19 summarizes the comparison between the three experimental data points included in Figures 4.21 and 4.22 and the relevant predictions of restrained torsional stiffness calculated using the simplified Vlasov analytical model that neglects the effects of warping-shear compliance (see equation (3.104) in Section 3.13).

Table 4.19: Comparison between restrained torsion tests and analytical predictions using simplified Vlasov analytical model that neglects the effects of warping-shear compliance. Note that the tabulated % discrepancy values were calculated with respect to the experimental data points.

Specimen Description	**Restrained Torsional Stiffness**		**Discrepancy (%)**
	Experimental Results (N·mm/Degree)	**Analytical Predictions (N·mm/Degree)**	
CFRP test # 1	488.2	684.8	40.3
CFRP test # 2	491.2	684.8	39.4
Aluminium test # 1	320.7	342.8	6.9

Analytical predictions were calculated using Vlasov analytical model that neglects warping-shear compliance

It is clear from comparing Tables 4.18 and 4.19 that the inclusion of provisions to account for the effects of warping-shear compliance is of critical importance when attempting to analytically model the restrained torsional stiffness of the CFRP slotted tube specimens; ignoring the effects of warping-shear compliance resulted in as much as a 40.3% over-prediction of restrained torsional stiffness. Conversely, in the context of the aluminium slotted tube specimen, ignoring the effects of warping-shear compliance resulted in a far less severe over-prediction of restrained torsional stiffness. This finding is consistent with the fact that, over the past half century, engineers have commonly employed classical Vlasov warping theory (which neglects the effects of warping-shear compliance) to accurately model the restrained torsional response of structural members having thin-walled open sections comprising conventional metallic engineering materials (such as aluminium). In fact, it is evident from Figure 4.22 that the effect that warping-shear compliance has upon the aluminium slotted tube specimens would only have become significant at very short torsional gauge lengths, whereby local stress concentrations near the supports would likely have disqualified the use of either of these unidimensional analytical beam models (with or without provisions to account for the effects of warping-shear compliance).

Figure 4.23 is a plot of the percent difference between equations (3.104) and (3.108) from Section 3.13, as a function of torsional gauge length, for the cases of both the CFRP and aluminium slotted tube specimens. As such, this figure illustrates the consequences of neglecting to account for warping-shear compliance for the case of both the CFRP and aluminium slotted tube specimens studied during the present investigation.

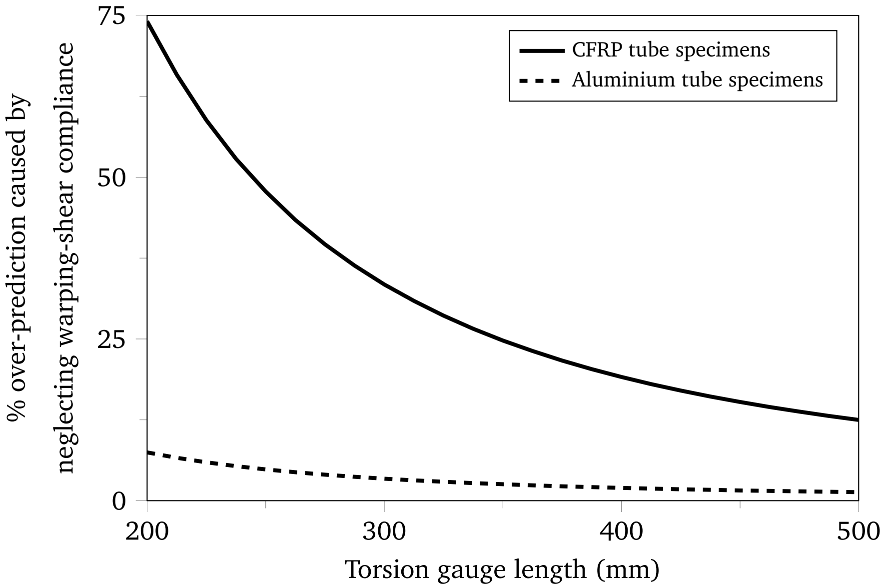

Figure 4.23: % over-prediction of restrained torsional (warping) stiffness of tube specimens due to exclusion of warping-shear compliance.

It is clear from Figure 4.23 that the conventional Vlasov model that neglects the effects of warping-shear compliance results in only a slight over-prediction of the restrained torsional stiffness of the slotted tube specimen. In fact, even at a torsional gauge length of 200 mm, which is only slightly more than 10 times the outside diameter of these tube specimens, the Vlasov model would only over-predict the restrained torsional stiffness of the aluminium slotted tube specimens by 7.5%. Conversely, at this same torsional gauge length of 200 mm, the Vlasov model would over-predict the restrained torsional stiffness of the CFRP slotted tube specimens by 74.5%. This dramatic difference in analytical fidelity afforded by the Vlasov model for the case of CFRP specimens or aluminium specimens is indicative of the dangers of employing classical analytical methods to model the elastic response and elastic stability of FRP composite structural members.

Chapter 5

Conclusions and Recommendations

5.1 Manufacturing of Hybrid Composite Co-Pultruded Structural Members

A novel hybrid composite co-pultruded structural member was proposed, and it was suggested that this new structural member could potentially offer a variety of benefits for applications in the aerospace and/or automotive industries. Once refined, the proposed hybrid co-pultrusion technology could likely facilitate the mass production of high performance FRP structural members having highly consistent and repeatable mechanical properties. This repeatability of mechanical properties might eventually lead to improved confidence in these FRP materials amongst engineers, which might allow for a reduction in the conservatism of FRP structural design. Ultimately, this reduced conservatism would allow for lighter weight structures, which is of critical importance in the aerospace industry. An experimental prototype manufacturing run was carried out in order to preliminarily assess the feasibility of this proposed hybrid composite co-pultrusion technology. The following conclusions have been drawn from this experimental pultrusion run:

1. The proposed hybrid composite co-pultruded aircraft stringer technology is likely capable of offering most of the light-weighting benefits afforded by the current state-of-the-art CFRP aircraft structural systems, while simultaneously retaining the manufacturability and serviceability that previously could only be afforded by conventional metallic (aluminium) aircraft structural systems constructed using mechanical fasteners. In fact, in Section 3.18.5, an example was used to demonstrate that a hypothetical CFRP-aluminium hybrid co-pultruded stringer could achieve a column buckling strength per unit weight that is approximately 80% greater than that attainable by a conventional aluminium stringer of identical exterior geometric dimensions.

2. Off-gassing of the epoxy primer applied to the aluminium strips caused the formation of gas-filled blisters at the interface between the FRP material and the embedded aluminium strips that were co-pultruded along with the FRP material. Although the manufacturer of the primer claims that it contains only a very small amount of volatile organic compounds (VOC), the author suspects that the high temperatures within the pultrusion die exacerbated the situation to the extent that even this small VOC content was enough to cause blistering of the prototype co-pultruded specimens.

3. As expected, the prototype hybrid co-pultruded members adopted a curved shape upon emerging from the pultrusion machine, which was caused by the dissimilar coefficients of thermal expansion possessed by each of the constituents present within each of these co-pultruded members. Since the embedded aluminium elements had the highest coefficient of thermal expansion of all of the materials present within these specimens, each co-pultruded specimen had a tendency to curve toward the region of its cross-section that contained the greatest amount of aluminium.

In response to the aforementioned conclusions, and in light of some of the observations and concerns discussed in previous sections of this dissertation, the author has compiled the following recommendations for future research pertaining to the proposed hybrid composite co-pultrusion technology:

1. Although a great deal was learned from fabricating the prototype hybrid composite co-pultruded specimens that are discussed in this dissertation, time and financial constraints prohibited the author from carrying out comprehensive experimental structural tests on these prototype specimens. As such, it is recommended that future experimental research is carried out to characterize the structural behaviour of this type of member, and to compare this behaviour with that of conventional metallic structural members of comparable dimensions.

2. Although one of the primary purposes of the embedded co-pultruded metallic elements is to serve as hard-points to accept mechanical fasteners, the exact nature of this mechanical connection was not explicitly discussed in this dissertation. As such, the author recommends that future research is carried out to develop methodologies and guidelines for the use of mechanical fasteners to connect hybrid composite co-pultruded structural members to adjacent components of a structural system.

3. Future prototype hybrid co-pultrusion runs should be carried out without the use of primer coatings applied to the embedded metallic elements. If embedded aluminium elements are to be employed, it is suggested that these aluminium elements undergo an unsealed anodizing treatment immediately prior to the pultrusion run. This unsealed anodized aluminium would have a highly porous surface, which would likely enhance adhesive bonding due to infiltration of the polymeric resin matrix into the pore spaces of the anodized surface. In addition,

the absence of a primer coating would eliminate concerns regarding blistering caused by high temperature off-gassing of VOC materials present within the primer coating.

4. Future prototype hybrid co-pultrusion runs should be carried out utilizing a curved pultrusion die in order to help prevent the development of curvatures due to thermal strains. In order to achieve this, it would first be necessary to predict the curvature caused by thermal strains using either computational or analytical modelling techniques. The pultrusion die could then be fabricated such that its cavity is curved in the opposite direction to the expected thermal deformation, but with the same magnitude of curvature. As such, upon exiting the pultrusion die, the co-pultruded specimens would initially adopt a curved shape, but it is expected that they would subsequently return to a nearly straight shape once they have cooled to ambient temperatures.

5. Future prototype hybrid co-pultrusion runs should be carried out to experiment with pre-stressing methods of preventing the development of curvatures due to thermal strains. This would be achieved by applying pre-stressing tensile forces to various select constituents within the co-pultruded specimen in the direction that is opposite to the progression of the pultrusion run. These pre-stressing forces would cause mechanical tensile strains to be generated within the loaded constituents as they enter the pultrusion die. If the coefficient of thermal expansion of each constituent is known, then it might be possible to calibrate the magnitude of the pre-stressing tensile forces such that the sum of the mechanical and thermal strains within each constituent of the member reaches the same value as it passes through the pultrusion die. If such a state of iso-strain can be achieved within the pultrusion die, then it is possible that the specimen will ultimately adopt a straight geometry geometry once all mechanical and thermal loads have been removed.

6. Future prototype hybrid co-pultrusion runs should be carried out to experiment with the use of titanium rather than aluminium for the embedded co-pultruded elements. Titanium has a considerably lower coefficient of thermal expansion than aluminium (less than half); as such, the use of titanium in place of aluminium might help to mitigate the development of thermal stresses and curvatures that would be developed during the pultrusion process, as well as during any in-service exposure to thermal loadings.

7. It was discussed in Section 2.5.4 that, in its current state, the proposed hybrid composite co-pultrusion technology is not appropriate for flange growing (local increases in cross-sectional area to accommodate mechanical fasteners) or flange scalloping (regional reductions in cross-sectional area to reduce mass) operations, which are popularly used to optimize and reduce the weight of aircraft wing-stringers. One potential method of simulating scalloped material

between fasteners might be to consider only removing material from the embedded metallic strips (perhaps by creating elliptical cut-outs), and then filling the resulting voids with a light-weight filler material (such as a closed-cell foam) prior to passing these metallic strips through the pultrusion die. As such, the net exterior cross-sectional geometry of the stringer would be constant, but the internal material composition would fluctuate along the length such that far more embedded metal is present in the vicinity of each mechanical fastener. The author recommends that future prototype hybrid co-pultrusion runs are carried out using the aforementioned scalloping technique in order to experimentally test its feasibility for aircraft wing-stringer applications.

8. It is recommended that future research is carried out to develop methods that can be used to detect and monitor unknown and/or dormant failures within the proposed hybrid composite co-pultruded structural members.
9. It is recommended that future research is carried out to study the response of the proposed hybrid co-pultruded members to hygrothermal effects.

5.2 Analytical Modelling of Hybrid Composite Co-Pultruded Structural Members

It is a prudent engineering practice to understand the mechanics that dictate the results of structural finite element analyses. When the structural behaviour of a beam or column is to be assessed, it is often necessary to validate the results of finite element analyses using simplified unidimensional beam-type analytical methods. The use of classical unidimensional beam-type analytical methods to model the behaviour of FRP composite structural members will often lead to over-predictions of stiffness and elastic stability; this unconservatism is often caused by the fact that many of these classical analytical models neglect the effects of shear compliance. As such, a comprehensive analytical model was developed to predict the linear flexural-torsional-shear buckling response of the proposed hybrid composite co-pultruded structural aircraft stringers. This analytical model comprises a system of smaller analytical procedures which are used together to ascertain a suite of engineering section constants that describe the structural response of the member; these section constants are subsequently used to calculate the linear flexural-torsional-shear buckling response of the member. The aforementioned analytical model was validated using a combination of experimental and computational (finite element) methods. The following conclusions have been drawn from the development and validation of this analytical model, and each of its constituent analytical procedures:

1. Conventional torsional analyses of laminated plates that are based upon CLPT will generally result in over-predictions of torsional stiffness. The severity of these over-predictions will be

exacerbated if the laminated plate has a low width-to-thickness aspect ratio, and/or if the laminated plate has a low through-thickness to in-plane shear modular ratio. Section 3.11 presented an analytical method of predicting the torsional stiffness of thick laminated plates. This analytical model was successfully computationally validated using the FE method. Of the 22 test cases that were studied, the largest discrepancy between the FE results and the results of the present analytical method was 1.315%. Conversely, for these same test cases, it was found that conventional torsional analysis techniques based upon CLPT tended to over-predict the FE results by as much as 111.3%.

2. In the context of torsional analyses, the geometric width-to-thickness aspect ratio η_{geom} of a thick laminated plate is not directly relevant to determining the validity of Kirchhoff-Love thin plate assumptions; on the contrary, the effective width-to-thickness aspect ratios $\eta_{eff\,PT}$ and/or $\eta_{eff\,FT}$ should be used for this determination. It is likely that similar effective width-to-thickness aspect ratios could be calculated to evaluate the validity of Kirchhoff-Love thin plate assumptions in the context of other structural loadings as well.

3. Southwell developed a method [70] of predicting the lateral perturbation of an initially curved column undergoing an axial compression loading. It was shown in Section 3.14.3 that Southwell's method can be modified to account for the effects of transverse shear compliance by simply replacing terms pertaining to the Euler flexural buckling load $P_{cr\,Eu\,Y'Y'}$ with the Engesser flexural-shear buckling load $P_{cr\,En\,Y'Y'}$.

4. Classical Vlasov warping analysis techniques that ignore warping-shear compliance can grossly over-predict the restrained torsional (warping) stiffness of beams comprising materials having relatively high longitudinal elastic moduli and relatively low in-plane shear moduli (such as longitudinally oriented unidirectional FRP). Sections 3.12 and 3.13 presented an analytical method of predicting the restrained torsional response of thin-walled open structural members, while accounting for the effects of warping-shear compliance. This analytical model was successfully validated using experimental methods (see Chapter 4). In the context of the specific test case that was used for this experimental validation, the present analytical method predicted the restrained torsional stiffness within 3.7% of the experimentally observed result; conversely, classical Vlasov warping analysis techniques over-predicted the experimentally observed restrained torsional stiffness by as much as 40.3%. If the experimental specimens were shortened to an effective warping length of 200 mm, it is expected that the classical Vlasov warping analysis techniques would have over-predicted the restrained torsional stiffness by 74.5%.

5. Classical unidimensional beam-type analytical methods that ignore shear effects can grossly over-predict the critical buckling loads of columns (such as aircraft wing-stringers) compris-

ing materials having relatively high longitudinal elastic moduli and relatively low in-plane shear moduli (such as longitudinally oriented unidirectional FRP). Section 3.18 demonstrated a successful and conclusive computational (finite element) validation of the present analytical modelling computer program to predict the critical flexural-torsional-shear buckling load of a column having an un-symmetric cross-sectional geometry. Various features of this model were then disabled to demonstrate the consequences of neglecting the effects of transverse shear and/or warping-shear compliance. In fact, when both of these shear effects were simultaneously ignored, the critical buckling load was over-predicted by as much as 103.63%.

In response to the aforementioned conclusions, and in light of some of the observations and concerns discussed in previous sections of this dissertation, the author has compiled the following recommendations for future research pertaining to the present analytical model, and each of its constituent analytical procedures:

1. Section 3.11 presented an analytical method of predicting the torsional stiffness of thick laminated plates. While this analytical method was validated using computational (finite element) methods, it is recommended that experimental tests are carried out in order to further substantiate this computational validation. Furthermore, although some of the limitations of this analytical method were discussed in Section 3.11.8, it is possible that some additional limitations might be revealed during such an experimental program. Upon completion of such an experimental validation, the author believes that the aforementioned torsional analytical method will be suitably reliable for use as a stand-alone means of ascertaining the torsional stiffness of thick laminated plates.

2. Section 3.14.3 presented a derivation for a new analytical unidimensional beam model to predict the lateral perturbation of an initially curved column undergoing an axial compression loading, while accounting for the effects of transverse shear compliance. Although this analytical model is largely based upon existing engineering science that has been broadly accepted by the engineering community, the author recommends that experimental and/or computational work is carried out in order to validate the aforementioned model.

3. Section 3.17 described a computer program that was written using all of the analytical procedures that were discussed in Chapter 3. While this computer program was demonstrated to be a valuable tool to aid structural engineers in the validation of their computational models, it was not written in a manner that is conducive for commercial use by industry engineers. On the contrary, the presently discussed computer program was merely written in manner that was intended to facilitate prototyping of the engineering science that was presented in Chapter 3. Therefore, it is recommended that a refined version of this computer program should be written to carry out each of the analytical procedures discussed in Chapter 3. This refined computer

program should employ efficient programming architecture, and should be written in such a manner that it can be compiled into a stand-alone executable that can be run on any personal computer without the aid of an expensive specialized commercial software package. The purpose of such a computer program would be to afford any structural engineer a fast means of approximating the structural response of a beam or column of open cross-sectional geometry; however, it should do so in a manner that could be understood by any structural engineer who is familiar with classical unidimensional beam-type analytical methods. As such, this computer program should present all of the engineering section constants that are calculated for the beam, in addition to the predicted structural response that is subsequently calculated using those section constants.

4. Chapter 4 presented an experimental validation of the restrained torsional stiffness analytical model that was described in Sections 3.12 and 3.13. Unfortunately, due to financial and time constraints, this experimental validation was only carried out using one effective warping length. Furthermore, one of the three warping specimens exhibited an erroneously low warping stiffness due to improperly cured epoxy potted joints. As such, it is recommended that additional experimental validation is carried out in order to further substantiate the validation results presented in Chapter 4. It is recommended that these additional validation experiments are carried out using a similar (or identical) procedure to that which was described in Chapter 4; however, it is recommended that the effective warping length is varied in order to more conclusively demonstrate correlation with the present analytical model.

Chapter 6

Summary of Contributions

This dissertation contains a broad spectrum of engineering science; it includes new theorems and concepts presented for the first time in this document, theorems that were presented in recent years by the present author and/or other contemporary researchers, and well established theorems that were presented by other scientists and engineers many years ago and have since become broadly accepted by the engineering community. This document has generally been formulated in a manner that focuses on the amalgamation of all of these theorems for practical engineering purposes, without discriminating between old and new theorems. As such, for the convenience of the reader, the following list has been compiled to summarize all of the new engineering science that has been contributed by the present author in this dissertation:

1. The author proposed a novel hybrid composite co-pultruded structural member, and carried out a prototype co-pultrusion run to develop a preliminary assessment of the feasibility of this technology (see Chapter 2). In addition, specific hypothetical applications of this technology were proposed, and described in detail. These hypothetical applications include: aircraft wing stringers, an automobile chassis structural system, and a railway car structural system.

2. The author developed provisions to account for the overlapped regions at the intersections of two or more legs of built-up open cross-sectional geometries (see Section 3.6). These provisions help to prevent erroneous predictions of axial, bending, or shear stiffnesses that would otherwise result if classical analytical methods were employed to model the elastic response of beams or columns having this type of cross-sectional geometry.

3. The author developed an analytical model to predict the torsional stiffness of thick laminated plates (see Section 3.11).

4. The author developed an analytical unidimensional beam model to quantify the additional restrained torsional compliance caused by warping-shear compliance (see Sections 3.12.3 and

3.13). Although similar analytical models have recently been presented by other researchers, a unanimous technique has not yet been established in the literature. The methodology presented in this dissertation is quite similar to the technique that was developed in 2012 by Wang, Zhao, Zhang, and Gong [89].

5. The author derived an analytical unidimensional beam model to predict the lateral perturbation of an initially curved column undergoing an axial compression loading, while accounting for the effects of transverse shear compliance (see Section 3.14.3). Coincidentally, several months after the present author completed the aforementioned derivation, a nearly identical derivation was published in a journal article [9], which somewhat detracted from the novelty of the present author's work on this subject matter.

6. The author carried out an experimental program that served to successfully validate the presented analytical model used to quantify the additional restrained torsional compliance caused by warping-shear effects (see Chapter 4). While numerous similar analytical models have recently been presented in the literature, the present author is not aware of any published works that have demonstrated experimental validations any of these similar analytical models.

7. The author developed a computer program that utilizes the aforementioned newly contributed analytical models, and combines them with a wealth of existing engineering theorems to generate a full suite of engineering sections constants for a beam having an open cross-section that comprises laminated composite materials (see Chapter 3). This suite of engineering section constants is sufficiently comprehensive such that a full flexural-torsional-shear linear buckling analysis can be carried out. Furthermore, some unique provisions were included in the model to facilitate the inclusion of moderately thick section walls, which are not uncommon in the context of aircraft wing-stringers. The aforementioned computer program, as well as each of the subordinate analytical procedures upon which it is based, were successfully and conclusively validated using the finite element method (see Section 3.18).

Bibliography

[1] M. Ahrens. U.S. vehicle fire trends and patterns. Technical report, Fire Analysis and Research Division, National Fire Protection Association, Quincy, Massachusetts, USA, 2004.

[2] L. Ascione, Giordano A., and S. Spadea. Lateral buckling of pultruded FRP beams. *Composites: Part B*, 42(4):819–824, 2011.

[3] L. Ascione, L. Feo, and G. Mancusi. On the statical behaviour of fibre-reinforced polymer thin-walled beams. *Composites: Part B*, 31(8):643–654, 2000.

[4] E.J. Barbero. *Introduction to Composite Materials*. Taylor and Francis Group, Philadelphia, Pennsylvania, USA, 1999.

[5] E.J. Barbero, R. Lopez-Anido, and J.F. Davalos. On the mechanics of thin-walled laminated composite beams. *Journal of Composite Materials*, 27(8):806–829, 1993.

[6] Z.P. Bažant. A correlation study of incremental deformations and stability of continuous bodies. *ASME Journal of Applied Mechanics*, 38:919–928, 1971.

[7] Z.P. Bažant. Shear buckling of sandwich,fiber composite and lattice columns, bearings, and helical springs: paradox resolved. *ASME Journal of Applied Mechanics*, 70(1):75–83, 2003.

[8] J.R. Betteridge, G.R. Bishop, and FibrePlas Extrusions Ltd. Thermoplastic pultrusion. International patent WO 2001/024993 A1, April 2001. EP1220748.

[9] A.P. Bonab, B.H. Hashemi, and M. Hosseini. Experimental evaluation of the elastic buckling and compressive capacity of laced columns. *Journal of Constructional Steel Research*, 86:66–73, 2013.

[10] R.G. Budynas. *Advanced Strength and Applied Stress Analysis*. The McGraw-Hill Companies, New York, New York, USA, 2^{nd} edition, 1999.

[11] M. Capurso. Sul calcolo delle travi di parete sottile in presenza di forze e distorsioni. Nota I: La teoria rigorosa e le equazioni fondamentali. *Ricerca Scientifica II-A*, 34(6):213, 1964.

[12] M. Capurso. Sul calcolo delle travi di parete sottile in presenza di forze e distorsioni. Nota II: La generalizzazione del problema del saint venant. *Ricerca Scientifica II-A*, 34(6):241, 1964.

[13] M. Capurso. Sul calcolo delle travi di parete sottile in presenza di forze e distorsioni. Nota III: Complementi analitici: il calcolo delle funzioni caratteristiche per alcuni tipi di travi di parete sottile di comune impiego. *Ricerca Scientifica II-A*, 34(7):5, 1964.

[14] M. Capurso. Sul calcolo delle travi di parete sottile in presenza di forze e distorsioni. Nota IV: L'effetto dei carichi trasversali sulle sollecitazioni e spostamenti delle travi di parete sottile. *Ricerca Scientifica II-A*, 34(7):43, 1964.

[15] C. Casteele, W. Dekeyser, E. Lokere, H. Pattyn, and N.V. Bekaert S.A. Pultruded composite profile reinforced by metal cords. International patent WO 2004/101909 A1, November 2004.

[16] C.E.S. Cesnik and D.H. Hodges. VABS: A new concept for composite rotor blade cross-sectional modeling. *Journal of the American Helicopter Society*, 42(1):27–38, 1997.

[17] C.C. Chamis and G.P Sendeckyj. Critique on theories predicting thermoelastic properties of fibrous composites. *Journal of Composite Materials*, 2(3):332–358, 1968.

[18] R.M. Christensen. The numbers of elastic properties and failure parameters for fiber composites. *Journal of Engineering Materials and Technology*, 120:110, 1998.

[19] M. Connolly, J. King, T. Shidaker, A. Duncan, and Huntsman International LLC. Pultruding polyurethane composite profiles: Practical guidelines for injection box design. In *proceedings of the COMPOSITES 2005 Convention and Trade Show*, Component Metering Equipment and Processing, Columbus, Ohio, USA, September 28–30 2005. American Composites Manufacturers Association.

[20] M. Connolly, J. King, T. Shidaker, A. Duncan, and Huntsman Polyurethanes. Characterization of pultruded polyurethane composites: Environmental exposure and component assembly testing. In *proceedings of the COMPOSITES 2006 Convention and Trade Show*, St. Louis, MO, USA, October 18–20 2006. American Composites Manufacturers Association.

[21] E. Cosentino and P. Weaver. An enhanced single-layer variational formulation for the effect of transverse shear on laminated orthotropic plates. *European Journal of Mechanics, A/Solids*, 29(4):567–590, 2010.

[22] L. De Lorenzis and A. La Tegola. Static behavior of pultruded fiber-reinforced polymer thin-walled beams. *Composite Structures*, 60(3):231–244, 2003.

[23] S.B. Dong, R.B. Matthiesen, K.S. Pister, and R.L. Taylor. Analysis of structural laminates. Technical Report ARL–76, Aeronautical Research Laboratory, Office of Aerospace Research, Wright-Patterson Air Force Base, Ohio, USA, September 1961.

[24] S.B. Dong, K.S. Pister, and R.L. Taylor. On the theory of laminated anisotropic shells and plates. *Journal of the Aerospace Sciences*, 29(8):969–975, 1962.

[25] R. Emre Erkmen and M. Mohareb. Torsion analysis of thin-walled beams including shear deformation effects. *Thin-Walled Structures*, 44(10):1096–1108, 2006.

[26] F. Engesser. Die knickfestigkeit gerader stäbe. *Z. Architekten und Ing. Verein zu Hannover*, 35:455, 1889.

[27] F. Engesser. Die knickfestigkeit gerader stäbe. *Zentralblatt des Bauverwaltung*, 11:483–486, 1891.

[28] L. Feo and G. Mancusi. Modeling shear deformability of thin-walled composite beams with open cross-section. *Mechanics Research Communications*, 37(3):320–325, 2010.

[29] J.C. Halpin and J.L. Kardos. The Halpin-Tsai equations: A review. *Polymer Engineering and Science*, 16(5):344–352, 1976.

[30] J. A. Haringx. On the buckling and lateral rigidity of helical springs. In *proceedings of the Koninklijke Nederlandse Akademie van Wetenschappen*, number 45, Amsterdam, Netherlands, 1942.

[31] J. A. Haringx. *Phillips Research Reports*. Phillips Research Laboratories, Eindhoven, Netherlands, 3rd & 4th edition, 1948-1949.

[32] M.D. Hayes. *Structural analysis of a pultruded composite beam: Shear stiffness determination and strength and fatigue life predictions*. Virginia Polytechnic Institute and State University, Blacksburg, Virginia, USA, 2003. PhD dissertation.

[33] R.L. Hewitt and M.C. de Malherbe. An approximation for the longitudinal shear modulus of continuous fibre composites. *Journal of Composite Materials*, 4(2):280–282, 1970.

[34] H. Honickman, J. Johrendt, and P. Frise. On the torsional stiffness of thick laminated plates. *Journal of Composite Materials*, pages 1–17. published online before print September 11, 2013, DOI 10.1177/0021998313501919.

[35] H. Honickman, J. Johrendt, D. Northwood, and P. Frise. Design of a pultruded steel-GFRP hybrid structural member. In *proceedings of the ASME 2010 International Mechanical Engineering Congress and Exposition*, number IMECE2010-37378, Vancouver, British Columbia, Canada, November 12–18 2010. American Society of Mechanical Engineers (ASME).

[36] H.N. Honickman, J.L. Johrendt, and P.R. Frise. Steel reinforced pultruded GFRP vehicle chassis structure. In *proceedings of the 2010 SAE World Congress*, number 2010-01-0021, Detroit, Michigan, USA, April 13–15 2010. Society of Automotive Engineers (SAE).

[37] MatWeb – the online materials information resource (http://www.matweb.com). internet website, accessed April 2010. “Overview of materials for Thermoset Polyurethane, Liquid”, “Overview of materials for Epoxy, Cast, Unreinforced”, “Overview of materials for Epoxy/Carbon Fiber Composite”, “Bedford Plastics Glass Reinforced Polyester Flat Sheet 1/8"”, “Bedford Plastics Glass Reinforced FR Polyester Structural Fiberglass Profiles”, “Bedford Plastics Glass Reinforced Vinylester Flat Sheet, 1/8"”, “Bedford Plastics Glass Reinforced Vinylester Structural Fiberglass Profiles”, “Overview of materials for Phenolic, Novolac, Fabric Filled”.

[38] Z. Jian and L. Sijian. Torsion of composite laminated bars with a large number of layers. *Applied Mathematics and Mechanics*, 19(6):585–591, 1998.

[39] R.M. Jones. *Mechanics of composite materials*. Hemisphere Publishing Corporation, New York, New York, USA, 1975.

[40] R.R. Joshi, E.H. Cheolas, E.F. Cassidy, W.J. Karoly, and H.D. Coffee. Polyurethane based pultruded resins improve the environmental image of composite materials. In *proceedings of the COMPOSITES 2001 Convention and Trade Show*, Tampa, Florida, USA, October 3–6 2001. American Composites Manufacturers Association.

[41] R.R. Joshi, L.L. Varas, and A.D. Padsalgikar. Polyurethane in pultrusion: Styrene free alternative systems. In *proceedings of the International Composites Expo 1999*, number 21–D, pages 1–6. Society of the Plastics Industry, 1999.

[42] F. Khouli, J. Griffiths, F.F. Afagh, and R.G. Langlois. Actuation of slender thin-wall anisotropic open cross-section beams based on asymptotically correct vlasov theory. *Journal of Intelligent Material Systems and Structures*, 21(5):529–540, 2010.

[43] G. Kirchhoff. Über das gleichgewicht und die bewegung einer elastischen scheibe. *Journal für die reine und angewandte Mathematik*, 40:51–88, 1850.

[44] L.P. Kollár. Flexural-torsional buckling of open section composite columns with shear deformation. *International Journal of Solids and Structures*, 38(42):7525–7541, 2001.

[45] L.P. Kollár and A Pluzsik. Analysis of thin-walled composite beams with arbitrary layup. *Journal of Reinforced Plastics and Composites*, 21(16):1423–1465, 2002.

[46] L. Lagunegrand, T. Lorriot, R. Harry, H. Wargnier, and J.M. Quenisset. Initiation of free-edge delamination in composite laminates. *Composites Science and Technology*, 66(10):1315–1327, 2006.

[47] D. Lee, H.H. Hilton, and A. Velicki. Optimum stress and material distributions in stitched prseus composites. In *proceedings of the 53rd AIAA/ASME/ASCE/AHS/ASC Structures, Structural Dynamics, and Materials Conference*, number paper number AIAA–2012–1765, Honolulu, Hawaii, USA, April 2012. American Institute of Aeronautics and Astronautics.

[48] J. Lee. Flexural analysis of thin-walled composite beams using shear-deformable beam theory. *Composite Structures*, 70(2):212–222, 2005.

[49] J. Lee and S.-h. Lee. Flexural-torsional behavior of thin-walled composite beams. *Thin-Walled Structures*, 42(9):1293–1305, 2004.

[50] S.G. Lekhnitskii. *Theory of elasticity of an anisotropic elastic body*. Holden-Day, New York, New York, USA, 1963.

[51] S.-R. Li and R.C. Batra. Relations between buckling loads of functionally graded Timoshenko and homogeneous Euler-Bernoulli beams. *Composite Structures*, 95:5–9, 2012.

[52] V. Li and A. Velicki. Advanced prseus structural concept design and optimization. In *proceedings of the 12th AIAA/ISSMO Multidisciplinary Analysis and Optimization Conference, MAO-7*, number paper number AIAA–2008–5840, Victoria, British Columbia, Canada, September 2008. American Institute of Aeronautics and Astronautics.

[53] A.E.H. Love. *A Treatise on the Mathematical Theory of Elasticity*. Cambridge University Press, Cambridge, UK, 4th edition, 1927.

[54] P.K. Mallick. *Fiber-Reinforced Composites: Materials, Manufacturing, and Design*. CRC Press – Taylor and Francis Group, Boca Raton, Florida, USA, 3rd edition, 2008. ISBN 978-0-8493-4205-9.

[55] C. Mittelstedt and W. Becker. Interlaminar stress concentrations in layered structures: Part 1 – a selective literature survey on the free-edge effect since 1967. *Journal of Composite Materials*, 38(12):1037–1062, 2004.

[56] MSC Software Corporation, Santa Ana, California, USA. *Marc Volume A: Theory and User Information*, 2011.

[57] MSC Software Corporation, Santa Ana, California, USA. *Marc Volume B: Element Library*, 2011.

[58] MSC Software Corporation, Santa Ana, California, USA. *Marc Volume C: Program Input*, 2011.

[59] P.L.N. Murthy and C.C. Chamis. Integrated composite analyzer (ICAN): Users and programmers manual. NASA Technical Paper NASA-TP-2515, NASA Glenn Research Center, Cleveland, Ohio, USA, 1986.

[60] P.L.N. Murthy, C.A. Ginty, and J.G. Sanfeliz. Second generation integrated composite analyzer (ICAN) computer code. NASA Technical Paper NASA-TP-3290, NASA Glenn Research Center, Cleveland, Ohio, USA, 1993.

[61] R.B. Pipes and N.J. Pagano. Interlaminar stresses in composite laminates under uniform axial extension. *Journal of Composite Materials*, 4(4):538–548, 1970.

[62] A. Pluzsik and L.P. Kollár. Effects of shear deformation and restrained warping on the displacements of composite beams. *Journal of Reinforced Plastics and Composites*, 21(17):1517–1541, 2002.

[63] L. Prandtl. Zur torsion von prismatischen stäben. *Physikalische Zeitschrift*, 4:758–759, 1903.

[64] A.H. Puppo and H.A. Evensen. Interlaminar shear in laminated composites under generalized plane stress. *Journal of Composite Materials*, 4(2):204–220, 1970.

[65] E. Reissner. The effect of transverse shear deformation on the bending of elastic plates. *Journal of Applied Mechanics*, 12:69–77, 1945.

[66] E. Reissner. A consistent treatment of transverse shear deformation in laminated anisotropic plates. *AIAA Journal*, 10:716–718, 1972.

[67] E. Reissner and Y. Stavsky. Bending and stretching of certain types of heterogeneous aeolotropic elastic plates. *Journal of Applied Mechanics*, 28(3):402–408, 1961.

[68] A. J. C. B. de Saint-Venant. Mémoire sur la torsion des prismes. *Mémoires présentés par divers savants à l'Académie des Sciences*, 14:233–560, 1855.

[69] M. Savoia and N. Tullini. Torsional response of inhomogeneous and multilayered composite beams. *Composite Structures*, 25(1-4):587–594, 1993.

[70] R.V. Southwell. On the analysis of experimental observations in problems of elastic stability. In *proceedings of the Royal Society of London*, number 135, pages 601–616, 1932.

[71] T.F. Starr. *Pultrusion for Engineers*. Woodhead Publishing Limited, Cambridge, England, CRC Press LLC, Boca Raton, Florida, USA, 2000. ISBN 978-1-85573-425-8.

[72] J.E. Sumerak. Variable cross-section pultruded profiles offer new design options for structural applications. In *proceedings of the 2nd International Conference on Composites Engineering (ICCE/2)*, New Orleans, Louisiana, USA, August 1995. International Community for Composites Engineering.

[73] J.E. Sumerak. Pultrusion method for making varible cross section thermoset articles. US patent 5,556,496, September 1996.

[74] J.E. Sumerak and Inc. Creative Pultrusions. Pultruded composites in impact and toughness driven applications achieve new performance levels with polyurethane resin. In *proceedings of the 48th International SAMPE Symposium*, Long Beach, California, USA, May 11–15 2003. Society of the Advancement of Material and Process Engineering (SAMPE).

[75] S.R. Swanson. Torsion of laminated rectangular rods. *Composite Structures*, 42(1):23–31, 1998.

[76] S.P. Timoshenko. On the correction for shear of the differential equation for transverse vibrations of prismatic bars. *Philosophical Magazine*, 41:744–746, 1921.

[77] S.P. Timoshenko. On the transverse vibrations of bars of uniform cross-section. *Philosophical Magazine*, 43:125–131, 1922.

[78] S.P. Timoshenko and J.M. Gere. *Theory of Elastic Stability*. McGraw-Hill Book Company, New York, New York, USA, 2^{nd} edition, 1961.

[79] S.P. Timoshenko and J.N. Goodier. *Theory of Elasticity*. McGraw-Hill Book Company, New York, New York, USA, 2^{nd} edition, 1951.

[80] J.G. Vaughan, E. Lackey, H.D. Coffee, N. Barksby, and J.L. Lambach. Pultrusion of fast-gel thermoset polyurethanes: Processing considerations and mechanical properties. In *proceedings of the Composites 2003 Convention and Trade Show*, Anaheim, California, USA, October 1–3 2003. Composites Fabricators Association.

[81] J.G. Vaughan, E. Lackey, D. Green, R. Swedo, T. Johnson, and D. Trauth. New fast-cure, high strength phenolic resin systems for pultrusion. In *proceedings of the American Composites Manufacturers Association Conference*, Tampa, Florida, USA, October 6–8 2004. American Composites Manufacturers Association.

[82] A. Velicki and D. Jegley. Prseus development for the hybrid wing body aircraft. In *proceedings of the 11th AIAA Aviation Technology, Integration, and Operations Conference*, number paper number AIAA–2011–7025, Virginia Beach, Virginia, USA, September 2011. American Institute of Aeronautics and Astronautics.

[83] A. Velicki and P.J. Thrash. Advanced structural concept development using stitched composites. In *proceedings of the 49th AIAA/ASME/ASCE/AHS/ASC Structures, Structural Dynamics, and Materials Conference*, number paper number AIAA–2008–2329, Schaumburg, Illinois, USA, June 2008. American Institute of Aeronautics and Astronautics.

[84] J.R. Vinson. Mechanical fastening of polymer composites. *Polymer Engineering & Science*, 29(19):1332–1339, 1989.

[85] V.Z. Vlasov. *Thin-Walled Elastic Beams*. Israel Program for Scientific Translations, Jerusalem, Israel, 2^{nd} edition, 1961. [First edition – Stroizdat (in Russian) Moscow, 1940].

[86] T.P. Vo and J. Lee. On sixfold coupled buckling of thin-walled composite beams. *Composite Structures*, 90(3):295–303, 2009.

[87] V.V. Volovoi and D.H. Hodges. Theory of anisotropic thin-walled beams. *Journal of Applied Mechanics*, 67(3):453–459, 2000.

[88] V.V. Volovoi, D.H. Hodges, C.E.S. Cesnik, and B. Popescu. Assessment of beam modeling methods for rotor blade applications. *Mathematical and Computer Modelling*, 33(10-11):1099–1112, 2001.

[89] Z. Wang, J. Zhao, D. Zhang, and J. Gong. Restrained torsion of open thin-walled beams including shear deformation effects. *Journal of Zhejiang University-SCIENCE A (Applied Physics & Engineering)*, 13(4):260–273, 2012.

[90] J.M. Whitney. Stress analysis of thick laminated composite and sandwich plates. *Journal of Composite Materials*, 6(3):426–440, 1972.

[91] J.M. Whitney. A modified shear deformation theory for laminated anisotropic plates. In *proceedings of the American Society for Composites Fifth Technical Conference: composite materials in transition*, pages 469–478, East Lansing, Michigan, USA, 1990. American Society for Composites.

[92] J.M. Whitney. Stress analysis of laminated, anisotropic plates subjected to torsional loading. In *proceedings of the AIAA/ASME/ASCE/AHS/ASC 32nd Structures, Structural Dynamics, and Materials Conference*, number AIAA 91-0956, pages 956–962, Baltimore, Maryland, USA, 1991. American Institute of Aeronautics and Astronautics (AIAA).

[93] J.M. Whitney. Analysis of anisotropic laminated plates subjected to torsional loading. *Composites Engineering*, 3(6):567–582, 1993.

[94] H. Wu, C.M. Ma, M. Lee, and Y. Wu. Pultruded fiber-reinforced polyurethane-toughened phenolic resin, I – reactivity and morphology. *Die Angewaniite MakromoIekulare Chemie*, 235:35–45, 1996.

[95] W.C. Young and R.G. Budynas. *Roark's Formulas for Stress and Strain*. The McGraw-Hill Companies, New York, New York, USA, 7^{th} edition, 2002.

[96] W. Yu and D.H. Hodges. Generalized Timoshenko theory of the variational asymptotic beam section analysis. *Journal of the American Helicopter Society*, 50(1):46–55, 2005.

[97] W. Yu, D.H. Hodges, V.V. Volovoi, and E.D. Fuchs. A generalized Vlasov theory for composite beams. *Thin-Walled Structures*, 43(9):1493–1511, 2005.

Appendices

Appendix A

Cross-Sectional Dimensions of Slotted Tube Specimens

Table A.1: Cross-sectional geometric measurements of CFRP tube specimens used in experimental validation of analytical model for restrained torsion (see Chapter 4).

Measurement #	**Outside Diameter (mm)**	**Wall Thickness (mm)**	**Width of Slot (mm)**
1	19.05	2.53	1.47
2	19.05	2.66	1.40
3	19.04	2.60	1.46
4	19.04	2.53	1.41
5	19.04	2.64	1.45
6	19.06	2.53	1.42
7	19.05	2.61	1.50
8	19.04	2.70	1.52
9	19.05	2.66	1.47
Average (mean)	19.0467	2.6067	1.4555
Standard Deviation	0.0071	0.0644	0.0403

Table A.2: Cross-sectional geometric measurements of aluminium tube specimens used in experimental validation of analytical model for restrained torsion (see Chapter 4).

Measurement #	**Outside Diameter (mm)**	**Wall Thickness (mm)**	**Width of Slot (mm)**
1	19.07	1.34	1.60
2	19.15	1.21	1.61
3	19.06	1.20	1.58
4	19.17	1.33	1.59
5	19.05	1.22	1.55
6	19.15	1.23	1.55
7	18.98	1.34	1.55
8	19.11	1.29	1.58
9	19.05	1.27	1.63
Average (mean)	19.0878	1.2700	1.5822
Standard Deviation	0.0618	0.0574	0.0286

Appendix B

Pure Torsional Response of Tube Specimens

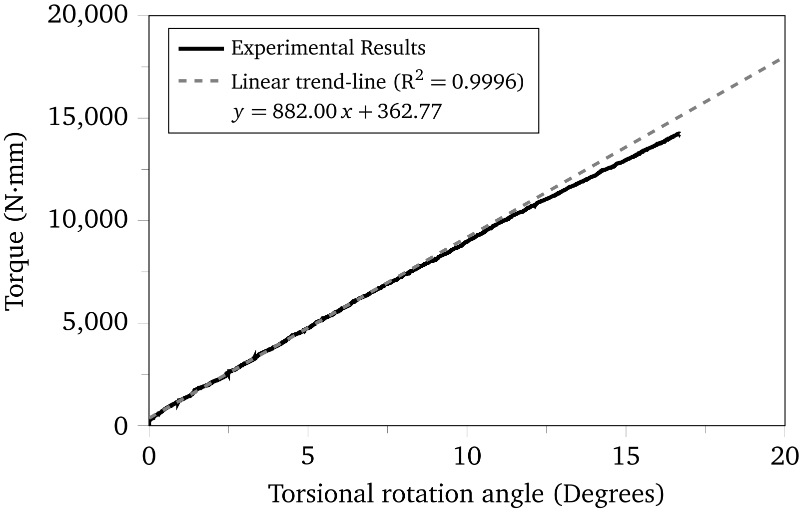

Figure B.1: Results of pure torsion test of CFRP tube specimen # 1. The plotted linear trend-line was fit through the data points from the first 6° of torsional rotation. The slope of this linear trend-line represents the pure torsional stiffness (882.0 N·mm/Degree) of this specimen.

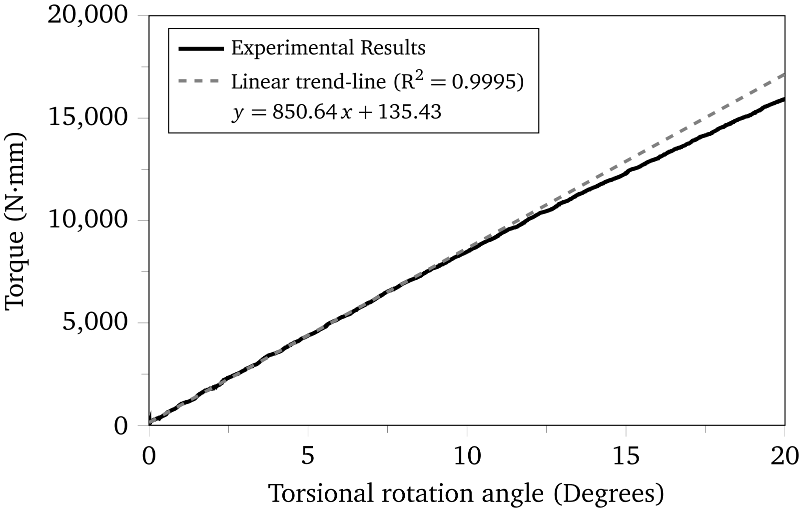

Figure B.2: Results of pure torsion test of CFRP tube specimen # 2. The plotted linear trend-line was fit through the data points from the first 6° of torsional rotation. The slope of this linear trend-line represents the pure torsional stiffness (850.6 N·mm/Degree) of this specimen.

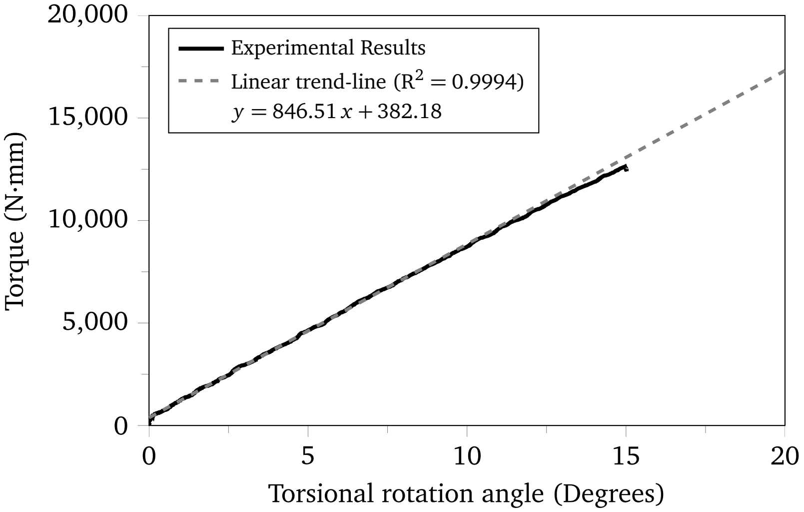

Figure B.3: Results of pure torsion test of CFRP tube specimen # 3. The plotted linear trend-line was fit through the data points from the first 6° of torsional rotation. The slope of this linear trend-line represents the pure torsional stiffness (846.5 N·mm/Degree) of this specimen.

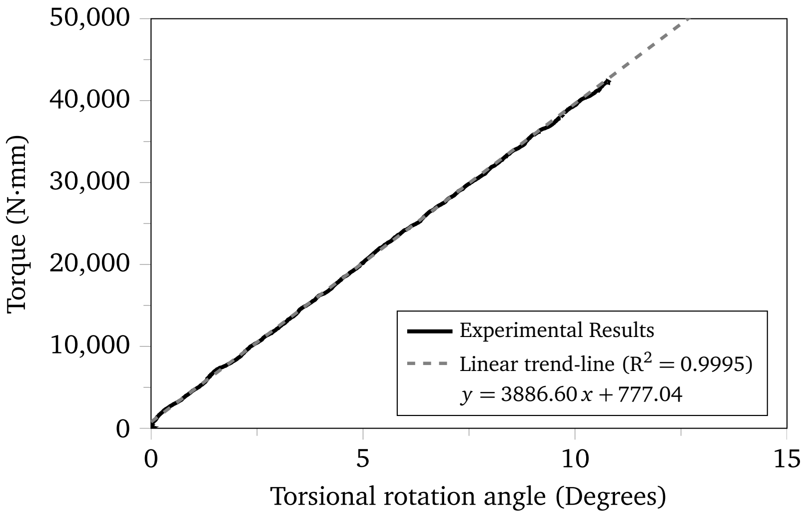

Figure B.4: Results of pure torsion test of aluminium tube specimen # 1. The plotted linear trend-line was fit through the data points from the first 6° of torsional rotation. The slope of this linear trend-line represents the pure torsional stiffness (3886.6 N·mm/Degree) of this specimen.

Appendix C

3-Point Bending Response of Tube Specimens

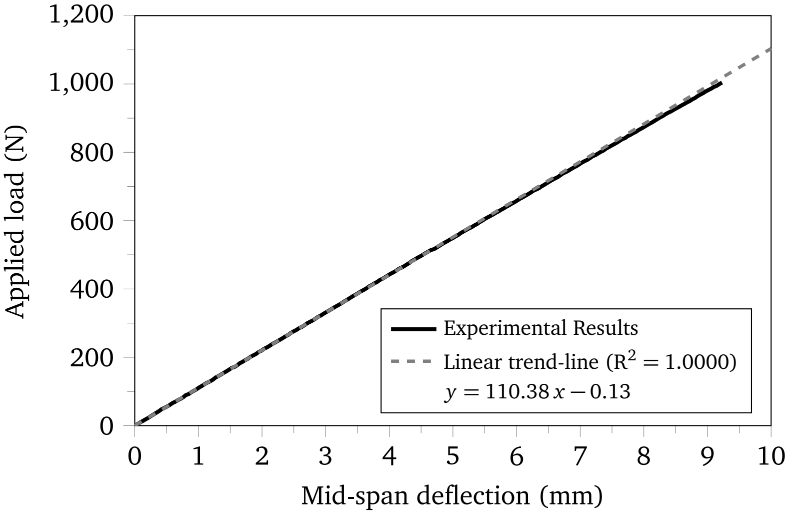

Figure C.1: Results of 3-point bending test of CFRP tube specimen # 1 with 590 mm span. The plotted linear trend-line was fit through the data points from the first 350 N of applied load. The slope of this linear trend-line represents the mid-span transverse stiffness (110.38 N/mm) of this specimen. The reciprocal of the slope of this linear trend-line represents the mid-span transverse compliance (0.00906 mm/N) of this specimen.

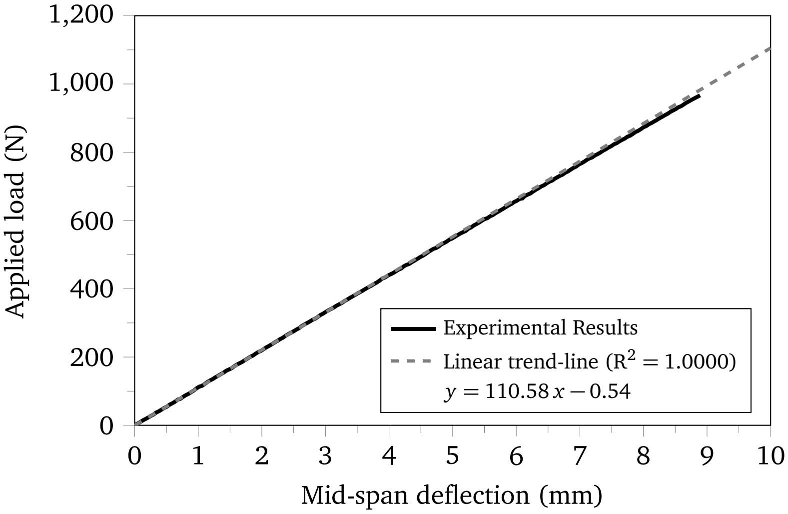

Figure C.2: Results of 3-point bending test of CFRP tube specimen # 2 with 590 mm span. The plotted linear trend-line was fit through the data points from the first 350 N of applied load. The slope of this linear trend-line represents the mid-span transverse stiffness (110.58 N/mm) of this specimen. The reciprocal of the slope of this linear trend-line represents the mid-span transverse compliance (0.00904 mm/N) of this specimen.

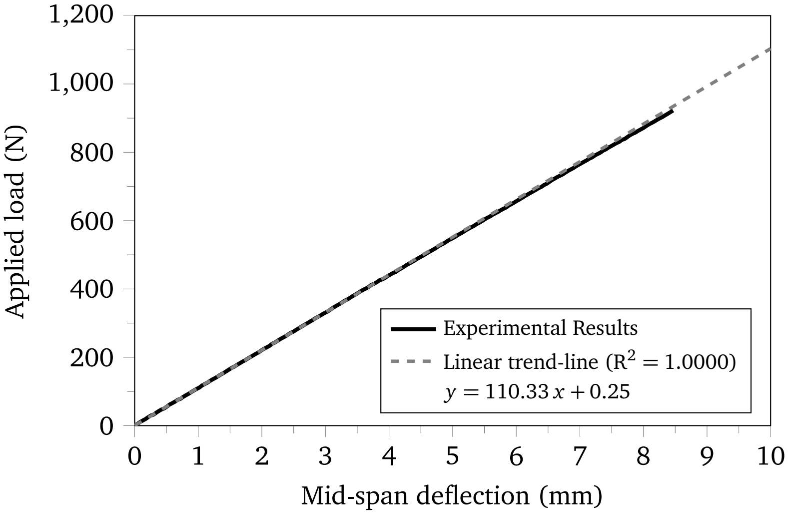

Figure C.3: Results of 3-point bending test of CFRP tube specimen # 3 with 590 mm span. The plotted linear trend-line was fit through the data points from the first 350 N of applied load. The slope of this linear trend-line represents the mid-span transverse stiffness (110.33 N/mm) of this specimen. The reciprocal of the slope of this linear trend-line represents the mid-span transverse compliance (0.00906 mm/N) of this specimen.

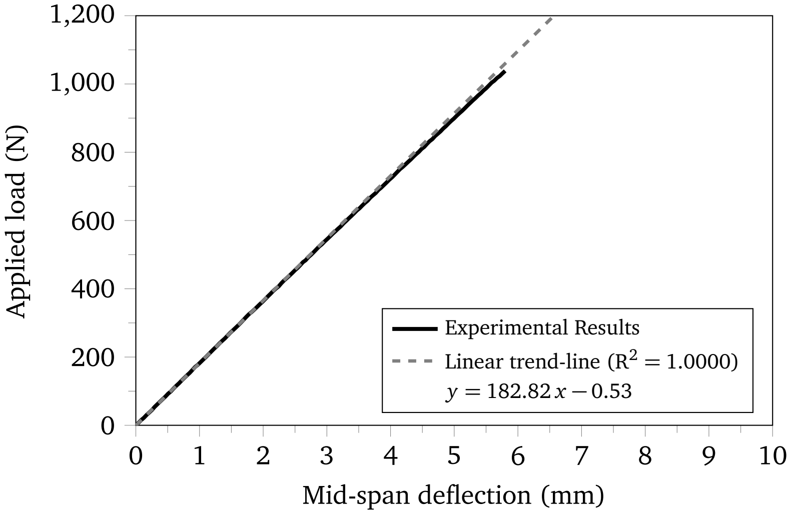

Figure C.4: Results of 3-point bending test of CFRP tube specimen # 4 with 490 mm span. The plotted linear trend-line was fit through the data points from the first 350 N of applied load. The slope of this linear trend-line represents the mid-span transverse stiffness (182.82 N/mm) of this specimen. The reciprocal of the slope of this linear trend-line represents the mid-span transverse compliance (0.00547 mm/N) of this specimen.

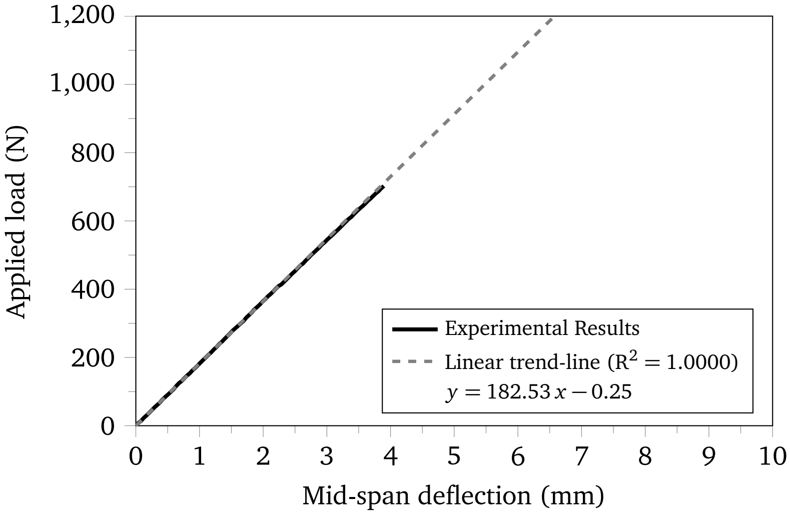

Figure C.5: Results of 3-point bending test of CFRP tube specimen # 5 with 490 mm span. The plotted linear trend-line was fit through the data points from the first 350 N of applied load. The slope of this linear trend-line represents the mid-span transverse stiffness (182.53 N/mm) of this specimen. The reciprocal of the slope of this linear trend-line represents the mid-span transverse compliance (0.00548 mm/N) of this specimen.

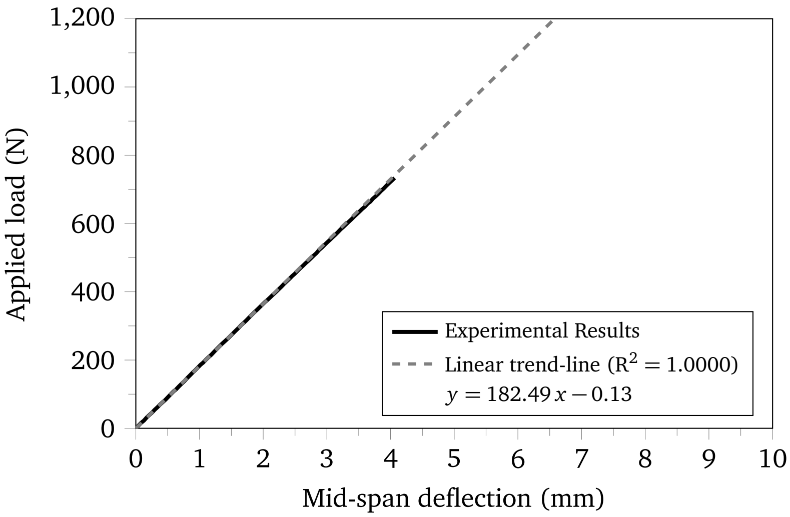

Figure C.6: Results of 3-point bending test of CFRP tube specimen # 6 with 490 mm span. The plotted linear trend-line was fit through the data points from the first 350 N of applied load. The slope of this linear trend-line represents the mid-span transverse stiffness (182.49 N/mm) of this specimen. The reciprocal of the slope of this linear trend-line represents the mid-span transverse compliance (0.00548 mm/N) of this specimen.

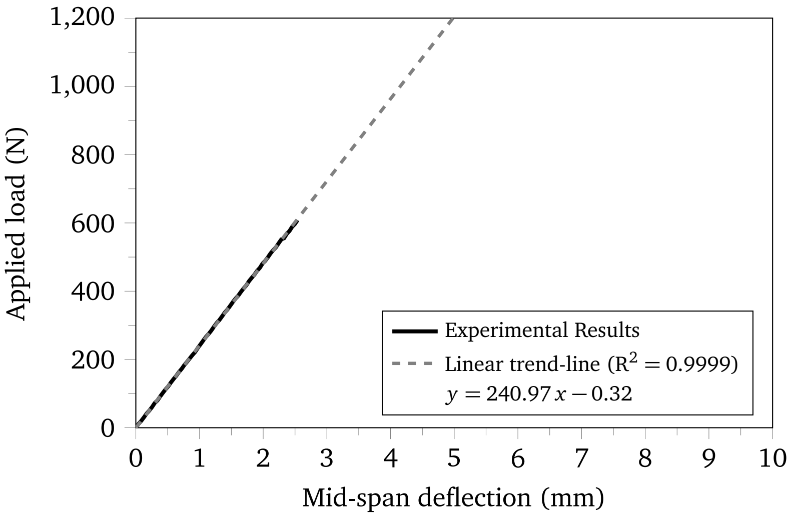

Figure C.7: Results of 3-point bending test of CFRP tube specimen # 7 with 440 mm span. The plotted linear trend-line was fit through the data points from the first 350 N of applied load. The slope of this linear trend-line represents the mid-span transverse stiffness (240.97 N/mm) of this specimen. The reciprocal of the slope of this linear trend-line represents the mid-span transverse compliance (0.00415 mm/N) of this specimen.

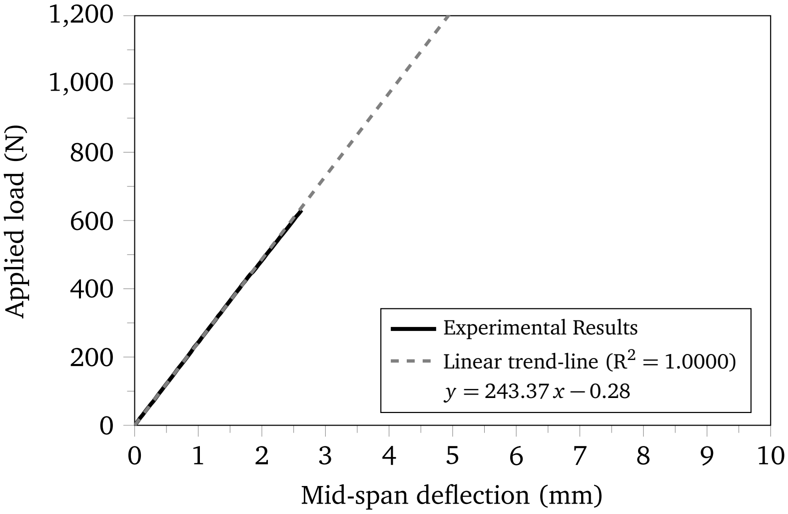

Figure C.8: Results of 3-point bending test of CFRP tube specimen # 8 with 440 mm span. The plotted linear trend-line was fit through the data points from the first 350 N of applied load. The slope of this linear trend-line represents the mid-span transverse stiffness (243.37 N/mm) of this specimen. The reciprocal of the slope of this linear trend-line represents the mid-span transverse compliance (0.00411 mm/N) of this specimen.

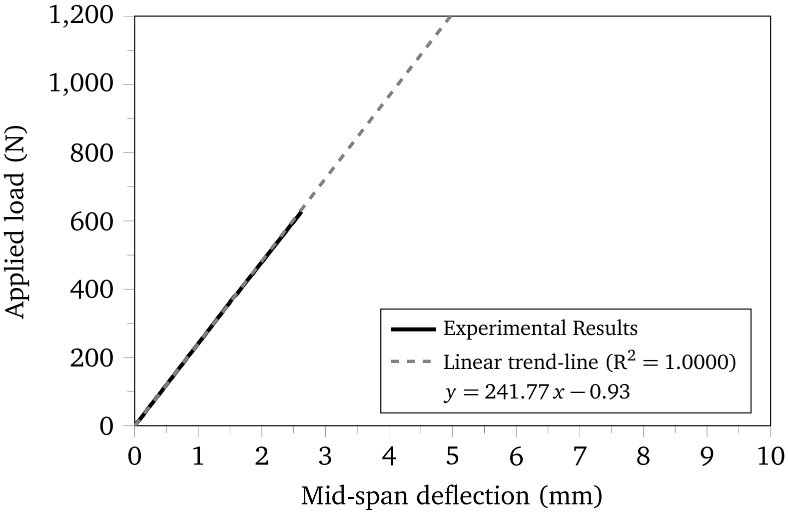

Figure C.9: Results of 3-point bending test of CFRP tube specimen # 9 with 440 mm span. The plotted linear trend-line was fit through the data points from the first 350 N of applied load. The slope of this linear trend-line represents the mid-span transverse stiffness (241.77 N/mm) of this specimen. The reciprocal of the slope of this linear trend-line represents the mid-span transverse compliance (0.00414 mm/N) of this specimen.

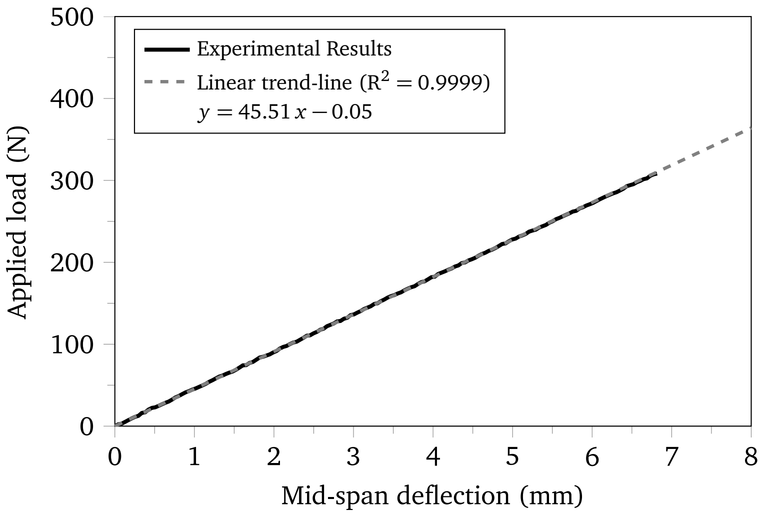

Figure C.10: Results of 3-point bending test of aluminium tube specimen # 1 with 590 mm span. The plotted linear trend-line was fit through the data points from the first 150 N of applied load. The slope of this linear trend-line represents the mid-span transverse stiffness (45.51 N/mm) of this specimen. The reciprocal of the slope of this linear trend-line represents the mid-span transverse compliance (0.02197 mm/N) of this specimen.

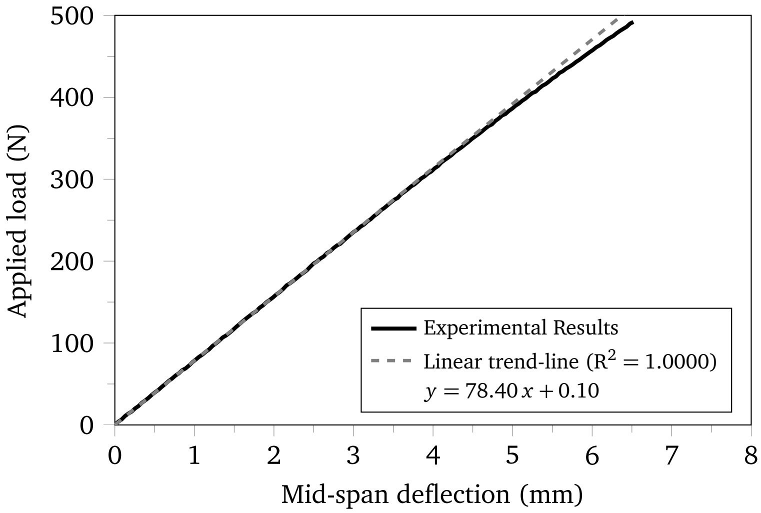

Figure C.11: Results of 3-point bending test of aluminium tube specimen # 2 with 490 mm span. The plotted linear trend-line was fit through the data points from the first 200 N of applied load. The slope of this linear trend-line represents the mid-span transverse stiffness (78.40 N/mm) of this specimen. The reciprocal of the slope of this linear trend-line represents the mid-span transverse compliance (0.01276 mm/N) of this specimen.

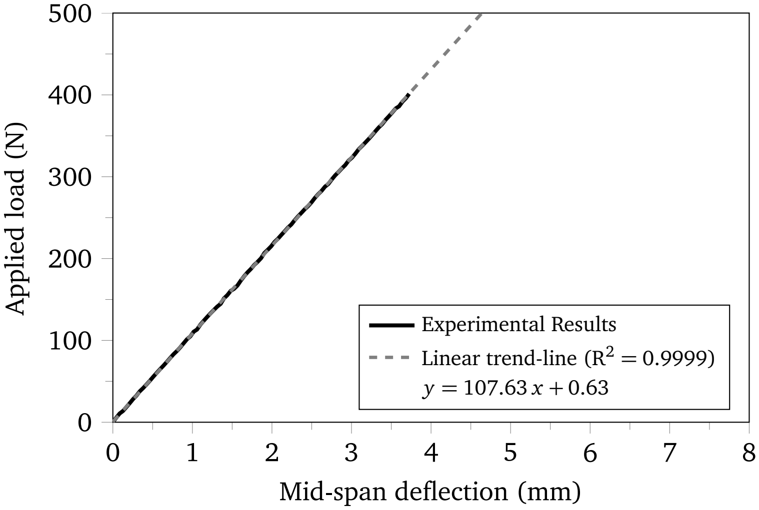

Figure C.12: Results of 3-point bending test of aluminium tube specimen # 3 with 440 mm span. The plotted linear trend-line was fit through the data points from the first 250 N of applied load. The slope of this linear trend-line represents the mid-span transverse stiffness (107.63 N/mm) of this specimen. The reciprocal of the slope of this linear trend-line represents the mid-span transverse compliance (0.00929 mm/N) of this specimen.

Appendix D

Restrained Torsional Response of Slotted Tube Specimens

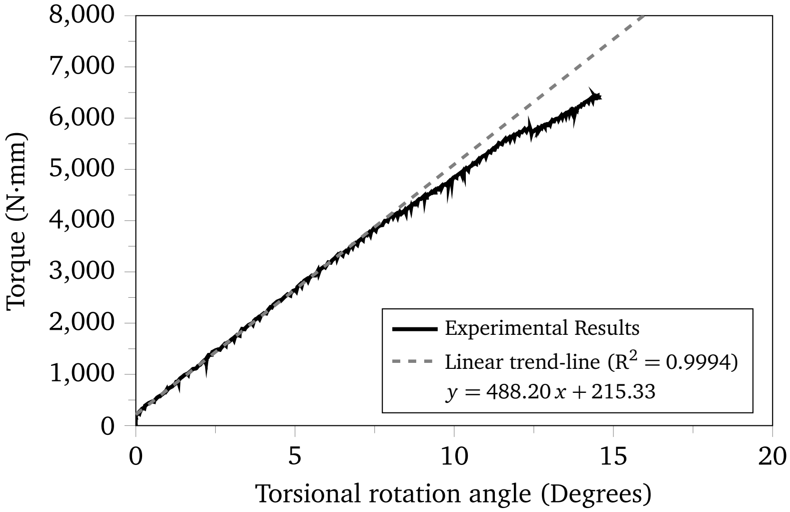

Figure D.1: Results of restrained torsion test of CFRP slotted tube specimen pair # 1. The plotted linear trend-line was fit through the data points from the first 6° of torsional rotation. The slope of this linear trend-line represents the restrained torsional stiffness (488.2 N·mm/Degree) of these specimens.

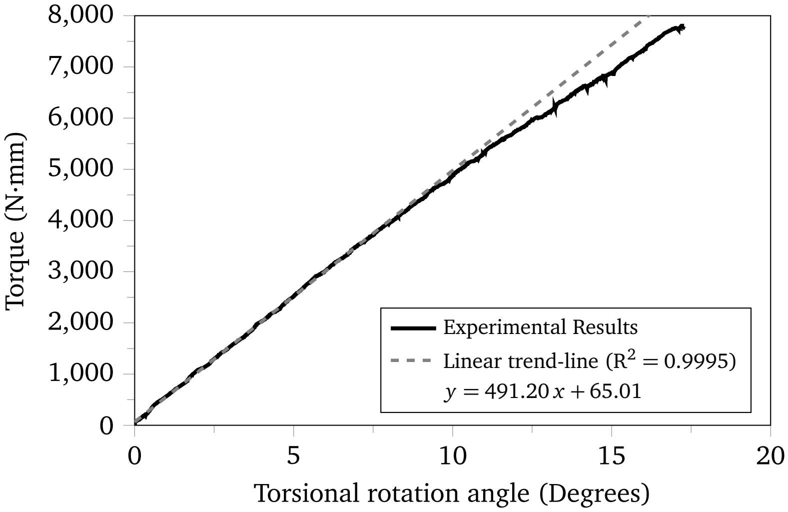

Figure D.2: Results of restrained torsion test of CFRP slotted tube specimen pair # 2. The plotted linear trend-line was fit through the data points from the first 6° of torsional rotation. The slope of this linear trend-line represents the restrained torsional stiffness (491.2 N·mm/Degree) of these specimens.

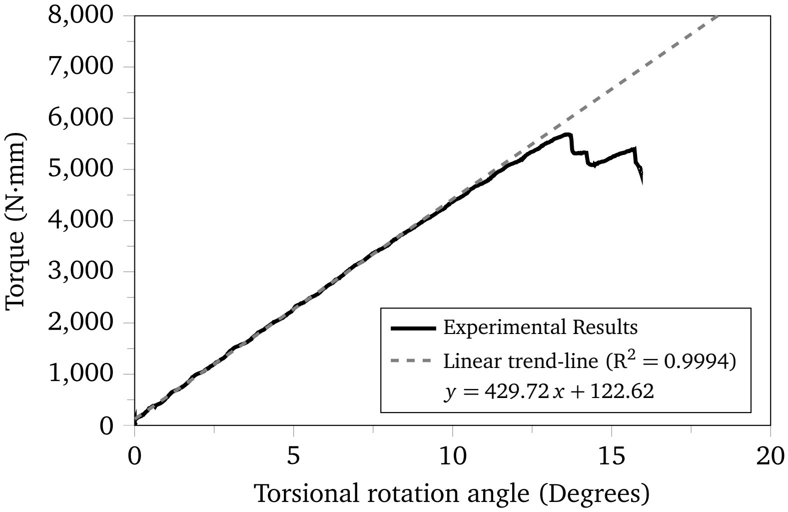

Figure D.3: Results of restrained torsion test of CFRP slotted tube specimen pair # 3. The plotted linear trend-line was fit through the data points from the first 6° of torsional rotation. The slope of this linear trend-line represents the restrained torsional stiffness (429.7 N·mm/Degree) of these specimens.

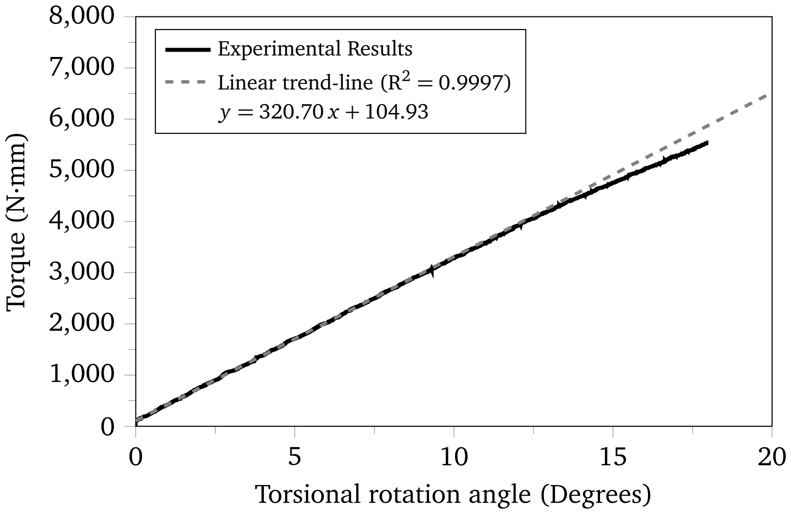

Figure D.4: Results of restrained torsion test of aluminium slotted tube specimen pair # 1. The plotted linear trend-line was fit through the data points from the first 6° of torsional rotation. The slope of this linear trend-line represents the restrained torsional stiffness (320.7 N·mm/Degree) of these specimens.

Appendix E

Permission for Use of Co-Authored Content

The following document demonstrates that the author has obtained permission from the co-author of [35] to reproduce and adapt parts of this manuscript for inclusion in Sections 1.2.3, 1.2.4, 1.2.5, & 1.2.9.

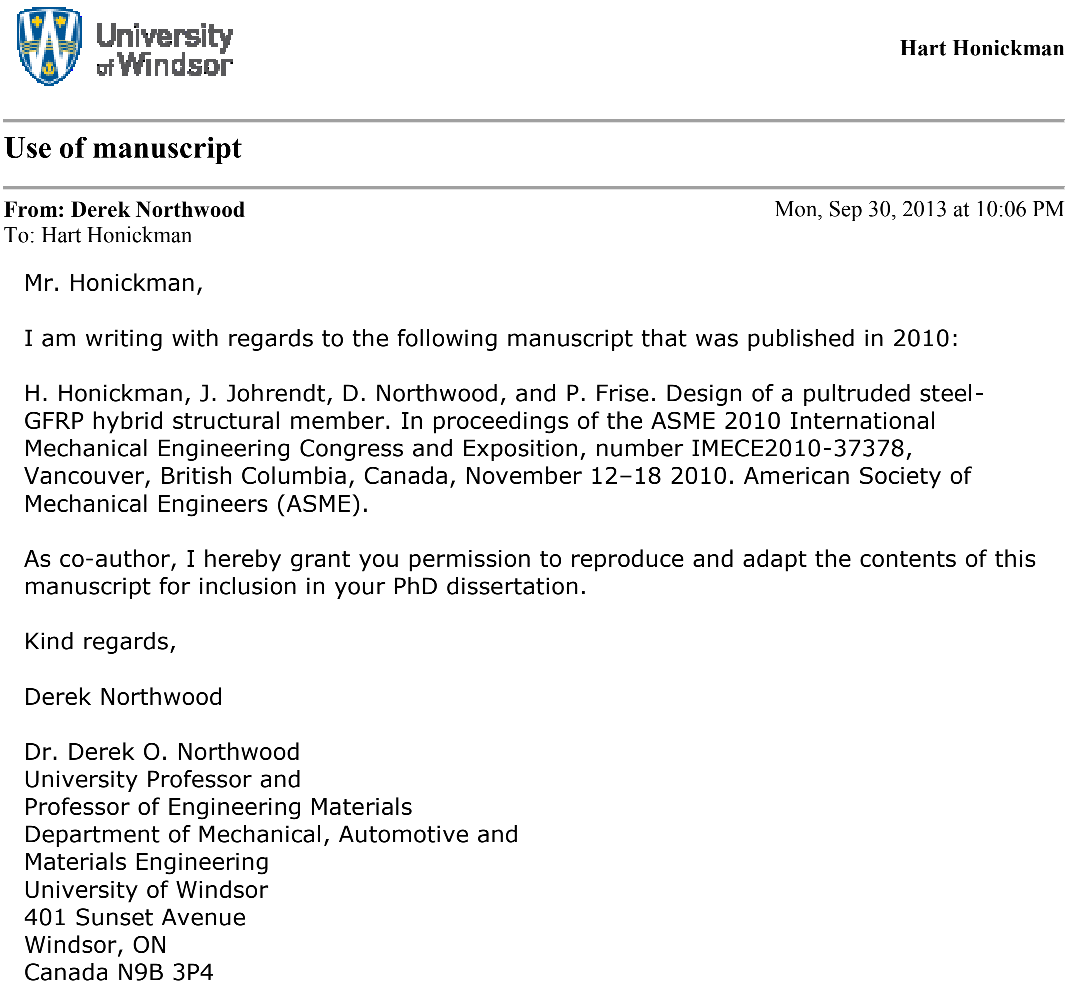

Hart Honickman

Use of manuscript

From: Derek Northwood Mon, Sep 30, 2013 at 10:06 PM
To: Hart Honickman

Mr. Honickman,

I am writing with regards to the following manuscript that was published in 2010:

H. Honickman, J. Johrendt, D. Northwood, and P. Frise. Design of a pultruded steel-GFRP hybrid structural member. In proceedings of the ASME 2010 International Mechanical Engineering Congress and Exposition, number IMECE2010-37378, Vancouver, British Columbia, Canada, November 12–18 2010. American Society of Mechanical Engineers (ASME).

As co-author, I hereby grant you permission to reproduce and adapt the contents of this manuscript for inclusion in your PhD dissertation.

Kind regards,

Derek Northwood

Dr. Derek O. Northwood
University Professor and
Professor of Engineering Materials
Department of Mechanical, Automotive and
Materials Engineering
University of Windsor
401 Sunset Avenue
Windsor, ON
Canada N9B 3P4

Appendix F

Permission for Use of Copyrighted Content

The following document demonstrates that the author has obtained permission from the copyright owner of [35] to reproduce and adapt parts of this manuscript for inclusion in Sections 1.2.3, 1.2.4, 1.2.5, & 1.2.9.

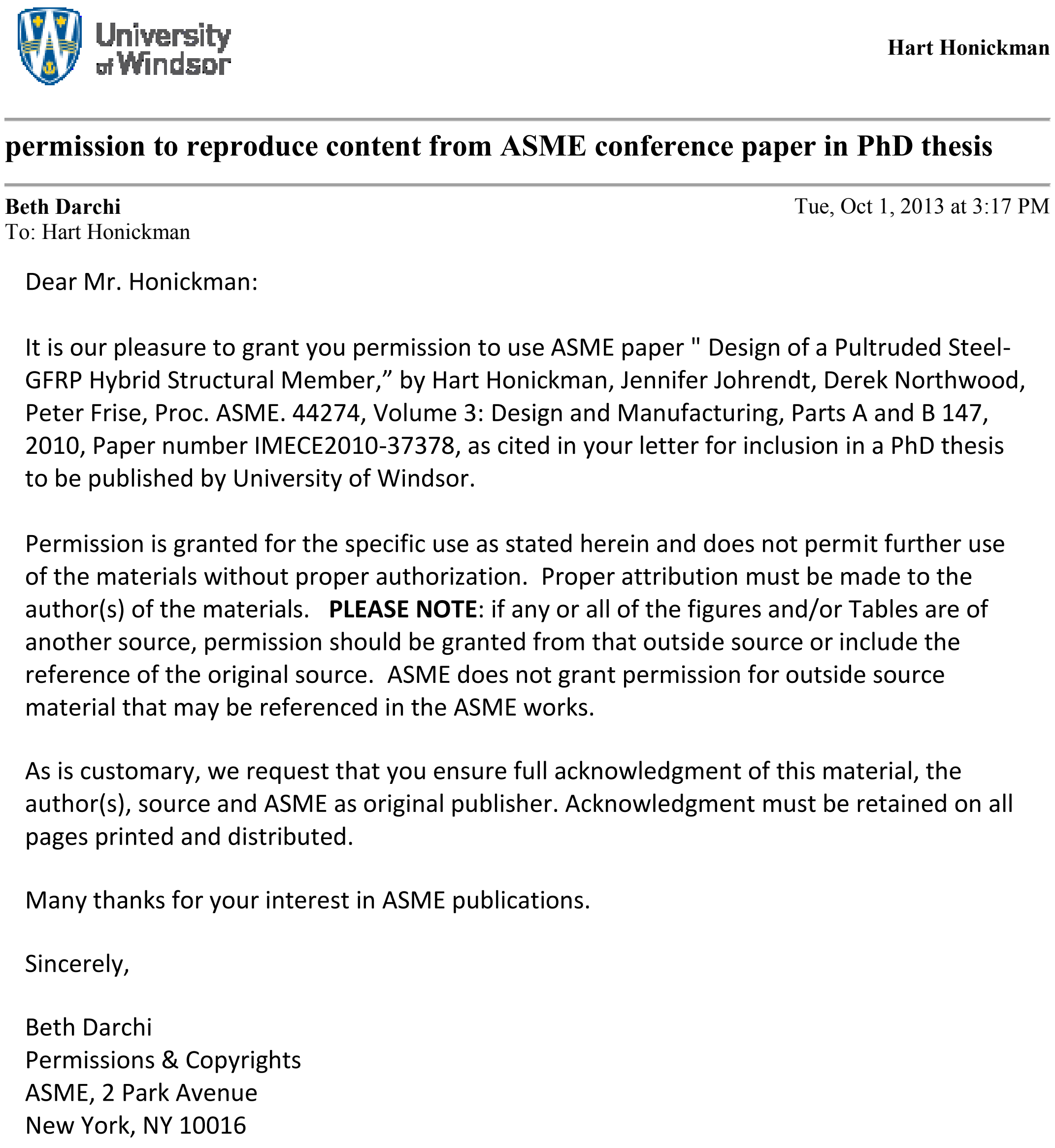

University of Windsor

Hart Honickman

permission to reproduce content from ASME conference paper in PhD thesis

Beth Darchi Tue, Oct 1, 2013 at 3:17 PM
To: Hart Honickman

Dear Mr. Honickman:

It is our pleasure to grant you permission to use ASME paper " Design of a Pultruded Steel-GFRP Hybrid Structural Member," by Hart Honickman, Jennifer Johrendt, Derek Northwood, Peter Frise, Proc. ASME. 44274, Volume 3: Design and Manufacturing, Parts A and B 147, 2010, Paper number IMECE2010-37378, as cited in your letter for inclusion in a PhD thesis to be published by University of Windsor.

Permission is granted for the specific use as stated herein and does not permit further use of the materials without proper authorization. Proper attribution must be made to the author(s) of the materials. **PLEASE NOTE**: if any or all of the figures and/or Tables are of another source, permission should be granted from that outside source or include the reference of the original source. ASME does not grant permission for outside source material that may be referenced in the ASME works.

As is customary, we request that you ensure full acknowledgment of this material, the author(s), source and ASME as original publisher. Acknowledgment must be retained on all pages printed and distributed.

Many thanks for your interest in ASME publications.

Sincerely,

Beth Darchi
Permissions & Copyrights
ASME, 2 Park Avenue
New York, NY 10016

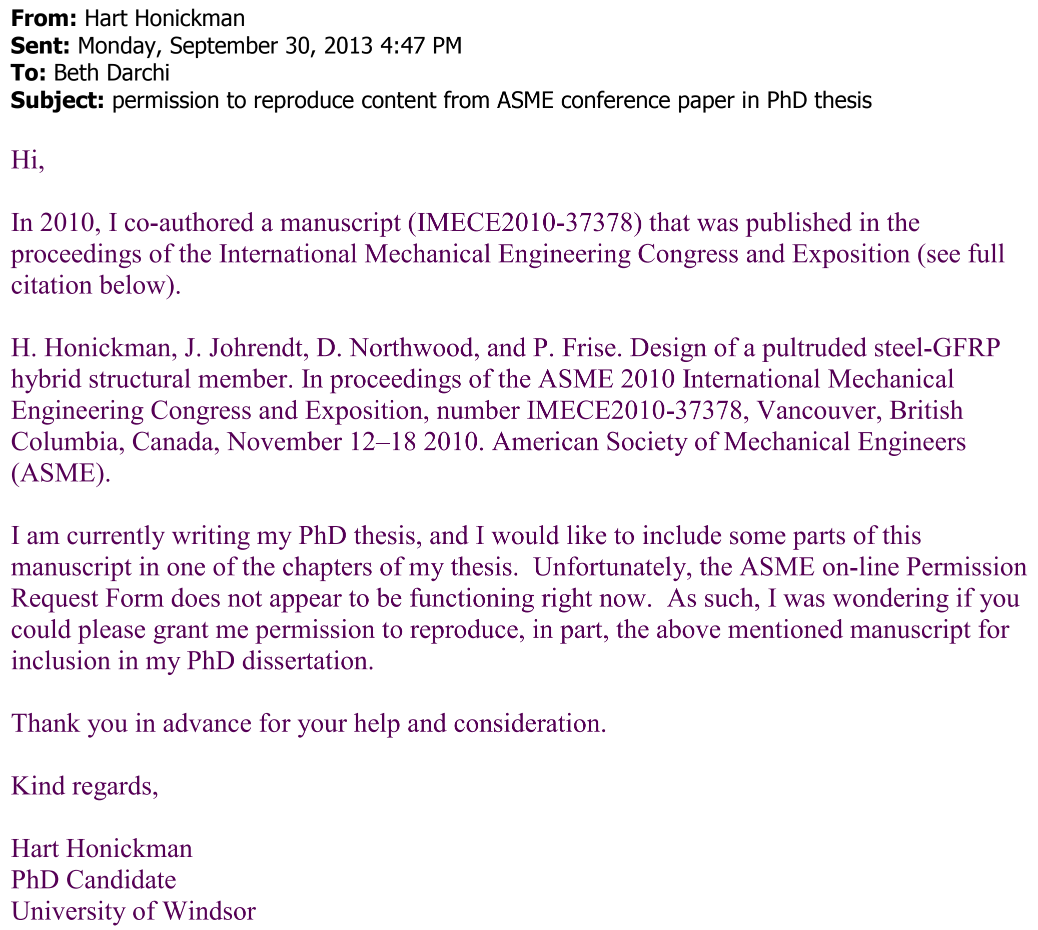

From: Hart Honickman
Sent: Monday, September 30, 2013 4:47 PM
To: Beth Darchi
Subject: permission to reproduce content from ASME conference paper in PhD thesis

Hi,

In 2010, I co-authored a manuscript (IMECE2010-37378) that was published in the proceedings of the International Mechanical Engineering Congress and Exposition (see full citation below).

H. Honickman, J. Johrendt, D. Northwood, and P. Frise. Design of a pultruded steel-GFRP hybrid structural member. In proceedings of the ASME 2010 International Mechanical Engineering Congress and Exposition, number IMECE2010-37378, Vancouver, British Columbia, Canada, November 12–18 2010. American Society of Mechanical Engineers (ASME).

I am currently writing my PhD thesis, and I would like to include some parts of this manuscript in one of the chapters of my thesis. Unfortunately, the ASME on-line Permission Request Form does not appear to be functioning right now. As such, I was wondering if you could please grant me permission to reproduce, in part, the above mentioned manuscript for inclusion in my PhD dissertation.

Thank you in advance for your help and consideration.

Kind regards,

Hart Honickman
PhD Candidate
University of Windsor

Appendix G

Proof of Copyright Ownership

The following documents demonstrate that the author retains ownership of the copyright pertaining to the manuscript [34] that was reproduced and adapted for inclusion in Section 3.11, and that explicit permission was obtained to reproduce its contents in the present dissertation.

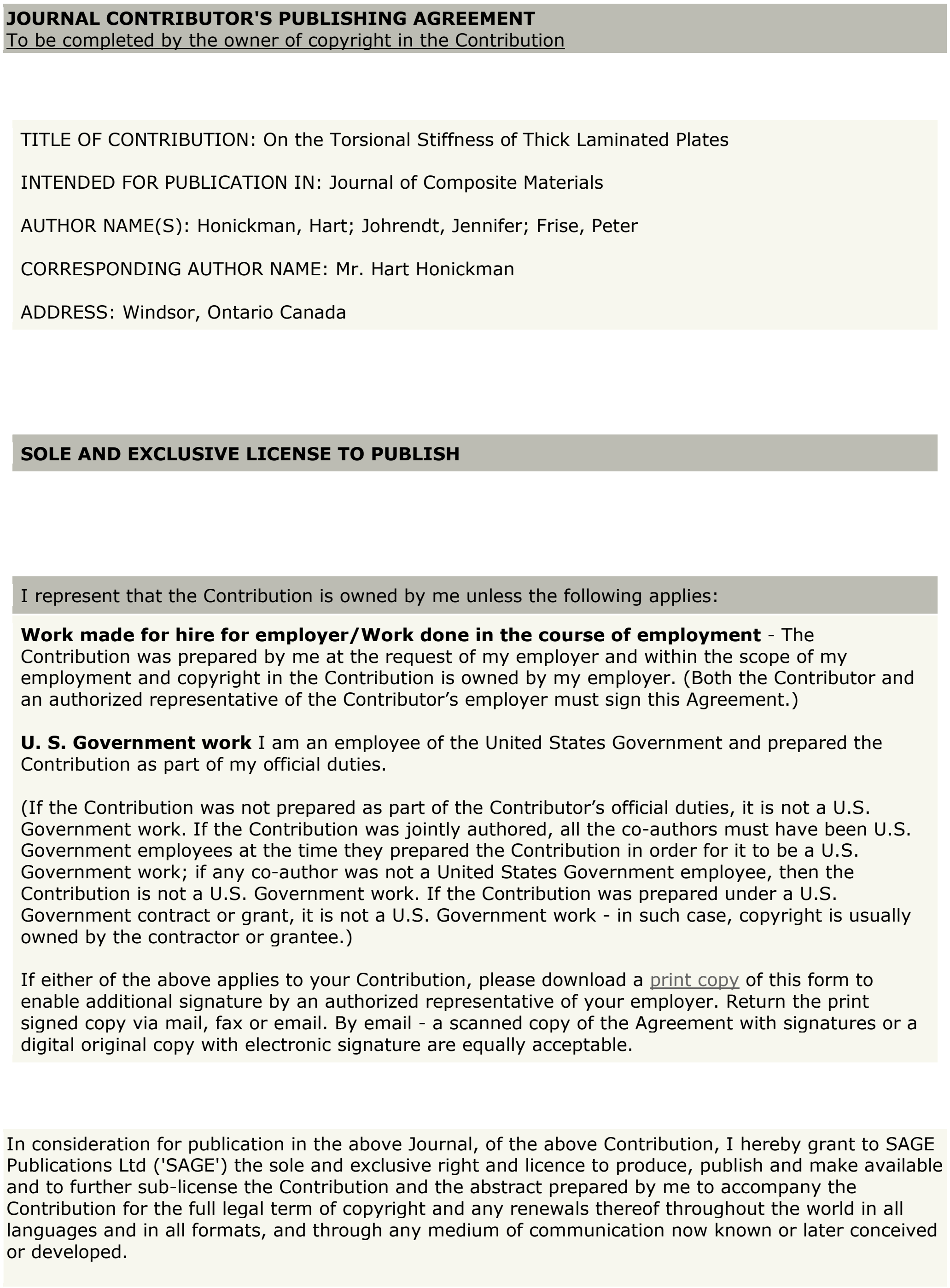

JOURNAL CONTRIBUTOR'S PUBLISHING AGREEMENT

To be completed by the owner of copyright in the Contribution

TITLE OF CONTRIBUTION: On the Torsional Stiffness of Thick Laminated Plates

INTENDED FOR PUBLICATION IN: Journal of Composite Materials

AUTHOR NAME(S): Honickman, Hart; Johrendt, Jennifer; Frise, Peter

CORRESPONDING AUTHOR NAME: Mr. Hart Honickman

ADDRESS: Windsor, Ontario Canada

SOLE AND EXCLUSIVE LICENSE TO PUBLISH

I represent that the Contribution is owned by me unless the following applies:

Work made for hire for employer/Work done in the course of employment - The Contribution was prepared by me at the request of my employer and within the scope of my employment and copyright in the Contribution is owned by my employer. (Both the Contributor and an authorized representative of the Contributor's employer must sign this Agreement.)

U. S. Government work I am an employee of the United States Government and prepared the Contribution as part of my official duties.

(If the Contribution was not prepared as part of the Contributor's official duties, it is not a U.S. Government work. If the Contribution was jointly authored, all the co-authors must have been U.S. Government employees at the time they prepared the Contribution in order for it to be a U.S. Government work; if any co-author was not a United States Government employee, then the Contribution is not a U.S. Government work. If the Contribution was prepared under a U.S. Government contract or grant, it is not a U.S. Government work - in such case, copyright is usually owned by the contractor or grantee.)

If either of the above applies to your Contribution, please download a print copy of this form to enable additional signature by an authorized representative of your employer. Return the print signed copy via mail, fax or email. By email - a scanned copy of the Agreement with signatures or a digital original copy with electronic signature are equally acceptable.

In consideration for publication in the above Journal, of the above Contribution, I hereby grant to SAGE Publications Ltd ('SAGE') the sole and exclusive right and licence to produce, publish and make available and to further sub-license the Contribution and the abstract prepared by me to accompany the Contribution for the full legal term of copyright and any renewals thereof throughout the world in all languages and in all formats, and through any medium of communication now known or later conceived or developed.

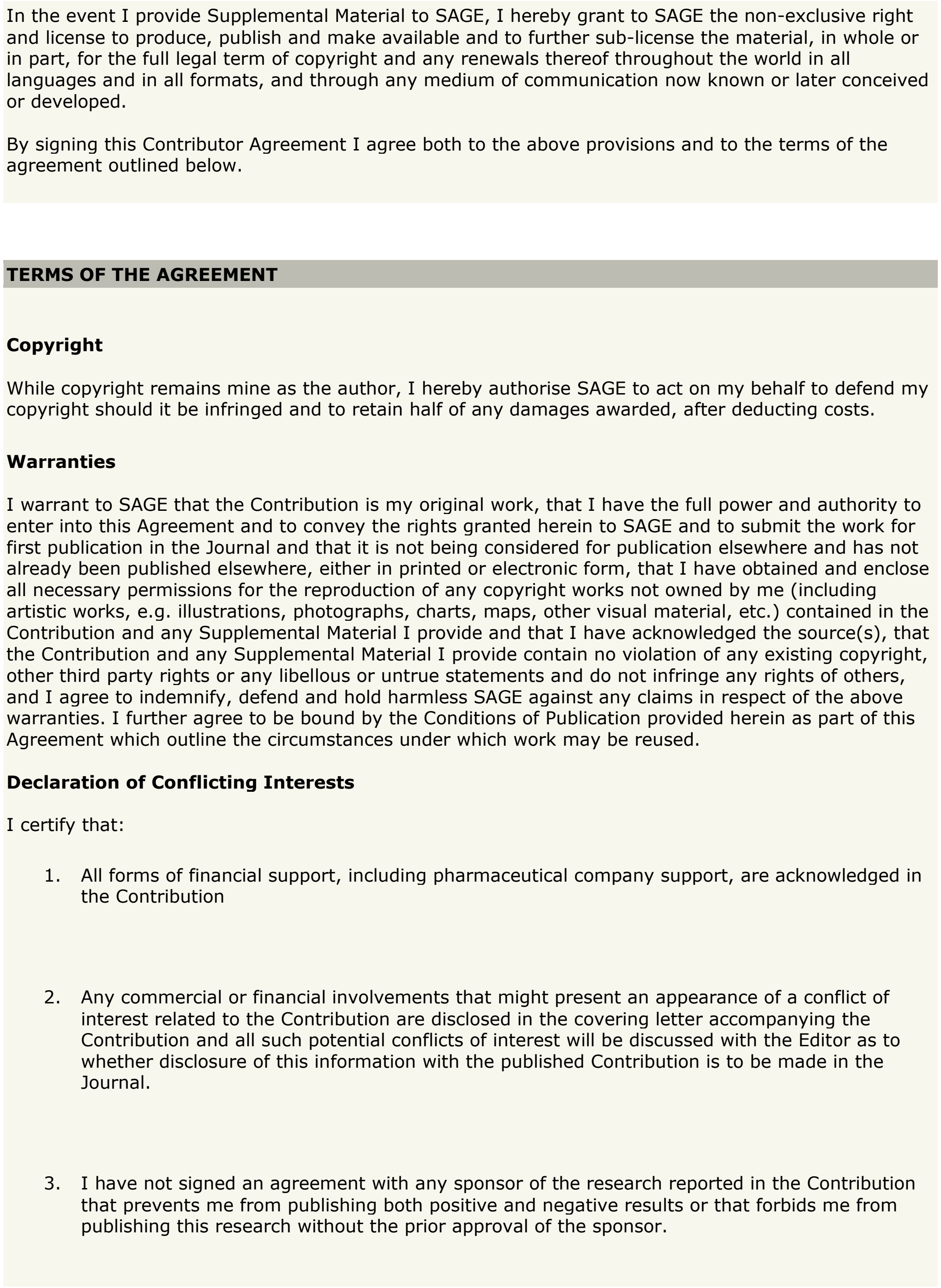

In the event I provide Supplemental Material to SAGE, I hereby grant to SAGE the non-exclusive right and license to produce, publish and make available and to further sub-license the material, in whole or in part, for the full legal term of copyright and any renewals thereof throughout the world in all languages and in all formats, and through any medium of communication now known or later conceived or developed.

By signing this Contributor Agreement I agree both to the above provisions and to the terms of the agreement outlined below.

TERMS OF THE AGREEMENT

Copyright

While copyright remains mine as the author, I hereby authorise SAGE to act on my behalf to defend my copyright should it be infringed and to retain half of any damages awarded, after deducting costs.

Warranties

I warrant to SAGE that the Contribution is my original work, that I have the full power and authority to enter into this Agreement and to convey the rights granted herein to SAGE and to submit the work for first publication in the Journal and that it is not being considered for publication elsewhere and has not already been published elsewhere, either in printed or electronic form, that I have obtained and enclose all necessary permissions for the reproduction of any copyright works not owned by me (including artistic works, e.g. illustrations, photographs, charts, maps, other visual material, etc.) contained in the Contribution and any Supplemental Material I provide and that I have acknowledged the source(s), that the Contribution and any Supplemental Material I provide contain no violation of any existing copyright, other third party rights or any libellous or untrue statements and do not infringe any rights of others, and I agree to indemnify, defend and hold harmless SAGE against any claims in respect of the above warranties. I further agree to be bound by the Conditions of Publication provided herein as part of this Agreement which outline the circumstances under which work may be reused.

Declaration of Conflicting Interests

I certify that:

1. All forms of financial support, including pharmaceutical company support, are acknowledged in the Contribution

2. Any commercial or financial involvements that might present an appearance of a conflict of interest related to the Contribution are disclosed in the covering letter accompanying the Contribution and all such potential conflicts of interest will be discussed with the Editor as to whether disclosure of this information with the published Contribution is to be made in the Journal.

3. I have not signed an agreement with any sponsor of the research reported in the Contribution that prevents me from publishing both positive and negative results or that forbids me from publishing this research without the prior approval of the sponsor.

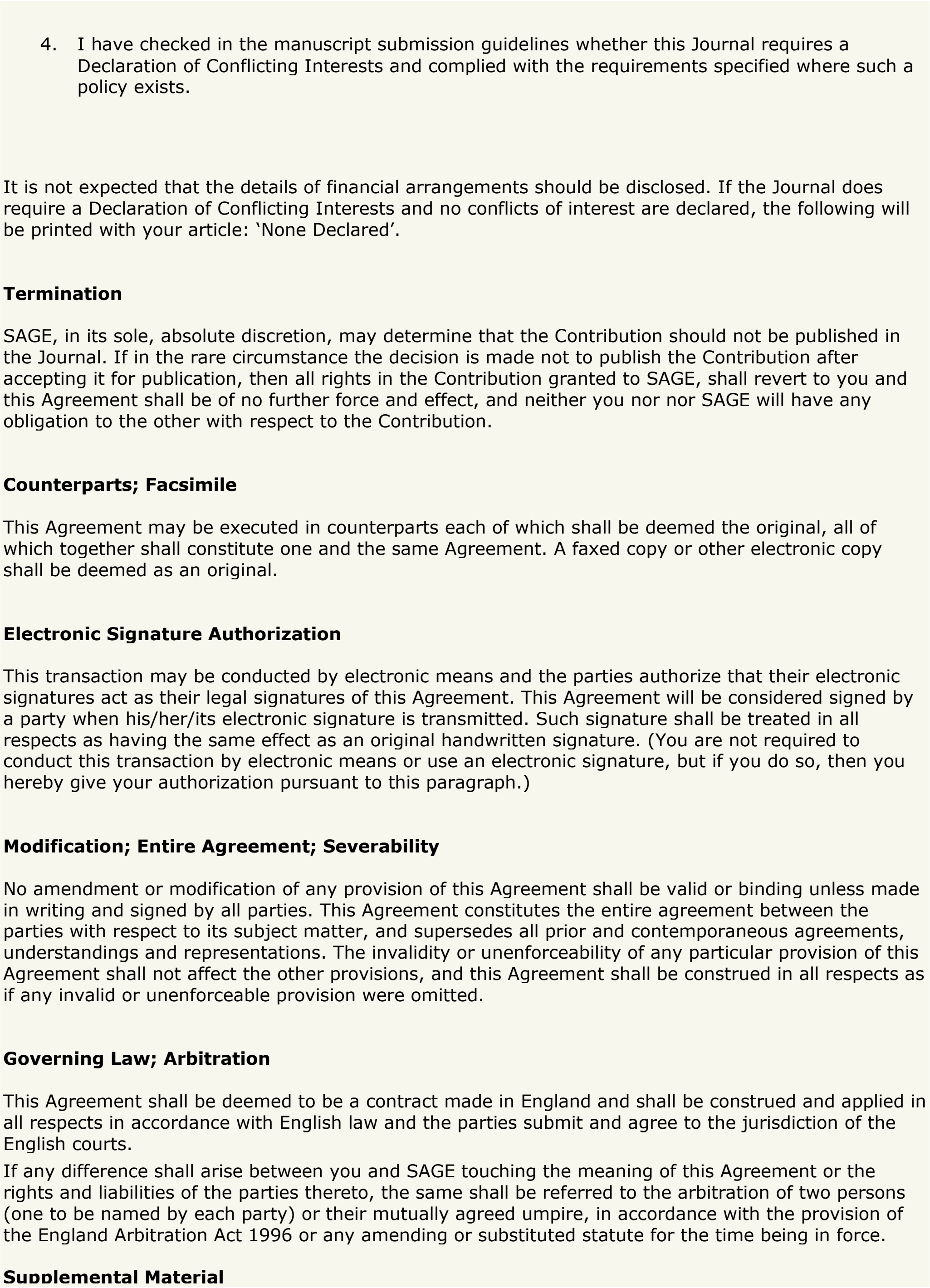

4. I have checked in the manuscript submission guidelines whether this Journal requires a Declaration of Conflicting Interests and complied with the requirements specified where such a policy exists.

It is not expected that the details of financial arrangements should be disclosed. If the Journal does require a Declaration of Conflicting Interests and no conflicts of interest are declared, the following will be printed with your article: ‘None Declared’.

Termination

SAGE, in its sole, absolute discretion, may determine that the Contribution should not be published in the Journal. If in the rare circumstance the decision is made not to publish the Contribution after accepting it for publication, then all rights in the Contribution granted to SAGE, shall revert to you and this Agreement shall be of no further force and effect, and neither you nor nor SAGE will have any obligation to the other with respect to the Contribution.

Counterparts; Facsimile

This Agreement may be executed in counterparts each of which shall be deemed the original, all of which together shall constitute one and the same Agreement. A faxed copy or other electronic copy shall be deemed as an original.

Electronic Signature Authorization

This transaction may be conducted by electronic means and the parties authorize that their electronic signatures act as their legal signatures of this Agreement. This Agreement will be considered signed by a party when his/her/its electronic signature is transmitted. Such signature shall be treated in all respects as having the same effect as an original handwritten signature. (You are not required to conduct this transaction by electronic means or use an electronic signature, but if you do so, then you hereby give your authorization pursuant to this paragraph.)

Modification; Entire Agreement; Severability

No amendment or modification of any provision of this Agreement shall be valid or binding unless made in writing and signed by all parties. This Agreement constitutes the entire agreement between the parties with respect to its subject matter, and supersedes all prior and contemporaneous agreements, understandings and representations. The invalidity or unenforceability of any particular provision of this Agreement shall not affect the other provisions, and this Agreement shall be construed in all respects as if any invalid or unenforceable provision were omitted.

Governing Law; Arbitration

This Agreement shall be deemed to be a contract made in England and shall be construed and applied in all respects in accordance with English law and the parties submit and agree to the jurisdiction of the English courts.

If any difference shall arise between you and SAGE touching the meaning of this Agreement or the rights and liabilities of the parties thereto, the same shall be referred to the arbitration of two persons (one to be named by each party) or their mutually agreed umpire, in accordance with the provision of the England Arbitration Act 1996 or any amending or substituted statute for the time being in force.

Supplemental Material

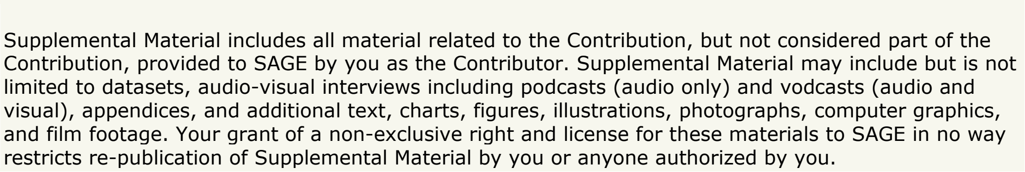

Supplemental Material includes all material related to the Contribution, but not considered part of the Contribution, provided to SAGE by you as the Contributor. Supplemental Material may include but is not limited to datasets, audio-visual interviews including podcasts (audio only) and vodcasts (audio and visual), appendices, and additional text, charts, figures, illustrations, photographs, computer graphics, and film footage. Your grant of a non-exclusive right and license for these materials to SAGE in no way restricts re-publication of Supplemental Material by you or anyone authorized by you.

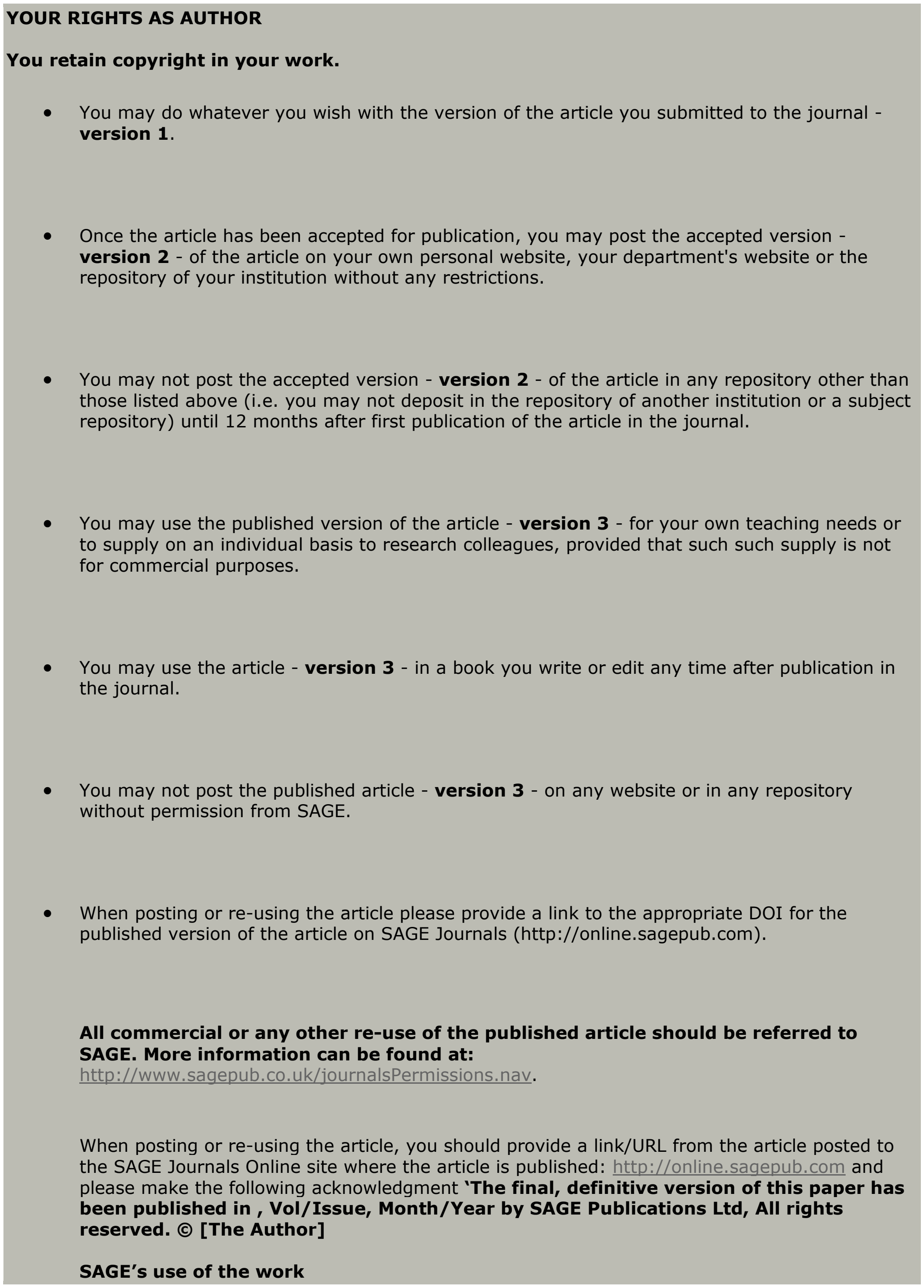

YOUR RIGHTS AS AUTHOR

You retain copyright in your work.

- You may do whatever you wish with the version of the article you submitted to the journal - **version 1**.
- Once the article has been accepted for publication, you may post the accepted version - **version 2** - of the article on your own personal website, your department's website or the repository of your institution without any restrictions.
- You may not post the accepted version - **version 2** - of the article in any repository other than those listed above (i.e. you may not deposit in the repository of another institution or a subject repository) until 12 months after first publication of the article in the journal.
- You may use the published version of the article - **version 3** - for your own teaching needs or to supply on an individual basis to research colleagues, provided that such such supply is not for commercial purposes.
- You may use the article - **version 3** - in a book you write or edit any time after publication in the journal.
- You may not post the published article - **version 3** - on any website or in any repository without permission from SAGE.
- When posting or re-using the article please provide a link to the appropriate DOI for the published version of the article on SAGE Journals (http://online.sagepub.com).

All commercial or any other re-use of the published article should be referred to SAGE. More information can be found at: http://www.sagepub.co.uk/journalsPermissions.nav.

When posting or re-using the article, you should provide a link/URL from the article posted to the SAGE Journals Online site where the article is published: http://online.sagepub.com and please make the following acknowledgment **'The final, definitive version of this paper has been published in , Vol/Issue, Month/Year by SAGE Publications Ltd, All rights reserved. © [The Author]**

SAGE's use of the work

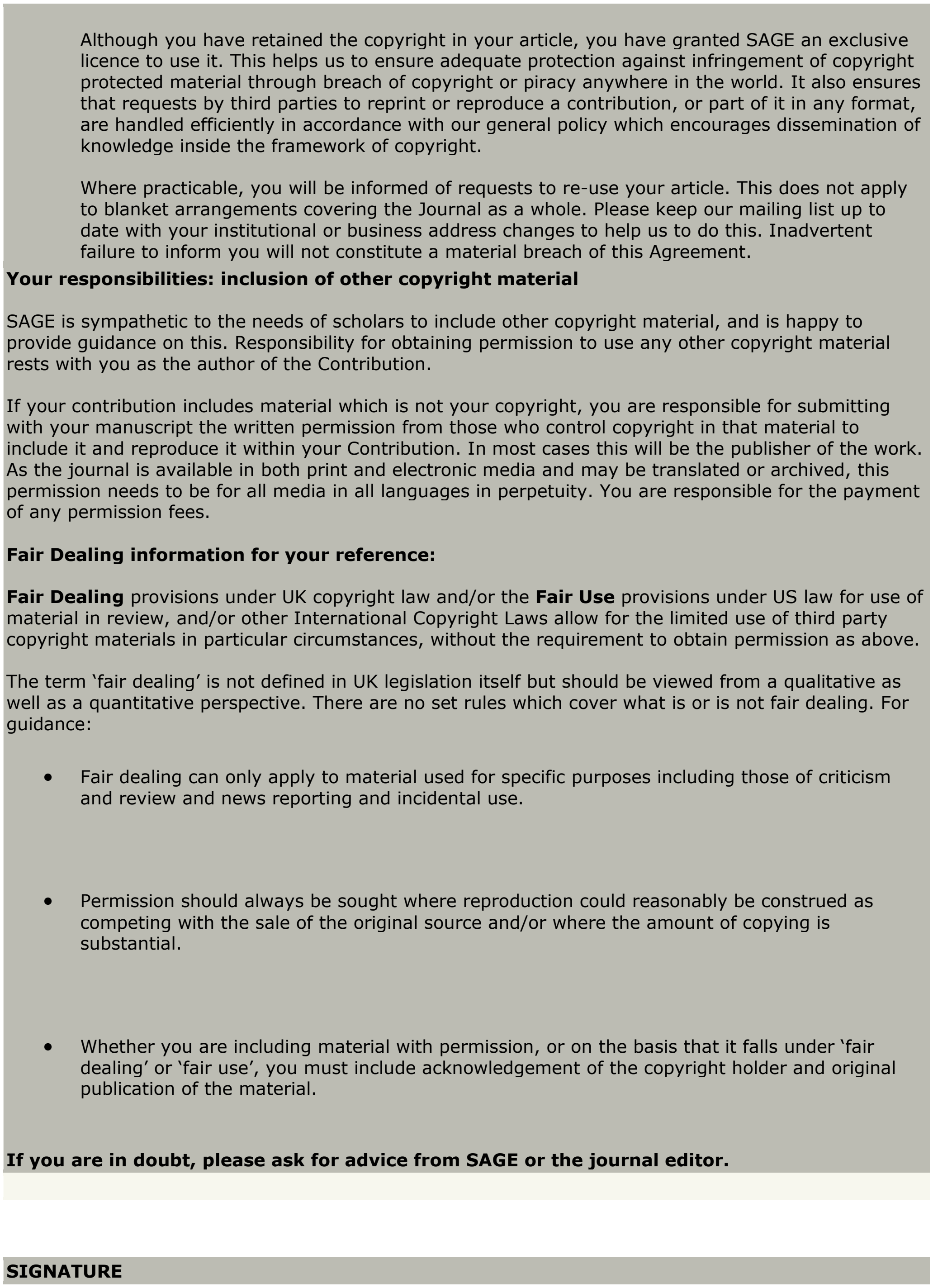

Although you have retained the copyright in your article, you have granted SAGE an exclusive licence to use it. This helps us to ensure adequate protection against infringement of copyright protected material through breach of copyright or piracy anywhere in the world. It also ensures that requests by third parties to reprint or reproduce a contribution, or part of it in any format, are handled efficiently in accordance with our general policy which encourages dissemination of knowledge inside the framework of copyright.

Where practicable, you will be informed of requests to re-use your article. This does not apply to blanket arrangements covering the Journal as a whole. Please keep our mailing list up to date with your institutional or business address changes to help us to do this. Inadvertent failure to inform you will not constitute a material breach of this Agreement.

Your responsibilities: inclusion of other copyright material

SAGE is sympathetic to the needs of scholars to include other copyright material, and is happy to provide guidance on this. Responsibility for obtaining permission to use any other copyright material rests with you as the author of the Contribution.

If your contribution includes material which is not your copyright, you are responsible for submitting with your manuscript the written permission from those who control copyright in that material to include it and reproduce it within your Contribution. In most cases this will be the publisher of the work. As the journal is available in both print and electronic media and may be translated or archived, this permission needs to be for all media in all languages in perpetuity. You are responsible for the payment of any permission fees.

Fair Dealing information for your reference:

Fair Dealing provisions under UK copyright law and/or the **Fair Use** provisions under US law for use of material in review, and/or other International Copyright Laws allow for the limited use of third party copyright materials in particular circumstances, without the requirement to obtain permission as above.

The term 'fair dealing' is not defined in UK legislation itself but should be viewed from a qualitative as well as a quantitative perspective. There are no set rules which cover what is or is not fair dealing. For guidance:

- Fair dealing can only apply to material used for specific purposes including those of criticism and review and news reporting and incidental use.

- Permission should always be sought where reproduction could reasonably be construed as competing with the sale of the original source and/or where the amount of copying is substantial.

- Whether you are including material with permission, or on the basis that it falls under 'fair dealing' or 'fair use', you must include acknowledgement of the copyright holder and original publication of the material.

If you are in doubt, please ask for advice from SAGE or the journal editor.

SIGNATURE

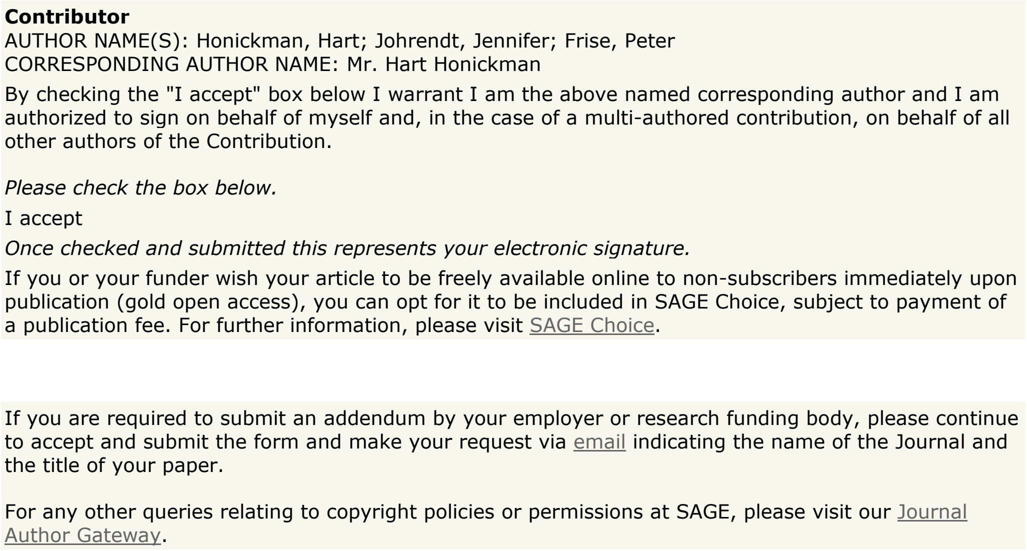

Contributor
AUTHOR NAME(S): Honickman, Hart; Johrendt, Jennifer; Frise, Peter
CORRESPONDING AUTHOR NAME: Mr. Hart Honickman

By checking the "I accept" box below I warrant I am the above named corresponding author and I am authorized to sign on behalf of myself and, in the case of a multi-authored contribution, on behalf of all other authors of the Contribution.

Please check the box below.

I accept

Once checked and submitted this represents your electronic signature.

If you or your funder wish your article to be freely available online to non-subscribers immediately upon publication (gold open access), you can opt for it to be included in SAGE Choice, subject to payment of a publication fee. For further information, please visit SAGE Choice.

If you are required to submit an addendum by your employer or research funding body, please continue to accept and submit the form and make your request via email indicating the name of the Journal and the title of your paper.

For any other queries relating to copyright policies or permissions at SAGE, please visit our Journal Author Gateway.

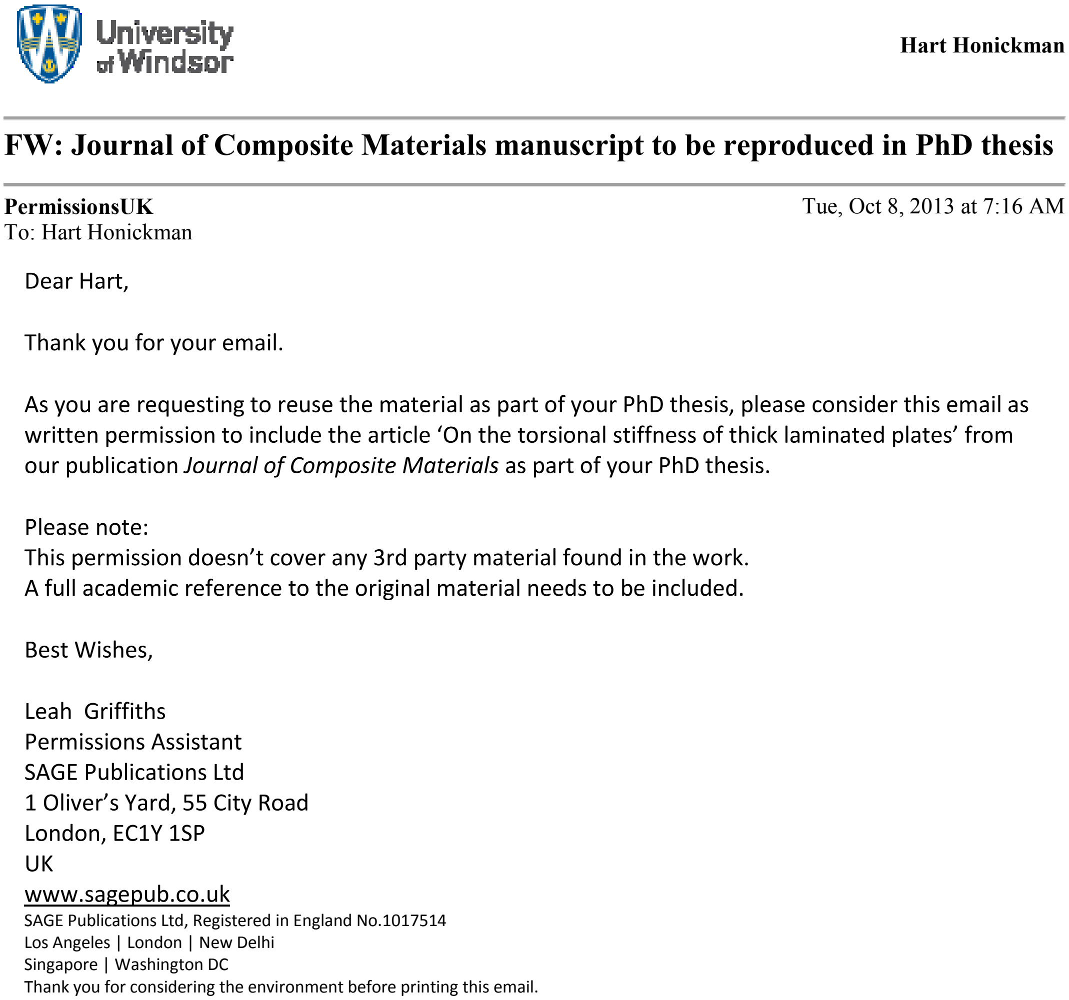

Hart Honickman

FW: Journal of Composite Materials manuscript to be reproduced in PhD thesis

PermissionsUK Tue, Oct 8, 2013 at 7:16 AM
To: Hart Honickman

Dear Hart,

Thank you for your email.

As you are requesting to reuse the material as part of your PhD thesis, please consider this email as written permission to include the article 'On the torsional stiffness of thick laminated plates' from our publication *Journal of Composite Materials* as part of your PhD thesis.

Please note:
This permission doesn't cover any 3rd party material found in the work.
A full academic reference to the original material needs to be included.

Best Wishes,

Leah Griffiths
Permissions Assistant
SAGE Publications Ltd
1 Oliver's Yard, 55 City Road
London, EC1Y 1SP
UK
www.sagepub.co.uk
SAGE Publications Ltd, Registered in England No.1017514
Los Angeles | London | New Delhi
Singapore | Washington DC
Thank you for considering the environment before printing this email.

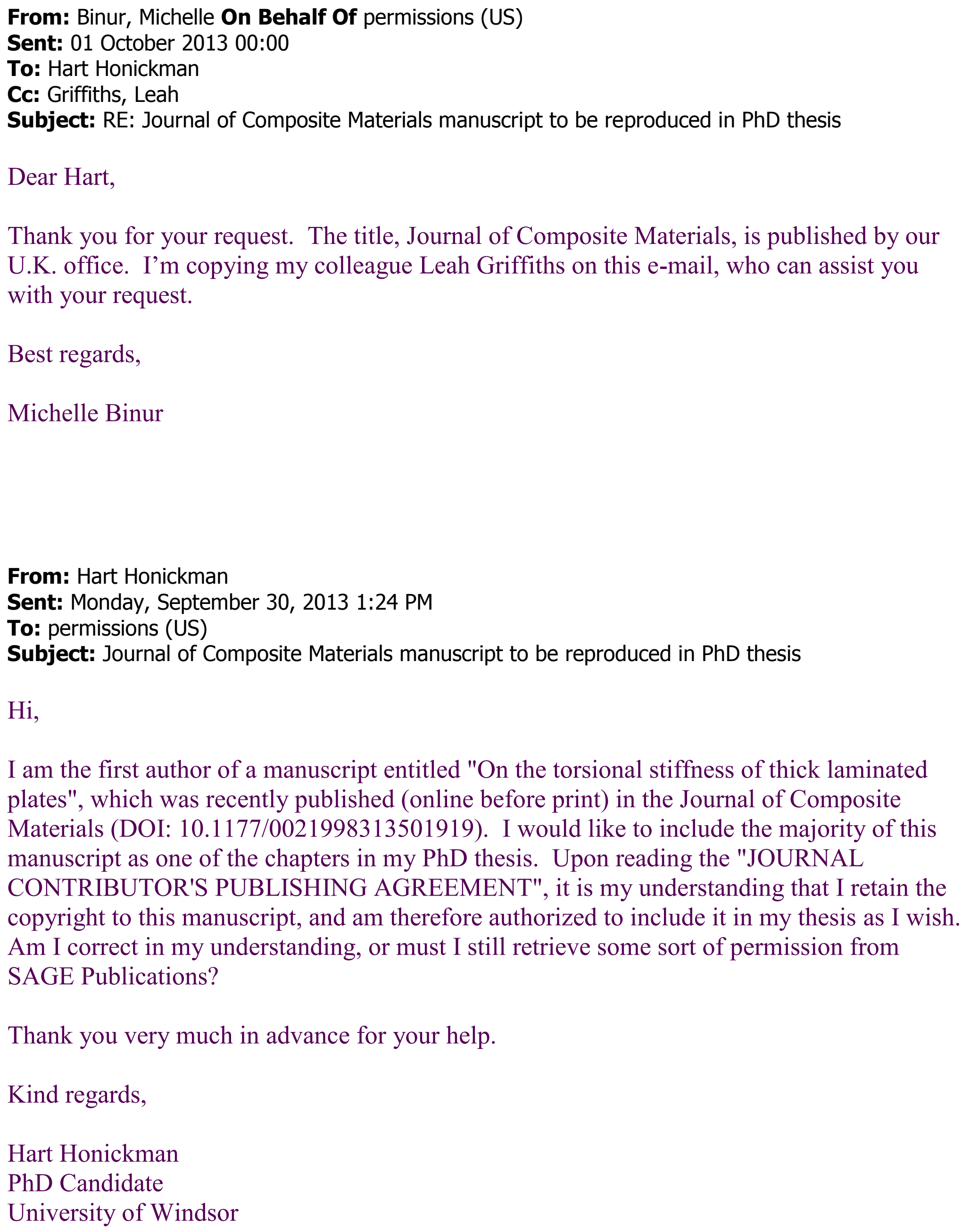

From: Binur, Michelle **On Behalf Of** permissions (US)
Sent: 01 October 2013 00:00
To: Hart Honickman
Cc: Griffiths, Leah
Subject: RE: Journal of Composite Materials manuscript to be reproduced in PhD thesis

Dear Hart,

Thank you for your request. The title, Journal of Composite Materials, is published by our U.K. office. I'm copying my colleague Leah Griffiths on this e-mail, who can assist you with your request.

Best regards,

Michelle Binur

From: Hart Honickman
Sent: Monday, September 30, 2013 1:24 PM
To: permissions (US)
Subject: Journal of Composite Materials manuscript to be reproduced in PhD thesis

Hi,

I am the first author of a manuscript entitled "On the torsional stiffness of thick laminated plates", which was recently published (online before print) in the Journal of Composite Materials (DOI: 10.1177/0021998313501919). I would like to include the majority of this manuscript as one of the chapters in my PhD thesis. Upon reading the "JOURNAL CONTRIBUTOR'S PUBLISHING AGREEMENT", it is my understanding that I retain the copyright to this manuscript, and am therefore authorized to include it in my thesis as I wish. Am I correct in my understanding, or must I still retrieve some sort of permission from SAGE Publications?

Thank you very much in advance for your help.

Kind regards,

Hart Honickman
PhD Candidate
University of Windsor

Vita Auctoris

Name:	Hart Noah Honickman
Year of birth:	1984
Place of birth:	Toronto, Ontario, Canada
Secondary education:	Crescent School Toronto, Ontario, Canada (1999 – 2002)
Post-secondary education:	Bachelor of Science in Engineering, with First Class Honours Civil Engineering – Infrastructure, Queen's University at Kingston Kingston, Ontario, Canada (2002 – 2006)
Post-graduate education:	Master of Science in Engineering Civil Engineering – Infrastructure, Queen's University at Kingston Kingston, Ontario, Canada (2006 – 2008)
	Doctor of Philosophy Mechanical Engineering, University of Windsor Windsor, Ontario, Canada (2008 – 2013) Expected date of awarding of degree: June 11, 2014